

*Advanced polymeric composites for
self-healing structural materials*

Raffaele Corvino



Unione Europea



*Ministero dell'Istruzione,
dell'Università e della Ricerca*



UNIVERSITÀ DEGLI
STUDI DI SALERNO

Department of Industrial Engineering

***Ph.D. Course in Chemical Engineering
(X Cycle-New Series)***

***Advanced polymeric composites for self-healing
structural materials***

Supervisor

Prof.ssa Liberata Guadagno

Ph.D. student

Raffaele Corvino

Scientific Referees

Prof. Pasquale Longo

Ing. Augusto Albolino

Ing. Salvatore Russo

Ing. Fiorenzo Lenzi

Ph.D. Course Coordinator

Prof. Ing. Paolo Ciambelli

To my family and...

... in loving memory of my dear uncles Domenico e Pasquale Corvino

On the cover: "The battle of the Argonne" René Magritte, oil on canvas –
1959 - Private collection, New York.
Fisciano, 23 February 2012.

Publications List

Patents:

Guadagno, Liberata; Raimondo, Marialuigia; Naddeo, Carlo; Mariconda, Annaluisa; Corvino Raffaele; Longo Pasquale; Vittoria, Vittoria; Russo, Salvatore; Iannuzzo, Generoso.

Process for preparing self-healing composite materials of high efficiency for structural applications.

Publication number: US 2011118385 (A1) Publication date: **May. 19, 2011**

Also published as:

EP 2325254 (A1) Publication date: November. 11, 2010

IT TO20090870 (A1) data di deposito: 13 novembre 2009

International Congress:

M. Raimondo, R. Corvino, L. Guadagno, P. Longo, C. Naddeo, A. Mariconda. **Advanced Polymeric Composites for Self-healing Structural Materials.** European Polymer Congress 2011 (XII Congress of the Specialized Group of Polymers (GEP), **26th June-1st July 2011, Granada, Spain.**

(Book of abstracts: p. 749, ISBN: 978-84-694-3124-5).

National Congress:

L. Guadagno, M. Raimondo, C. Naddeo, R. Corvino, V. Vittoria, G. Russo, S. Russo, K. Lafdi. **Composites for Self-healing Structural Materials.** Workshop “Advances in Polymer based Materials and Related Technologies”. **May 29th – June 1st, 2011, Capri (Italy)** (book of abstracts: p. 122).

Summary

Summary	I
Figures Index	VII
Table Index	XV
Abstract	XVII
Introduction	- 1 -
1. Concept of Self-healing	- 1 -
1.1 Composite Materials	- 4 -
1.1.2 Constituents of Composites	- 5 -
1.2 Fracture mechanisms and traditional repair methods for polymeric composites materials	- 6 -
1.2.1 Welding	- 8 -
1.2.2 Patching and resin injection	- 8 -
1.3 Progress beyond the state-of-art of Self-healing materials-	10 -
1.3.1 Intrinsic self-healing	- 11 -
1.3.1.1 Diels-Alder Polymers	- 11 -
1.3.1.2 Dispersed Thermoplastic Polymers	- 15 -
1.3.1.3 Ionomeric Self-healing materials	- 16 -
1.3.1.4 UV initiated Self-healing	- 17 -
1.3.1.5 Supramolecular Self-healing materials	- 18 -
1.3.1.6 Self-healing via molecular diffusion	- 20 -
1.3.2 Extrinsic self-healing	- 23 -
1.3.2.1 Self-healing in terms of healant loaded pipelines (hollow fiber approach)	- 23 -
1.3.2.2 Microvascular Networks	- 27 -
1.3.2.3 Capsule-Based Self-healing Materials	- 30 -

1.3.2.3.1 Microcapsule-Parameters	- 32 -
1.3.2.3.2 Microencapsulated healing agents	- 37 -
1.3.3 Assessment of Self-healing efficiency _____	- 43 -
1.4 Ph.D. Aim _____	- 46 -
Materials	- 51 -
2. Materials _____	- 51 -
2.1 Materials: polymeric matrix _____	- 51 -
2.2 Materials: Catalysts active in the ROMP reaction _____	- 55 -
2.2.1 First and second generation Grubbs' catalysts _____	- 55 -
2.2.2 First and second generation Hoveyda-Grubbs' catalysts-	56 -
2.3 Materials: Microcapsules and healing agents _____	- 57 -
Methods.....	- 61 -
3 Methods _____	- 61 -
3.1 Thermal Analysis _____	- 61 -
3.1.1 Thermogravimetric Analysis (TGA) _____	- 62 -
3.1.2 Differential Scanning Calorimetry (DSC) _____	- 63 -
3.1.2.1 Characterization of epoxy resins using differential scanning calorimetry	- 65 -
3.1.3 Dynamic Mechanical Analysis (DMA) _____	- 68 -
3.2 Nuclear Magnetic Resonance Spectroscopy and Infrared Analysis _____	- 70 -
3.2.1 Nuclear Magnetic Resonance (NMR) _____	- 70 -
3.2.2 Infrared Spectroscopy (IR spectroscopy) _____	- 72 -
3.3 Morphological Analysis: Scanning Electron Microscope-	75 -
3.4 Method for evaluation of Self-healing Efficiency _____	- 78 -
Results and Discussions:.....	- 81 -
Early Systems	- 81 -
4 Early Systems: Introduction _____	- 81 -

4.1 Curing of Epoxy Matrix _____	- 82 -
4.1.1 Differential Scanning Calorimetry _____	- 82 -
4.1.2 Dynamic Mechanical Analysis _____	- 90 -
4.1.3 Infrared Spectroscopy Analysis _____	- 93 -
4.2 Microcapsules Manufacturing and Characterization ____	- 94 -
4.2.1 Check of healing agent content: ¹ H NMR Analysis __	- 97 -
4.2.2 Metathesis reaction of DCPD contained in synthesized microcapsules in presence of first generation Grubbs' catalyst: FT/IR Analysis _____	- 99 -
4.2.3 Microcapsules Thermal Analysis: TGA, DSC _____	- 102 -
4.2.3.1 Thermogravimetric analysis	- 102 -
4.2.3.2 Differential Scanning Calorimetry	- 103 -
4.3 Grubbs' Catalyst (G1) Characterization _____	- 104 -
4.3.1 First Generation Grubbs' Catalyst (G1) Morphology	- 104 -
4.3.2 First Generation Grubbs' Catalyst (G1) Thermal Analysis _____	- 106 -
4.3.3 Thermolytic stability of First Generation Grubbs' Catalyst (G1): ¹ H NMR Spectroscopy _____	- 108 -
4.4 Self-healing Systems _____	- 118 -
4.4.1 Thermogravimetric analysis _____	- 119 -
4.4.2 Grubbs' Catalyst Stability inside Self-healing System: FT/IR and ¹ H NMR Analysis _____	- 120 -
4.4.2.1 Infrared Analysis of Catalyst inside Self-healing sample	- 120 -
4.4.2.2 Spectroscopy Analysis of Catalyst inside Self-healing sample	- 121 -
4.4.3 Dynamic Mechanical Analysis on Self-Healing Samples-	123 -
4.5 Romp Reaction of DCPD with 1st Generation Grubbs' Catalyst _____	- 127 -
4.6 Early Systems: Conclusions _____	- 129 -

Results and Discussions:..... - 131 -**New Systems - 131 -**

- 5 New Systems: Introduction _____ - 131 -
- 5.1 Microcapsules Characterization _____ - 133 -
 - 5.1.1 Check of ENB healing agent content: ¹H NMR Analysis- 134 -
 - 5.1.2 Microcapsules filled with ENB: Thermal Analysis
(TGA-DSC) _____ - 136 -
- 5.2 Romp Reaction of ENB with 1st Generation Grubbs'
Catalyst. _____ - 138 -
- 5.3 Romp Reaction of ENB with 2nd Generation Grubbs'
Catalyst _____ - 140 -
- 5.4 Thermolytic Decomposition of 2nd Generation Grubbs'
Catalyst: ¹H NMR Analysis _____ - 142 -
- 5.5 New Systems: Conclusions _____ - 144 -

Results and Discussions:..... - 145 -**Latter Systems..... - 145 -**

- 6 Latter Systems: Introduction _____ - 145 -
 - 6.1 Morphology of Hoveyda Grubbs' Catalys HG1 and HG2- 147 -
 - 6.2 Evaluation of Thermal Stability of Hoveyda Grubb's
Catalysts, HG1 and HG2 _____ - 151 -
 - 6.2.1 Thermogravimetric Analysis (TGA) _____ - 151 -
 - 6.2.2 Thermolytic decomposition of HG1 and HG2 - ¹H NMR
Analysis _____ - 152 -
 - 6.2.3 Thermolytic decomposition of HG1 and HG2 - Infrared
Analysis _____ - 155 -
-

6.3 Romp Reaction of ENB with first and second generation	
Hoveyda-Grubbs' Catalysts _____	- 158 -
6.3.1 Evaluation of Cross-linked Fraction of Metathesis	
Products _____	- 160 -
6.3.2 Phase Separation Tests for DCPD + ENB blends in	
diferrent proportions (2.5%, 5% of DCPD) at -50 °C _	- 161 -
6.4 Self-healing Systems _____	- 164 -
6.4.1 Dynamic Mechanical Properties of Self-healing Systems-	165 -
6.4.2 Thermal Analysis of Self-healing Systems _____	- 170 -
6.4.2.1 Differential Scanning Calorimetry of self-healing	
samples _____	- 170 -
6.4.2.2 Thermogravimetric Analysis of self-healing samples	- 172 -
6.5 Evaluation of Self-healing Efficiency _____	- 173 -
6.5.1 Design and Realization of the molds for the	
manufacturing of self-healing specimens _____	- 174 -
6.5.2 Self-healing Efficiency Tests _____	- 177 -
6.6 System Scale - up: Development of Carbon Fiber	
Composite _____	- 188 -
Conclusions	- 193 -
7.Conclusions _____	- 193 -
Bibliography	- 197 -

Figures Index

Figure 1. Damage modes in polymer composites. Indentation, impact, corrosive environments, ballistic punctures, surface scratching, and fatigue can lead to various damage modes in polymer composites, as shown here: (a) delamination, (b) impact/indentation surface cracking, (c) fiber debonding, (d) fiber rupture and pullout, (e) transverse and shear cracking, (f) puncture, (g) deep cut in coating, (h) corrosion in protected metal, (i) crazing, (j) scratch, (k) ablation, (l) microcracking, and (m) opening crack - 7 -

Figure 2. Chemical structures of a thermally reversible, DA based thermoset polymer with the generalised DA reaction between a substituted furan and a substituted maleimide - 12 -

Figure 3: (a) Mending efficiency of furan/maleimide polymer obtained by fracture toughness testing of compact tension test specimens; (b) image of a broken specimen before thermal treatment; (c) image of the specimen after thermal treatment; (d) SEM image of the surface of a healed sample: the left side is the as-healed surface and the right side is the scraped surface; (e) enlarged image of the boxed area in (d) - 13 -

Figure 4: Left: schematic of DCDC sample geometry. Dotted lines represent the location of the pre-crack and subsequent crack extension. Right: fracture and healing sequence of a single sample. (a) Virgin sample with hole and pre-cracks visible; (b) sample after first fracture event; (c) sample after first healing treatment; (d) sample after second fracture event - 14 -

Figure 5: Diels-Alder cycloaddition reaction of cyclopentadiene to form dicyclopentadiene - 15 -

Figure 6: Photo-induced [2+2] cycloaddition reaction of coumarin to form the butane-containing dimer - 17 -

Figure 7: UV based healing of cracks in cyclobutane containing polymers of tricinnamates - 18 -

Figure 8: Synthetic scheme of a self-healing, supramolecular elastomer. Red bonds are hydrogen acceptor groups, and green bonds are hydrogen donor groups	- 19 -
Figure 9: Mechanisms involved in self healing via molecular interdiffusion	- 21 -
Figure 10: Self-healing concept using hollow fibre storage vessels (left) and ruptured hollow vessels containing healing agent (right)	- 24 -
Figure 11: Hollow fibres with open ends (left) and hollow fibres with open surface pores (right)	- 24 -
Figure 12 Cross section of Glass Fiber Reinforced Polymer laminate containing dye to visualize healing agent flow.....	- 26 -
Figure 13: Microvascular based self-healing concept: a) a capillary network in the outer skin layer with a cut; b) schematic of an epoxy specimen containing a microvascular network, loaded in a four-point bending configuration monitored with an acoustic emission sensor	- 29 -
Figure 14: Autonomic healing concept incorporating encapsulated healing agent and embedded catalyst particles in an epoxy matrix; (a) damage event causes crack formation in the matrix; (b) crack ruptures the microcapsules, releasing liquid healing agent into crack plane; (c) healing agent polymerizes upon contact with embedded catalyst, bonding crack closed	- 31 -
Figure 15: Urea- formaldehyde microcapsules containing dicyclopentadiene (DCPD).....	- 33 -
Figure 16: Stress state in the vicinity of a planar crack as it approaches a spherical filler particle embedded in a linearly elastic matrix	- 34 -
Figure 17: Nanocapsules prepared via ultrasonication and miniemulsion techniques	- 36 -
Figure 18. Ring opening metathesis polymerization of DCPD.....	- 37 -
Figure 19: Monomers used as liquid healing agents.....	- 38 -
Figure 20: Principal structural units on an aircraft	- 46 -
Figure 21: Material Design (Epoxy matrix).....	- 47 -
Figure 22: Epon Resin 828 (n=2)	- 52 -
Figure 23: Phenol, 2,4,6-tris[(dimethylamino) methyl]	- 53 -
Figure 24: Flexibilizer Heloxy 71.....	- 54 -

Figure 25: Reactive diluent (BDE) 1-4 Butandioldiglycidylether	54 -
Figure 26:(a) G1(1st generation Grubbs' catalyst); (b) G2 (2nd generation Grubbs' catalyst)	55 -
Figure 27:(a) Hoveyda-Grubbs I (HG1); (b) Hoveyda-Grubbs II (HG2).....	56 -
Figure 28: Dicyclopentadiene and its bubble and melting points.....	58 -
Figure 29: 5-ethylidene-2-norbornene (ENB) and its bubble and melting points.-	59 -
Figure 30: (a) poly(urea-formaldehyde); (b) ethylene maleic anhydride copolymer (EMA)	59 -
Figure 31: DSC curve for a generic material.....	64 -
Figure 32: DSC curve for an uncured epoxy resin	66 -
Figure 33: DSC Tg as function of curing process curve for an epoxy resin	66 -
Figure 34: Decrease in cure exotherm as resin cure increaes	67 -
Figure 35: Phasor diagram for complex modulus $E = E' + iE''$	69 -
Figure 36: Vibrational modes of stretching and bending	74 -
Figure 37: TDCB geometry and dimensions (mm)	79 -
Figure 38: First self-healing system formulation.....	82 -
Figure 39: DSC curves for Epon 828	83 -
Figure 40: DSC curve for Epon 828 – first heating.....	84 -
Figure 41: DSC curve for Epon 828 – second heating	84 -
Figure 42: DSC curves for Heloxy 71	85 -
Figure 43: DSC curve for Heloxy 71– first heating.....	85 -
Figure 44: DSC curve for Heloxy 71– second heating	86 -
Figure 45: DSC curves for formulations: Sample1, Epon 828/Ancamine K54 (10/1) and Sample 2, Heloxy 71/Ancamine K54 (10/1).....	87 -
Figure 46: DSC curves (in dynamic regime) for EHA sample.....	88 -

Figure 47: Dynamic DSC for residual cure after isothermal treatments of sample EHA.....	- 89 -
Figure 48: DMA plot of $\tan \delta$ versus temperature of EHA sample cured at temperatures between 50 and 100 °C	- 90 -
Figure 49: DMA plot of $\tan \delta$ versus temperature for EHA-[80 °C, 9h + 120 °C, 2h] and EHA-[80 °C, 9h] samples	- 92 -
Figure 50: FTIR spectra of EHA resin as a function of reaction time during a two stage curing process at 80 and 120 °C	- 93 -
Figure 51: Sem image of microcapsules synthesized at pH value of 3.5-3.7, Magnification = 5000X	- 96 -
Figure 52: Sem image of microcapsules synthesized at pH value of 3.5-3.7, Magnification = 10000X.....	- 96 -
Figure 53: Sem image of microcapsules synthesized at pH value of 3.5-3.7, Magnification = 15000X.....	- 97 -
Figure 54: ^1H NMR spectrum of the soluble fraction (in CDCl_3) extracted from the microcapsules	- 98 -
Figure 55: ^1H NMR spectrum of DCPD used in the experimentation	- 99 -
Figure 56: FT/IR spectra of microcapsules (blue curve), dicyclopentadiene (green curve), insoluble fraction of the microcapsules obtained after extraction of DCPD (red curve) and metathesis product (brown curve) in the spectral range from 500 to 4000 cm^{-1}	- 100 -
Figure 57: FT/IR spectra of microcapsules (blue curve), dicyclopentadiene (green curve), insoluble fraction of the microcapsules obtained after extraction of DCPD (red curve) and metathesis product (brown curve) in the spectral range from 500 to 2400 cm^{-1}	- 101 -
Figure 58: FT/IR spectra of first generation Grubbs' catalyst (red curve), product of metathesis PM (brown curve), metathesis product with 1/5000 catalyst/monomer ratio (green curve) and metathesis product with 1/2000 catalyst/monomer ratio (blue curve)	- 101 -
Figure 59: TGA curves in air (red) and in nitrogen (blue) of the microcapsules synthesized at different pH values	- 102 -
Figure 60: DSC curves for microcapsules synthesized at different pH values ..	- 103 -
Figure 61: SEM image of the G1 catalyst (magnification 1.5 KX)	- 105 -

Figure 62: SEM image of the G1 catalyst (magnification 600X).....	- 105 -
Figure 63: SEM image of the G1 catalyst after treatment (magnification 1000X)-	106 -
Figure 64: TGA curves for first generation Grubbs' catalyst in air (red) and in nitrogen (blu).....	- 107 -
Figure 65: DSC curve for first generation Grubbs' catalyst	- 107 -
Figure 66: ¹ H NMR spectrum for Grubb's catalyst dissolved in TCDE at room temperature	- 108 -
Figure 67: ¹ H NMR spectrum for Grubb's catalyst after a thermal treatment of 1 h at 120 °C in nitrogen	- 109 -
Figure 68: ¹ H NMR spectrum for Grubb's catalyst after a thermal treatment of 15 h at 120 °C in nitrogen	- 110 -
Figure 69: ¹ H NMR spectrum for Grubb's catalyst after a thermal treatment of 1 h at 150 °C in nitrogen	- 111 -
Figure 70: ¹ H NMR spectrum for Grubb's catalyst after a thermal treatment of 3.58 h at 150 °C in nitrogen.....	- 112 -
Figure 71: ¹ H NMR spectrum for Grubb's catalyst after a thermal treatment of 2.25 h at 150 °C in air.....	- 113 -
Figure 72: ¹ H NMR spectrum for Grubb's catalyst after a thermal treatment of 3 h at 120 °C in air	- 114 -
Figure 73: ¹ H NMR spectrum for Grubb's catalyst after a thermal treatment of 6 h at 25 °C in air	- 115 -
Figure 74: ¹ H NMR spectrum for Grubb's catalyst after a thermal treatment of 24 h at 25 °C in air.....	- 116 -
Figure 75: TGA curves of Microcapsules (blu) and Sample C (red).....	- 119 -
Figure 76: FT/IR spectrum of Sample C powder treated with DCPD	- 120 -
Figure 77: ¹ H NMR spectrum first generation Grubbs' catalyst extracted from Sample C cured at 80 °C 9h + 120 °C 2h	- 121 -
Figure 78: Loss factor tan δ for EHA [80 °C, 9h + 120 °C, 2h], Sample B and Sample C	- 123 -
Figure 79: SEM image of self-healing specimen section (Sample C) after DMA up to 200 °C (Magnification 100X).....	- 125 -

Figure 80: SEM image of an area of self-healing specimen (Sample C) after DMA up to 200 °C (Magnification 385X).....	- 126 -
Figure 81: SEM image of a different area of self-healing specimen (Sample C) after DMA up to 200 °C (Magnification 400X)	- 126 -
Figure 82: Self- healing systems: (a) EHA + G1 + ENB filled microcapsules; (b) EHA + G2 + ENB filled microcapsules.....	- 132 -
Figure 83: Microcapsules filled of ENB, 1700X magnifications	- 133 -
Figure 84: Microcapsules filled of ENB, 10120X magnifications	- 134 -
Figure 85: ¹ H NMR spectrum of 5-ethylidene-2-norbornene in CDCl ₃ solvent -	135 -
Figure 86: ¹ H NMR spectrum of soluble part of microcapsules	- 135 -
Figure 87: ¹ H NMR spectrum of soluble part of microcapsules and 5-ethylidene-2-norbornene.....	- 136 -
Figure 88 TGA curves in air (red) and nitrogen (black) of Microcapsules filled with ENB	- 137 -
Figure 89 DSC curve of Microcapsules filled with ENB	- 138 -
Figure 90: Self- healing systems: (a) Epoxy matrix + HG1 + ENB filled microcapsules; (b) Epoxy matrix+ HG2 + ENB filled microcapsules	- 146 -
Figure 91: SEM image of a sample of HG1 powders (Magnification 855X)	- 148 -
Figure 92: SEM image of a different sample of HG1 powders (Magnification 650X).....	- 148 -
Figure 93: SEM image of HG1 powders (Magnification 230X)	- 149 -
Figure 94: SEM image of HG2 powders (Magnification 224X)	- 150 -
Figure 95: SEM image of HG2 powders (Magnification 58X)	- 150 -
Figure 96 TGA curves obtained in a dry air atmosphere in the temperature range of 0°C–1000 °C. Insert: TGA curves in the temperature range of 150 °C–300 °C-	151 -
Figure 97: FTIR spectra of the EHA-HG1(180) and EHA-HG2 (170) powders treated with ENB. The highlighted peak at 966 cm ⁻¹ is characteristic of ring-opened poly(ENB).....	- 155 -

Figure 98: FTIR spectra of EHG2 sample between 100 °C and 180 °C for increasing times. The highlighted peak at 916 cm-1 is characteristic of the oxirane ring	- 156 -
Figure 99: FTIR spectra of E sample between 100 °C and 180 °C for increasing times	- 158 -
Figure 100: ENB/ 2.5% DCPD and ENB/ 5%DCPD blends after 1h at -50 °C.-	- 162 -
Figure 101: ENB/ 2.5% DCPD and ENB/ 5%DCPD blends after 5h at -50 °C.-	- 162 -
Figure 102: Last Self-healing system, based on Romp reaction of ENB triggered by HG1	- 164 -
Figure 103: Scheme of different matrix compositions, EHA, EBA1, EBA2	- 165 -
Figure 104: Dynamic Elastic Modulus for EBA1 and EBA2 formulations cured at 80 °C (4h) + 170 or 180 °C (2h).....	- 166 -
Figure 105: Loss factor (Tan δ) for EBA1 and EBA2 formulations cured at 80 °C (4h) + 170 or 180 °C (2h).....	- 167 -
Figure 106: Glass transition temperatures (Tg) for self-healing formulations cured up 170 or 180 °C.....	- 168 -
Figure 107: Dynamic Elastic Modulus for self-healing formulations cured up 170 or 180 °C	- 169 -
Figure 108: DSC curves of self-healing specimens with EBA1 matrix formulation cured up 170 and 180 °C	- 171 -
Figure 109: DSC curves of self-healing specimens with EBA1 matrix formulation cured up 170 and 180 °C	- 171 -
Figure 110: TGA curves in air and nitrogen for self-healing system EBA1 + HG1 5% + Mic 10 % cured up 170 °C	- 172 -
Figure 111: TGA curves in air and nitrogen for self-healing system EBA1 + HG1 5% + Mic 10 % cured up 180 °C	- 173 -
Figure 112: Silicone Rubber Molds for self-healing specimens with TDCB geometry.....	- 174 -
Figure 113: Project designs of metallic molds for self-healing specimens with TDCB geometry	- 175 -
Figure 114 Metallic Molds (with teflon sprayed) for self-healing specimens with TDCB geometry	- 176 -

Figure 115: Cured Self-healing Samples before extraction from the molds.....	- 176 -
Figure 116: Cured Self-healing samples after extraction from metallic molds .	- 177 -
Figure 117: Load-Displacement Curves for Virgin and Healed sample <u>EBA1</u> <u>HG1 5% Mic 10%</u> cured up 170 °C	- 178 -
Figure 118: Load-Displacement Curves for Virgin and Healed sample <u>EBA1</u> <u>HG1 5% Mic 10%</u> cured up 180 °C	- 179 -
Figure 119: Load-Displacement Curves for Virgin and Healed sample <u>EBA2</u> <u>HG1 5% Mic 10%</u> cured up 170 °C	- 180 -
Figure 120: Load-Displacement Curves for Virgin and Healed sample <u>EBA2</u> <u>HG1 5% Mic 10%</u> cured up 180 °C	- 181 -
Figure 121: Load-Displacement Curves for Virgin and Healed sample <u>EHA</u> <u>HG1 5% Mic 10%</u> cured up 170 °C	- 182 -
Figure 122: Load-Displacement Curves for Virgin and Healed sample <u>EHA</u> <u>HG1 5% Mic 10%</u> cured up 180 °C	- 183 -
Figure 123: Load-Displacement Curves for Virgin and Healed sample <u>EBA1</u> <u>HG1 5% Mic 17.2%</u> cured up 170 °C	- 184 -
Figure 124: Load-Displacement Curves for Virgin and Healed sample <u>EBA1</u> <u>HG1 10% Mic 20%</u> cured up 170 °C	- 185 -
Figure 125: Self-healing efficiency with different formulations and curing cycles	- 186 -
Figure 126: Self-healing efficiency of samples with different amounts of microcapsules	- 187 -
Figure 127. (C) Self-healing specimen sections with metathesis product inside of the microcapsules after damage; (B) magnification on the metathesis product inside the microcapsule; (A) healed crack faces closed by means of the metathesis product inside a crack.	- 187 -
Figure 128 Schematic configuration of tools in a Liquid Infusion Process	- 188 -
Figure 129: Vacuum bag realized.....	- 189 -
Figure 130: Moment of Fiber Impregnation	- 189 -
Figure 131 Autoclave used for curing process of the panel.....	- 190 -
Figure 132 Realized panel	- 190 -

Table Index

Table 1.1: Self-healing efficiency evaluation based on recovery of different material properties.....	- 44 -
Table 4.1 Degree of Cure (DC) of EHA samples after each isothermal cure of 9h at the temperatures 50, 60, 70, 80, and 100 °C.....	- 89 -
Table 4.2 Glass Transition Temperature measured by DMA of EHA Samples cured at temperatures between 50 and 100 °C.....	- 91 -
Table 4.3 Elastic Modulus (MPa) of EHA-[80 °C, 9h], and EHA-[80 °C, 9h + 120 °C, 2 h] samples.....	- 92 -
Table 4.4: Summary of results on thermolytic decomposition of Grubbs' catalyst in different environment at different temperatures.....	- 117 -
Table 4.5: Thermolytic decomposition of first generation Grubbs' catalyst embedded in epoxy matrix.....	- 122 -
Table 4.6: Elastic modulus (MPa) of EHA [80 °C, 9h + 120 °C, 2h], Sample B and Sample C in the temperature range between -50 and 50 °C	- 124 -
Table 4.7: Reaction rate and yield of ROMP reaction of DCPD with 1 st generation Grubbs' catalyst.....	- 129 -
Table 5.1: Reaction rate and yield of ROMP reaction of ENB with 1 st generation Grubbs' catalyst.....	- 139 -
Table 5.2: Reaction rate and yield of ROMP reaction of ENB with 2 nd generation Grubbs' catalyst.....	- 141 -
Table 5.3: Reaction rate and yield of ROMP reaction of ENB with G1 and G2 catalysts.....	- 142 -
Table 5.4: Summary results on thermolytic decomposition in air and nitrogen atmosphere of 2 nd generation Grubbs' catalyst.....	- 143 -

Table 5.5: Summary results on thermolytic decomposition of 2 nd generation Grubbs' catalyst embedded in epoxy matrix for different curing cycles.....	- 143 -
Table 6.1 Results of NMR spectra in air and Nitrogen for HG1 and HG2	- 152 -
Table 6.2 Comparison of thermolytic decomposition results for HG1 and HG2, with G1 and G2.....	- 153 -
Table 6.3 Results of thermolytic decomposition of Grubbs and Hoveyda-Grubbs' catalysts extracted from epoxy matrices.....	- 154 -
Table 6.4: Conversion percentage (Yields %) in the ROMP reaction of ENB with HG1 catalyst.....	- 159 -
Table 6.5: Conversion percentage (Yields %) in the ROMP reaction of ENB with HG2 catalyst.....	- 159 -
Table 6.6: Cross-linked fraction of metathesis products of ENB with HG1 and HG2 catalysts.....	- 161 -
Table 6.7: Cross-linked fraction of metathesis product of ENB/DCPD blends in different proportions and at different temperature.....	- 163 -
Table 6.8 Dynamic elastic moduli for self-healing formulation in the range of temperature between -50 and 50 °C.....	- 170 -

Abstract

This research work rises from collaborative activities between Alenia Aeronautica (Pomigliano D'Arco, Napoli) and the Industrial Engineering Department of University of Salerno.

One of the biggest challenge facing materials scientists is the idea to put in action self-healing composites in aeronautical applications. Polymeric composite materials, recently introduced in aeronautics, are subject to weakening due to mechanical, chemical, thermal, stress.

This could lead to the formation of microcracks deep within the structure where detection and external intervention are difficult or impossible. The presence of the microcracks in the polymer matrix can affect both the fiber and matrix dominated properties of a composite. In the case of a transport vehicle, the propagation of microcracks may compromise the structural integrity of the polymeric components, and so threatening passengers' safety.

In this work, we have developed a multifunctional autonomically healing composite with a self-healing functionality active at the severe operational conditions of aircrafts (temperature range: -50 °C/80 °C). The self-repair function in this new self-healing system, inspired by the design of White et al., is based on the metathesis polymerization of ENB (or ENB/DCPD blend) activated by Hoveyda-Grubbs'1st generation catalyst. The self-healing epoxy mixture, containing Hoveyda-Grubbs'1st generation catalyst, allows a cure temperature up to 180 °C without becoming deactivated. A quantitative assessment of self-healing functionality showed very high values of self-healing efficiency. Before reaching these amazing results several systems were investigated that differ for the nature and the composition of the epoxy matrix, catalysts and active monomers used: these systems have been gradually improved to suit performance requirements for a structural advanced material to be applied to aeronautical vehicles.

Introduction

1. Concept of Self-healing

The past decades have witnessed a tremendous increase in the use of polymers and polymer matrix composites which are supplanting traditional metal alloys, ceramic and wood counterparts.

Polymers and structural composites are used in a variety of applications, such as transport vehicles, sporting goods, civil engineering, and electronics.

Polymer composites have been selected and used because of their advantages including light weight, good processibility and chemical stability in atmospheric conditions.

However, durability and reliability are still problematic in the field of structural materials.

In fact continuous exposure of these polymers to environmental stresses including radiation damage, chemical attack, mechanical abrasion, impact and thermal decomposition can result in degradation of the material's physical properties and lead to irreversible damage [1].

This process starts at the microscopic level with the formation of microvoids [2] which then expand to generate microcracks deep within the structure where detection and external intervention are difficult or impossible.

The presence of the microcracks in the polymermatrix can affect both the fiber- and matrix-dominated properties of a composite.

The resulting loss of structural integrity leads to diminution of mechanical performance and ultimately to failure of the polymeric component.

In the case of a transport vehicle, the propagation of microcracks may affect the structural integrity of the polymeric components, shorten the life of the vehicle, and potentially compromise passenger safety.

With polymers and composites being increasingly used in structural applications (aircraft, cars,ships, defence and construction industries) several techniques have been developed for repairing visible or detectable damages on the polymeric structures.

Conventional repair methods such as welding or patching can sometimes be applied at the macroscopic level to either rejoin or reinforce damaged areas. However, these solutions are not always useful either as a result of inaccessibility to the damaged area or because they lead to changes in the dimensions and surface finish of the material.

Polymers which are conventionally crosslinked or which (when linear) have molecular weights exceeding the entanglement limit must necessarily fracture by breaking covalent bonds.

Restoration of the physico-mechanical properties of such materials, once fractured, requires either new covalent chemistry to generate additional crosslinks, or long periods of annealing to enable thermal diffusion of unbroken, linear polymer chains into the damage-zone.

These conventional repair methods are not effective for healing invisible microcracks within the structure during its service life.

The concept of self-healing polymeric materials was proposed in the 1980s [3] as a means of healing invisible microcracks for extending the working life and safety of the polymeric components.

Self-healing polymeric materials have the built-in capability to recover their load transferring ability after damage. Such recovery can occur autonomously or be activated after an application of an external stimulus (heat, radiation).

These materials are expected to contribute greatly to the safety and durability of polymeric components without the high costs of active monitoring or external repair.

In the past few decades, the growing interaction between biological and material sciences is leading researchers to incorporate biomimetic features, such as sensing and self-healing into newly developed materials. Biomimetics refers to human-made processes, substances, devices, or systems that imitate nature, and has led to the development of new biologically inspired materials based on biological analogs . One such remarkable property of biological materials is their ability to autonomically heal when they are damaged. This is achieved by

hierarchical structuring, adjusted development instead of production, and constant amending and healing.

Mimicking of biological systems has been a source of inspiration for design and development of this new range of smart materials.

Biology provides an abundance of self-healing systems that embody the guiding principles behind the design of synthetic versions. In either case, the initial response is triggered by injury.

A self-healing strategy used by biological tissues is that of a direct replacing of their building blocks, the cells [4].

A flux of biomarkers triggers the whole process of tissue regeneration. Cutaneous wound healing is a good example of the complexity of tissue self-reparation.

After the formation of a clot which re-establishes the haemostasis, wound healing has three main phases, inflammation, tissue formation and tissue remodelling.

Each step triggers the next one and is stopped when its goal is reached. Initially, a set of biological signals induces the accumulation of neutrophils and macrophages in order to clean the wounded area of microbes.

In the intermediate phase, epidermal cells nearby begin to proliferate and undergo structural modifications which allow their migration to the wounded region.

Collagen is degraded around the wounded area for facilitating cell migration. In the third phase, the new tissue and a capillary network gradually advance in the wound. Epidermal cells revert their structural modifications and firmly adhere to the tissue, while fibroblasts produce collagen until the replenishment of the wound area.

When the scar is formed, non epidermal cells in the wound undergo controlled apoptosis and collagen production slows down.

The biological example shows that very efficient self-healing mechanisms are dynamic processes with many actors playing interconnected roles and with transport of active components. In particular, we can notice the importance of biomarkers which activate specific repairing processes and of a hierarchical organization both for structures and functions.

Some of the characteristics of self-healing biological processes, like the multifunctionality, the self-replication ability, the self-assembly ability and the markers for the activation of specific processes should be considered for the design of new biomimetic materials.

Synthetic self-healing systems share this three-step process, in a more simplistic fashion and at an accelerated rate: the first response is

triggering which is closely coupled to the timescale of damage; the second response is transport of materials to the site of damage, again at a relatively rapid rate; the third response, analogous to matrix remodeling, is the chemical repair process, at a timescale that is dependent on the type of healing mechanism employed (e.g., polymerization, entanglement, reversible cross-linking) [5].

Conceptually similar to the vascular systems of many plants and animals, perhaps the most biomimetic self-healing system is the vascular-style bleeding of healing agents following the original self-healing composites proposed by Dry and Sottos [6]. These materials may also be able to heal damage caused by insertion of other sensors/actuators, cracking due to manufacturing-induced residual stresses, and fiber de-bonding.

An ideal self-healing material is capable of continuously sensing and responding to damage over the lifetime of the polymeric components, and restoring the material's performance without negatively affecting the initial materials properties.

This will make the polymeric materials safer, more reliable and durable while reducing costs and maintenance. Development of self-healing materials offers great opportunities for new applications of these lightweight materials into the manufacture of advanced structural materials.

1.1 Composite Materials

Composite materials or composites are engineered materials made from two or more constituent materials with significantly different physical or chemical properties which remain separate and distinct on a macroscopic level within the finished structure. The properties of composite materials obtained by combining the different constituent materials usually cannot be achieved by any one of the components acting alone.

Composite materials have been used for thousands of years in various man-made structures. The most primitive composite materials in recorded history were straw and mud combined to form bricks for building construction. Straw was used by the Israelites to strengthen mud bricks. Ply-wood was used by the ancient Egyptians when they realized that wood could be rearranged to achieve superior strength and resistance to thermal expansion as well as bloating caused by the absorption of moisture.

The history of modern composites however began in the late 1930's with the invention of fiberglass. The pace of the development of composite materials accelerated during World War II and the decades following. The development of new and improved resins has also contributed to the expansion of the composites market, especially for high temperature and high corrosion resistance applications. The most advanced applications are routinely found on spacecraft in demanding environments. The most visible applications pave our roadways in the form of either steel and aggregate reinforced cement or asphalt concrete. Furthermore, composites closest to our personal hygiene form modern day shower stalls and bath tubs made of fiberglass. Even though most composites that are used in modern engineering structures are man-made, composites do exist in nature as well. A piece of wood is a composite with long fibers of cellulose (a very complex form of starch) held together by a much weaker substance called lignin. Cellulose is also found in cotton and linen. However, the binding power of the lignin makes a piece of timber much stronger than a bundle of cotton fibers. An example of a man-made composite is concrete. It is made of cement, aggregates (such as gravel and sand), water, and chemical admixtures and is used more than any other man-made material in the world.

1.1.2 Constituents of Composites

Composites are made up of individual materials referred to as constituent materials. There are two categories of constituent materials: matrix and reinforcement. At least one portion of each type is required to fabricate a composite. The matrix material surrounds and supports the reinforcement materials by maintaining their relative positions. The reinforcements impart their special mechanical and physical properties to enhance the matrix properties. A synergism produces material properties unavailable from the individual constituent materials, while the wide variety of matrix and strengthening materials allows the designer of the product or structure to choose an optimum combination. The matrix material can be introduced to the reinforcement before or after the reinforcement material is placed into the mold cavity or onto the mold surface. The matrix material experiences a merging event, after which the part shape is essentially set. Depending upon the nature of the matrix material, this merging event can occur in various ways such as chemical polymerization or solidification from the melted state.

Most commercially produced composites use a polymer matrix material often called a resin solution. There are many different polymers available depending upon the applications. There are several broad categories, each with numerous variations. The most common are known as polyester, vinyl ester, epoxy, phenol, polyimide, polyamide, and polypropylene.

The reinforcement materials are often fibers but ground minerals such as metals and ceramics are used commonly. The reinforcing materials are usually strong with low densities. The principal fibers in commercial use are various types of carbon and glass, as well as aramid fibers such as Kevlar. The fiber orientation can be controlled in each layer of the laminate to create a broad range of mechanical and physical properties. Based on the type of reinforcement used, composites are often divided into fibrous composites and particulate composites.

Because of their excellent mechanical properties such as high strength, low specific weight, and impact and corrosion resistance, as well as advanced manufacturing methods and tailor ability of the lay-up, fiber-reinforced polymer matrix composites are attractive candidates for use in many performance oriented structures. Composite materials are ideal for structural applications where high strength-to-weight ratio and stiffness-to-weight ratios are important. Weight sensitive applications such as aircraft and space vehicles are the primary consumers of composites, especially fiber-reinforced polymer matrix composites. However, their use is limited due to the difficulty in damage detection and repair as well as lack of extended fatigue resistance. Several ideas have been suggested by researchers to help improve the damage detection and repair difficulty in composites, self-healing being one of them.

1.2 Fracture mechanisms and traditional repair methods for polymeric composites materials

When polymer composites used as structural materials become damaged, there are only a few methods available to attempt to extend their functional life time. Ideal repair methods are ones that can be executed quickly and effectively on site, eliminating the need to remove a component for repair.

The mode of damage must also be taken into consideration, as repair strategies that work well for one mode might be completely useless for another.

Figure 1 [7] shows a series of possible damage modes in a polymer composite: for example, impact loading can lead to surface cracking, subsurface delamination, polymermatrix cracking, and transverse cracking, which taken together can severely affect mechanical and barrier properties. The damage volume depends on the loading conditions, the geometry, and the undamaged material properties [7].

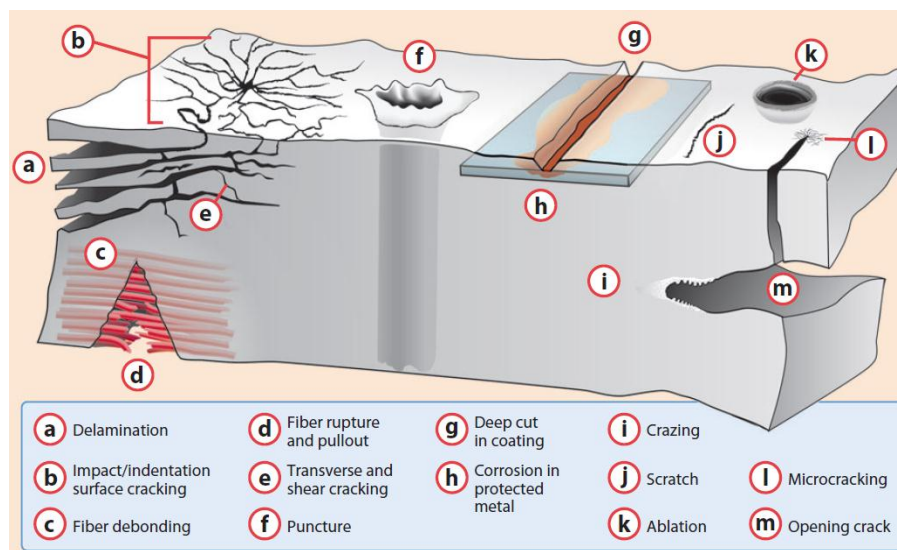


Figure 1. Damage modes in polymer composites. Indentation, impact, corrosive environments, ballistic punctures, surface scratching, and fatigue can lead to various damage modes in polymer composites, as shown here: (a) delamination, (b) impact/indentation surface cracking, (c) fiber debonding, (d) fiber rupture and pullout, (e) transverse and shear cracking, (f) puncture, (g) deep cut in coating, (h) corrosion in protected metal, (i) craze, (j) scratch, (k) ablation, (l) microcracking, and (m) opening crack

Impact and cyclic fatigue associated failures are the most studied for structural applications of polymeric materials, although thermal, chemical and other environmental factors can cause damage in polymers, [8]. Both of impact and cyclic failure mechanisms proceed via crack propagation, with a monotonic load experienced during impact type incidents and cyclic loads experienced during fatigue.

For a crack to propagate, the energy released during cracking must be equal to, or larger than the energy required to generate new surfaces on the material [9]

Most crack propagation modeling is based on a parameter called the stress intensity factor (K_I) [10,11]. During mode I crack opening type

failure growth, K_I is related to crack depth, material/crack geometry and the applied stresses. As the applied stress and crack geometry change during monotonic or cyclic loading, a critical stress intensity factor (K_{IQ}) is reached and then crack growth occurs. During an impact damage incident (consisting of a monotonic load) the extent of crack propagation is related to the maximum stress intensity factor ($K_{I\text{Max}}$) experienced.

During fatigue-type damage crack propagation is related to both $K_{I\text{Max}}$ and the change in K_I during cycling (ΔK) [12]. In order to heal cracked polymers, the fractured surfaces need to be resealed or alternatively crack growth must be impaired.

Crack growth retardation occurs when energy is dissipated within the loaded material without extending an existing crack.

1.2.1 Welding

One of the earlier healing methods for fractured surfaces is hot plate welding, where polymer pieces are brought into contact above the glass transition temperature of the material, and this contact is maintained long enough for interdiffusion across the crack face to occur and restore strength to the material. It has been shown, however, that the location of the weld remains the weakest point in the material and thus the site for future damage to occur.

Welding enables the rejoining of fractured surfaces (closing cracks) or fusing new materials to the damaged region of the polymer composite. It relies on formation of chain entanglements between two contacting polymer surfaces [13] and is designed to reinstate the original physical properties of the damaged area [14,15]. During welding, the two polymer surfaces pass through a series of transitions including surface rearrangement, surface approach, wetting and then diffusion [14,16]. Once these processes have been completed and entanglement of the polymer chains has occurred, the two surfaces are fused together and the repair is complete.

Factors such as welding temperature, surface roughness, chemical bonding between the surfaces or the presence of solvents directly affect the rate and extent of repair that can be achieved [17].

1.2.2 Patching and resin injection

For fiber breakage in a laminate composite, a reinforcing patch is often used to restore some of the strength to the material. Often, a

reinforcing patch is used in conjunction with resin injection to restore as much as the greatest amount of strength possible

Patching repairs differ from the welding repairs in that they involve the covering or replacing of the damaged material with a new material.

The extent of property recovery as a result of the repair is dependent upon factors such as the interface between the patch and the original material, the presence/orientation of reinforcing fibers and the thickness of the patch.

For laminate composites, resin injection is often employed to repair damage in the form of delamination. The uncured resin diffuses into the damaged component and deepens the adhesive region that holds the patch in place. This can be problematic, however, if the crack is not easily accessible for such an injection [18]

None of these methods of repair is an ideal solution to damage in a structural composite material. They are mainly applicable to the repair of external and accessible damages instead of the internal and invisible microcracks.

They are temporary solutions to prolong the lifetime of the material and each of these repair strategies requires monitoring of the damage and manual intervention to enact the repair.

The development of self-healing polymeric materials is therefore of great interest.

1.3 Progress beyond the state-of-art of Self-healing materials

In recent years polymer composites are increasingly used in structural applications, ranging from civil infrastructure to high performance vehicles such as racing cars and military aircraft.

This popularity is due to their lower weight, as well as to a continuous improvement of their performance aided in recent years by nanotechnology.

However, limited storage stability and reliability are critical for polymer composites designed for structural applications.

One of the main structural problems in these materials can arise from the effects of impact damage on the structural integrity of the material. Internal damage is difficult to detect and, once developed, even more difficult to repair and therefore, the integrity of the structure is greatly compromised.

In addition to conventional methods for damage detection, (such as non destructive testing techniques; ultrasonic, infrared thermography, X-ray tomography, and computerized vibro thermography), and common repair methods (for example reinforced patch bonded or bolted to the composite structure), there has recently been the development of efficient re-mendable materials and self-healing composites which are expected to significantly extend the life of polymeric components by autonomically healing micro-cracks whenever and wherever they develop.

According to the ways of healing, self-healing polymers and polymer composites can be classified into two categories:

- 1) *intrinsic* ones that are able to heal cracks by the polymers themselves;
- 2) *extrinsic* in which healing agent has to be pre-embedded.

For structural applications such as aeronautic materials, the extrinsic self-healing systems are of great interest because they would overcome the difficulties connected to damage diagnosis and the following appropriate interventions to be reduced. In the case of extrinsic self-healing, the matrix resin itself is not healable [19]. The healing agent, which partially restores the mechanical properties after damage, has to be in advance stored inside composite materials.

1.3.1 Intrinsic self-healing

The intrinsic self-healing polymers and polymer composites are based on specific performance of the polymers and polymeric matrices that enables crack healing under certain stimulation (e.g.: heating).

In these materials autonomic healing without external intervention is not available.

Intrinsic self-healing materials achieve repair through inherent reversibility of bonding of the matrix polymer.

Intrinsic self-healing can be accomplished through thermally reversible reactions, hydrogen bonding, ionomeric coupling, a dispersed meltable thermoplastic phase, or molecular diffusion.

For intrinsic systems, the matrix is inherently self-healing, and sequestration of healing agents is not required, avoiding many of the problems with integration and healing-agent compatibility that arise in vascular and capsule-based self-healing materials.

However, intrinsic self-healing materials must also meet the desired mechanical, chemical, and optical properties for intended applications.

1.3.1.1 Diels-Alder Polymers

Polymers with controlled reversible polymerisation processes have shown great potential for self-healing.

These unique polymers, sometimes called ‘mendomers’ or ‘dynamers’, contain specific bonds that are reversible in response to a generally mild external stimulus.

A bulk mendomer has the potential to repeatedly heal itself in such a way that the virgin material is fully restored, even at the molecular level.

The reversible bonds in mendomers can be engineered to behave as ‘weak links’ that preferentially break in response to stress, preserving the intactness of the irreversible bonds.

This is especially important for self-healing applications: if large scale damage can translate to the molecular level exclusively as cleavage of the ‘weak links’, then molecular structure can be completely restored upon employing the external stimuli to reform these broken ‘weak links’.

One limitation in these systems is that applying the required external stimulus to initiate the depolymerisation/polymerisation cycle of damaged mendomers requires manual intervention, and the healing is therefore not fully autonomic.

For a large number of polymers that heal via bond reformation, heat is the external stimulus that begins the healing process.

The most widely used and intensely studied reversible covalent bonds are found in the Diels-Alder (DA) cycloaddition reaction.

Diels-Alder [20] reaction involves the concerted addition of a conjugated diene with a dienophile to form a cyclohexene ring containing two newly formed C-C bonds.

The diene and dienophile components of this reaction can be altered to incorporate almost any functionality imaginable, and thus the reaction is an extremely versatile one in organic chemistry.

This cycloaddition reaction is also thermally reversible, leading to its application in the field of healable materials as a thermal stimulus responsive material.

The first use of Diels-Alder chemistry for healable materials was in 2002 by Chen et al. [21], in which the furan and maleimide moieties were incorporated into the polymer backbone for the first time.

The initial Diels-Alder (DA) healing system was devised by Chen et al. and utilized the DA and retro Diels-Alder (rDA) reaction between furan and maleimide (Figure 2).

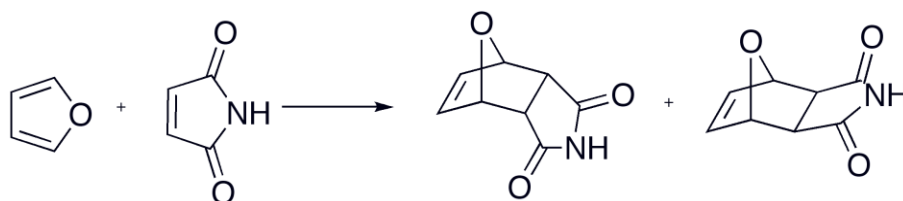


Figure 2. Chemical structures of a thermally reversible, DA based thermoset polymer with the generalised DA reaction between a substituted furan and a substituted maleimide

Chen et al. developed thermoset polymers based on the DA reaction between the multifuran and multimaleimide monomers which resulted in a polymer with tensile, compressive and flexural mechanical properties similar to commercially available epoxies and unsaturated polyesters.. The rDA reaction was proposed as the major reason for crack propagation, as the bonds formed in the DA adduct are weaker than the other covalent bonds in the system; this also means that DA active functional groups are exposed following crack propagation, and therefore healing of the material via the reformation of DA adducts is possible.

The studies of these polymers showed a 57% healing efficiency when fractured in a compact tension protocol upon application of a thermal stimulus (120-150°C) and after cooling (Figure 3).

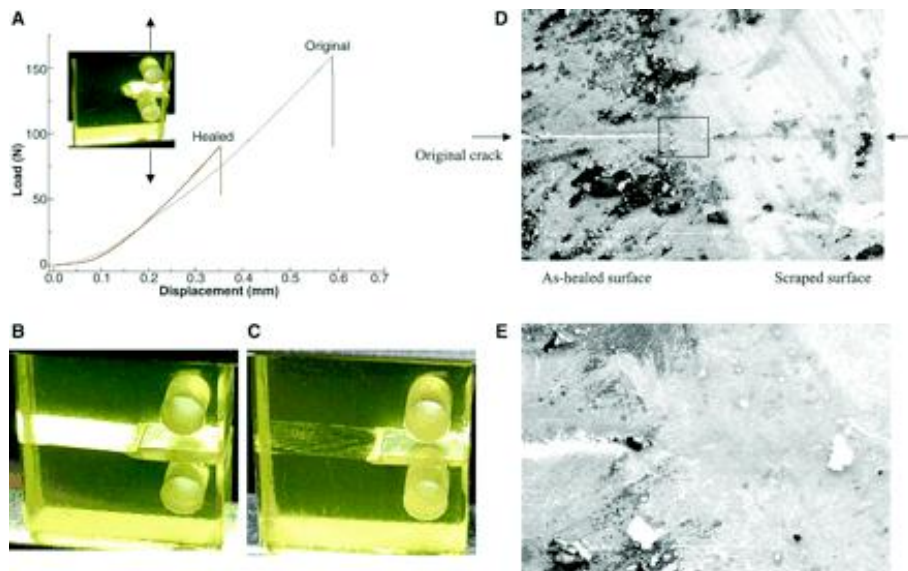


Figure 3: (a) Mending efficiency of furan/maleimide polymer obtained by fracture toughness testing of compact tension test specimens; (b) image of a broken specimen before thermal treatment; (c) image of the specimen after thermal treatment; (d) SEM image of the surface of a healed sample: the left side is the as-healed surface and the right side is the scraped surface; (e) enlarged image of the boxed area in (d)

This furan/maleimide healable material system was revisited in 2007 by Plaisted and Nemat-Nasser [22], utilizing sample geometry that allowed for controlled incremental crack growth.

Double cleavage drilled compression (DCDC) specimens were used, in which crack growth is self-arrested to leave the sample in one piece after testing, as well as allowing for multiple data points to be extracted from a single specimen (Figure 4).

The healing efficiency was found to be near 100% after several cycles of fracture and healing and it was shown that the degree of healing did not increase past one hour application of a thermal stimulus.

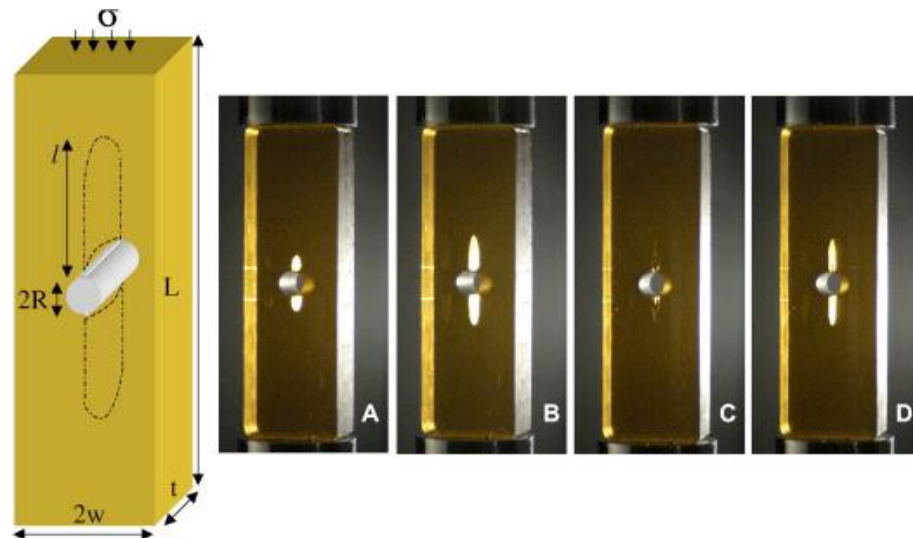


Figure 4: Left: schematic of DCDC sample geometry. Dotted lines represent the location of the pre-crack and subsequent crack extension. Right: fracture and healing sequence of a single sample. (a) Virgin sample with hole and pre-cracks visible; (b) sample after first fracture event; (c) sample after first healing treatment; (d) sample after second fracture event

In 2009, Tian et al. [23] reported a healable epoxy that contained furan and maleimide moieties. Traditional epoxy materials cannot be altered after they undergo curing.

Incorporating DA components to the material, the ability to heal can be introduced to the system. The furan functionality was attached to an epoxy compound via a two-step procedure. This epoxy could then be cured as usual, leaving pendant furan groups free to react with an added bis-maleimide compound. Polymer specimens were fabricated and the mechanical properties found to be comparable to commercial epoxy materials. No data of efficiency are disponible.

Also cyclic dienes are favorable for Diels-Alder reactions, as they lock the diene into the required *s-cis* conformation. Besides furan, a widely studied cyclic diene for DA reactions is cyclopentadiene, in which the oxygen of furan is replaced with a methylene group. In addition to being a desirable diene for this reaction, cyclopentadiene can also act as a dienophile and self-react to form a DA adduct as shown in Figure 5

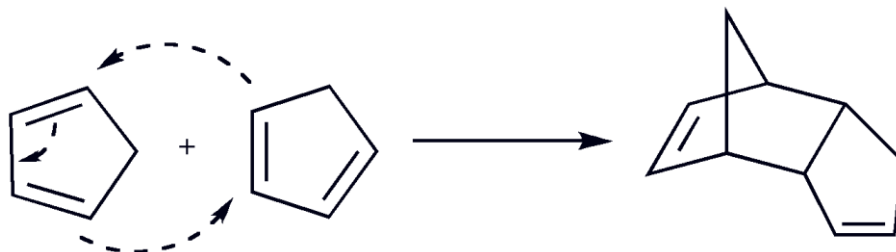


Figure 5: Diels-Alder cycloaddition reaction of cyclopentadiene to form dicyclopentadiene

Murphy et al. have developed a series of self-healing DA based monomers that use cyclopentadiene as both the diene and dienophile. In this approach, a macrocyclic derivative of DCPD, which is the DA adduct of two molecules of cyclopentadiene, was synthesised using several short organic linkers in such a way that the rDA reaction of the macrocycle would yield an α,ω -bis(cyclopentadiene) [24] Upon cooling to below rDA temperatures, this linear molecule will preferentially undergo intermolecular DA reactions, as opposed to intramolecular cyclisation, to form the polymer backbone.

This material was shown to undergo healing upon exposure to a thermal stimulus, giving an average 46% healing efficiency when heated to 120 °C for 20 minutes.

1.3.1.2 Dispersed Thermoplastic Polymers

Self-healing in thermoset materials can be achieved by incorporating a meltable thermoplastic additive. Self-healing occurs by the melting and subsequent redispersion of the thermoplastic material into the crack plane, filling the crack and mechanically interlocking with the surrounding matrix material.

Hayes [25] developed a self-healing material based on a thermoset/thermoplastic blend.

A thermoplastic polymer was dissolved into the thermoset epoxy resin, and E-glass/epoxy composites were fabricated.

The selected thermoplastic was poly(bisphenol-A-co-epichlorohydrin), which is highly compatible with the matrix diglycidyl ether of bisphenol-A based resin. Upon heating a fractured resin system, the thermoplastic material would mobilize and diffuse through the thermosetting matrix, with some chains bridging closed cracks and thereby facilitating healing.

After tensile or impact loading, significant decreases in delamination area and increases in extension at failure, fracture toughness and impact strength were observed after a short heat treatment at temperatures (100-140 °C), resulting from the thermoplastic polymer melt diffusing through and filling the damage region.

The healing agent should be reversibly bonded (e.g. through hydrogen bonding) to the crosslinked network of the cured resin below the minimum healing temperature to limit its effect on thermomechanical properties.

The healing agent should become mobile above this minimum healing temperature so that it can diffuse across a hairline crack, such as a transverse crack, to provide a recovery in strength.

The addition of the linear chain molecule should not significantly reduce the thermomechanical properties of the resin matrix.

1.3.1.3 Ionomeric Self-healing materials

Another form of reversible interaction that has been utilized in polymer systems as reversible cross-linking are ionic interactions.

Ionomeric copolymers are a class of materials with ionic segments that can form clusters that act as reversible cross-links.

These clusters can be activated by external stimuli such as temperature or ultraviolet (UV) irradiation

Polymers that contain up to 15% ionic content are called ionomers and these materials have the ability to restore cross-linking after damage to a material, restoring mechanical strength.

Projectile testing of poly(ethylene-*co*-methacrylic acid) (EMAA) copolymers with ionic segments was conducted by Kalista et al. [26].

The heat generated during projectile damage served as the trigger for self-healing in these cases.

During impact, energy is passed to the ionomer heating it to 98 °C. the material exhibits viscoelastic recovery to seal the hole and the ionic interactions re-form to restore strength to the material.

During room temperature projectile tests, hole edges retract to close the puncture following the passage of the projectile, leaving only a small scar in the material.

The healing of these ionomers under simulated ballistic condition were also investigated by Varley & van der Zwaag [27]

1.3.1.4 UV initiated Self-healing

Reversible covalent bonding can be brought about through cycloaddition reactions.

The alternative type of cycloaddition reactions are photoinitiated, undergoing cyclization upon irradiation of a certain wavelength of light and cleavage upon irradiation of a shorter wavelength of light.

One type of chemistry identified by Cho et al.[28] as suitable for this type of healing is the [2+2] cycloaddition of cinnamoyl groups.

Many olefin-containing compounds can undergo a [2+2] cycloaddition reaction upon irradiation with light to form cyclobutane; these newly formed covalent bonds can then be reversibly cleaved upon irradiation with a shorter wavelength of light to give the starting olefins (Figure 6).

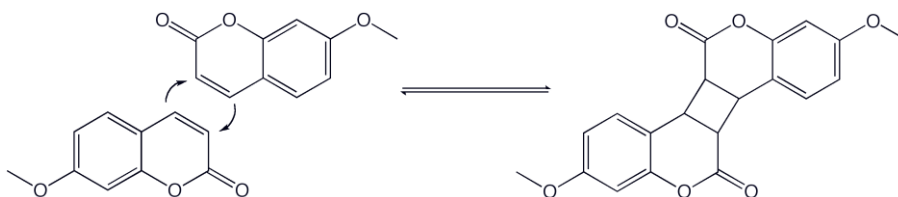


Figure 6: Photo-induced [2+2] cycloaddition reaction of coumarin to form the butane-containing dimer

If these photosensitive groups are incorporated into a polymer system, reversible cross-linking can be achieved photolytically.

Several tricinnamates were synthesised by Cho et al.[28] and photoirradiated to form cyclobutane containing cross-linked polymer films, and it was observed after crack damage of these films, the cyclobutyl groups at the damage regions cyclorevert to reform cinnamoyl functionalities (Figure 7).

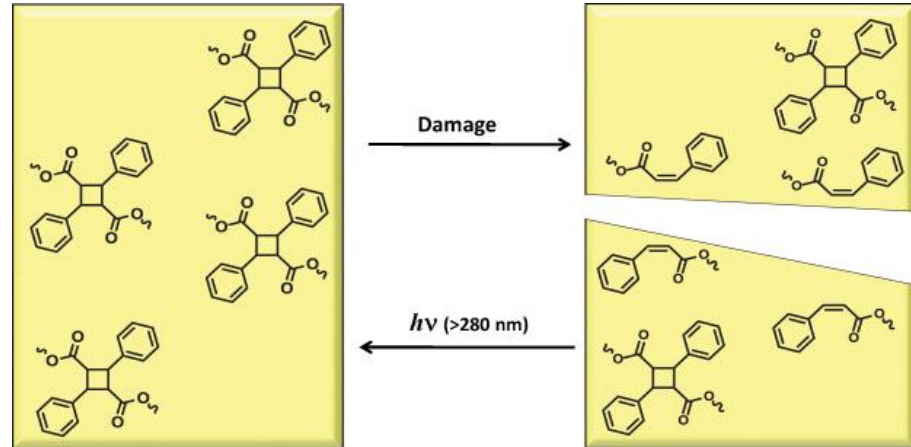


Figure 7: UV based healing of cracks in cyclobutane containing polymers of tricinnamates

1.3.1.5 Supramolecular Self-healing materials

Polymers can be designed to form strong endgroup and/or side-group associations via multiple complementary, reversible hydrogen bonds, resulting in a self-healing elastomeric polymer.

Cordier et al. [29] utilized hydrogen bonding to form a supramolecular healable rubber, taking advantage not only of the reversible nature of hydrogen bonds but also their directionality as a tool for self-association of the chains within the network.

The resulting material would require a mechanical stimulus to initiate healing, in the form of bringing the damaged surfaces into contact with one another, thus allowing for the self-associating nature of the hydrogen bonds to reform the network.

The hydrogen bonding groups used in this material were amido imidazolones and ureas, mixed in such a way as to allow for a supramolecular network to form without any crystalline regions to maintain the elastomeric properties of the material.

After being cut into two pieces and brought back into contact, the sample will self-heal over time at room temperature. With a contact time of 15 minutes, the healed sample was able to be deformed up to near 200% without breaking.

Montarnal et al. [30] reported the bulk synthesis of a hydrogen bonding supramolecular polymer by first reacting dimeric or trimeric fatty acid derivatives with diethylenetriamine, followed by a subsequent reaction with urea (see Figure 8).

When this elastomer was fractured and the damage surfaces brought together, nearly full recovery of the virgin material's elongation at break was achieved after 180 min. Healing was only able to fully recover virgin properties when the fracture surfaces of broken specimens were brought into contact with each other immediately after fracture, with maximum possible healing decreasing at longer waiting times.

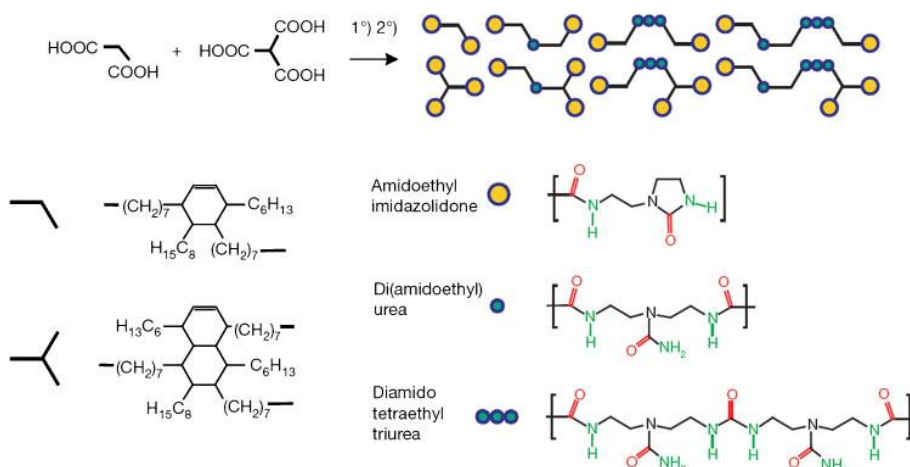


Figure 8: Synthetic scheme of a self-healing, supramolecular elastomer. Red bonds are hydrogen acceptor groups, and green bonds are hydrogen donor groups

Besides hydrogen bonding, another supramolecular interaction that has been investigated for its use in healable materials is that of metal-ligand coordination.

Ideal design of polymers that heal via bond reformation lies with the placement of 'weak link' moieties, sacrificial bonds designed to break in response to stress, thereby preserving the generally irreversible organic covalent bonds. With the appropriate chemistry, these 'weak links' can recombine to reform the virgin polymer network and heal damage.

Coordination polymers, which contain metal-ligand bonds in their backbone, may satisfy these requirements given that metal-ligand bonds are generally known to be much more labile than their organic covalent counterparts, but, if the metal and ligand are chosen wisely, have a high enough thermodynamic affinity to rapidly reassociate.

In 2007, Kersey et al. [31] reported the inclusion of metal-ligand complexes within a polymer system.

A material was created from a covalently bound polymer network that contained pyridine pendant groups, which formed a metal-ligand coordination complex with a bifunctional Pd(II) or Pt(II) compound. After first demonstrating the association between the metal and ligand, these stress-bearing groups were incorporated into a hybrid polymer gel composed of a pyridine functionalized methacrylate cross-linked network.

Paulusse [32] synthesised diphosphine telechelic poly(tetrahydrofuran) polymers, and the phosphine endgroups were complexed to palladium or platinum halides to yield polymers with multiple metal coordination sites along the polymer backbone.

Stress was applied to a solution of the metal-phosphine coordination polymers via ultrasonication, and chain scission was observed to occur predominantly through metal-phosphine dissociation.

Such systems containing reversible interactions that dissociate and re-associate with applied stress could be useful as a mechanically stimulated healable material in the future.

1.3.1.6 Self-healing via molecular diffusion

An alternate method for achieving intrinsic selfhealing is molecular diffusion of a mobile species to create chemical or physical adhesive linkages.

O'Connor & Wool [33,34] and McGarel & Wool [35] investigated the mechanisms involved in healing of damage in styrene-isoprene-styrene block copolymers and polystyrene. Wool and O'Connor suggested a five stages model to explain the crack healing process in terms of surface rearrangement, surface approach, wetting, diffusion and randomization (see Figure 9)

Utilizing thermoplastics chain mobility with a minimal application of heat, Lin et al. [36] studied crack healing in poly(methylmethacrylate) PMMA by methanol treatment from 40 to 60 °C. The authors found that the tensile strength of PMMA treated by methanol can be fully recovered to that of the virgin material. The extent of the healing defined by the recovery of tensile strength is found to depend on wetting and diffusion. The presence of methanol facilitates both

processes as a result of reducing the T_g and promoting diffusion of the polymer chains across the interface.

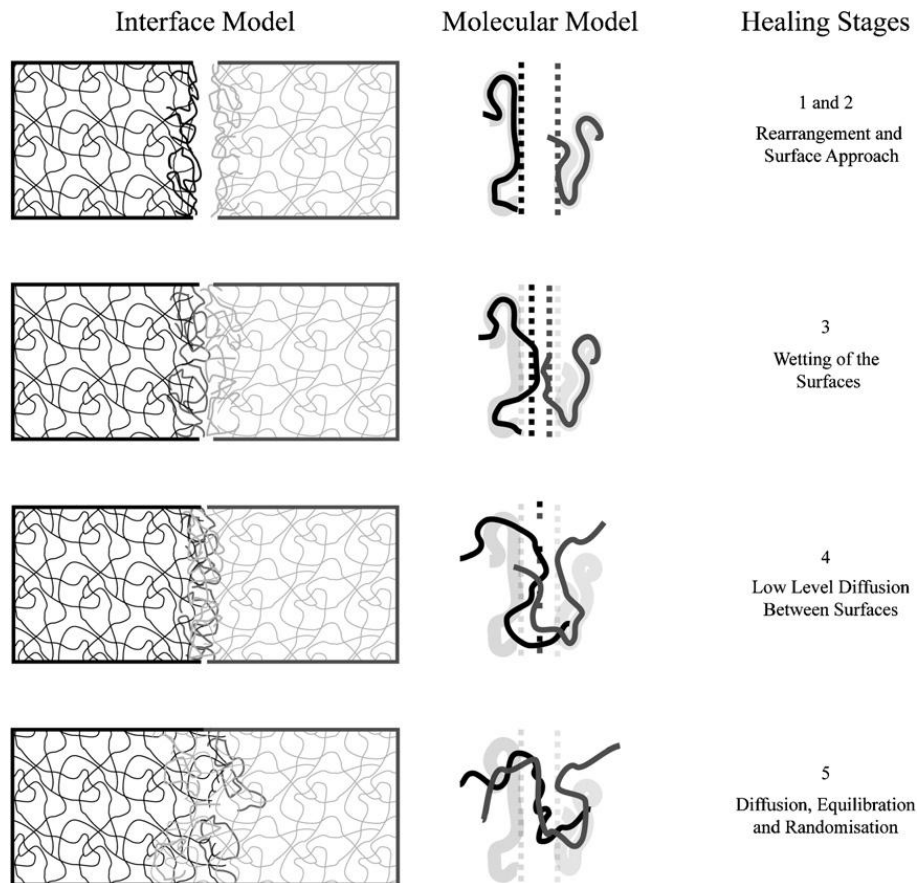


Figure 9: Mechanisms involved in self healing via molecular interdiffusion

The healing phenomena for these polymers were time dependent and temperature dependent and occurred via void closure, surface interaction, and molecular entanglement between the damaged faces.

Rahmathullah and Palmese [37] investigated the ability of thermoset epoxy/amine polymers, which are often used for structural applications, to heal via topological diffusion mechanisms.

Fractured halves of compact tension test specimens were brought into intimate contact with each other, clamped at either high or low pressures, and healed with a heat treatment of 185 °C for 1 h.

Elevated healing temperatures were required to bring the epoxy into its rubbery state, which allowed for enhanced molecular mobility of the topological polymer chains.

Significant diffusion across the crack plane occurred to recover up to 50–60% of the maximum load at failure, which was repeatable over numerous damage/healing cycles.

1.3.2 Extrinsic self-healing

In the case of extrinsic self-healing, the matrix resin itself is not a healable one. Healing agent has to be encapsulated or stored in other type of vessels and embedded into the materials in advance.

As the cracks destroy the fragile vessels in which the healing agent is stored, this would be released into the crack planes due to capillary forces and heals the cracks.

1.3.2.1 Self-healing in terms of healant loaded pipelines (hollow fiber approach)

It is well known that the mechanical properties of polymeric materials can be greatly improved with the addition of a reinforcing fiber or other filler, giving the composite desired high strength and stiffness to weight ratios [38]. The main disadvantage to these composites, however, is their pure poor performance under impact loading; this is an indication of their susceptibility to damage, which manifests mainly in the form of delamination. Utilizing reinforcing fillers that contain healing agent would not only add the desired strength to the system but would also allow for self repair of healing damage that occurred via repair molecules pre-embedded into the material.

Of the two main additives for structural enhancement in composite materials, glass and carbon fibers the former are ideal to accomplish the desired dual purposes; while solid glass fibers are common components in reinforced plastics, hollow glass fibers are also been shown to augment structural performance of materials without creating sites of weakness within the composites [39].

In this sense, significant effort has been dedicated to incorporating healing agents into hollow fibres, which can be used both as a structural reinforcement and as large storage vessels.

Once failure occurs in composites filled with these resin infused fibres, fibres rupture and healing agent(s) can diffuse into the damaged regions (Figure 10).

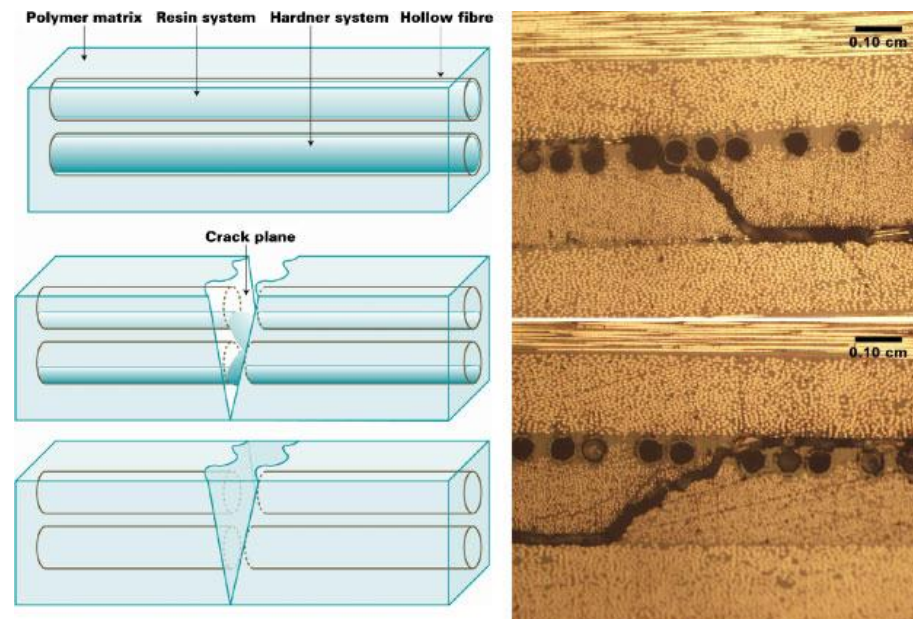


Figure 10: Self-healing concept using hollow fibre storage vessels (left) and ruptured hollow vessels containing healing agent (right)

These hollow fibres have been filled either through open ends, with either capillary action or vacuum assistance, or through surface pores, which need to be covered after resin infusion (Figure 11).

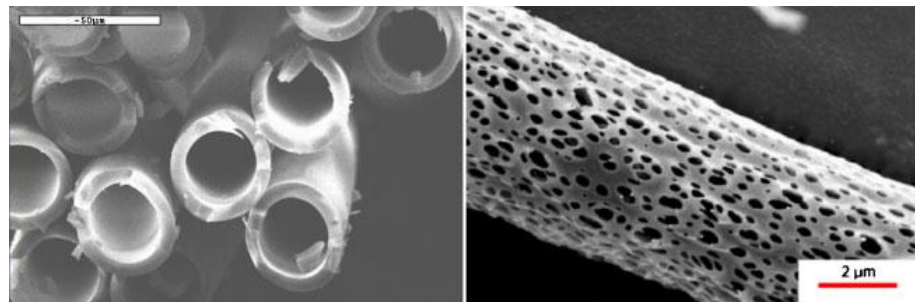


Figure 11: Hollow fibres with open ends (left) and hollow fibres with open surface pores (right)

Dry and Sottos [6, 40] pioneered the concept of releasing healing chemicals stored in hollow fibers to repair damage. This concept has been initially applied to cementitious materials to alter the cement matrix permeability, repair cracks, prevent corrosion.

This first system utilized cyanoacrylate [41], ethyl cyanoacrylate [42], and methyl methacrylate as healing agents to repair cracks in concrete.

The feasibility of this approach was subsequently extended to polymeric materials by Motoku et al. [43].

The healing agents contained within the glass fibers has been either a one-part adhesive, such as cyanoacrylate, or a two-part epoxy system containing both a resin and a hardener where either both are loaded in perpendicular fibers or one embedded into the matrix and the other inside fibers.

One of the initial challenges encountered when creating this type of self-healing system is the development of a practical technique for filling the hollow glass fibers with repair agent. When approaching this problem, the dimensions of the glass fiber itself must be considered, including diameter, wall thickness, and fiber hollowness, as well as the viscosity and healing kinetics of the repair agent. Bleay et al.[44] were among the first to develop and implement a fiber filling method involving capillary action that is assisted by vacuum, now a commonly utilized technique.

The glass fiber chosen must be also evaluated for its ability to withstand the composite manufacturing process without breakage, while still possessing the ability to rupture during a damage event in order to release the required agent(s) for healing. It was early on determined by Motoku [43] that hollow glass fibers were best suited for this kind of application, as opposed to polymer tubes or those made of metal, which often did not provide controlled fracture upon impact damage. Hucker et al.[45] showed that hollow glass fibers of a larger diameter showed an increased compressive strength, from 30-60 μm , while also allowing for a larger volume of repair agent to be stored within the composite. In certain cases, Dry and Sottos applied a brittle polymer coating to the outer surface of the fibers to promote damage-induced cracking.

Provided these parameters have been adequately optimized, the next factor to be considered is the ability of the repair agent to adequately reach the site of damage and subsequently undergo healing; this will depend upon the viscosity, and the extent of cure of the healing agent within a given time period. For instance, the cyanoacrylate system studied by Bleay et al.[44] was shown to indeed have the ability to restore mechanical strength to damage specimens, but also caused significant problems by curing upon contact with the mouth of the fiber, which prevented the healing agent from reaching the site of damage in the sample. A number of research groups [46-49] have utilized liquid dyes in their composites in order to serve as a damage detection mechanism, providing a visible indicator of the damage

site(s) within a structure, as well as allowing for assessment of the flow of repair agents to these sites.

In Figure 12 it is possible to observe liquid dyes in composites.

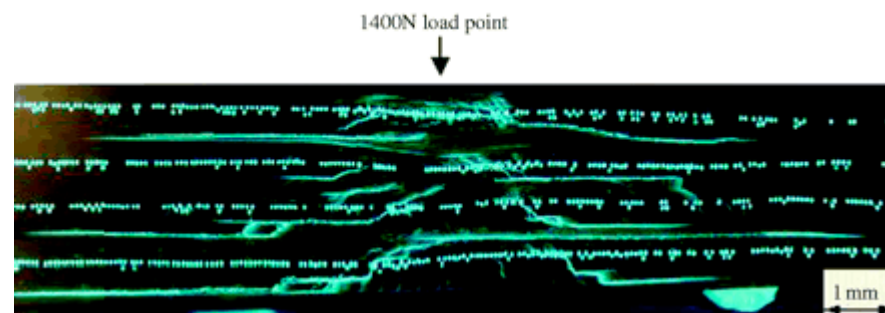


Figure 12 Cross section of Glass Fiber Reinforced Polymer laminate containing dye to visualize healing agent flow

Once the repair agent has successfully reached the site of damage, it must then undergo its curing or cross-linking process in order to restore strength to the material; the rate at which this is accomplished will determine the extent that crack propagation is halted.

The last parameters to optimize are the concentration of healing fibers within the matrix, the most effective special distribution of these fibers, and the dimensions of the final specimen, all while keeping in mind the corresponding effects on the mechanical properties of the resulting composite material. As Jang et al.[50] discovered, the stacking sequence of the fibers within the composite plays a role in inhibiting plastic deformation and delamination, and will also affect the response to an impact damage event. In order to maintain good mechanical properties, adequate spacing between the repair fibers within the composite is needed, and Motuku et al. have shown that thicker composites perform better in healing studies.

Much of the work that has been done on self-healing hollow fiber composites has focused on proving that this concept for self-repair is feasible, and have only reported qualitatively on the healing capabilities of the investigated system, only recently quantitative studies on mechanical properties associated with healing of the materials have been reported.

The inclusion of hollow glass fibers into a composite system was shown by Williams, Trask, and Bond[51,52] to give an initial reduction in the strength of the material, either by 16% in glass fiber

reinforced polymer (GFRP) composites or by 8% in carbon fiber reinforced polymer (CFRP) composites.

These “self-repairing” composites were shown to recover 100% of the virgin strength for GFRP and 97% of the virgin strength for CFRP but in both cases the composite materials were subjected to a heat treatment to aid in delivery of the resin to the damaged area as well as in curing of the healing agent.

In a different approach, Liu et al. reported a coating that can heal its ability to act as a water permeation barrier [53]. In this work, hollow, water degradable poly(lactic acid) (PLA) fibres were filled with a metal oxide precursor healing agent, TiCl_4 , and subsequently incorporated into subsurface polymer layers of multilayer films. Once damage penetrated deep enough in the multilayer film to reach the PLA layers, atmospheric moisture degraded the PLA fibres, releasing TiCl_4 into the damaged region. On contact with ambient humidity, the healing agent oxidises to a TiO_2 film to form an effective water permeation barrier.

Another healing agent reported to adequately self-heal a polymer when infused in hollow fibres is DCPD, otherwise well known in the realm of microcapsule based self-healing[54].

A commercially available borosilicate glass tube (external diameter: 125 mm, degree of hollowness: 64%) was filled with either DCPD or a suspension of functionalised MWNT in DCPD by capillary action, sealed at both ends and coated with Grubbs’ catalyst at its exterior walls. After damage and a short waiting time, healing with DCPD was able to recover 90% of its virgin tensile strength, with even higher values of strength recovery possible at low loadings of the functionalised MWNT.

1.3.2.2 Microvascular Networks

In conventional extrinsic self-healing composites it is hard to perform repeated healing, because rupture of the embedded healant-loaded containers would lead to depletion of the healing agent after the first damage.

Infusing larger storage vessels, such as the hollow fibres with healing agent, will likely result in multiple healing events of one damage site, but the total volume of liquid in each fibre is still finite.

A logical progression to supplying even larger volumes of healing agent to damage sites is through a series of healing agent filled interconnected channels, which could potentially be linked to an external, refillable liquid pump to deliver a constant supply of healing agent.

Healing with connected networks of healing agent is mechanistically similar to that of the hollow fibre approach, and conceptually similar to the vascular systems of many plants and animals.

Appropriately, connected networks of flowing healing agent is called 'microvascular' networks (Figure. 13a)

Toohey *et al.* proposed a self-healing system consisting of a three-dimensional microvascular network capable of autonomously repairing repeated damage events [55]. Their work mimicked architecture of human skin. When a cut in the skin triggers blood flow from the capillary network in the dermal layer to the wound site, a clot would rapidly form, which serves as a matrix through which cells and growth factors migrate as healing ensues. The 3D microvascular networks were fabricated by deposition of fugitive ink (a mixture of Vaseline/microcrystalline wax (60/40 by weight)) in terms of direct-write assembly through a cylindrical nozzle. Then, the yielded multilayer scaffold was infiltrated with epoxy resin. When the resin was consolidated, structural matrix was obtained. With the help of heating and light vacuum, the fugitive ink was removed and 3D microvascular networks were created. By inserting a syringe tip into an open channel at one end of the microvascular networks, fluidic polymerizable healing agent was injected into the networks.

The healing chemistry of this method used ring opening metathesis polymerization of dicyclopentadiene (DCPD) monomer by Grubbs' catalyst, benzylidenebis(tricyclohexylphosphine) dichlororuthenium, which was used successfully in microencapsulated composites.

In the crack plane, the healing agent interacted with the catalyst particles in the composites to initiate polymerization, rebonding the crack faces autonomously. After a sufficient time period, the cracks were healed and the structural integrity of the coating was restored.

As cracks reopened under subsequent loading, the healing cycle was repeated. By means of four-point bending configuration monitored with an acoustic-emission sensor (Figure 13 b), the above approach proved to be feasible.

The system showed up to 70% recovery of fracture toughness after damage in the four-point bending protocol.

The authors imagined extending this approach further to integrate pumps, valves and internal reservoirs, as well as to introduce new functionalities, including selfdiagnosis or self-cooling, through the circulation of molecular signals, coolants or other species.

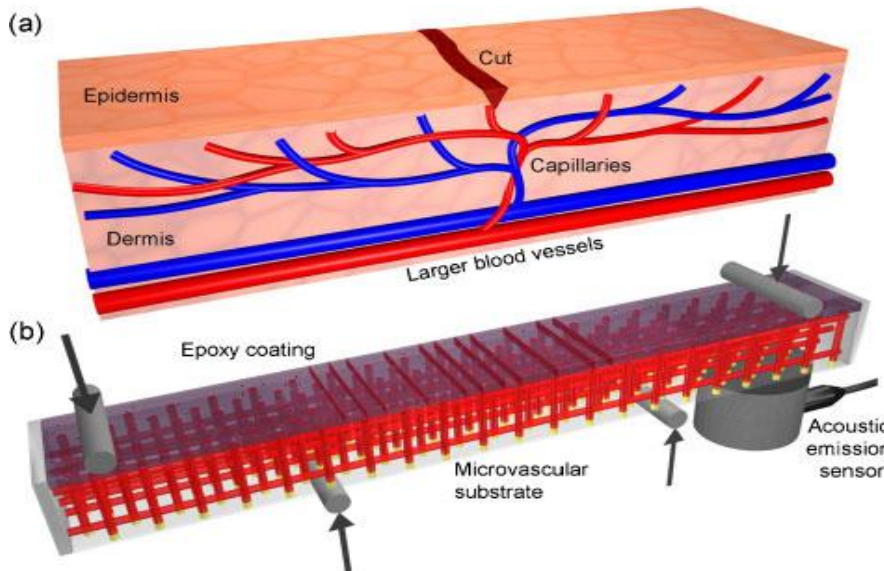


Figure 13: Microvascular based self-healing concept: a) a capillary network in the outer skin layer with a cut; b) schematic of an epoxy specimen containing a microvascular network, loaded in a four-point bending configuration monitored with an acoustic emission sensor

During the same timeframe, Williams et al. [56] published their version of a microvascular-containing mechanically stimulated healable material in the form of a sandwich structure composite. Sandwich structures use high performing skin materials, such as glass or carbon fiber composites, separated by a lightweight core to obtain a material with very high specific flexural stiffness. A vascular network incorporated into a sandwich structure would address the larger damage volume expected of these systems, as well as allowing for multiple healing events to occur. Samples were fabricated with channels containing a healing agent, which had a negligible effect on the mechanical properties of the composite. Rupture of the vessels released the healing fluid, filling the void that formed as a result of impact damage on the sample. Initial tests were run on samples containing pre-mixed resin and hardener, to demonstrate the healing capability of the system. Indeed, these samples showed consistent and

complete recovery of compressive stress at failure after impact damage.

After this recovery of mechanical properties was successfully accomplished, the two sets of orthogonal channels in the material (horizontal and vertical) were each filled with a component of the two-part epoxy healing system, resin and hardener; after impact damage and a subsequent four-point bending test, it was determined that only half of the samples achieved self-healing. For the healed samples, it was clearly demonstrated that rupture of the two types of vessel under impact allowed for adequate mixing of the two components to initiate the cure reaction and successfully restore the mechanical properties of the material. In the samples that did not recover their strength, however, it was determined that there was failure of the vessels to properly rupture under impact damage; either resin or hardener was released in these cases, but not both components.

1.3.2.3 Capsule-Based Self-healing Materials

Capsule-based self-healing materials sequester the healing agent in discrete capsules until damage triggers rupture and release of the capsule contents.

The microencapsulation approach is by far the most studied self-healing concept in recent years.

This particular approach involves incorporation of a microencapsulated healing agent and a dispersed catalyst within a polymer matrix. Upon damage-induced cracking, the microcapsules are ruptured by the propagating crack fronts resulting in release of the healing agent into the cracks by capillary action. Subsequent chemical reaction between the healing agent and the embedded catalyst heals the material and prevents further crack growth (see Figure 14).

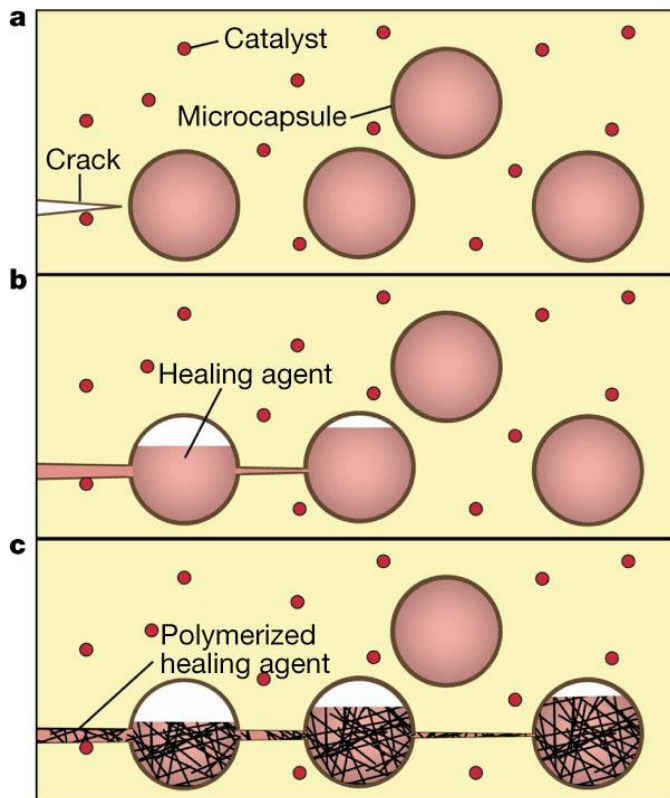


Figure 14: Autonomic healing concept incorporating encapsulated healing agent and embedded catalyst particles in an epoxy matrix; (a) damage event causes crack formation in the matrix; (b) crack ruptures the microcapsules, releasing liquid healing agent into crack plane; (c) healing agent polymerizes upon contact with embedded catalyst, bonding crack closed

There are some obvious similarities between the microencapsulation and hollow fiber approaches, but the use of microcapsules alleviates the manufacturing problems experienced in the hollow fiber approach. The microencapsulation approach is also potentially applicable to other brittle material systems such as ceramics and glasses.

Although the feasibility of the technology has been mainly tested in epoxy matrices, other matrices such as polyester and vinyl ester have also been investigated. Unlike the hollow fiber approach, the microencapsulation approach could be used for producing self-healing coating systems.

The key to realising a successful microcapsule based self-healing system lies with carefully choosing a healing agent/catalyst combination with the requisite features to be compatible with the

healing mechanism. For example, the healing agent and the catalyst must have a long shelf life and be stable to the composite processing conditions without undergoing decomposition, uncatalysed polymerisation, or leaching out of the microcapsule shell.

Furthermore, once the microcapsules rupture, the healing agent must have a sufficiently low viscosity to flow out of the capsules and completely fill the crack volume in a reasonable timeframe, good wetting properties on the crack surface, and minimal loss of the healing agent from the crack plane through, for example, volatilisation or diffusion into the polymer matrix. And finally, the healing agent must have rapid catalyst dissolution (or for liquid catalysts, rapid mixing) and polymerisation kinetics, low shrinkage upon polymerisation, and the resulting polymer should have good mechanical and adhesive properties.

Not only is the choice of healing agent and catalyst of the utmost importance, but varying the specific parameters associated with each of the self-healing components can affect other pieces of the system, often unexpectedly.

Choice and control of microcapsule parameters and catalyst powders parameters (structural and morphological organization) are critical points for manufacturing of an efficient material.

1.3.2.3.1 Microcapsule-Parameters

The encapsulation technique should, ideally, be simple and user friendly, and the liquid healing agent should be chemically inert to the microencapsulation conditions. The healing agent should not leach out of the capsules over time, nor should any other components destructively permeate into the microcapsule. The capsules should be robust enough to withstand handling and fabrication of self-healing composites, but fragile enough to break and subsequently release core material once the self-healing polymer is fractured. And finally, these capsules should also have a compatible outer shell wall to promote good adhesion to the surrounding polymer matrix.

Polymeric microcapsules are often prepared via miniemulsion polymerization technique, as described by Asua [57], involving submicron oil-in water dispersions of the polymeric material (Figure 15).

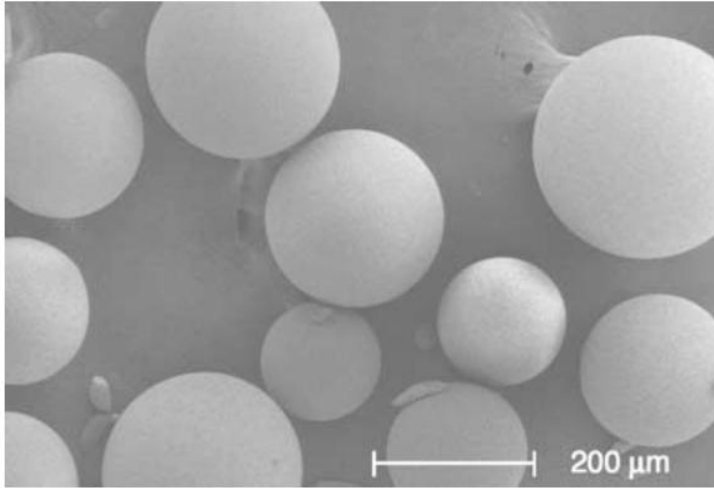


Figure 15: Urea- formaldehyde microcapsules containing dicyclopentadiene (DCPD)

For the majority of self-healing composite systems that have been so far studied, the microcapsules are a urea-formaldehyde polymer encapsulating dicyclopentadiene as the liquid healing agent. During the *in situ* polymerization process, urea and formaldehyde react in the water phase to form a low molecular weight pre-polymer; as the weight of this pre-polymer increases, it deposits at the dicyclopentadiene-water interface. This urea-formaldehyde polymer becomes highly cross-linked and forms the microcapsule shell wall. Nanoparticles of urea-formaldehyde pre-polymer then deposit on the surface of the microcapsules, providing a rough surface morphology that aids in the adhesion of the microcapsules with the polymer matrix during composite processing. Brown et al.[58] report that the microcapsules made in this manner average 10-1000 μm in diameter, with a smooth inner membrane that is 160-220 nm thick and a fill content of 83-92% liquid healing agent.

The mechanical rupture of the microcapsule is the triggering event for the healing process; without it, no healing will occur. It is exceedingly important, therefore, to fabricate microcapsules with optimal mechanical properties and wall thickness. The relationship between the stiffness of the capsule and the stiffness of the surrounding matrix will determine how the crack will propagate in the sample. Keller and Sottos [59] have described how a capsule with a higher elastic modulus than the matrix material will create a stress field that tends to deflect cracks away from the capsule; a more compliant shell wall, on

the other hand, will produce a stress field that attracts the crack towards the microcapsule (Figure 16).

The image on the left in Figure 16 corresponds to an inclusion three times stiffer than the surrounding matrix, and the image on the right corresponds to an inclusion three times more compliant than the surrounding matrix.

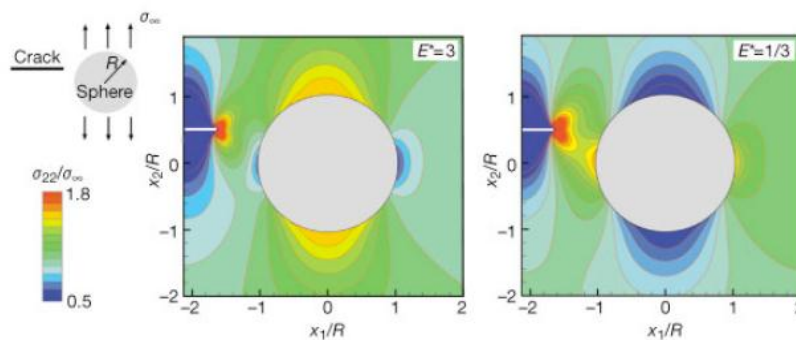


Figure 16: Stress state in the vicinity of a planar crack as it approaches a spherical filler particle embedded in a linearly elastic matrix

This latter relationship will facilitate the rupture, ensuring that the healing process will be triggered in the event of mechanical damage to the system.

The wall thickness of the microcapsule is another critical parameter to be investigated. If the shell wall is too thick, the microcapsule will not easily rupture, and healing will not occur. If the shell wall is too thin, however, the microcapsules can rupture during composite manufacture and processing, or the healing agent could leak or diffuse into the matrix over time. As noted by Brown et al., [58] the shell wall thickness is largely independent of manufacturing parameters and is typically between 160-220 nm thick; however, slight adjustments can be made during the encapsulation procedure to alter the resulting microcapsules.

The size of the microcapsule also plays a role in the performance of the system, in terms of the effect on toughness of the composite as well as the fill content and resulting amount of healing agent available during crack propagation. The microcapsule size is controlled mainly via the rate of agitation during the encapsulation process; typical agitation rates reported by Brown et al. [58] range from 200-2000 rpm, with finer emulsions and therefore smaller diameter capsules being produced with increasing rates.

In 2004, Brown et al.[60] noted that smaller microcapsules exhibit maximum toughening at lower concentrations; on the other hand, Rule et al.[61] reported in 2007 that specimens that contain larger microcapsules perform better than those with smaller microcapsules at the same weight fraction, presumably due to the amount of healing agent present in the specimen.

In the latter study, the best healing achieved was on a specimen containing 10 wt% of 386 μm capsules, which corresponds to 4.5 mg of healing agent being delivered per unit crack area (assuming all capsules in the crack plane rupture). In that report, Rule et al. postulated, based on measured crack face separation values (length and height of crack), that the crack volume is $2.6\mu\text{L}/\text{cm}^2$ over the damaged area in a sample; this means that at least $2.6\mu\text{L}/\text{cm}^2$ of healing agent would need to be delivered in order to completely fill the crack. Indeed, they found a rapid decline in effectiveness of healing when the amount of healing agent delivered to the crack dropped below this value.

The amount of healing agent available for delivery to the crack plane was calculated based on the microcapsule size and weight fraction incorporated into the composite, and verified by comparing the data from these autonomously healing samples with that of samples in which a known volume of healing agent was manually injected into the crack plane to initiate the healing process.

Blaiszik et al.[62] reported that nanocapsules have been made via ultrasonication and other minienapsulation techniques (Figure 17).

Capsules as small as 220 nm and as large as 1.65 μm have been fabricated with a 94% fill content and nearly all of the capsules ruptured during fracture testing. In addition, a substantial increase in fracture toughness per volume fraction of capsules was observed for 1.5 μm capsules, as compared to the 180 μm capsules previously studied by Brown et al[60].

At a capsule volume fraction of 1.5%, the epoxy composite showed a 59% increase in fracture toughness. These nanocapsules will allow for self-healing applications in thin films and coatings widening the range of potential uses for capsule containing healable composite materials.

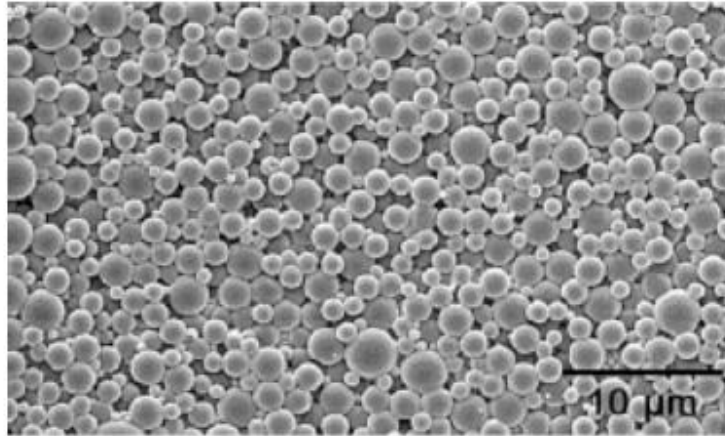


Figure 17: Nanocapsules prepared via ultrasonications and miniemulsion techniques

In addition to the parameters involving the microcapsule itself, the properties of the healing agent must also be investigated.

The relationship between the kinetics of the healing process and the mechanical crack growth are of the utmost importance. Jones et al.[63] described how if the crack grows too fast as compared to the healing polymerization process, then little or no healing will occur.

However, if the healing agent cures too quickly and catalyst dissolution is slow, then there will be insufficient coverage of the crack plane and healing will occur in isolated locations around the catalyst particles; this will reduce the healing efficiency of the system. If the healing agent cures too slowly, rest periods will need to be introduced to allow for maximum recovery of mechanical strength between damage events.

Brown et al.[60] have shown that the polymerization of the healing agent provides both a short term adhesion effect to retard crack growth and a long term closure effect to restore strength to the material.

These dual advantages of a carefully optimized polymerization process allow for maximum healing efficiencies to be obtained in these composite samples.

1.3.2.3.2 Microencapsulated healing agents

The group of White *et al.*, the pioneer in developing self-healing polymeric materials, systematically investigated self-healing strategy based on ring opening metathesis polymerization (ROMP) of microencapsulated dicyclopentadiene (DCPD) and reported a series of important findings [64,65,66].

DCPD was encapsulated in a poly(urea-formaldehyde) shell and embedded with the Grubbs' catalyst in an epoxy matrix.

Healing is triggered when damage in the form of a crack ruptures the microcapsules, causing DCPD to be released into the crack plane where it comes in contact and mixes with the pre-embedded Grubbs' catalyst (Figure 18).

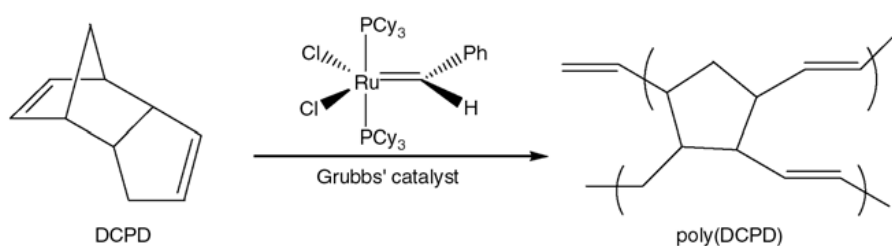


Figure 18. Ring opening metathesis polymerization of DCPD

The choice of healing agent, dicyclopentadiene, was made based on its low cost, wide availability, long shelf life, low viscosity and volatility, and its rapid polymerization at ambient conditions upon contact with a suitable catalyst.

The catalyst chosen, first generation Grubbs' catalyst: bis(tricyclohexylphosphine)benzylidene ruthenium (IV) dichloride is well known for promoting olefin metathesis, showing high activity while being tolerant of a wide range of functional groups.

After failure, his system could recover up to 75% of its virgin fracture toughness; by optimising various parameters (catalyst and microcapsule size and loading), it was found that up to 90% toughness recovery could be achieved.

Also fatigue lifetime of these systems could be improved to over 30 times longer than that of a polymer without a self-healing functionality, and under certain conditions (low applied stress and short rest periods), fatigue crack growth was indefinitely retarded [67].

Kessler, Sottos, and White [68] introduced the same microcapsules and catalyst into a fiber-reinforced polymer composite to test the healing ability on the most common mode of composite failure, delamination.

The healing efficiency for the self-healing specimens under optimized conditions, was 66%.

Brown, Sottos, and White [65] also examined the effect of the inclusion of microcapsules and catalyst particles on the mechanical properties of the epoxy matrix: the virgin fracture toughness increased with an increase in the concentration of microcapsules, reaching a maximum at 15 wt%, corresponding to a toughness more than double that of the neat epoxy.

The catalyst particle size also affected the fracture toughness, with both virgin and healed toughness values increasing with an increase in particle size; the maximum increase in toughness was achieved with 180-355 μm catalyst particles.

Much effort has been dedicated to optimising existing microcapsule based self-healing that uses ROMP healing agents. A large amount of this effort has been focused on improving the kinetics of healing, which is a crucial factor when deciding the appropriate applications for self-healing polymers that may be subject to constant or frequent stress.

Two ROMP based monomers that have received significant attention as more rapid healing agents are ethylidene norbornene (ENB) and the exo-isomer of DCPD (Figure 19)

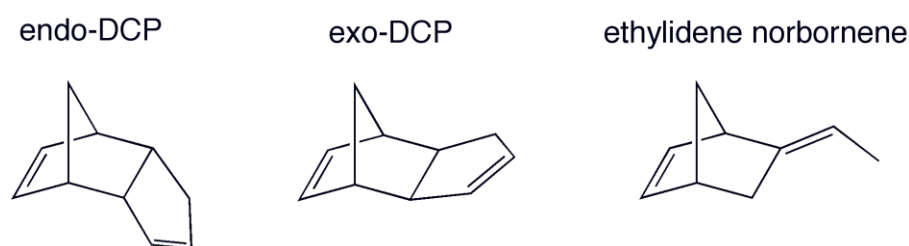


Figure 19: Monomers used as liquid healing agents

DCPD is most easily obtained as the commercially available endo-isomer, and all ROMP based selfhealing systems. However, Rule and Moore [69] found that the exo-isomer, which can be prepared from endo-DCPD in a two-step isomerisation process, undergo ROMP

nearly 20 times faster than its endo-counterpart.[70] So when exo-DCPD was incorporated into a self-healing polymer steady-state healing was reached after only about 30 min, nearly 20 times faster than the time required to fully heal with the endo-isomer.

ENB, a monomer also active towards the ROMP chemistry, is particularly attractive as a healing agent because it is a cheap, commercially available chemical with an extremely rapid bulk polymerisation rate.

ENB also has a much lower freezing point than that of DCPD (15°C). The drawback to using this monomer, however, is that the resulting polymer is linear and thus has inferior mechanical properties as compared to polyDCPD.

Liu et al. [71] tested a system that used a blend of the two monomers as the liquid healing agent to increase the rate of polymerization and range of usable temperatures, while at the same time maintaining desirable mechanical properties. The polymerization was indeed faster with the addition of ethylidene norbornene and could be completed at a lower catalyst loading. Hence, a blend of DCPD with ENB was believed to provide a more reactive healing system with acceptable mechanical properties, making it more suitable for practical use.

There are some issues regarding the stability and reactivity of the catalyst chosen for this systems. First generation Grubbs' catalyst is deactivated upon prolonged exposure to air and moisture and also loses its reactivity upon exposure to diethylenetriamine (DETA), the agent used to cure the epoxy matrix of these composites.

Grubbs' catalyst can exist in different crystal morphologies and each has a effect on the dissolution kinetics and corresponding healing performance of the material.

Smaller catalyst particles will have faster dissolution kinetics but will then have a larger reduction in activity due to exposure to DETA.

Therefore, the key to achieving optimal healing efficiency is to balance the competing effects of better catalyst protection during fabrication with the larger crystals and faster dissolution in the DCPD healing agent with the smaller crystals.

Rule and co-workers [72] proposed to encapsulate Grubbs' catalyst by wax to overcome the deactivation problem. This was achieved by a hydrophobic congealable disperse phase encapsulation process already established in pharmaceutical applications. The average diameters of the wax encapsulated catalyst ranged from 50 to 150 nm.

The encapsulated Grubbs' catalyst was protected against deactivation by the DETA curing agent, retaining 69% of its reactivity. The wax microspheres also proved to aid in the dispersion of the catalyst within the epoxy matrix, leading to more uniform healing.

The greater drawback of using ROMP based self-healing is economics, the Grubbs' catalyst uses ruthenium – a precious metal that is much expensive.

One way this problem can be addressed is using the monomers described above with faster healing kinetics (such as ENB and exo-DCPD), which require lower loadings of catalyst to achieve high degrees of cure in a reasonable time period.

Additionally, increasing the rate of catalyst dissolution in healing agent, either by treating the catalyst particles to have a larger surface area or selecting catalysts and healing agents with inherently matching chemical compatibilities, is known to reduce the amount of catalyst required in a self-healing polymer.

An alternative to the ruthenium catalysts was also recently explored, as they tend to be costly and have limited availability, and so would not be practical for larger scale commercial applications. Tungsten (VI) catalysts were investigated by Kamphaus et al.[73] as a cost-effective alternative to using Grubbs' Ru catalyst; in these systems WCl_6 would act as a catalyst precursor, becoming active either following alkylation with phenylacetylene or oxidation from contact with air. In addition to the alkylating agent, a dissolution agent (nonylphenol) would need be added to ensure miscibility with DCPD in order for polymerization to be initiated.

The samples prepared with WCl_6 initially showed a 50% decrease in virgin fracture toughness, most likely due to poor bonding between the catalyst and the epoxy matrix. Upon addition of a silane coupling agent, the toughness was increased to 75% that of the neat epoxy. The as-received WCl_6 catalyst had a tendency to agglomerate into particle clusters within the matrix and so mechanical stirring was used to obtain a better catalyst distribution within the sample.

The highest healing efficiency obtained was 20% for a completely autonomous sample, which was achieved using 12 wt% WCl_6 , 15 wt% exo-DCPD, 0.5 wt% phenylacetylene, and 1.0 wt% nonylphenol.

Cho et al. [74] developed a totally different healing system using di-n-butyltin dilaurate (DBTL) as the catalyst and a mixture of hydroxyl end-functionalized polydimethyl-siloxane (HOPDMS) and

polydiethoxysiloxane (PDES) as the healing agent. The polycondensation of HOPDMS with PDES is alleged to occur rapidly at room temperature in the presence of the organotin catalyst even in open air. This system possesses some advantages, including (i) the healing chemistry remains stable in humid or wet environments, (ii) the chemistry is stable to an elevated temperature ($>100^{\circ}\text{C}$), enabling healing in higher-temperature thermoset systems, (iii) the components are widely available and comparatively low in cost, and (iv) the concept of phase separation of the healing agent simplifies processing, as the healing agent can now be simply mixed into the polymer matrix.

In this system the catalyst was encapsulated instead of the siloxane-based healing agent, both of which were simply phase-separated in the vinyl ester matrix (VE) Polyurethane microcapsules containing a mixture of DBTL catalyst and chlorobenzene were formed (prior to embedding in the matrix) through interfacial polymerization. Despite the potentially more stable healing agent, this system actually achieved a healing efficiency value of 46%, which is lower than the 75–90% reported for the DCPD/Grubbs' catalyst-based healing system.

Keller et al.[75] investigated healing in a poly(dimethylsiloxane) elastomer (PDMS) with a healing agent that, when polymerised, is identical to the polymer matrix. In this system, a two-capsule healing agent was used: the first capsule contained a vinyl functionalised PDMS resin and a platinum catalyst, and in the second, capsule was a liquid initiator containing a hydrosiloxane copolymer diluted with 20% solvent to reduce its viscosity. Both components were encapsulated in urea–formaldehyde shells. Upon rupture of the microcapsules and release of the two shell materials into the damage area, the platinum catalyst adds the Si–H bonds of the hydrosiloxane copolymer across the vinyl groups of the PDMS resin to cure and heal damage. This system was shown to heal tear damage by recovering 70–100% of tear strength and significantly retard fatigue crack growth.

An alternative approach to self-healing systems containing an embedded healing agent utilizes epoxy as the encapsulated healing agent. This healing process would produce the same material that comprises the matrix of the composite, thus ensuring good adhesion between the healing material and the matrix, as well as allowing for

recovery of the initial mechanical properties. A second component, a hardener, would also need to be incorporated into the composite; in the event of crack formation and propagation the epoxy capsules would be ruptured and upon exposure of this epoxy to the hardener in the composite, polymerization would occur, filling the crack and restoring strength to the material.

One of the first successful attempts to match a healing agent to its epoxy matrix was done by Rong et al.[76], in which a diglycidyl ether bisphenol-A (DGEBA) based epoxy resin was encapsulated in a urea-formaldehyde microcapsule and, along with a commercially available capsulated imidazole hardener, embedded in an epoxy matrix made from the same DGEBA epoxy resin as in the microcapsules. Healing with this system showed 100% recovery in fracture toughness.

Yin et al. [77] used uncured epoxy resin as a healing agent, utilizing a imidazole-metal complex as a latent hardener. This $\text{CuBr}_2(2\text{-MeIm})_4$ hardener complex was soluble in the epoxy matrix and so could be evenly mixed in to form a homogenous matrix material capable of initiating healing at any point. The epoxy resin was encapsulated in urea-formaldehyde microcapsules and these were then embedded into the matrix material. This system shown to achieve up to 111% healing efficiency of , however, the main limitation is that it was not fully autonomous. In order for the imidazole complex to dissociate into its reactive species, it required heating to between 130-170°C.

The last system that integrates an encapsulated healing agent into a polymer matrix makes use of solvent-promoted healing. There are five stages to the healing process: surface rearrangement, surface approach, wetting, diffusion, and randomization.

In addition to the polymerizable healing agent, Caruso *et al.*[78] used solvents to heal cracks in thermoset materials. Chlorobenzene was encapsulated by urea-formaldehyde and embedded in epoxy matrix. The solvent would induce crosslinking of the incompletely cured resin and heal cracks. Composites were fabricated with 20 wt% chlorobenzene microcapsules, which showed a maximum 82% healing efficiency. The technique might be an economical, simple, and potentially robust alternative to the recovery of virgin properties of a material after crack damage has occurred.

1.3.3 Assessment of Self-healing efficiency

There are different methods for calculation of self-healing efficiency that are applicable for each individual mode of damage as well as each unique damaged material. This makes quantifying the extent of healing within the material and comparing it to healing in other systems rather difficult.

The quality of healing, generally referred to as ‘healing efficiency’ (η), is defined as the per cent recovery of a virgin material property as equation below:

$$\eta = \frac{P_{Healed}}{P_{Virgin}} \% \quad (\text{Eq. 1.1})$$

where η is healing efficiency, P_{Healed} is the property of healed material and P_{Virgin} is the property of the same virgin material.

Some factors may complicate any direct interpretation of healing efficiency values.

First generally very brittle polymers are chosen as reference materials. Healing efficiencies using polymers employed in real applications, which often utilise stronger and tougher polymer matrices, will likely be lower due to their superior material properties.

Second, most healing additives have either a beneficial or detrimental effect on the virgin material properties of the polymers in which they are incorporated and this makes full recovery of these properties either more or less difficult respectively. For example, it is often the case that higher loadings of healing components imparts both decreasing virgin properties and increasing healing ability to a polymer, which can greatly amplify the effect of adding higher amounts of healing components. For this reason, alternative definitions of healing efficiency are sometimes used that normalise healed material properties by the virgin properties of polymers without added healing components as shown in equation 1.2:

$$\eta = \frac{P_{Healed}}{P_{NoHealing}} \% \quad (\text{Eq. 1.2})$$

where $P_{NoHealing}$ is the propertie of virgin material without added healing components.

In most cases, evaluation of healing requires a controlled and measurable application of damage to the virgin polymer, followed by

a similar application of damage to the healed polymer and several different damage methods have been used to evaluate healing. Most often, damage is induced through various different tensile, compression or bending test protocols, but numerous different damage modes have also been utilised: impact, cutting, scratching, sawing, needle puncture, nail puncture, hammering and indentation. Also, different studies employ different extents of damage using these testing protocols, which have ranged from applying only enough stress to induce measurable cracking and delamination to catastrophic failure of specimens into multiple pieces. Many of the material properties that have been used to quantify self-healing efficiency are listed In Table 1.1. The healing efficiency definition is chosen depending on the virgin polymer properties, desired failure mode, self-healing mechanism.

Material property	Efficiency evaluation	Nomenclature
Fracture toughness	$\eta = \frac{K_{ICHealed}}{K_{ICVirgin}} \%$	K_{IC} =Fracture toughness
Strength	$\eta = \frac{\sigma_{Healed}}{\sigma_{Virgin}} \%$	σ =strength;
Strain energy	$\eta = \frac{G_{ICHealed} / A_{Healed}}{G_{ICVirgin} / A_{Virgin}} \%$	G_{IC} =strain energy release rate; A=surface area create by fracture
Stiffness	$\eta = \frac{E_{Healed}}{E_{Virgin}} \%$	E=Young's modulus

Table 1.1: Self-healing efficiency evaluation based on recovery of different material properties

For exemple, susceptibility of a given material to fracture can be expressed in terms of the plane strain fracture toughness, K_{IC} . The recovery of fracture toughness allows for a measurement of mode I crack opening, and is similar to the mechanism of microcrack growth that is often observed in real applications. It has become standard practice to assess the healing ability of a particular material/technique by comparing the fracture toughness of the material both before and after healing.

The self-healing efficiency, can therefore be expressed as:

$$\eta = \frac{K_{ICHealed}}{K_{ICVirgin}} \% \quad (\text{Eq. 1.3})$$

where $K_{ICVirgin}$ is the fracture toughness of the virgin specimen and $K_{ICHealed}$ is the fracture toughness of the healed specimen.

Healing efficiencies have also been expressed as a ratio of the strain energy release rate, G_{IC} , of the healed and virgin materials. Healing efficiency based on strain energy or tear strength is a better fit for elastomers or plasticised polymers that undergo highly ductile failure. Recovery of impact, compression after impact or flexural after impact strength may be more appropriate metrics for evaluating fibre reinforced polymers since impact damage is well suited to target delamination and fibre–matrix debonding failure mechanisms.

The definition of healing efficiency shown in equation (1.1) is inappropriate for quantifying fatigue lifetime in self-healing polymers under cyclic fatigue loading. Characterization of fatigue response is more complex than monotonic fracture because it depends on a number of factors such as the applied stress intensity range, the loading frequency, the ratio of applied stress intensity, the healing kinetics, and the rest periods employed [67].

The fatigue-healing efficiency (ϕ) is defined by fatigue life-extension:

$$\phi = \frac{N_{Healed} - N_{control}}{N_{control}} \% \quad (\text{Eq. 1.4})$$

Using protocol outlined by Brown et al. [65] fatigue life extension (ϕ) is evaluated as a function of the total number of cycles to failure for a sample with self-healing functionalities (N_{Healed}) normalised by the number of cycles to failure of an other identical specimen without self-healing functionalities ($N_{control}$).

A second approach was developed by Lewis et al. [79, 80] and is similar to the first, but instead utilises the mean fatigue crack propagation rate (FCPR) as shown in equation below:

$$\phi = \frac{FCPR_{Healed} - FCPR_{control}}{FCPR_{control}} \% \quad (\text{Eq. 1.5}).$$

1.4 Ph.D. Aim

The aim of my Ph.D. research has been the formulation and characterization of self-healing polymer composites active under the severe operational conditions of the aeronautical vehicles.

This self-healing system is applicable both to the primary and secondary structure of the aircrafts (see Figure 20).

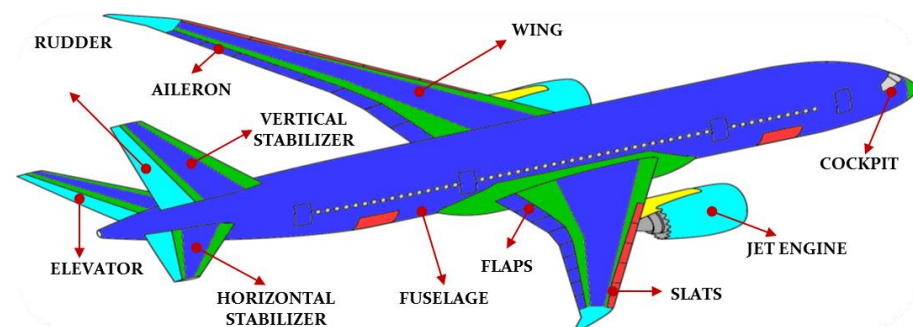


Figure 20: Principal structural units on an aircraft

The primary structure sustains aerodynamic loads. If parts of the primary structure are damaged, the stability of the vehicle is completely compromised.

Contrary to the primary structure, secondary structures permit to keep control of the aircraft even after possible damages.

Our self-healing system for aircraft polymer composites was inspired by design already proposed in literature, as described in the State of art, the design of White et al.[64-68].

This system consists in incorporating a microencapsulated healing agent and a catalytic chemical trigger within an epoxy matrix.

An approaching crack ruptures the embedded microcapsules releasing a healing agent into the crack plane through capillary action. Polymerization of the healing agent is triggered by contact with the embedded catalyst, bonding the crack faces (Figure 21).

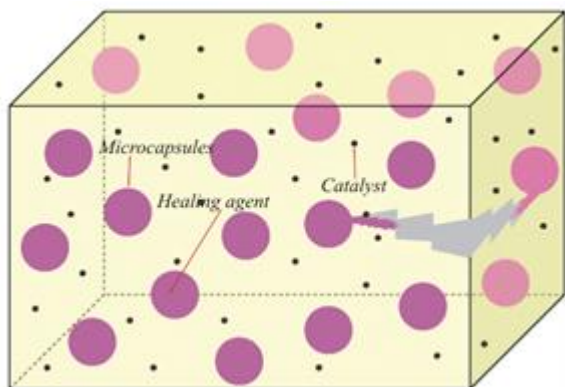


Figure 21: Material Design (Epoxy matrix)

In such a system the efficiency of self-repair function, in terms of trigger, speed and yield, is related to ring-opening metathesis polymerization (ROMP) of the healing agent by appropriate catalysts.

Ring-opening metathesis polymerization is a type of olefin metathesis polymerization that produces industrially important products. The ROMP catalytic cycle requires a strained cyclic structure because the driving force of the reaction is relief of ring strain. After formation of the metal-carbene species, the carbene attacks the double bond in the ring structure forming a highly strained metallacyclobutane intermediate. The ring then opens giving the beginning of the polymer: a linear chain double bonded to the metal with a terminal double bond as well. The new carbene reacts with the double bond on the next monomer, thus propagating the reaction. The catalysts used in the ROMP reaction include a wide variety of metals and range from a simple RuCl_3 /alcohol mixture to Grubbs or Hoveyda Grubbs catalyst. This system is a challenge for epoxy structural composites: however, some drawbacks have to be re-evaluated in order to be fully applied to advanced applications. These mainly regard:

- the thermal stability of the catalyst inside the epoxy resin during the curing cycle;
- the impossibility to utilize primary amines as hardeners, since they can poison the catalyst;
- it is critical that self-healing activity functions at low working temperatures which can reach values as low as -50°C .

Concerning self-healing composites based on the ring-opening metathesis polymerization, it is important to resolve problem of catalyst stability which can be seriously compromised because of the chemical environment and the cure temperature necessary for good performance of composite. Generally, to impart suitable mechanical properties for fully operational system in aeronautics application, the temperature used in the last step of curing cycle is up to 180 °C. For all these aspects the technical targets of my research are:

- working temperatures required at which the self-healing functionality must be active: -50 °C/80 °C;
- curing temperature required for high mechanical properties' system: 170 °C / 180 °C;
- efficiency of self-healing system: over 80%.

Therefore the research development of my PhD has been carried out in the following stages:

I stage (Materials and Reactions)-tasks :

- Screening of potential new matrix/healing agent systems using chemical and mechanical compatibility criteria;
- optimization of the ring-opening-metathesis-polymerization (ROMP) chemistry for self-healing applications at the temperatures of aircrafts working;
- investigation of new catalysts, and their thermal stability.

II stage (Microcapsules Manufacturing - Characterization and Dispersion Methods, Catalyst Powders)-tasks:

- encapsulation of the best healing agent (the choice has been done also in function of the selected catalyst);
- microcapsule and catalyst dispersion into the epoxy formulations;
- epoxy formulation characterization and analysis of the interactions of the self-healing components in the epoxy matrix.

III stage (Manufacturing Process- Testing)-tasks:

- development of the manufacturing process;
 - mechanical characterization;
-

- analysis of healing efficiency at various temperatures;
 - characterizations of the self-healing composites, after damage.
-

Materials

2. Materials

For the design of our self-healing system attention has been focused on a composite material consisting of a thermosetting matrix (resin epoxy) in which are dispersed powders of catalyst active in metathesis reactions of olefins, and microcapsules containing a reactive monomer capable of polymerize after a metathesis reaction and then to crosslink.

Several systems were investigated that differ for the nature and the composition of the epoxy matrix, catalyst and active monomer used.

2.1 Materials: polymeric matrix

a) Epoxy Resin

The polymeric matrix of our self-healing system is a thermosetting polymeric matrix.

It was decided to carry out the experiment by choosing an epoxy matrix resin. Epoxy resins are a family of thermosetting polymeric materials which do not lead to the formation of reaction products when they harden (crosslink) and therefore have a low shrinkage of crosslinking.

Epoxy has a wide range of applications, including fiber-reinforced plastic materials and general purpose adhesives.

The resin consists of monomers or short chain polymers with an epoxide group at either end.

The choice of epoxy resin is a linear polymer with low molecular weight that has to the ends very reactive epoxy groups; it is

commercially available under the name of "**EPON 828**" (UPAC name: **Bisphenol A diglycidyl ether**).

Epon 828 is a liquid epoxy resin made from bisphenol-A and epichlorohydrin. When Epon 828 is hardened or cross-linked with curing agents, excellent mechanical, dielectric, and adhesive properties are obtained, as well as vastly improved chemical resistance.

The chemical structure of the polymer synthesized is shown in Figure 22:

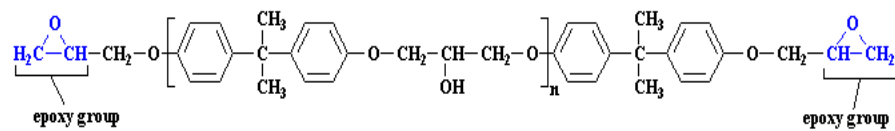


Figure 22: Epon Resin 828 (n=2)

The typical properties of Resin 828 are the following:

Epoxide equivalent weight (grams of resins containing one gram-equivalent of Epoxide – ASTM D1652)= 185-192.

Viscosity, at 25 °C, poise (kinematic viscosity – determination of the viscosity of liquids by Ubbelohde Viscometer– ASTM Method D445)= 110-150.

Density, lbs/gal, at 25 °C = 9.7.

Physical form(25 °C) – clear liquid.

The EPON 828 is a low molecular weight linear polymer (the reaction of polycondensation between bisphenol A and epichlorohydrin can be conducted in order to have different molecular weights of the resulting polymer); based on the polymer molecular weight can be a viscous liquid or a fragile high-melting solid. The concentration of epoxy groups (in the EPON 828) and their high reactivity with curing agents such as amines, provides a high degree of crosslinking and thus high mechanical and chemical resistance. Since no byproducts are formed during the crosslinking reaction, you realize low shrinkage during curing.

b) Curing agent

We have investigated the possibility to cure the epoxy resin at moderate temperatures and pressures, using a tertiary amine not poisoning the Grubbs' catalysts used in the formulation of our composite.

The curing agent investigated for this study, is an anionic initiator Phenol, 2,4,6-tris[(dimethylamino) methyl] (Trade name **Ancamine K54**).

The Figure 23 shows the chemical structure of Ancamine K54:

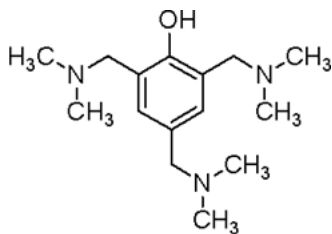


Figure 23: Phenol, 2,4,6-tris[(dimethylamino) methyl]

Since tertiary amine, Ancamine K54 does not deactivate the catalytic sites of the Grubbs' catalyst.

It's a polyfunctional tertiary amine (with multiple attachment points in the reaction of reticulation) very efficient as activator for the "curing" of epoxy resins.

It has the distinction of being efficient at moderate temperatures.

It has a delayed cross-linking (which allow reasonable time for the formulation "as homogeneous as possible" of composites with complex structures, such as designed, which requires a homogeneous dispersion of the microcapsules within the epoxy matrix).

c) Flexibilizer

Heloxy 71 (Figure 24) is an undiluted low-viscosity liquid, aliphatic ester resin that imparts increased flexibility and resistance to thermal shock when blended with conventional liquid bisphenol A based epoxy resins. It also serves as a viscosity depressing agent. This epoxy functional material react into the resin system and once reacted it becomes permanently bound into the polymer network and do not migrate to the interface under normal conditions.

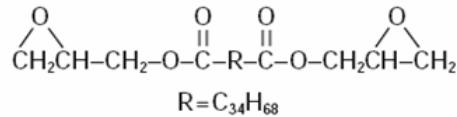


Figure 24: Flexibilizer Heloxy 71

The typical properties measured for this component are as follows:

Epoxide equivalent weight (grams of resins containing one gram-equivalent of Epoxide – ASTM D1652) = 390-470.

Viscosity, at 25 °C, poise (kinematic viscosity – determination of the viscosity of liquids by Ubbelohde Viscometer– ASTM Method D445) = 4-9.

Density, lbs/gal, at 25 °C = 8.2.

Physical form(25 °C) – clear amber liquid.

This flexibilizer help improve cured system flexibility, increase impact strength, increase the level of filler loading, improve resin wetting action, and reduce viscosity and surface tension.

Areas of application include coatings, structural engineering, adhesives, fiber-reinforced (FRP) applications, potting and molding.

d) Reactive diluent

In the development of my research the Heloxy 71 was soon replaced with a reactive diluent which allows a smoother mix at the initial stage of preparation of the mixture, further reduce viscosity and also improve mechanical properties of the polymeric matrix.

The diluent is 1-4 Butandiol diglycidylether (BDE) and the chemical formula is shown in Figure 25:



Figure 25: Reactive diluent (BDE) 1-4 Butandiol diglycidylether

Epoxide equivalent weight (grams of resins containing one gram-equivalent of Epoxide – ASTM D1652)= 120 -140.

Viscosity, at 25 °C, cP (kinematic viscosity – determination of the viscosity of liquids by Ubbelohde Viscometer– ASTM Method D445)= 10 -25 cP.

The molecule has the same oxirane groups of precursor of the epoxy (EPON 828), and crosslinks in the structure of the resin matrix. The BDE, at room temperature and atmospheric pressure, is liquid. The melting temperature of this component is between -40 and 0 °C

2.2 Materials: Catalysts active in the ROMP reaction

2.2.1 First and second generation Grubbs' catalysts

In early phases of this research, the choice of catalysts fell on first and second generation Grubbs' catalysts (Figure 26).

- *G1-Benzylidenebis(tricyclohexylphosphine)dichlororuthenium;*
- *G2-1,3-Bis-(2,4,6-trimethylphenyl)-2-(imidazolidinylidene)(dichlorophenylmethylene)(tricyclohexylphosphine)ruthenium.*

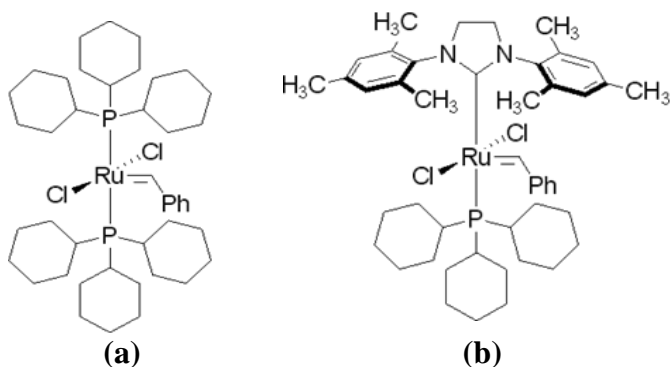


Figure 26:(a) G1(1st generation Grubbs'catalyst); (b) G2 (2nd generation Grubbs'catalyst)

These olefin metathesis catalyst systems have attracted considerable attention over the past few years, largely as a consequence of their excellent functional group tolerance, ease of use, and relatively high catalytic activity.

First generation Grubbs' catalyst is still the most widely used catalyst for many self-healing applications. Second generation Grubbs' catalyst is derived from G1 by exchange of one *phosphine* ligand (PCy_3) with a *N-heterocyclic carbene (NHC)* ligand [81].

The development of this class of new ligands has improved the thermal catalyst stability while simultaneously increasing the overall catalytic activity as a result of superior metathesis propagation [81].

These catalysts are pretty stable in air, allowing less critical reaction conditions of other catalysts used in olefin metathesis.

These catalysts have excellent compatibility with epoxy functional groups, alcohols, carbonyls, which are usually present in the thermosetting resins, but are poisoned by particular Lewis bases (primary aliphatic and aromatic amines): this is the reason why a tertiary amine (Ancamine K54) was chosen as curing agent of the epoxy matrix.

2.2.2 First and second generation Hoveyda-Grubbs' catalysts

In pursuing of research, first and second generation Grubbs' catalysts were soon replaced with more recent ruthenium catalysts: Hoveyda-Grubbs' catalysts (see Figure 27):

- *HG1-Dichloro(o-isopropoxyphenylmethylene)-(tricyclohexylphosphine)ruthenium(II)*;
- *HG2-(1,3-Bis-(2,4,6-trimethylphenyl)-2-imidazolidinylidene) dichloro (o-isopropoxyphenylmethylene)ruthenium*

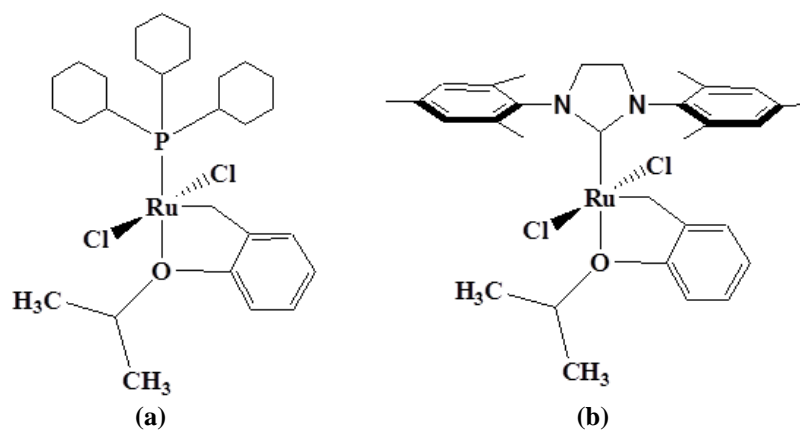


Figure 27:(a) Hoveyda-Grubbs I (HG1); (b) Hoveyda-Grubbs II (HG2)

Hoveyda-Grubbs' catalysts are active in the ROMP reaction and have been developed for use at higher temperatures and critical environments [81].

Hoveyda-Grubbs catalysts are more thermally stable than the first and second generation Grubbs' catalysts.

These catalysts bring coordinated to the metal center a heteroatom (oxygen) that, breaking away from the metal center during the metathesis reaction, allow the olefin coordination. As can be seen from chemical formulas, the catalyst HG1 has only a phosphine group (PCy₃) coordinated to the ruthenium, whereas HG2 is completely free: this represents a great advantage for these catalysts.

In fact, at high temperatures, PCy₃ groups, lose the ability to coordinate to ruthenium, contributing to the deactivation of catalyst.

2.3 Materials: Microcapsules and healing agents

The healing agent must be a sterically tensioned olefin with two functional groups, one for the metathesis reaction, the other for the crosslinking reaction: the olefin has to polymerize and crosslink within the fracture to ensure that the area repaired does not have toughness and strength lower than the polymeric matrix.

For the choice of healing agent some features have to be considered.

First the choice is related to the type of catalyst used for the "ROMP" reaction.

The healing agent must have a wide stability of the liquid phase in the operating conditions of the final composite material. The choice of the agent must take into account the formulation of microcapsules and must not compromise the thermal and chemical stability over time.

The healing agent must have an adequate capacity to release: the reactive monomer have to flow under the influence of capillary action in the void volume of the crack.

The monomer must come into contact with the catalyst (interface crack) and must have a viscosity to allow the wetting of the resin into the fracture, but the viscosity must not be too low because a low vapor pressure would make the monomer too volatile (with an advance on the rate of cure).

The reactivity of the monomer is very crucial because after filling the crack, it must react with appropriate kinetics (to tie together the surfaces of the crack) in a timely fashion. The reaction must occur before the monomer is lost by evaporation or absorption, but it should not even be too fast, do not fill the crack prior to curing. The

conversion of the reactive monomer to cross-linked polymer must proceed without large variations in volume.

Two different diene monomers [dicyclopentadiene (DCPD) and 5-ethylidene-2-norbornene (ENB)] as self-healing agents for polymeric composites were microencapsulated by *in situ* polymerization of urea and formaldehyde.

a) *Dicyclopentadiene (DCPD)*

DCPD (Figure 28) is a sterically tensioned cyclic olefin, with double unsaturation, able to polymerize and crosslink.



(bp:170 °C, mp: 32°C)

Figure 28: Dicyclopentadiene and its bubble and melting points

The DCPD flow under the action of capillary forces and has a viscosity that allows the monomer to wet the sides of any fracture in the resin.

One of the drawbacks of the DCPD is its high melting point (32 °C). The monomer must be microencapsulated liquid to flow into the damaged sites.

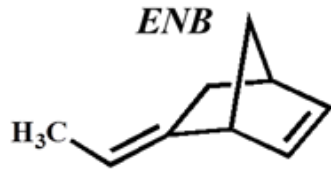
The original design (inspired to the White system) is ineffective at temperatures below or close to 32 °C.

For this reason we have additivated DCPD, in order to reach melting temperature of -1 °C.

The additive used (paraterbutylcatechol), not only broad the range of stability of the liquid phase, but also acts as a "stabilizer". The dicyclopentadiene (commercially available as a mixture of exo and endo isomers), for its particular chemical structure, is particularly susceptible to radical species that can be created for interaction with (UV) radiation that could penetrate the surface of the composite material reaching the microcapsules. The additive used chemically stabilizes the DCPD to ensure the durability of the microcapsules inside.

b) 5-ethylidene-2-norbornene (ENB)

ENB (Figure 29) is a sterically tensioned cyclic olefin, with double unsaturation, able to polymerize and crosslink.



(bp: 147 °C, mp: -80 °C)

Figure 29: 5-ethylidene-2-norbornene (ENB) and its bubble and melting points

The ENB has the following advantages:

- low monomer viscosity and volatility;
- rapid polymerization in a wide range of temperatures;
- low shrinkage upon polymerization;
- the monomer is liquid in a wide range of temperatures.

Microcapsules containing the healing agent were successfully formed from both of the diene monomers. The microcapsules outer shell composed of poly(urea-formaldehyde) (Figure 30a) and inner shell of ethylene maleic anhydride copolymer (EMA) (Figure 30b) were prepared by *in situ* polymerization in an oil-in-water emulsion.

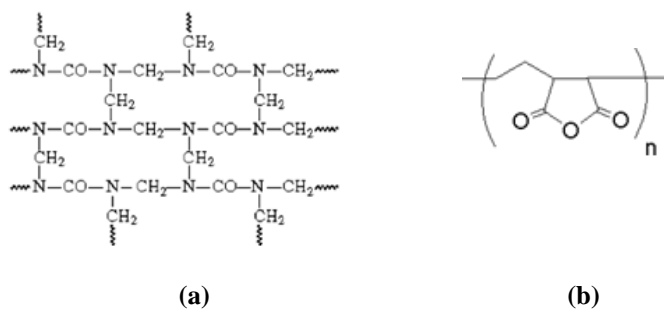


Figure 30: (a) poly(urea-formaldehyde); (b) ethylene maleic anhydride copolymer (EMA)

Methods

3 Methods

The experimental part of this research covers the following stages:

1. Choice of curing conditions for obtaining thermoset resin matrix of the self-healing composite;
2. characterization of thermal, morphological and dynamic mechanical properties of the polymer matrix;
3. thermal and morphological characterization of the components added to the matrix for the complete formulation of the self-healing composite;
4. characterization of thermal, morphological and dynamic mechanical properties of the self-healing composite;
5. verification of the metathesis reaction;
6. evaluation of self-healing efficiency.

3.1 Thermal Analysis

Thermal Analysis refers to that group of analytical techniques that have in common the following operating principle: register one or more physico-chemical properties as a function of temperature, when the sample is heated or cooled according to a particular program, or register one or more physico-chemical properties as a function of time when the sample is maintained at a constant temperature.

These analytical techniques include Thermogravimetric Analysis (TGA), Differential Scanning Calorimetry (DSC), Dynamic Mechanical Analysis (DMA).

3.1.1 Thermogravimetric Analysis (TGA)

TGA is the determination of changes in weight of a sample when subjected to a temperature change according to a particular program. Such analysis relies on a high degree of precision in three measurements: weight, temperature, and temperature change.

A thermogravimetric curve is usually a graph that shows the weight loss of a sample as a function of temperature. As many weight loss curves look similar, the weight loss curve may require transformation before results may be interpreted. A derivative weight loss curve can identify the point where weight loss is most apparent. Again, interpretation is limited without further modifications and deconvolution of the overlapping peaks may be required.

With this technique it is then possible to study the thermal behavior of materials in relation to their thermal degradation, thus assessing the maximum temperature above which a given material is not thermally stable. It is commonly employed in research and testing to determine characteristics of materials such as polymers, to determine degradation temperatures, absorbed moisture content of materials, the level of inorganic and organic components in materials, decomposition points and solvent residues.

The TGA analyzer usually consists of a high-precision microbalance, devised for measuring smaller samples on the order of a microgram, with a pan (generally alumina or platinum) loaded with the sample. The sample is placed in a small electrically heated oven with a thermocouple to accurately measure the temperature. The atmosphere may be purged with an inert gas to prevent oxidation or other undesired reactions. A computer is used to control the instrument.

TGA is a process that utilizes heat and stoichiometry ratios to determine the percent by mass of a solute. Analysis is carried out by raising the temperature of the sample gradually and plotting weight (percentage) against temperature. The temperature in many testing methods routinely reaches 1100 °C or greater. After the data are obtained, curve smoothing and other operations may be done to find the exact points of inflection.

The thermogravimetric analysis were performed using a **Mettler Toledo instrument TGA/SDTA 851** interfaced to a Mettler PC with software for data acquisition; the samples, weighing about 7-8 mg, were heated in air and nitrogen atmosphere, from room temperature to

1100 °C with heating rate of 10 °C/min and gas flow rate of 60 ml/min.

3.1.2 Differential Scanning Calorimetry (DSC)

A particularly useful group of thermoanalytical techniques is based on the detection of changes in enthalpy or specific heat of a sample as a function of temperature.

Providing energy to the sample increases its enthalpy and consequently its temperature depending on its specific heat. The specific heat of a material changes slowly with temperature in a particular physical state but varies discontinuously in a change of state.

As the temperature increases, the heat supplied can cause chemical or physical processes in the sample accompanied by changes in enthalpy (latent heat of fusion, etc.). The enthalpy change can be detected by thermal analysis and put in relation with the process that is occurring in the sample.

In this way it is possible to obtain informations on the glass transition, associated to the disordered component of the material, and also on all the phase transitions involving the ordered component of the materials.

DSC is a thermoanalytical technique in which the difference in the amount of heat required to increase the temperature of a sample and reference is measured as a function of temperature. Both the sample and reference are maintained at nearly the same temperature throughout the experiment. Generally, the temperature program for a DSC analysis is designed such that the sample holder temperature increases linearly as a function of time. The reference sample should have a well-defined heat capacity over the range of temperatures to be scanned.

When the sample undergoes a physical transformation such as phase transitions, more or less heat will need to flow to it than the reference to maintain both at the same temperature. Whether less or more heat must flow to the sample depends on whether the process is exothermic or endothermic. By observing the difference in heat flow between the sample and reference, differential scanning calorimeters are able to measure the amount of heat absorbed or released during such transitions. Differential scanning calorimetry can be used to measure a number of characteristic properties of a sample. Using this technique

it is possible to observe fusion and crystallization events as well as glass transition temperatures T_g .

The result of a DSC experiment is a curve of heat flux versus temperature or versus time (Figure 31).

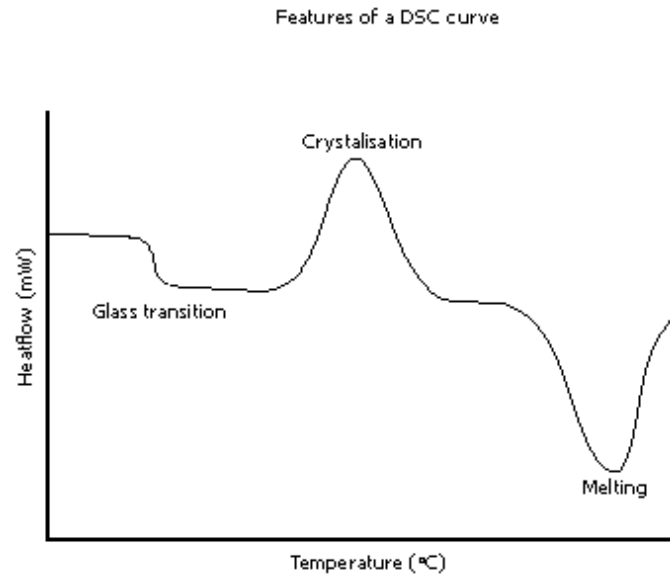


Figure 31: DSC curve for a generic material

This curve can be used to calculate enthalpies of transitions. This is done by integrating the peak corresponding to a given transition. It can be shown that the enthalpy of transition can be expressed using the following equation:

$$\Delta H = KA$$

where ΔH is the enthalpy of transition, K is the calorimetric constant, and A is the area under the curve.

Glass transitions may occur as the temperature of an amorphous solid is increased. These transitions appear as a step in the baseline of the recorded DSC signal. This is due to the sample undergoing a change in heat capacity; no formal phase change occurs. As the temperature increases, an amorphous solid will become less viscous. At some point the molecules may obtain enough freedom of motion to spontaneously arrange themselves into a crystalline form. This is known as the crystallization temperature (T_c). This transition from amorphous solid

to crystalline solid is an exothermic process, and results in a peak in the DSC signal. As the temperature increases the sample eventually reaches its melting temperature (T_m). The melting process results in an endothermic peak in the DSC curve.

3.1.2.1 Characterization of epoxy resins using differential scanning calorimetry

The thermosetting polymers are generally in a state of unreacted or partially reacted and when mixed with a suitable curing agent or heated to high temperatures undergo crosslinking. The properties of thermosetting polymers depend greatly on their chemical structure as well as by conditions (eg. time and temperature) to which the resins are exposed during the process. Small variations in the formulation or process conditions, which may also affect the curing process of the resin, may significantly affect the properties of the finished product.

Differential scanning calorimetry has become an indispensable widely analytical technique, for the characterization of thermoset materials.

The differential scanning calorimetry gives us very useful informations about the chemical and physical properties of thermosetting polymers, which include:

- glass transition temperature (T_g);
- start and completion of the curing process;
- maximum speed of curing;
- percentage of curing.

In Figure 32 are shown the results obtained by heating a generic not cured epoxy at a heating rate of 20 °C/min. The graph shows the heat flux as a function of sample temperature.

The glass transition temperature (T_g) is observed at about 0 °C as an endothermic increase heat flow. The glass transition temperature is the point of passage in which the resin is transformed from hard and glassy solid to a viscous liquid. With a further increase in temperature of the sample, the resin undergoes a cure and this is manifested as a large exothermic peak.

The temperature of the beginning of cure is temperature at which the heat flow deviates from a linear response. Once the curing process is completed (crosslinking), the heat flow returns to have a nearly linear trend.

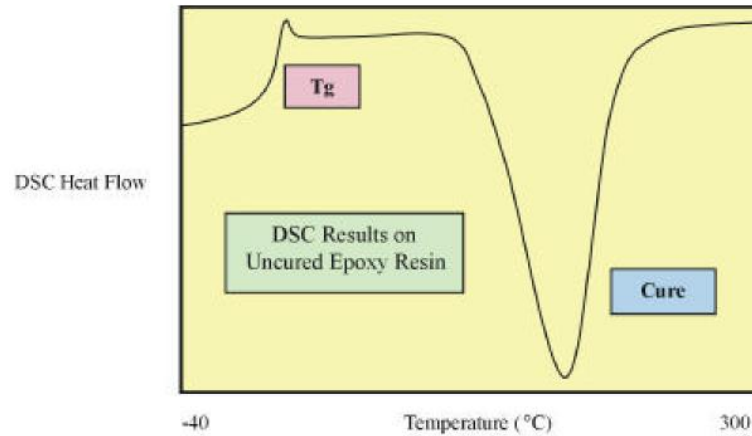


Figure 32: DSC curve for an uncured epoxy resin

The area under the exothermic peak can be integrated to calculate the heat produced by the curing process ΔH_{curing} (J/g).

Once the resin has been cured, the glass transition temperature increases and the heat developed by the curing process decreases.

The changes in Tg and heat treatment can be used to characterize and quantify the degree of curing of the resin. Once the resin has reached full cure, the Tg will have a maximum value, $T_g(\infty)$ (see Figure 33)

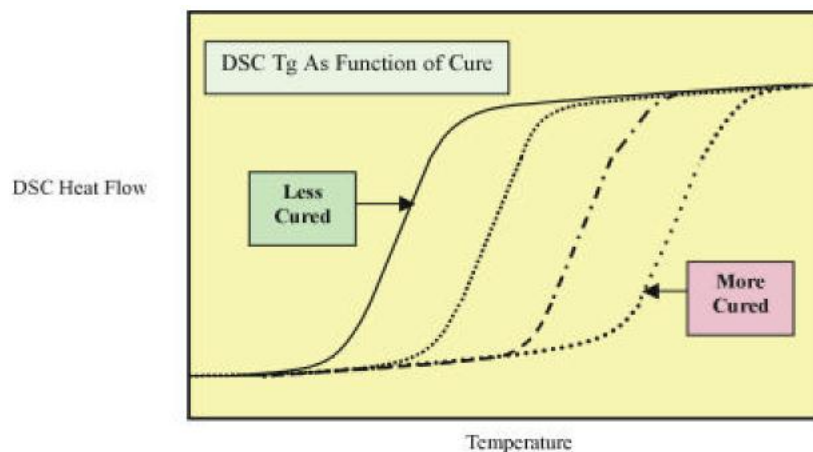


Figure 33: DSC Tg as function of curing process curve for an epoxy resin

Once the resin becomes crosslinked, heat developed becomes smaller and smaller, and when the cure is complete, the heat becomes negligible. This is shown in Figure 34.

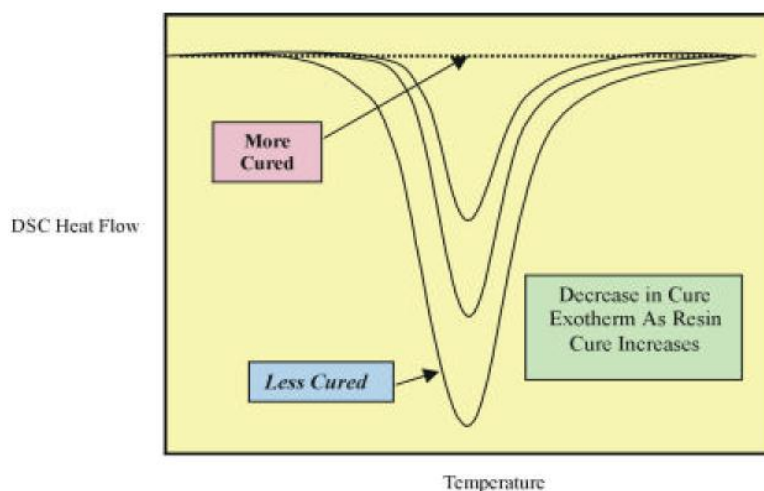


Figure 34: Decrease in cure exotherm as resin cure increases

The heat of cure may be used to determine the percentage of cure of the resin:

$$\% \text{Curing} = \left(\frac{[\Delta H_{\text{not cured}} - \Delta H_{\text{cured}}]}{[\Delta H_{\text{not cured}}]} \right) * 100$$

where $\Delta H_{\text{not cured}}$ is the curing heat of uncured resin and ΔH_{cured} is the curing heat of cured resin. If no heat treatment is observed, then the value of % curing will be 100% and it is assumed that the resin is completely cured. Percentage of curing is important in the evaluation of thermosetting resins, as it relates to the properties of the cured product such as fragility, impact resistance, thermal and chemical stability, resistance to creep and resistance to solvents.

In this research has been used a **DSC-Mettler Toledo 822**; samples weighing about 8-9 mg were subjected to specific thermal cycles in air and nitrogen atmosphere (60ml/min).

3.1.3 Dynamic Mechanical Analysis (DMA)

Dynamic Mechanical Analysis (DMA) is a technique used to study and characterize materials, in particular, is most useful for studying the viscoelastic behavior of polymers.

These materials have both features of viscous fluids, with the ability to dissipate energy and not store it, and those of elastic solids which store energy without dissipating it.

When a polymeric material is deformed part of the energy is stored as potential energy and part is dissipated as heat; the latter manifests itself as a mechanical damping (internal friction) and is higher in amorphous viscoelastic polymers.

The viscoelastic property of polymer is studied by dynamic mechanical analysis where a sinusoidal force (stress σ) is applied to a material and the resulting displacement (strain e) is measured. For a perfectly elastic solid, the resulting strain and the stress will be perfectly in phase. For a purely viscous fluid, there will be a 90 degree phase lag of strain with respect to stress. Viscoelastic polymers have the characteristics in between where some phase lag will occur during DMA tests.

For linear viscoelastic behavior, when equilibrium is reached, the stress and strain will both vary sinusoidally, but the strain lags behind the stress[82].

We can write:

$$\text{Strain } e = e_0 \sin \omega t$$

$$\text{Stress } \sigma = \sigma_0 \sin (\omega t + \delta),$$

where ω is the angular frequency and δ the phase lag.

Expandig: $\sigma = \sigma_0 \sin (\omega t + \delta) = \sigma_0 \sin \omega t \cos \delta + \sigma_0 \cos \omega t \sin \delta$
we observe that the stress have two components:

1. the first of magnitude $\sigma_0 \cos \delta$ in phase with the strain;
2. the second of magnitude $\sigma_0 \sin \delta$ 90° out of phase with the strain.

The stress-strain relationship can therefore be defined by a quantity E' in phase with the strain and a quantity E'' which is 90° out of phase with the strain:

$$\sigma = e_0 E' \sin \omega t + e_0 E'' \cos \omega t,$$

where $E' = (\sigma_0/e_0) \cos \delta$ and $E'' = (\sigma_0/e_0) \sin \delta$.

Figure 35 shows a phasor diagram that indicates that E' and E'' define a complex modulus E .

If $e = e_0 \exp(i\omega t)$, then $\sigma = \sigma_0 \exp[i(\omega t + \delta)]$, so we can write:

$$\sigma/e = E = (\sigma_0/e_0)e^{i\delta} = (\sigma_0/e_0)(\cos\delta + i \sin\delta) = E' + iE''$$

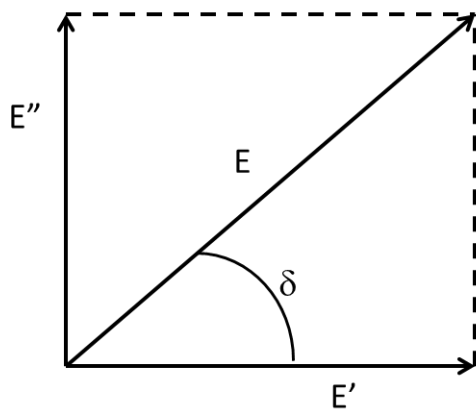


Figure 35: Phasor diagram for complex modulus $E = E' + iE''$

The real part E' is called storage modulus because it is tied to the energy stored as elastic energy during deformation of the specimen. E' is thus a measure of the stiffness of the material.

The imaginary part E'' is called loss modulus and is associated with the dissipation of energy as heat when the material is deformed.

The ratio between the energy dissipated and that stored is called loss tangent or damping or internal friction ($\tan\delta = E''/E'$).

The values of E' , E'' and $\tan\delta$ define the dynamic mechanical behaviour of a material.

These values vary with increasing temperature: while E' decreases, E'' and $\tan\delta$ show peaks corresponding to the inflection points of the curve E' , which indicate changes in material properties: the material undergoes some transitions during which dissipates the energy absorbed.

Transition refers to a relaxation, an internal rearrangement at which the excess energy is dissipated as heat.

Among all phenomena of relaxation that occurs at the glass transition process has unique aspects: the elastic modulus decreases by a factor

of 10 to 1000 (depending on whether the polymer is highly crystalline or completely amorphous) and $\tan\delta$ has a maximum. So the peak of the loss tangent is representative of glass transition temperature of the material.

The dynamic mechanical analysis were performed on rectangular samples with a **TA Instruments Q800 DMA** instrument.

Test mode was “temperature sweep” , increasing temperature in the range of -100 °C to 300 °C with a heating rate of 3 °C/min, applying a constant frequency of 1Hz and a constant deformation “ ϵ ” of 0.1%.

3.2 Nuclear Magnetic Resonance Spectroscopy and Infrared Analysis

Thermolytic decomposition of catalysts and metathesis activity were evaluated using two analytical techniques: Proton Nuclear Magnetic Resonance spectroscopy ($^1\text{H-NMR}$) and Fourier Transform Infrared spectroscopy (FTIR).

3.2.1 Nuclear Magnetic Resonance (NMR)

The molecular spectroscopy is the experimental procedure by which are measured the frequencies of electromagnetic radiation absorbed or emitted by a substance that can be related to specific types of molecular structure [83].

Nuclear magnetic resonance spectroscopy, (NMR spectroscopy), is a research technique that exploits the magnetic properties of certain atomic nuclei to determine physical and chemical properties of atoms or the molecules in which they are contained. It relies on the phenomenon of nuclear magnetic resonance and can provide detailed information about the structure, dynamics, reaction state, and chemical environment of molecules.

As the electrons, even the nuclei of ^1H and ^{13}C , isotopes of the two most common elements in organic compounds, have a spin and behave as if they were tiny magnets.

When placed between the poles of a powerful magnet, the nuclear spins of ^1H and ^{13}C or are aligned according to the applied magnetic field, or against it.

Nuclei whose spin is aligned according to the magnetic field are at a lower energy state, and those with the spin aligned against the magnetic field are at a higher energy level.

When the nuclei in the spin state of lowest energy are irradiated with a frequency of appropriate energy, energy is absorbed and the nucleus “jumps” from the state of spin aligned to magnetic field, to the spin state opposite to the applied magnetic field.

The resonance in this context is absorption of electromagnetic radiation by nuclei in the rotation and the resulting jump between the nuclear spin states.

The resonant frequency, energy of the absorption and the intensity of the signal are proportional to the strength of the magnetic field.

Depending on the local chemical environment, different protons in a molecule resonate at slightly different frequencies. Since both this frequency shift and the fundamental resonant frequency are directly proportional to the strength of the magnetic field, the shift is converted into a field-independent dimensionless value known as the chemical shift. The chemical shift is reported as a relative measure from some reference resonance frequency.

For the nuclei ^1H , ^{13}C , TMS (tetramethylsilane) is commonly used as a reference. This difference between the frequency of the signal and the frequency of the reference is divided by frequency of the spectrometer to give the chemical shift [83]:

$$\delta = \frac{\text{frequency shift respect TMS(Hz)}}{\text{Spectrometer Frequency(Hz)}} \times 10^6$$

The frequency shifts are extremely small in comparison to the fundamental NMR frequency.

By understanding different chemical environments, the chemical shift can be used to obtain some structural information about the molecule in a sample. The shape and size of peaks are indicators of chemical structure too.

Proton NMR (^1H -NMR) is the application of nuclear magnetic resonance in NMR spectroscopy with respect to hydrogen-1 nuclei within the molecules of a substance, in order to determine the structure of its molecules.

In samples where natural hydrogen (H) is used, practically all of the hydrogen consists of the isotope ^1H .

Simple NMR spectra are recorded in solution, and solvent protons must not be allowed to interfere. Deuterated solvents especially for use in NMR are preferred, e.g. deuterated water, D_2O , deuterated

acetone, $(\text{CD}_3)_2\text{CO}$, deuterated methanol, CD_3OD , deuterated dimethyl sulfoxide, $(\text{CD}_3)_2\text{SO}$, and deuterated chloroform, CDCl_3 . Also solvent without hydrogen, such as carbon tetrachloride, CCl_4 or carbon disulphide, CS_2 , may also be used.

Another type of information can be obtained from the scheme of spin-spin coupling. Because nuclei themselves possess a small magnetic field, they influence each other, changing the energy and hence frequency of nearby nuclei as they resonate—this is known as spin-spin coupling.

The spin-spin coupling consists in a NMR signal splitting into a set of peaks due to the influence of neighboring nuclei.

In spin-spin coupling the ^1H -NMR signal resulting from an equivalent group of hydrogens is split into a multiplet due to the influence of adjacent non-equivalent hydrogens.

The degree of coupling spin-spin and the number of line of a multiplet can be expected based on the rule of $(n + 1)$.

According to this rule, if a hydrogen has n hydrogens not equivalent to it, but equivalent to each other on the same atom or on an adjacent atom, its ^1H -NMR signal is split into $(n + 1)$ peaks.

^1H -NMR analysis and ^1H -NMR spectra were recorded on an **AV300 Bruker spectrometer**, using CDCl_3 as solvent and tetramethyl silane (TMS) as internal reference.

3.2.2 Infrared Spectroscopy (IR spectroscopy)

In infrared spectroscopy (IR) a compound is irradiated with infrared radiation which causes the shift of covalent bonds from a lower vibrational energy level to one higher.

So it is possible to detect the functional groups from the vibrations of their bonds.

Infrared spectroscopy exploits the fact that molecules absorb specific frequencies that are characteristic of their structure. These absorptions are resonant frequencies, i.e. the frequency of the absorbed radiation matches the frequency of the bond or group that vibrates. The energies are determined by the shape of the molecular potential energy surfaces, the masses of the atoms, and the associated vibronic coupling.

Covalent bonds bend and stretch as if the atoms bonded together were joined by flexible springs. The energy required to elicit vibrational transitions correspond to radiation in the IR region of the electromagnetic spectrum [83].

The infrared portion of the electromagnetic spectrum is usually divided into three regions; the near-, mid- and far- infrared, named for their relation to the visible spectrum. The higher energy near-IR, approximately $14000\text{--}4000\text{ cm}^{-1}$ ($0.8\text{--}2.5\text{ }\mu\text{m}$ wavelength) can excite overtone or harmonic vibrations. The mid-infrared, approximately $4000\text{--}400\text{ cm}^{-1}$ ($2.5\text{--}25\text{ }\mu\text{m}$) may be used to study the fundamental vibrations and associated rotational-vibrational structure. The far-infrared, approximately $400\text{--}10\text{ cm}^{-1}$ ($25\text{--}1000\text{ }\mu\text{m}$), lying adjacent to the microwave region, has low energy and may be used for rotational spectroscopy.

However only the mid infrared is used routinely in organic chemistry. The radiation in this region is commonly referred to its wave number (ν), i.e. the number of waves per centimeter:

$$\frac{\nu}{\text{cm}^{-1}} = \frac{1}{\lambda(\text{cm})} = \frac{1000}{\lambda(\mu\text{m})}$$

An advantage of wave numbers is that they are directly proportional to energy: the higher the wave number, the greater is the energy of the radiation.

The energy of molecular vibration is quantized rather than continuous, meaning that a molecule can only stretch and bend at certain “allowed” frequencies. If a molecule is exposed to electromagnetic radiation that matches the frequency of one of its vibrational modes, it will in most cases absorb energy from the radiation and jump to a higher vibrational energy state - what this means is that the amplitude of the vibration will increase, but the vibrational frequency will remain the same. The difference in energy between the two vibrational states is equal to the energy associated with the wavelength of radiation that was absorbed. It turns out that it is the infrared region of the electromagnetic spectrum which contains frequencies corresponding to the vibrational frequencies of organic bonds.

In order for a vibrational mode in a molecule to be “IR active”, it must be associated with changes in the dipole. A permanent dipole is not necessary, as the rule requires only a change in dipole moment.

A molecule can vibrate in many ways, and each way is called a vibrational mode. For molecules with n atoms in them, linear molecules have $3n - 5$ degrees of vibrational modes, whereas nonlinear molecules have $3n - 6$ degrees of vibrational modes (vibrational degrees of freedom) [84].

Simple diatomic molecules have only one bond and only one vibrational band. If the molecule is symmetrical, e.g. N_2 , the band is not observed in the IR spectrum, but only in the Raman spectrum. Unsymmetrical diatomic molecules, e.g. CO, absorb in the IR spectrum. More complex molecules have many bonds, and their vibrational spectra are correspondingly more complex, i.e. big molecules have many peaks in their IR spectra.

The simplest vibrational motions that give rise to absorption of infrared radiation are stretching and bending modes (see Figure 36).

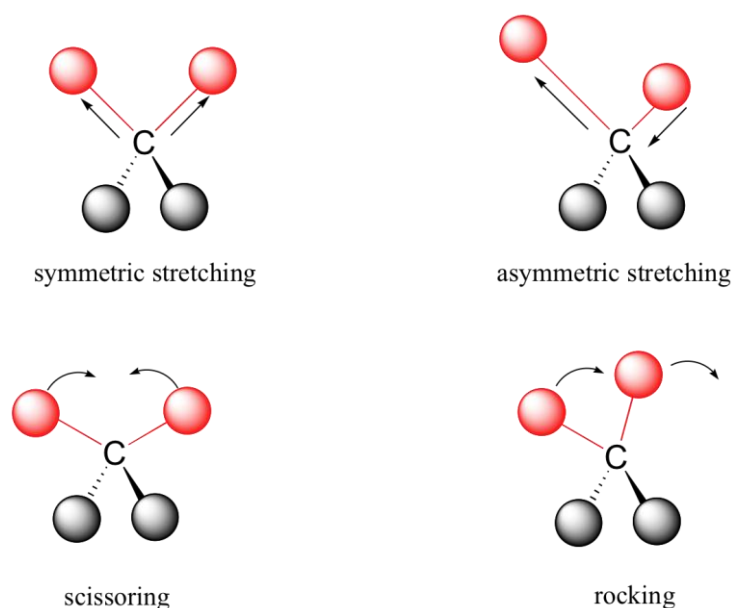


Figure 36: Vibrational modes of stretching and bending

The power of infrared spectroscopy arises from the observation that different functional groups have different characteristic absorption frequencies. The data concerning the absorption of characteristic functional groups are tabulated in so called correlation tables.

In these tables intensity of a particular absorption is often referred to as strong, medium or weak.

Fourier transform infrared (FTIR) spectroscopy is a measurement technique that allows one to record infrared spectra. Infrared light is guided through an interferometer and then through the sample (or vice versa). A moving mirror inside the apparatus alters the distribution of infrared light that passes through the interferometer. The signal directly recorded, called an “interferogram”, represents light output as

a function of mirror position. A data-processing technique called Fourier transform turns this raw data into the desired result (the sample's spectrum): Light output as a function of infrared wavelength (or equivalently, wavenumber).

In this work infrared spectra were performed at room temperature by using a **Bruker Vertex 70 FTIR-spectrophotometer** with 2 cm^{-1} resolution (64 scan collected).

3.3 Morphological Analysis: Scanning Electron Microscope

A scanning electron microscope (SEM) is a type of electron microscope that images a sample by scanning it with a high-energy beam of electrons in a raster scan pattern.

The signals that derive from electron-sample interactions reveal information about the sample including external morphology (texture), chemical composition, and crystalline structure and orientation of materials making up the sample.

In most applications, data are collected over a selected area of the surface of the sample, and a 2-dimensional image is generated that displays spatial variations in these properties. Areas ranging from approximately 1 cm to 5 microns in width can be imaged in a scanning mode using conventional SEM techniques (magnification ranging from 20X to approximately 30,000X, spatial resolution of 50 to 100 nm). The SEM is also capable of performing analyses of selected point locations on the sample; this approach is especially useful in qualitatively or semi-quantitatively determining chemical compositions (using EDS), crystalline structure, and crystal orientations (using EBSD).

Accelerated electrons in an SEM carry significant amounts of kinetic energy, and this energy is dissipated as a variety of signals produced by electron-sample interactions when the incident electrons are decelerated in the solid sample. These signals include secondary electrons (that produce SEM images), backscattered electrons (BSE), diffracted backscattered electrons (EBSD that are used to determine crystal structures and orientations of minerals), photons (characteristic X-rays that are used for elemental analysis and continuum X-rays), visible light (cathodoluminescence - CL), and heat. Secondary electrons and backscattered electrons are commonly used for imaging samples: secondary electrons are most valuable for showing

morphology and topography on samples and backscattered electrons are most valuable for illustrating contrasts in composition in multiphase samples (i.e. for rapid phase discrimination).

SEMs always have at least one detector (usually a secondary electron detector), and most have additional detectors. The specific capabilities of a particular instrument are critically dependent on which detectors it accommodates.

In a typical SEM, an electron beam is thermionically emitted from an electron gun fitted with a tungsten filament cathode. Tungsten is normally used in thermionic electron guns because it has the highest melting point and lowest vapour pressure of all metals, thereby allowing it to be heated for electron emission, and because of its low cost. The electron beam, which typically has an energy ranging from 0.5 keV to 40 keV, is focused by one or two condenser lenses to a spot about 0.4 nm to 5 nm in diameter.

The beam passes through pairs of scanning coils or pairs of deflector plates in the electron column, typically in the final lens, which deflect the beam in the x and y axes so that it scans in a raster fashion over a rectangular area of the sample surface.

The energy exchange between the electron beam and the sample results in the reflection of high-energy electrons by elastic scattering, emission of secondary electrons by inelastic scattering and the emission of electromagnetic radiation, each of which can be detected by specialized detectors.

The beam current absorbed by the specimen can also be detected and used to create images of the distribution of specimen current. Electronic amplifiers of various types are used to amplify the signals, which are displayed as variations in brightness on a cathode ray tube. The raster scanning of the CRT display is synchronised with that of the beam on the specimen in the microscope, and the resulting image is therefore a distribution map of the intensity of the signal being emitted from the scanned area of the specimen.

The image may be captured by photography from a high-resolution cathode ray tube, but in modern machines is digitally captured and displayed on a computer monitor and saved to a computer's hard disk.

The SEM is routinely used to generate high-resolution images of shapes of objects (SEI) and to show spatial variations in chemical compositions: 1) acquiring elemental maps or spot chemical analyses using EDS, 2) discrimination of phases based on mean atomic number (commonly related to relative density) using BSE, and 3) compositional maps based on differences in trace element “activators”

(typically transition metal and Rare Earth elements) using CL. The SEM is also widely used to identify phases based on qualitative chemical analysis and/or crystalline structure. Precise measurement of very small features and objects down to 50 nm in size is also accomplished using the SEM. Backscattered electron images (BSE) can be used for rapid discrimination of phases in multiphase samples. SEMs equipped with diffracted backscattered electron detectors (EBSD) can be used to examine microfabric and crystallographic orientation in many materials.

Samples must fit into the microscope chamber. Maximum size in horizontal dimensions is usually on the order of 10 cm, vertical dimensions are generally much more limited and rarely exceed 40 mm. For most instruments samples must be stable in a vacuum on the order of 10^{-5} - 10^{-6} torr.

For conventional imaging in the SEM, specimens must be electrically conductive, at least at the surface, and electrically grounded to prevent the accumulation of electrostatic charge at the surface. Metal objects require little special preparation for SEM except for cleaning and mounting on a specimen stub. Nonconductive specimens tend to charge when scanned by the electron beam, and especially in secondary electron imaging mode, this causes scanning faults and other image artifacts. They are therefore usually coated with an ultrathin coating of electrically conducting material, commonly gold, deposited on the sample either by low-vacuum sputter coating or by high-vacuum evaporation. Conductive materials in current use for specimen coating include gold, gold/palladium alloy, platinum, osmium, iridium, tungsten, chromium, and graphite.

In this research Scanning electron microscopy (SEM) pictures were obtained with a **LEO 1525 microscope**. The samples were covered with a 250-Å-thick gold film using a sputter coater (**Agar mod. 108 A**).

3.4 Method for evaluation of Self-healing Efficiency

We are equipped for getting quantitative results on the self-healing functionality. The experimental procedure uses the protocol established by White et al. [40, 65,67].

As mentioned elsewhere in this text, crack healing efficiency, η , is defined as the ability of a healed sample to recover fracture toughness[14, 16]:

$$\eta = \frac{K_{IChealed}}{K_{ICvirgin}} \quad (\text{eq.3.1})$$

where $K_{ICvirgin}$ is the fracture toughness of the virgin specimen and $K_{IChealed}$ is the fracture toughness of the healed specimen.

According to the protocol established by White, the fracture toughness and healing efficiency of the formulated composites were measured by controlled fracture tests using a tapered double-cantilever beam (TDCB) specimens.

The tapered double-cantilever beam (TDCB) geometry, ensures controlled crack growth along the centerline of the brittle specimen. The TDCB fracture geometry, developed by Mostovoy et al. [85] provides a crack length independent measure of fracture toughness:

$$K_{IC} = 2P_C \frac{\sqrt{m}}{\beta} \quad (\text{eq.3.2})$$

Where P_C is critical fracture load and m and β are geometric terms. The value of β depends on the specimen and crack widths b and b_n , respectively. The value of m is defined by the theoretical relation:

$$m = \frac{3a^2}{h(a)^3} + \frac{1}{h(a)} \quad (\text{eq. 3.3})$$

m values can also be empirically evaluated by the method of Irwin-Kies [86]:

$$m = \frac{Eb}{8} \frac{dC}{da} \quad (\text{eq. 3.4})$$

where E is Young's modulus, C is the compliance, a is the crack length from the line of loading, and $h(a)$ is the specimen height profile.

For the TDCB geometry, the healing efficiency is simply calculated as the ratio of critical fracture loads for the healed and virgin samples:

$$\eta = \frac{P_{\text{Healed}}}{P_{\text{Virgin}}} \quad (\text{eq.3.5})$$

Valid profiles for a TDCB fracture specimen are determined by finding a height profile that, when inserted into eq. 3.3, yields a constant value of m over a desired range of crack lengths. [65].

Inspired by Brown, White et co. studies, for the manufacturing of our samples, in this research we used a modified version of TDCB geometry with the dimensions indicated in Figure 37 [65,67].

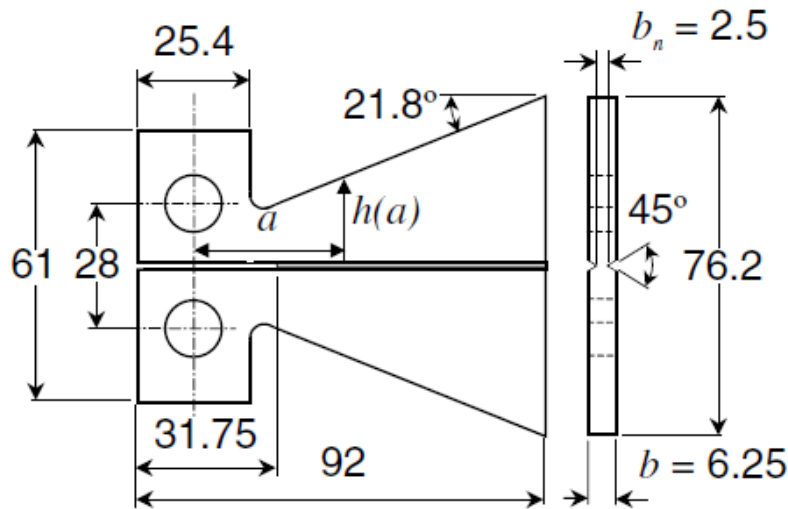


Figure 37: TDCB geometry and dimensions (mm)

In a brittle material a crack propagating exhibits a propensity to deflect significantly from the centerline when the taper angle is small. Failure commonly occurs as arm breakoff. To ensure fracture follows along the desired path, side grooves are incorporated into the TDCB geometry. The addition of side grooves is valid for the TDCB geometry, as there is no restriction that b and b_n be the same. Stable

crack propagation with maximum crack width, b_n , is obtained by selecting a groove with 45° internal angle.

For this geometry Brown et al. [65] have also evaluated the geometric terms m and β in eq. 3.2:

$$\beta = b^{0.61} b_n^{0.39}$$

$$m = 0.6 \text{ mm}^{-1} .$$

Fracture tests for self-healing efficiency evaluation was conducted by a dynamometer **INSTRON 4301** with a constant crosshead speed of 0.5 mm/min.

Results and Discussions:

Early Systems

4 Early Systems: Introduction

Our self-healing system for aircraft polymer composites was inspired by the design of White et al. [64-68].

This system consists in an epoxy matrix in which a microencapsulated healing agent and catalyst particles are incorporated.

Several systems were investigated that differ for the nature and the composition of the epoxy matrix, catalyst and active monomer used: this was necessary to obtain a high performances material and to achieve our technical targets (already outlined in section 1).

In this section we describe the first system studied and the first attempts to design an efficient self-healing system.

The healing agent used in this first phase was DCPD. This monomer was encapsulated by in situ polymerization using an already reported procedure [58-62].

The catalyst used in the matrix was Grubbs' catalyst [bis(tricyclohexylphosphine) benzyldiene ruthenium (IV) dichloride].

The epoxy matrix used was a blend of diglycidyl ether of bisphenol A (trade name EPON 828—Acronym DGEBA) and a high molecular-weight epoxy flexibilizer, Dimer Acid Diglycidyl Ester (trade name HELOXY 71—Acronym DADGE), which was used in small percentages to improve the toughness of the material and consequently crack growth stability.

The curing agent investigated for this study is an anionic initiator Phenol, 2,4,6-tris[(dimethylamino) methyl] (Trade name Ancamine K54).

The scheme of the formulation used is shown in Figure 38 (for chemical structures and details of compounds see Materials section).

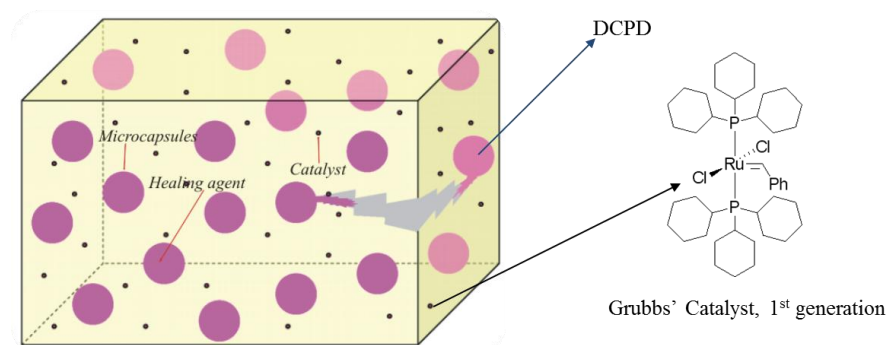


Figure 38: First self-healing system formulation

4.1 Curing of Epoxy Matrix

Cure behavior of the thermoset matrix was investigated with thermal analysis techniques (DSC, DMA) and infrared spectroscopy analysis.

4.1.1 Differential Scanning Calorimetry

DSC has high sensitivity to any reaction involving heat flow changes and for this reason is especially useful for studying the cure of reactive epoxy systems whose curing is accompanied by the release of heat.

A combination of dynamic and isothermal experiments can provide information on reaction rates, cure rates, and degree of cure.

Here DSC has been used for the estimation of the Degree of cure (DC) of epoxy matrix under the assumption that the exothermic heat evolved during cure is proportional to the extent of reaction.

The DC can be determined from the total heat of reaction, ΔH_T , of the curing reaction and the residual heat of reaction, ΔH_{resid} , of the partially polymerized material:

$$DC = \frac{\Delta H_T - \Delta H_{resid}}{\Delta H_T} \times 100 \text{ (eq. 4.1)}$$

A series of isothermal experiments were performed to obtain fraction reacted at various temperatures, which are very useful for cure cycle.

To calculate ΔH_T values from isothermal studies, dynamic runs were made after each isothermal cure to obtain the residual heat of reaction. The total heat of reaction was calculated as shown in equation 4.2:

$$\Delta H_T = \Delta H_{iso} + \Delta H_{resid} \text{ (eq.4.2)}$$

where ΔH_{iso} and ΔH_{resid} are the areas under the isothermal and dynamic thermograms, respectively.

Before analyzing the matrix, we proceeded to perform a characterization of the individual components of the mixture.

In Figure 39 are shown the DSC curves for Epon 828. The cycle consists of three thermal steps in nitrogen flow:

1. Heating from -30 °C to 300 °C (scan rate 10 °C min)
2. Cooling from 300 °C to -30 °C (scan rate 50 °C min)
3. Second heating from -30 °C to 300 °C (scan rate 10 °C min)

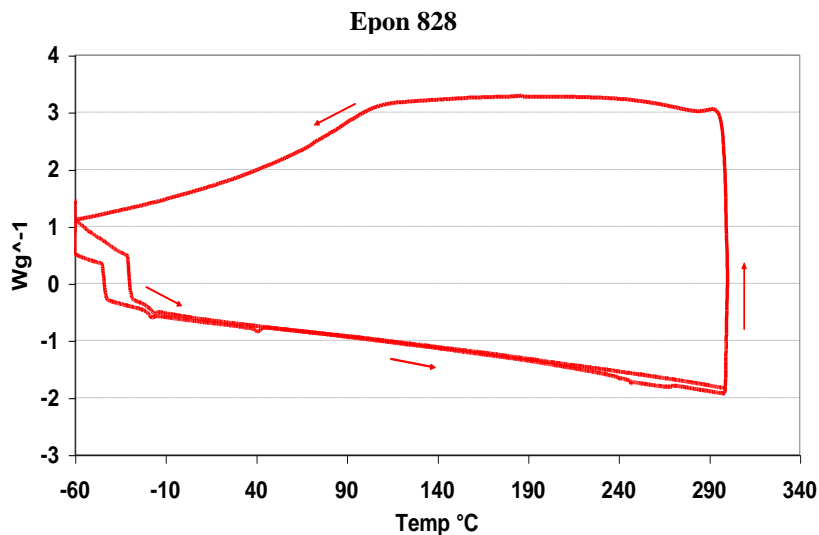


Figure 39: DSC curves for Epon 828

In the next figure (Figure 40) we reported the thermogram of the first step:

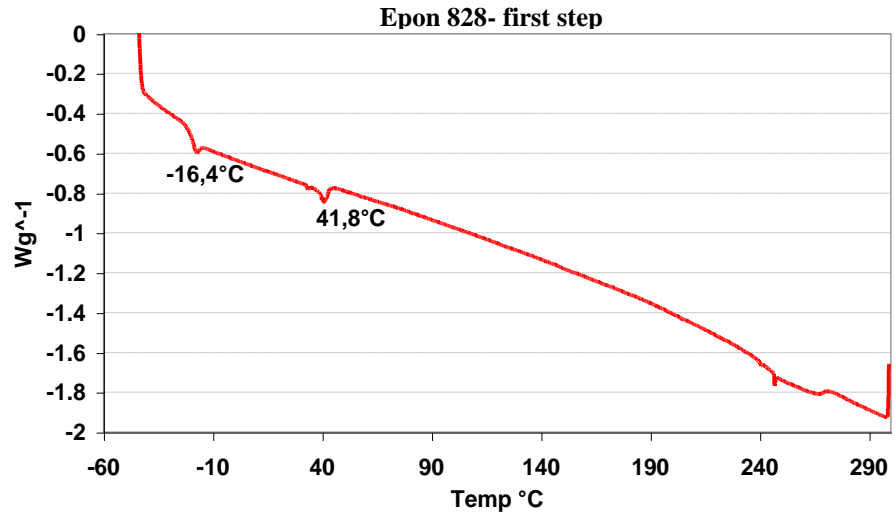


Figure 40: DSC curve for Epon 828 – first heating

In the Figure 41 is shown the thermogram of the third step (second heating) for Epon 828:

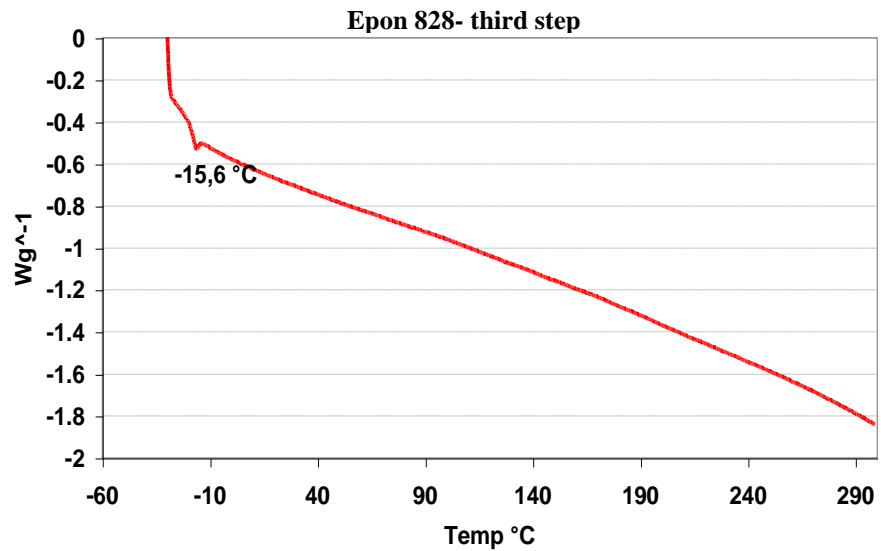


Figure 41: DSC curve for Epon 828 – second heating

We performed the thermal characterization on the Heloxy 71, with the same thermal cycle steps (see Figure 42):

1. Heating from -30 °C to 300 °C (scan rate 10 °C min)
2. Cooling from 300 °C to -30 °C (scan rate 50 °C min)
3. Second heating from -30 °C to 300 °C (scan rate 10 °C min)

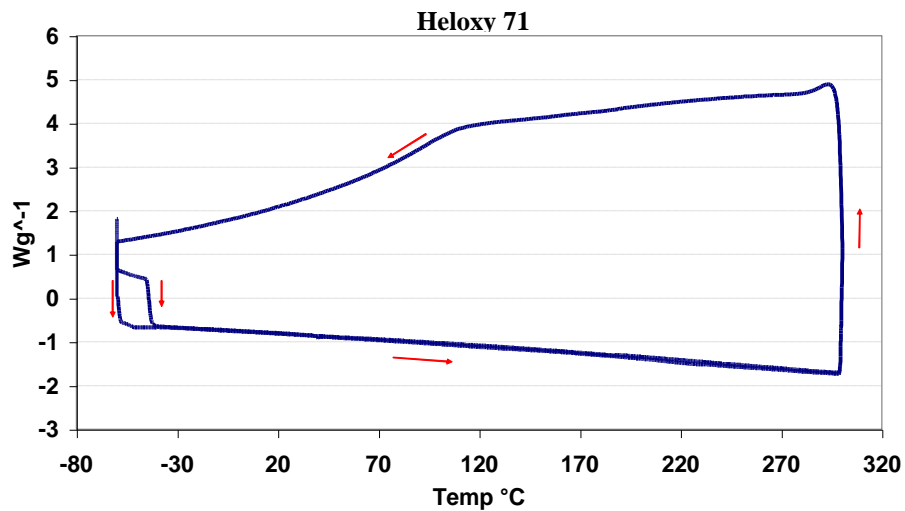


Figure 42: DSC curves for Heloxy 71

In Figure 43 is shown the first heating step for Heloxy 71

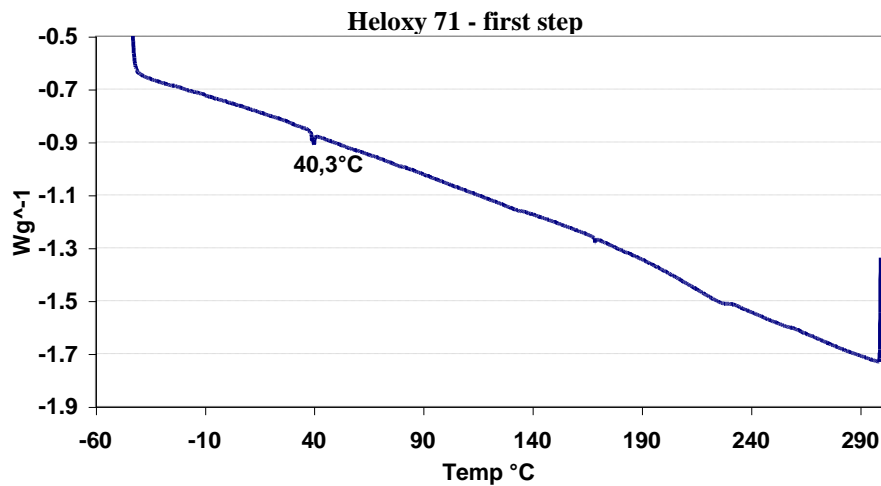


Figure 43: DSC curve for Heloxy 71– first heating

The second heating step (third step) for Heloxy 71 is shown in Figure 44

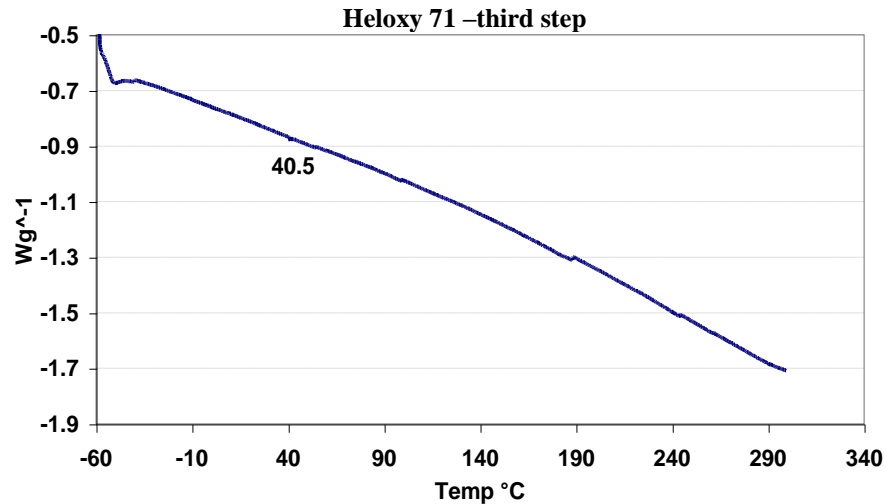


Figure 44: DSC curve for Heloxy 71– second heating

This preliminary calorimetric analysis indicated that, in the absence of the curing agent (Ancamine K54), Epon 828 and Heloxy 71 were not reactive up to 300 °C.

From all the thermograms shown it is evident that, under the dynamic heating, the Epon 828 (pure) and Heloxy 71 (pure) did not result in cross-linking phenomena.

For both components can be seen very small endothermic peak due to the effects of gelation of the material (negligible fusions associated with small crystal aggregations).

After this preliminary analysis, calorimetric tests were performed on three samples of the following formulations:

Sample1: obtained by mixing Ancamine K54 with Epon 828 at the concentration of 10:100 (by wt) hardener to resin Epon 828.

Sample2: obtained by mixing Ancamine K54 with Heloxy 71 at the concentration of 10:100 (by wt) hardener to resin Heloxy 71.

Sample EHA: obtained by mixing Epon 828 with Heloxy 71 flexibilizer at the concentration of 63%: 37% (by wt) epoxide to

flexibilizer. Ancamine K54 was added at the concentration of 10:100 (by wt) hardener to mixture (Epon 828 and Heloxy 71).

In Figure 45 are shown the DSC curves for the two formulations containing the tertiary amine, Sample 1 and Sample 2.

The exothermic peaks in both the DSC scans (in dynamic regime) provides an indication of the considerable reactivity of the ancamine K54 in the curing reactions of the two resins (Epon and Heloxy).

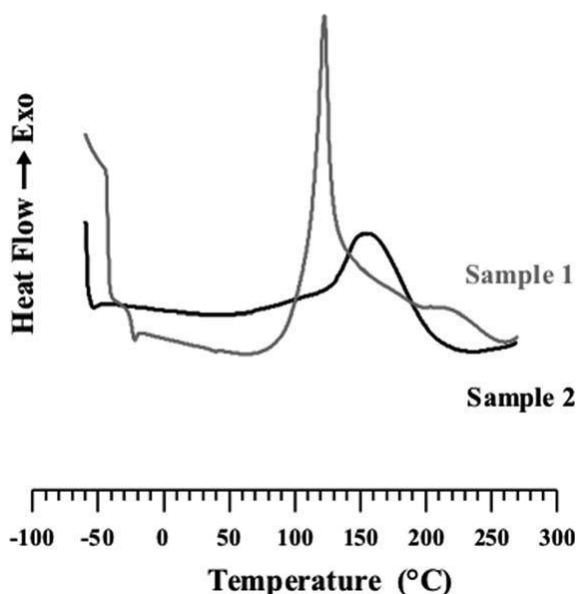


Figure 45: DSC curves for formulations: Sample1, Epon 828/Ancamine K54 (10/1) and Sample 2, Heloxy 71/Ancamine K54 (10/1)

In Figure 46 are shown DSC scans (in dynamic regime) for sample EHA. The cycle is composed of three parts:

1. Heating from -60 °C to 300 °C (scan rate 10 °C min)
2. Cooling from 300 °C to -60 °C (scan rate 50 °C min)
3. Second heating from -60 °C to 300 °C (scan rate 10 °C min)

The DSC curve shows two overlapped exothermic peaks between 90 and 230 °C. A comparison of this DSC trace with calorimetric curves relative to Sample 1 and Sample 2 of Figure 45 clarifies the nature of the complex two exothermic peaks: the first (maximum at 120 °C) is ascribable to the reactions of Ankamine with Epoxide rings of Epon

828 and, therefore, to the homopolymerization of the epoxy resin; the second, to the homopolymerization of the Heloxy flexibilizer resin. The flat DSC curve of the third scan indicates that, in dynamic regime, the curing reactions in the formulation are closed at the end of the first scan, ΔH_T (calculated for the first scan) is 329.44 J/g.

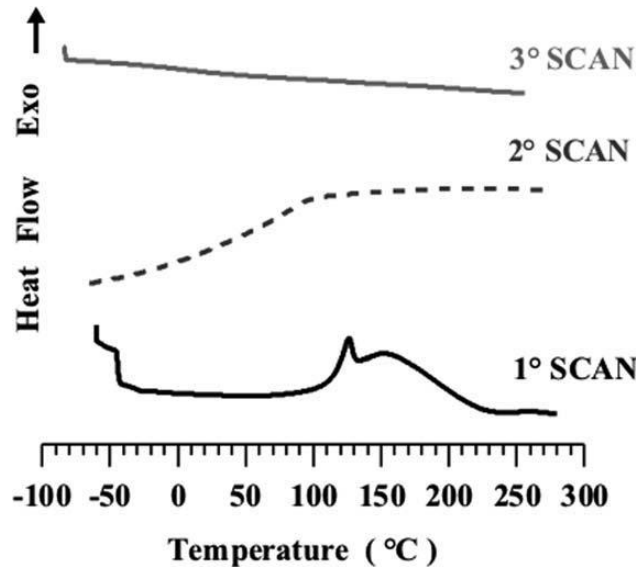


Figure 46: DSC curves (in dynamic regime) for EHA sample

The EHA samples was cured by a isothermal stage at different temperature between 50 and 100 °C.

In Figure 47, dynamic runs of EHA mixture after each isothermal cure of 9 h at the chosen temperatures (50, 60, 70, 80, 100 °C) are shown. We can notice a decrease in cure exotherm, as isothermal curing temperature increases.

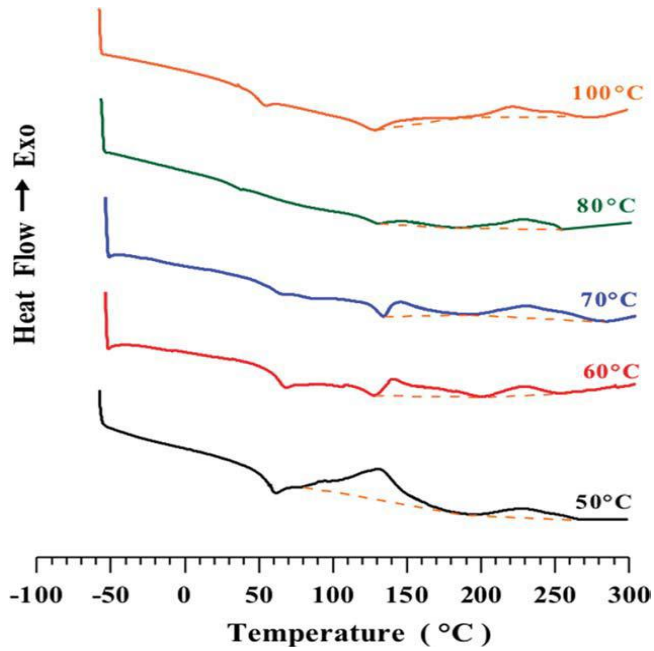


Figure 47: Dynamic DSC for residual cure after isothermal treatments of sample EHA

The Degrees of Cure for each curing temperature (calculated from equations 4.1 and 4.2) are listed in Table 4.1. Curing temperatures above 70 °C give cure degrees higher than 96%.

Curing Temperature (°C)	Curing Degree DC (%)
50	94
60	95
70	96
80	98
100	97

Table 4.1 Degree of Cure (DC) of EHA samples after each isothermal cure of 9h at the temperatures 50, 60, 70, 80, and 100 °C

4.1.2 Dynamic Mechanical Analysis

Dynamic mechanical data provide useful information on the relaxation processes that become operative in the polymer in a temperature range depending on the examined system.

Here are the results of investigation carried out to understand the influence of curing temperature on the dynamic mechanical properties of the EHA samples cured in isothermal conditions at temperatures as previously described (Figure 48).

The spectra were recorded in the flexural mode, obtaining the loss factor, $\tan \delta$, at a frequency of 1 Hz, as a function of temperature. The heating rate was 3 °C/min in the range of -100 to 160 °C.

In the dynamic mechanical spectra of epoxy resins, the maximum of $\tan \delta$ is considered as the glass transition point and its temperature designated as $(T_g)_{DMA}$. Glass transition points measured by DMA of the samples cured at the chosen temperatures are reported in Table 4.2.

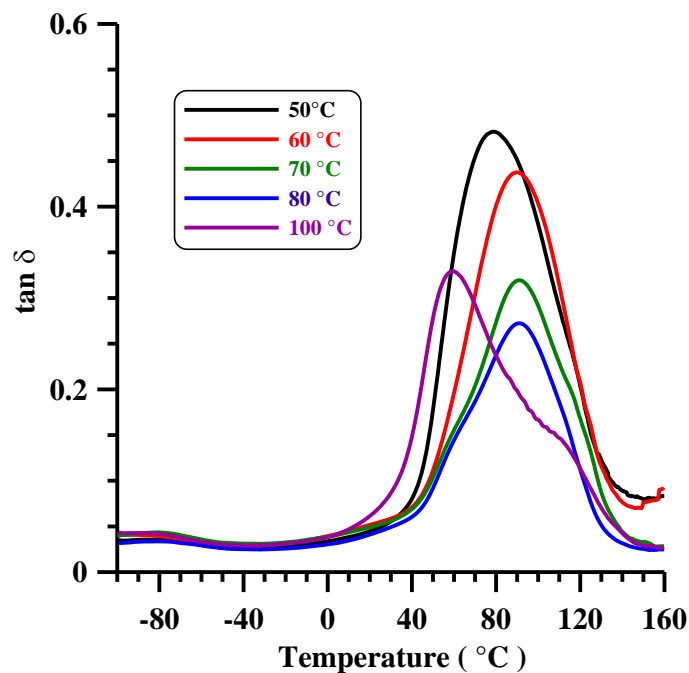


Figure 48: DMA plot of $\tan \delta$ versus temperature of EHA sample cured at temperatures between 50 and 100 °C

Curing Temperature (°C)	T _{gDMA} (°C)
50	78
60	93
70	94
80	93
100	58/110

Table 4.2 Glass Transition Temperature measured by DMA of EHA Samples cured at temperatures between 50 and 100 °C

Figure 48 and Table 4.2 show that a curing temperature between 60 °C and 80 °C gives the highest glass-transition temperature, whereas the sample cured at 100 °C shows the peak of the main transition at 58°C indicating the presence of a significant fraction of the material with a lower transition temperature. The presence of a secondary peak, active at higher temperature (110 °C), suggests the presence of a small fraction with lower mobility due to a different degree of crosslinking. It can be suggest that this behavior is due to the high reactivity of the catalytic curing agent at 100 °C. That causes a fast hardening in some small zones making the thinness of the epoxy mixture unsuitable to obtain a homogeneous cross-linked structure throughout the sample. DSC and DMA data have allowed the choice of the best cure conditions: the highest T_g and maximum Degree of cure were obtained at a “curing” temperature of 80 °C.

This temperature was chosen for the “curing” process of matrix of the self-healing system. To further improve the mechanical parameters of the samples cured at 80 °C, a post cure at a temperature of 120 °C was performed obtaining sample EHA-[80 °C, 9 h + 120 °C, 2 h].

For the second step of the curing cycle, a temperature lower than 150 °C has been considered because the Grubbs’ catalyst had shown decomposition in air after a treatment of 150 °C for 2 - 3h (we will show this result later, in the catalyst section).

In Table 4.3, the elastic modulus of the sample EHA-[80 °C, 9 h + 120 °C, 2 h] is compared with that of sample EHA-[80 °C, 9 h] in the temperature range between -50 and 50 °C.

Temperature (°C)	EHA [80 °C, 9h] Elastic Modulus (MPa)	EHA [80 °C, 9h + 120 °C, 2h] Elastic Modulus (MPa)
-50	705	1240
-25	666	1160
0	615	1042
25	525	820
50	345	490

Table 4.3 Elastic Modulus (MPa) of EHA-[80 °C, 9h], and EHA-[80 °C, 9h + 120 °C, 2 h] samples

Sample EHA-[80 °C, 9h + 120 °C, 2h] shows a higher modulus for all the investigated temperatures. The increase of the elastic modulus is more intense at lower temperatures. At -50 °C, the modulus is 76% higher than sample EHA-[80 °C, 9h]; whereas, at 50 °C an increase of 42% is observed. This strong increase of modulus does not correspond to a similar strong increase in the glass transition temperature, as evident in Figure 49, where the temperature profiles of $\tan \delta$ for EHA-[80 °C, 9h + 120 °C, 2h] and EHA-[80 °C, 9h] samples are compared.

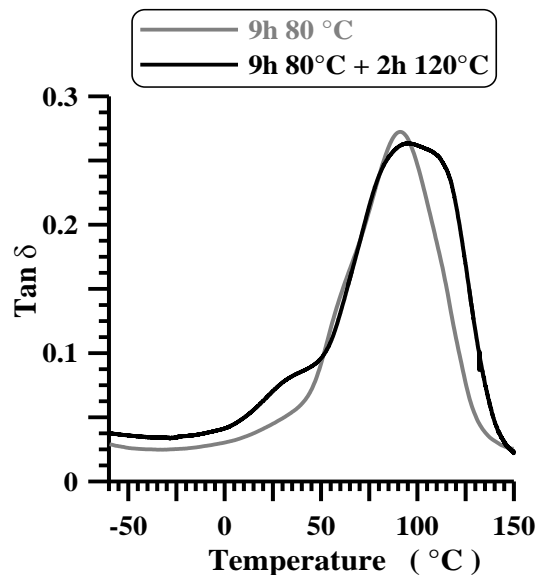


Figure 49: DMA plot of $\tan \delta$ versus temperature for EHA-[80 °C, 9h + 120 °C, 2h] and EHA-[80 °C, 9h] samples

4.1.3 Infrared Spectroscopy Analysis

To follow the curing progress of the epoxy matrix (EHA sample), infrared spectroscopy was used for determining the decrease of the band due to the epoxy group.

The FTIR spectra of the EHA sample were recorded in the interval 400–1800 cm^{-1} as a function of the reaction time during a two stage curing process composed of a treatment at 80 °C for 9h and a following treatment at 120 °C for 2h (Figure 50).

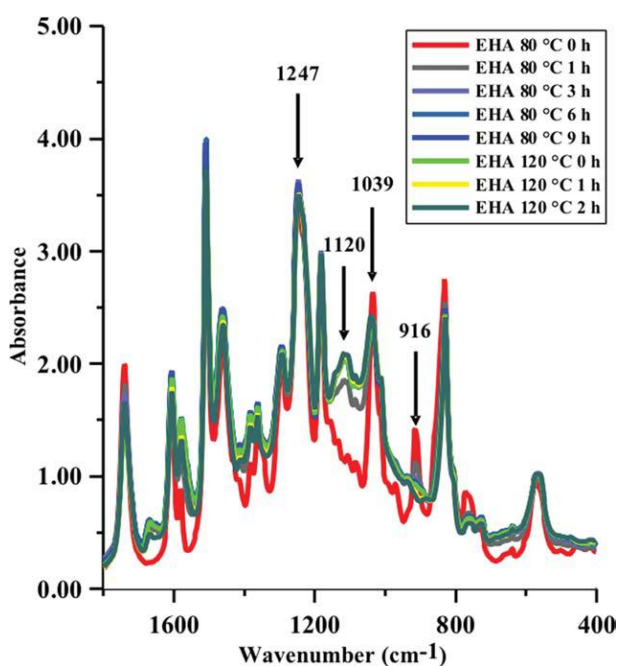


Figure 50: FTIR spectra of EHA resin as a function of reaction time during a two stage curing process at 80 and 120 °C

The most remarkable changes are recorded in the ether and epoxy ring regions. The characteristic response of ethers in the IR is associated with the stretching vibration of the C—O—C system.

In the initial spectrum EHA-[80 °C, 0h], we can note the vibrational bands of the aryl alkyl ethers which give two peaks; asymmetric C—O—C stretch at 1247 cm^{-1} and a symmetric stretch at 1039 cm^{-1} .

These two bands are due to the structure of the epoxy resin precursor [87]. In the interval 1157–1065 cm^{-1} , thermal treatment causes a noticeable increase of the absorbance due to the appearance and growth of the band at 1120 cm^{-1} , characteristic of aliphatic ethers;

confirming that the curing process of the resin lead to polyetherification as looked-for in epoxy resin cured with a tertiary amine. The most intense signal of the epoxy ring is the band centered at 916 cm^{-1} attributed to asymmetrical ring stretching in which the C—C bond is stretching during contraction of the C—O bond. In the initial spectrum (red curve), the band at 916 cm^{-1} is very evident, and it decreases with increasing reaction time and temperature. It completely disappears for a treatment time of 2 h at $120\text{ }^{\circ}\text{C}$, indicating the time for the complete consumption of the epoxy rings, due to the homopolymerization reaction, and so indicating the time for the complete curing process, which explains the higher modulus for the sample cured up to $120\text{ }^{\circ}\text{C}$. We have carried out also a monitoring of the absorbance (percentage) peak at 916 cm^{-1} as a function of the reaction time during the curing process composed of a treatment at $80\text{ }^{\circ}\text{C}$ for 9 h and a following treatment at $120\text{ }^{\circ}\text{C}$ for 2 h. We found that the intensity of the epoxy ring shows a rapid decrease at $80\text{ }^{\circ}\text{C}$ in the first 60 min, followed by a slower decrease up to 180 min, after which a plateau is reached and, even increasing the time up to 540 min, no further consumption of the oxirane rings is observed. An increase of temperature up to $120\text{ }^{\circ}\text{C}$, however, is necessary to cause the reaction of the residual epoxy groups. So, the described curing cycle composed of two stages up to $120\text{ }^{\circ}\text{C}$ was chosen to formulate our self-healing specimens.

4.2 Microcapsules Manufacturing and Characterization

The microcapsules outer shell composed of poly(urea-formaldehyde) and inner shell of ethylene maleic anhydride copolymer (EMA) were prepared by in situ polymerization in an oil-in-water emulsion. The polymerization process in situ with urea formaldehyde has the following advantages:

- High process yield (it is the only process that allows to encapsulate in a single preparation about 80% by weight of the healing agent used).
 - Possibility to modulate the stiffness of the microcapsules compared to that of the matrix. This process allows to synthesize the walls of the microcapsules with a thickness such as to modulate the stiffness of the microcapsules compared to that of the matrix.
-

The walls of the microcapsules should have a stiffness sufficient to withstand handling during the process of formulating and curing of the composite, but they must also be weak so that the crack can propagate through the walls. The microcapsules are synthesized using an already reported procedure [58-62] and have a core of dicyclopentadiene, an outer shell composed of poly (urea-formaldehyde) and an inner shell of a copolymer poly (ethylene maleic anhydride). In essence, this process of "in situ polymerization" consists in coating very small droplets of healing agent (dicyclopentadiene) - prepared by emulsion - with thin membranes that form the wall of polymeric microcapsules. This polymeric wall is obtained by "in situ" cross-linking of urea and formaldehyde. The drops of healing agent are maintained homogeneously dispersed in the emulsion through the control of chemical and physical parameters. The apparatus used for the production of microcapsules is essentially composed of:

- Mixer - dissolver Silverson Machines Ltd. mod. L4RT with electronic variable speed for a maximum speed rating up to 8000 rev/min., equipped with interchangeable heads disintegrating and mixing;
- Programmable digital heating electromagnetic stirrer (20 - 450 °C) mod. C04046-10 Cole Palmer Ltd. U.S.A. complete with immersion temperature probe;
- pH meter Crison Digital SA mod. micropH 2002 for measurements in the range of 0 to 14 pH, with a measurement accuracy of ± 0.01 pH, complete with temperature probe, electrode combined for viscous solutions.

Parameters such as temperature, pH, time and agitation speed, hole of emulsifier sieve, catalyst for the start of polymerization phase, urea/formaldehyde ratio, type of emulsifying agent, ionic strength, affect the quality of the microcapsules.

All tested microencapsulation processes were carried out by equipping the head emulsion with a stator diameter of round holes with holes 1/16". Best results were achieved maintaining the pH of the emulsion during polymerization to a range between 3.5 -3.7. During the polymerization (4 hours) the temperature was maintained at 55 °C and the speed of the stator at 1400 rpm. In the Figure 51, 52, 53 SEM

images at different magnifications of this preparation are shown. The photographs show spherical shape of microcapsules. They are sufficiently robust to be incorporated into the epoxy formulation without bursting, as well as being found in SEM images of the manufactured self-healing composite (see section 4.4).

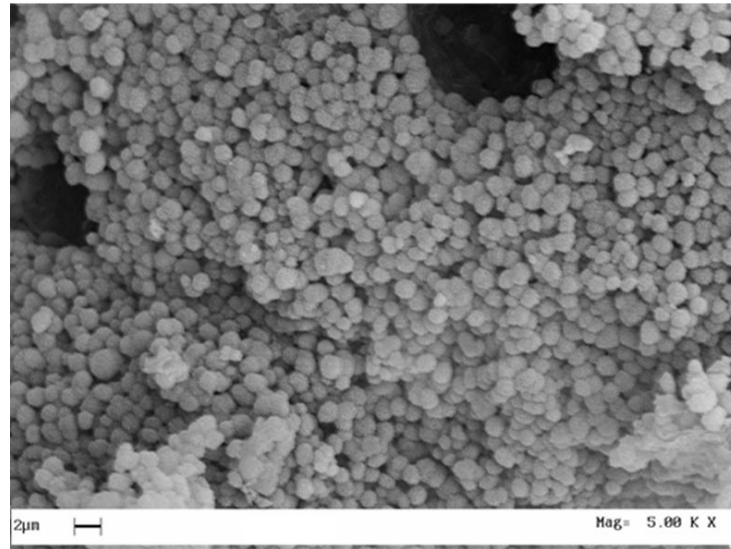


Figure 51: Sem image of microcapsules synthesized at pH value of 3.5-3.7, Magnification = 5000X

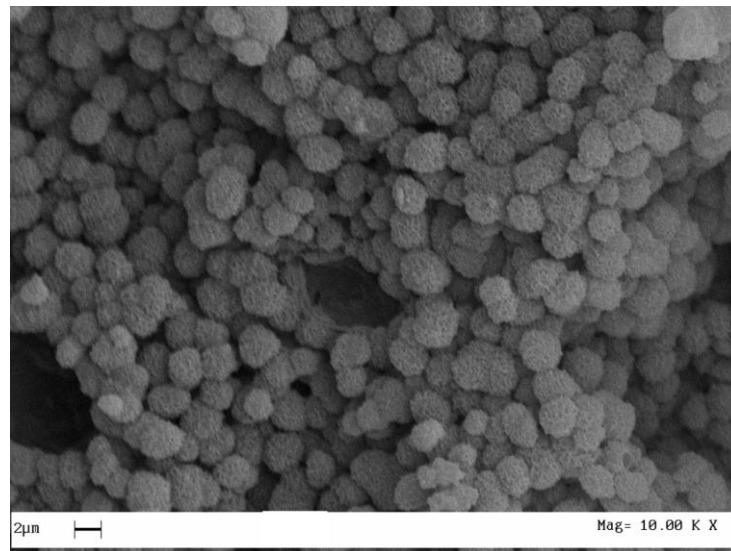


Figure 52: Sem image of microcapsules synthesized at pH value of 3.5-3.7, Magnification = 10000X

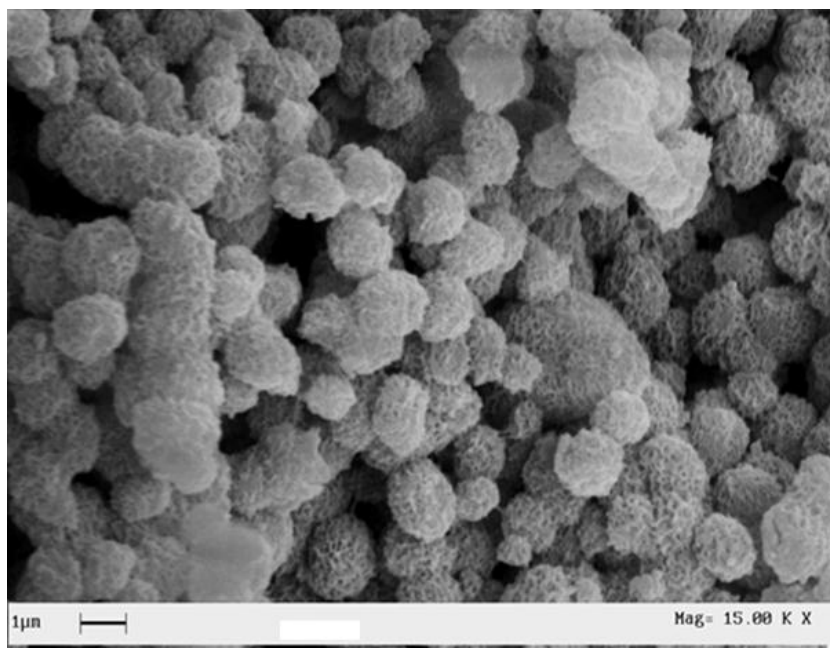


Figure 53: Sem image of microcapsules synthesized at pH value of 3.5-3.7, Magnification = 15000X

This preparation has been very satisfactory. The powders of microcapsules were not filtered either with a net of 80 mesh (177 microns), or with a 400-mesh (37 microns). This indicates that in this case, the microcapsules were obtained as fluid "separated" powders. From the images we see that good results have been achieved as regards the size distribution of microcapsules (the diameter of almost all microcapsules is of the order of 2 micron) and the presence of debris.

In other microcapsules preparations carried out at pH less than 3, without control of equilibrium of hydrolysis, the polymerization was very quickly leading to more spurious aggregates and precipitates, with low yield in the process of microencapsulation.

4.2.1 Check of healing agent content: ^1H NMR Analysis

We verified the healing agent (DCPD) content in the synthesized microcapsules with ^1H NMR spectroscopy.

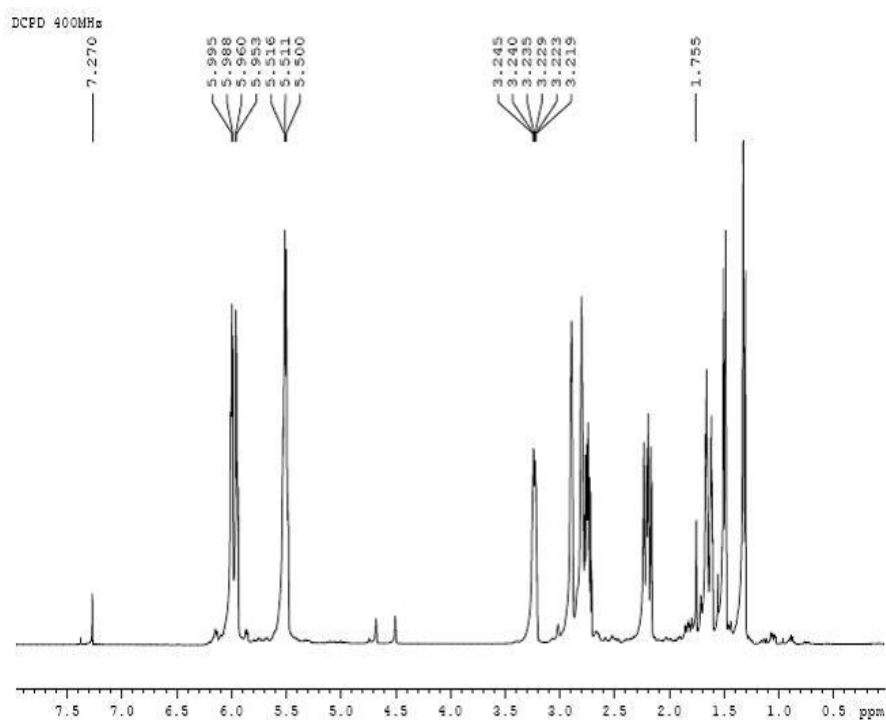


Figure 55: ^1H NMR spectrum of DCPD used in the sperimentation

4.2.2 Metathesis reaction of DCPD contained in synthesized microcapsules in presence of first generation Grubbs' catalyst: FT/IR Analysis

Spectroscopic investigation was performed to identify in FT/IR spectra characteristic bands of the metathesis product; for this purpose have also been conducted metathesis reactions with different DCPD/catalyst ratios and metathesis products were all subjected to a spectroscopic investigation.

In a vial 65.8 mg of microcapsules (previously crushed in a mortar, to facilitate the escape of dicyclopentadiene contained in them) were mixed with 7 mg of first-generation Grubbs' catalyst previously weighed in a dry box. After about 5 minutes the reaction was stopped by introducing a few drops ethyl vinyl ether and everything was poured into a beaker containing methanol to coagulate the polymer. The product of metathesis (PM) was filtered, dried under vacuum and analyzed at FT/IR.

In Figure 56 are shown FT/IR spectra of microcapsules (blue curve), dicyclopentadiene (green curve), insoluble fraction of the microcapsules obtained after extraction of DCPD (red curve) and metathesis product (brown curve).

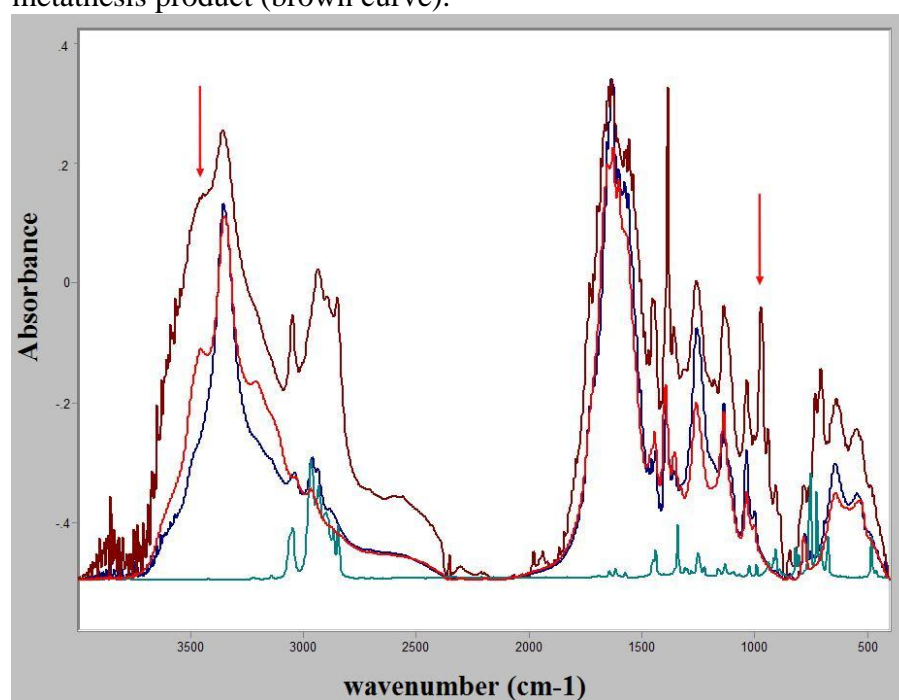


Figure 56: FT/IR spectra of microcapsules (blue curve), dicyclopentadiene (green curve), insoluble fraction of the microcapsules obtained after extraction of DCPD (red curve) and metathesis product (brown curve) in the spectral range from 500 to 4000 cm^{-1}

It can be seen that the spectrum of the metathesis product (obtained as a result of the reaction between DCPD in the microcapsules and catalyst G1) has a flared shoulder centered at 3429 cm^{-1} (see red arrow) and a band at 968 cm^{-1} (see red arrow). The shoulder at 3429 cm^{-1} is due to O-H stretching of water molecules trapped in the metathesis product. The part of the spectrum where is the 968 cm^{-1} band is magnified in Figure 57: the band at 968 cm^{-1} is not present in the spectra of the microcapsules and the residue after extraction of the DCPD. This band is in fact characteristic of the only metathesis product. Experimentation carried out has shown that this band is between 952 and 990 cm^{-1} , the exact frequency and shape are influenced by the ratio catalyst/monomer (see Figure 58)

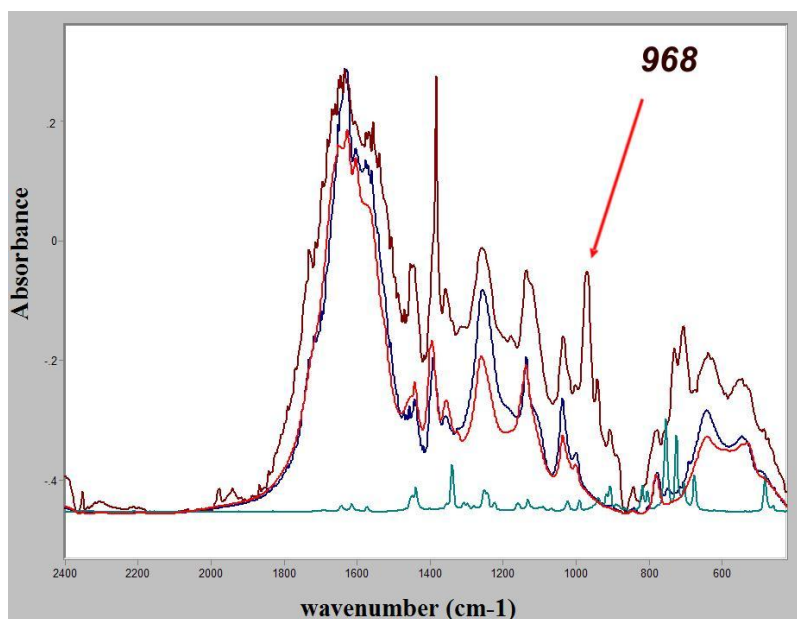


Figure 57: FT/IR spectra of microcapsules (blue curve), dicyclopentadiene (green curve), insoluble fraction of the microcapsules obtained after extraction of DCPD (red curve) and metathesis product (brown curve) in the spectral range from 500 to 2400 cm⁻¹

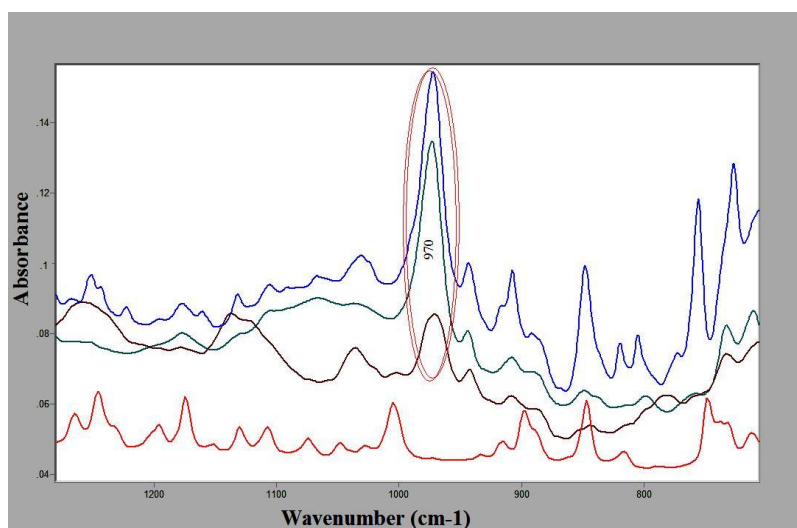


Figure 58: FT/IR spectra of first generation Grubbs' catalyst (red curve), product of metathesis PM (brown curve), metathesis product with 1/5000 catalyst/monomer ratio (green curve) and metathesis product with 1/2000 catalyst/monomer ratio (blue curve)

4.2.3 Microcapsules Thermal Analysis: TGA, DSC

4.2.3.1 Thermogravimetric analysis

Thermogravimetric analysis allowed an evaluation of the degradation temperature and rates of mass loss as a function of temperature (under air and nitrogen flow) of the microcapsules synthesized. Figure 59 shows results for microcapsules obtained at pH less than 3 and pH between 3.5 – 3.7.

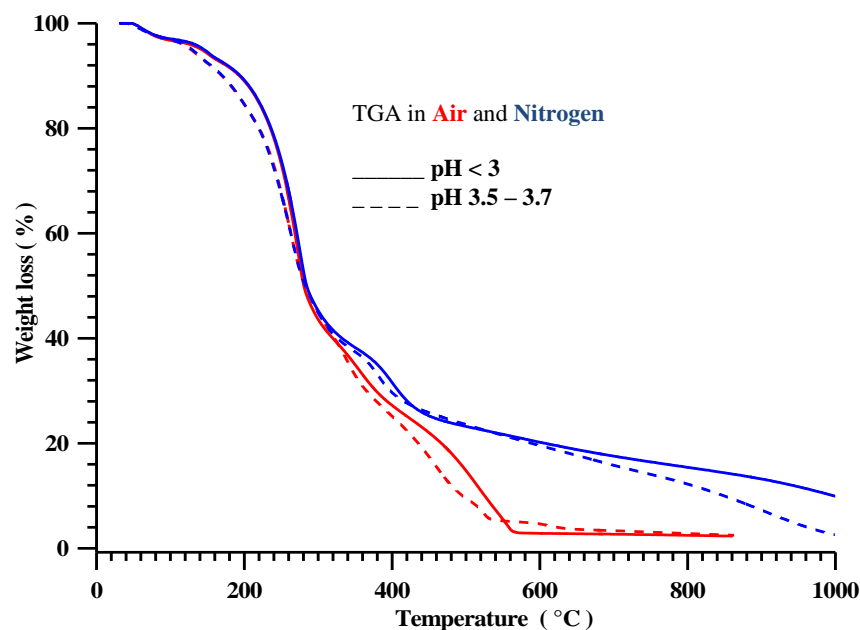


Figure 59: TGA curves in air (red) and in nitrogen (blue) of the microcapsules synthesized at different pH values

The trend of the curves in Figure 59 shows that, below 300 °C, the curves are nearly coincident; above 300 °C there is a faster weight loss for the thermal degradation conducted in the presence of air. The complete degradation is recorded at 550 °C in air and about 1000 °C in an inert atmosphere.

Thermal degradation of the microcapsules was affected by atmospheric oxygen as an agent for acceleration of thermal degradation processes only at temperatures higher than 340 °C. The fragmentation of the structure of the polymer begins consistently in the air and in inert atmosphere up to 200 °C with the elimination of ammonia, amines, carbon dioxide, etc.

The weight loss is achieved through three different stages of degradation (the first ending at about 280 - 300 °C, the second at 400 °C and the third at 560 °C in air and 1000 °C in an nitrogen). The presence of different stages of degradation in the thermogravimetric traces indicates that fragmentation is followed by cross-linking processes involving structures characterized by different thermal stability, which once formed cause a slowdown in the thermal degradation.

4.2.3.2 Differential Scanning Calorimetry

Figure 60 shows the thermograms of the microcapsules synthesized at two different pH values.

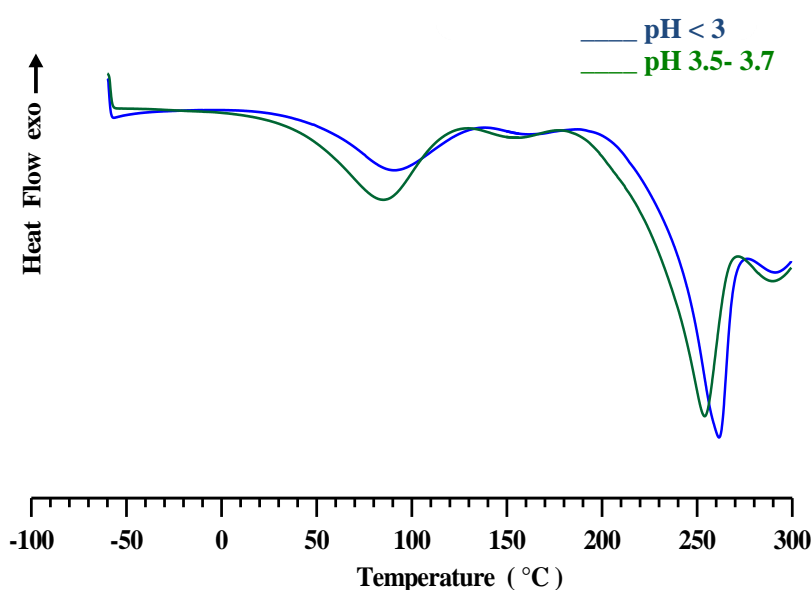


Figure 60: DSC curves for microcapsules synthesized at different pH values

From the thermograms we notice that the different pH values do not change the profile curves, it can be observed only a slight increase in the maximum of endothermy at higher temperatures for the capsules synthesized at slightly more acidic pH values.

In both the curves we can see three endothermy.

The first endothermic peak, centered at about 80 °C, is due to impurities of water and free formaldehyde (not condensed) that are removed during the heat treatment (this peak is reduced in intensity or disappears when the microcapsules are kept under vacuum or are left to air for a long time).

The second endothermy centered at 150-160 °C extends almost up to 200 °C and is probably due to the presence of dicyclopentadiene in the “core” of the microcapsules.

The third endothermic peak, centered at 260 °C, corresponds to the first step of weight loss in the thermogravimetric curve (see thermogravimetric analysis) and is due to the explosion of the microcapsules and evaporation of healing agent.

Endothermy close to 280 °C, where the faster stage of mass loss is completed. The process of decomposition slows down after a partial loss in weight of 60%.

4.3 Grubbs' Catalyst (G1) Characterization

4.3.1 First Generation Grubbs' Catalyst (G1) Morphology

The crystal morphology has a significant effect on the dissolution kinetics of the DCPD/Grubbs' catalyst system. Smaller particles of Grubbs' catalyst dissolve more quickly, leading to a high concentration of catalyst available for the healing agent and consequently for the metathesis reaction.

Morphological investigation was carried out through scanning electron microscopy to evaluate the size of catalyst particles and the suitability for use in the our self-healing system.

Figure 61 and 62 show SEM images of catalyst particles as supplied by Aldrich.

From the images we see that many catalyst particles have a rod shape with dimensions that can reach 40 – 50 µm wide and 185 µm in length.

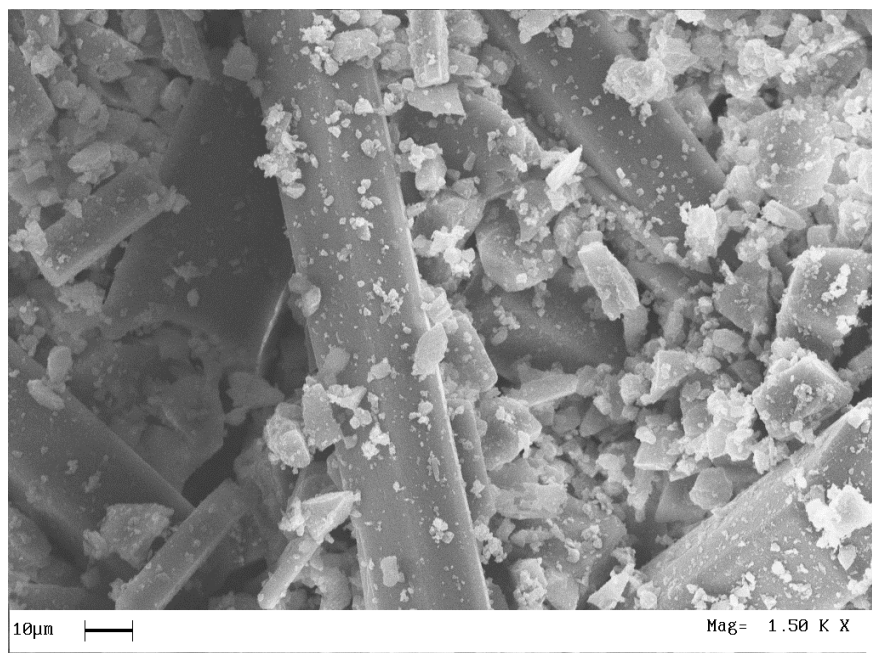


Figure 61: SEM image of the G1 catalyst (magnification 1.5 KX)

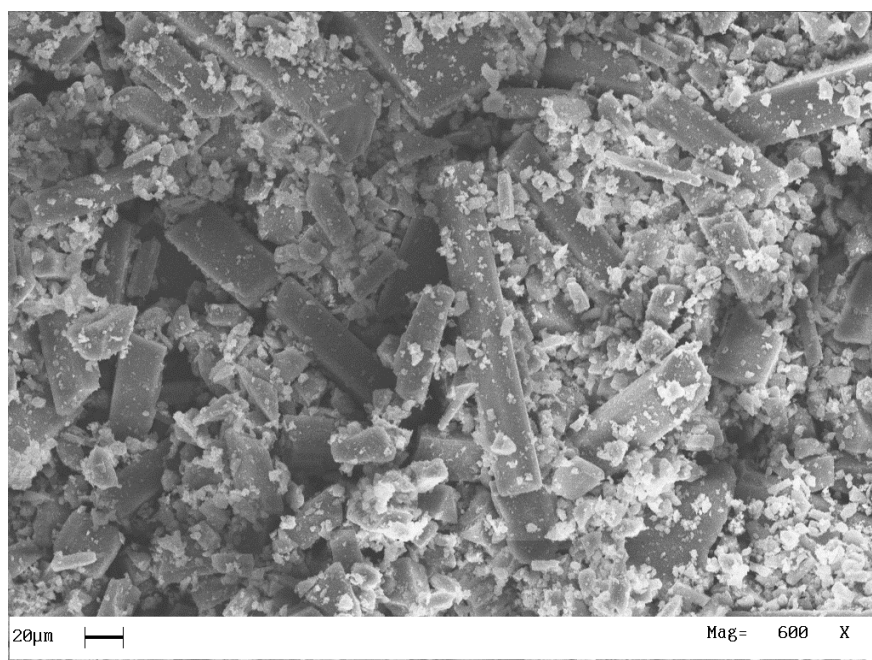


Figure 62: SEM image of the G1 catalyst (magnification 600X)

It is clear that these particles have, for our purposes, unacceptable size. For this reason the catalyst was subjected to a treatment to reduce the size of the particles.

The Grubbs' catalyst, as-received from Sigma–Aldrich, was placed in a vial and pulverized by a small magnet in rotation for 30 min.

Morphology of G1 after treatment is shown in Figure 63.

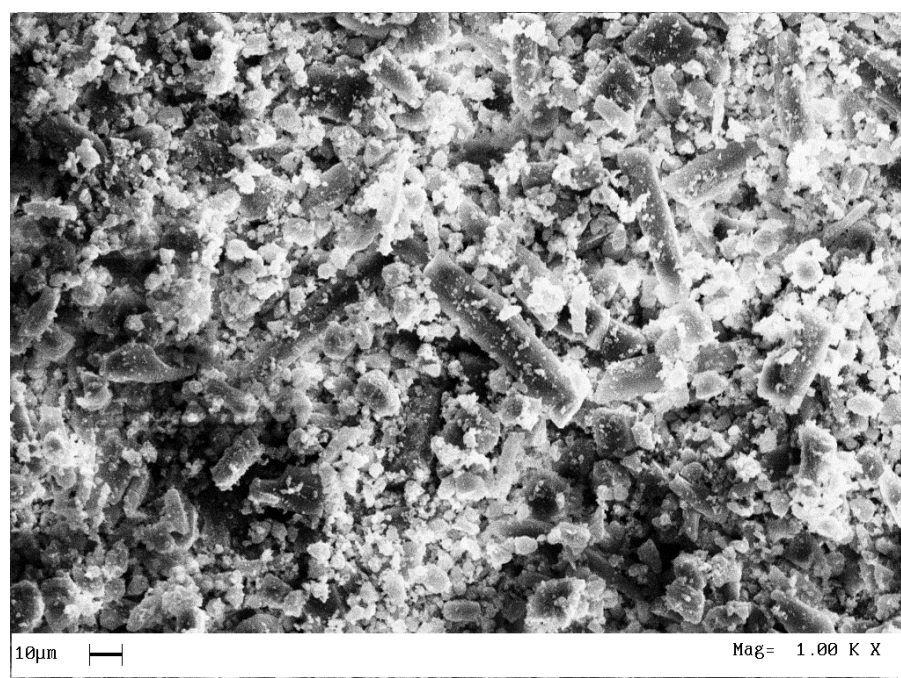


Figure 63: SEM image of the G1 catalyst after treatment (magnification 1000X)

The comparison between the acquired images shows that the processing has significantly reduced the particle size of the Grubbs' catalyst.

4.3.2 First Generation Grubbs' Catalyst (G1) Thermal Analysis

In Figure 64 are shown the thermogravimetric curves of Grubbs' catalyst. It can be seen that the catalyst G1 pure (under dynamic heating 10 °C/min) begins to degrade at about 200 °C. The sample loses approximately 80% of its mass at 400 °C in an inert atmosphere, whereas the same loss of mass occurs at a temperature of 300 °C in air. DSC curve for Grubbs' catalyst is shown In Figure 65. Thermogram shows that endothermy is centered on the values of

temperature corresponding to the various stages of mass loss found in thermogravimetric trace of Figure 63 (see blu curve in Figure 63).

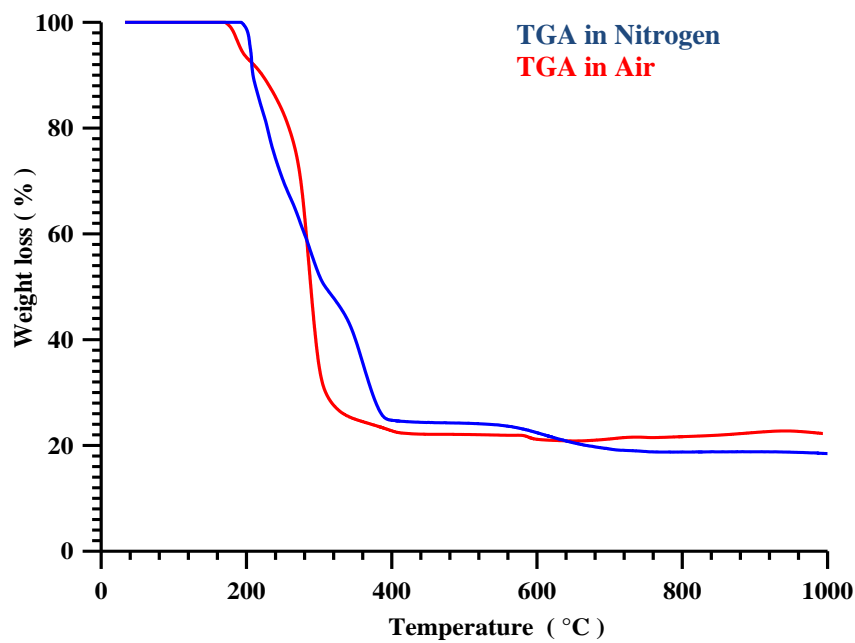


Figure 64: TGA curves for first generation Grubbs' catalyst in air (red) and in nitrogen (blue)

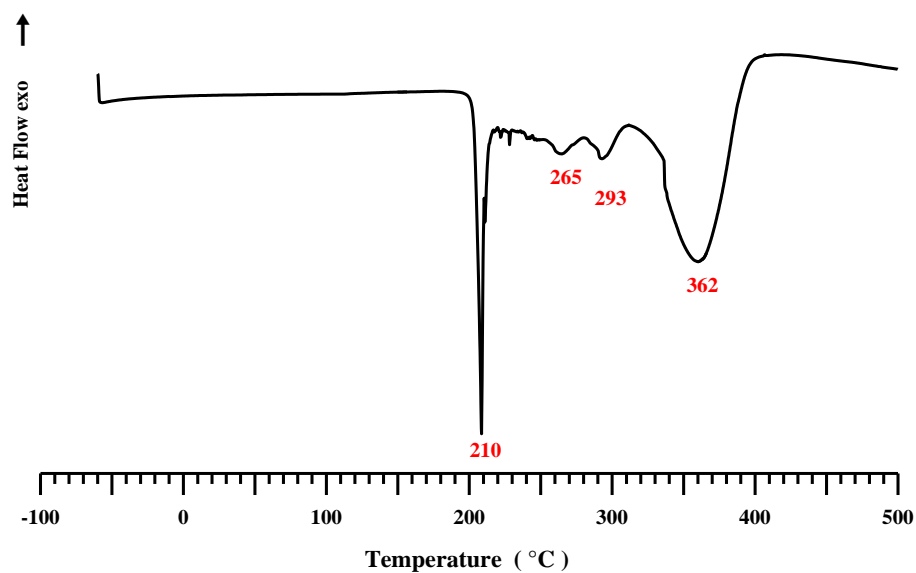


Figure 65: DSC curve for first generation Grubbs' catalyst

4.3.3 Thermolytic stability of First Generation Grubbs' Catalyst (G1): ^1H NMR Spectroscopy

The thermolytic stability of G1 catalyst was evaluated in air and nitrogen atmosphere with the catalysts in powder form kept at different temperatures. The catalyst powder, after the thermal treatment, was dissolved in the deuterated solvent immediately before the ^1H -NMR spectra recording.

In Figure 66 is shown ^1H NMR spectrum obtained for the catalyst G1 dissolved in deuterated tetrachloroethane (TCDE) at room temperature; the graph shows also the chemical shifts of all proton signals.

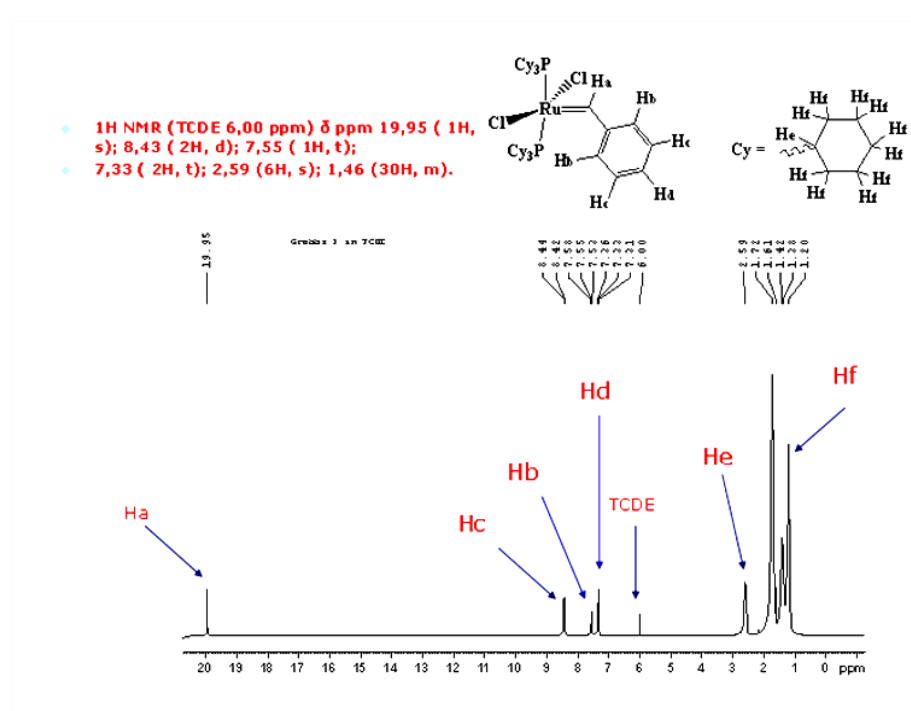


Figure 66: ^1H NMR spectrum for Grubbs' catalyst dissolved in TCDE at room temperature

All the following tests were performed with the catalyst in powder form kept at different temperatures: the catalyst was dissolved in deuterated solvent only after the thermal treatment.

The deuterated solvent was used only to take high-resolution NMR spectrum.

Test 1 - nitrogen

The Grubbs catalyst was placed in a vial with screw cap in dry-box, this to allow an inert environment. The vial was then placed in an oil bath at a temperature of 120 °C for 1 h. After this time, the catalyst was characterized by ^1H NMR analysis, using as a solvent TCDE. Color solution: purple. The spectrum (Figure 67) shows all signals of first generation Grubbs' complex.

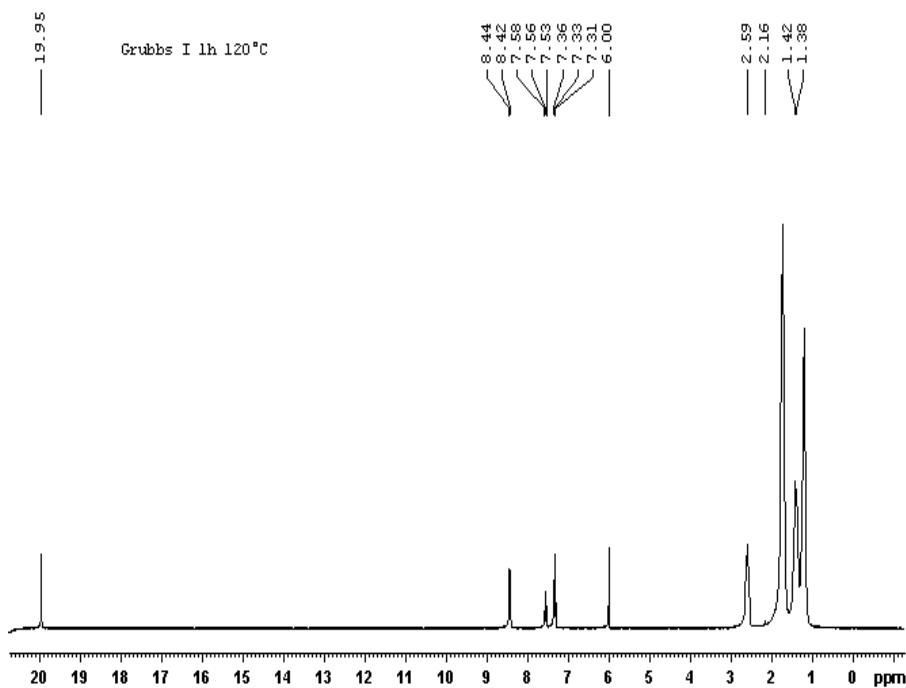


Figure 67: ^1H NMR spectrum for Grubb's catalyst after a thermal treatment of 1 h at 120 °C in nitrogen

Test 2 - nitrogen

The Grubbs catalyst was placed in a vial with screw cap in dry-box, this to allow an inert environment. The vial was then placed in an oil bath at a temperature of 120 °C for 15 h. After this time, the catalyst was characterized by ^1H NMR analysis, using as a solvent TCDE. Color solution: purple. The spectrum (Figure 68) shows all signals of first generation Grubbs' complex.

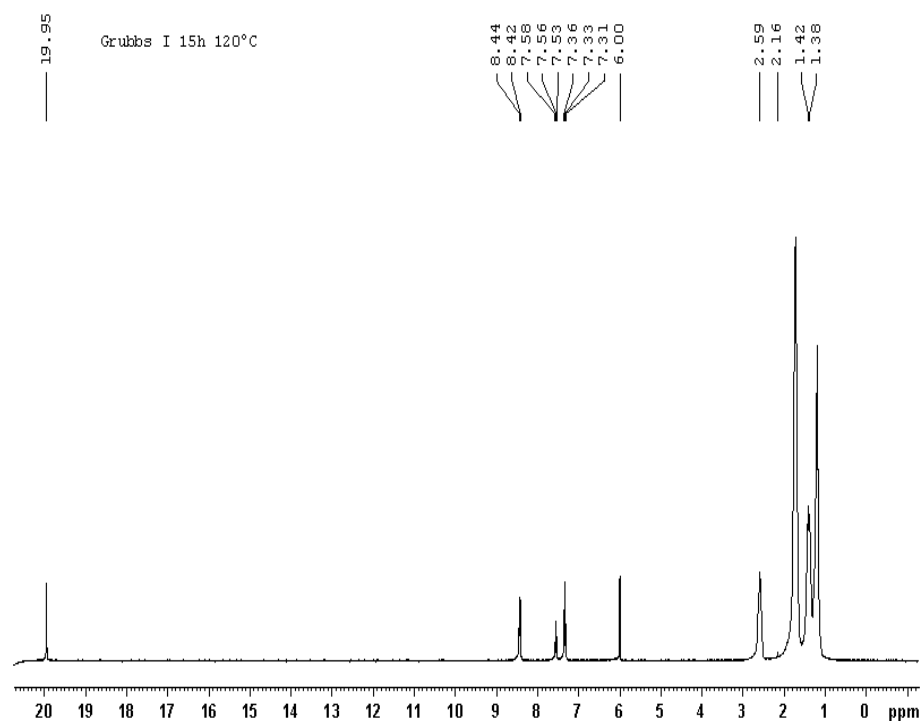


Figure 68: ^1H NMR spectrum for Grubbs' catalyst after a thermal treatment of 15 h at 120 °C in nitrogen

Test 3 - nitrogen

The Grubbs catalyst was placed in a vial with screw cap in dry-box, this to allow an inert environment. The vial was then placed in an oil bath at a temperature of 150 °C for 1 h. After this time, the catalyst was characterized by ^1H NMR analysis, using as a solvent TCDE. Color solution: purple. The spectrum (Figure 69) shows all signals of first generation Grubbs' complex.

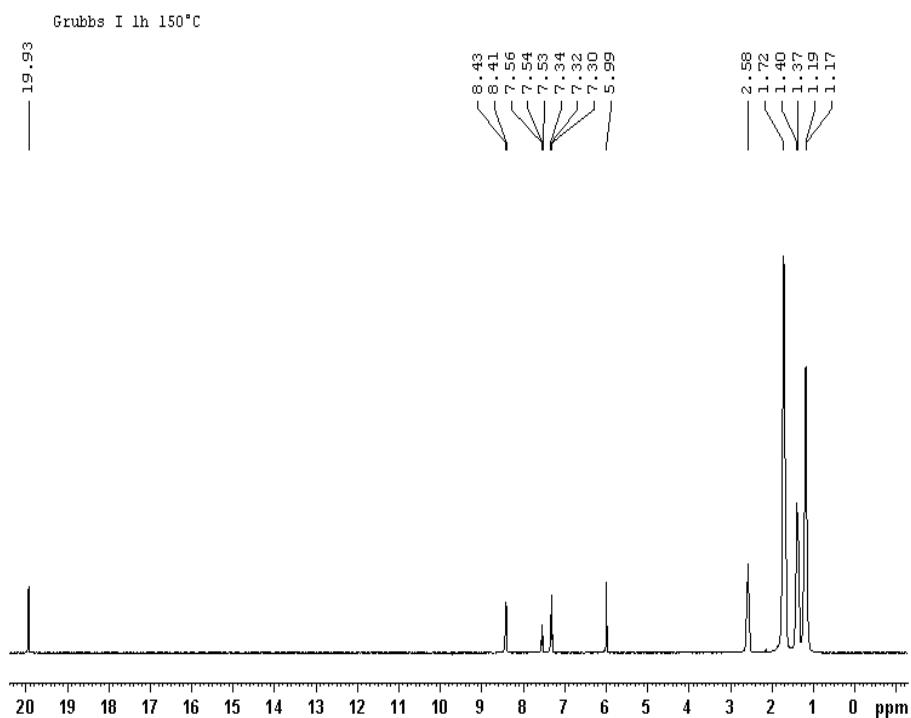


Figure 69: ^1H NMR spectrum for Grubbs' catalyst after a thermal treatment of 1 h at 150 °C in nitrogen

Test 4 - nitrogen

The Grubbs catalyst was placed in a vial with screw cap in dry-box, this to allow an inert environment. The vial was then placed in an oil bath at a temperature of 150 °C for 3.58 h. After this time, the catalyst was characterized by ^1H NMR analysis, using as a solvent TCDE. Color solution: purple. The spectrum (Figure 70) shows all signals of first generation Grubbs' complex.

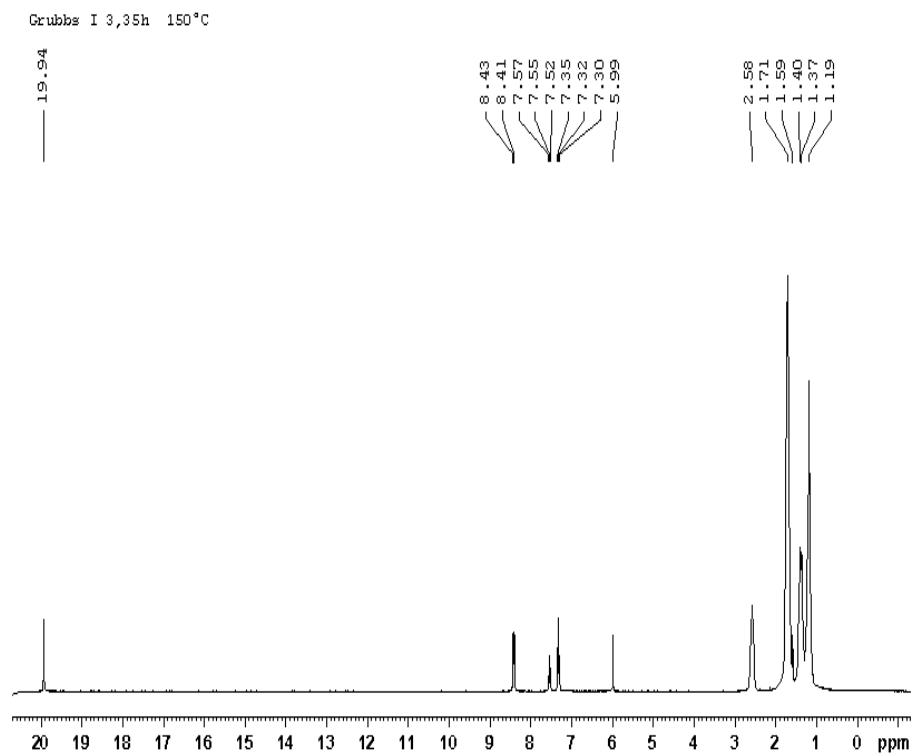


Figure 70: ^1H NMR spectrum for Grubbs' catalyst after a thermal treatment of 3.58 h at 150 °C in nitrogen

Test 5 - air

The Grubbs catalyst was placed in a vial left to the air. The vial was then placed in an oil bath at a temperature of 150 °C for 2.25 h. After this time, the catalyst was characterized by ^1H NMR analysis, using as a solvent TCDE. Solution color: brown. The spectrum (Figure 71) shows no signals of first generation Grubbs' complex. Treatment at 150 °C for 2.25 h in air decomposes the catalyst.

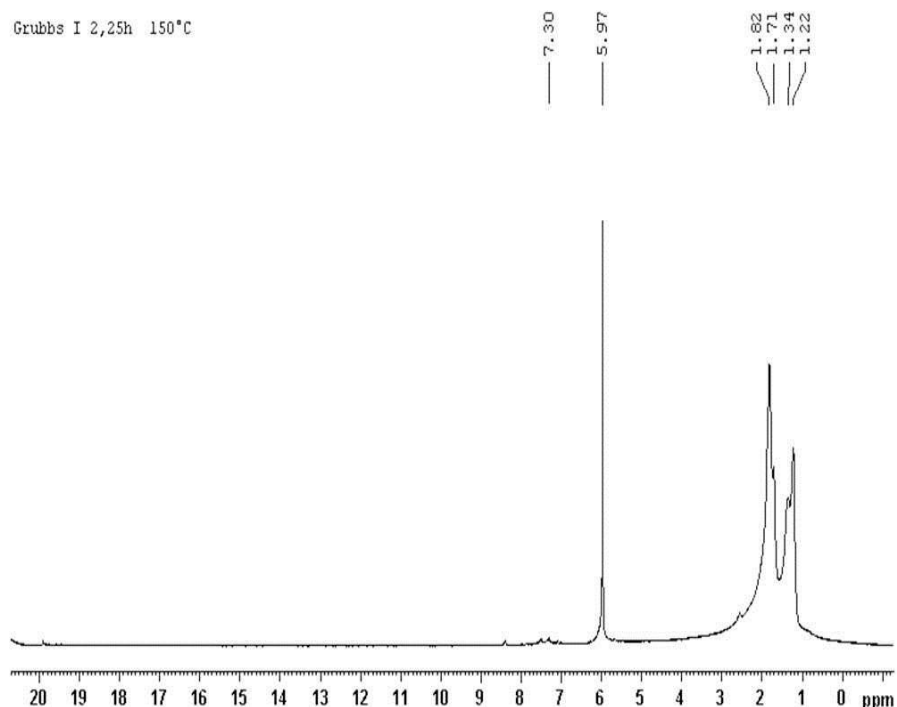


Figure 71: ^1H NMR spectrum for Grubbs' catalyst after a thermal treatment of 2.25 h at 150 °C in air

Test 6 - air

The Grubbs catalyst was placed in a vial left to the air The vial was then placed in an oil bath at a temperature of 120 °C for 3 h. After this time, the catalyst was characterized by ^1H NMR analysis, using as a solvent TCDE. Solution color: purple. The spectrum (Figure 72) shows all signals of first generation Grubbs' complex

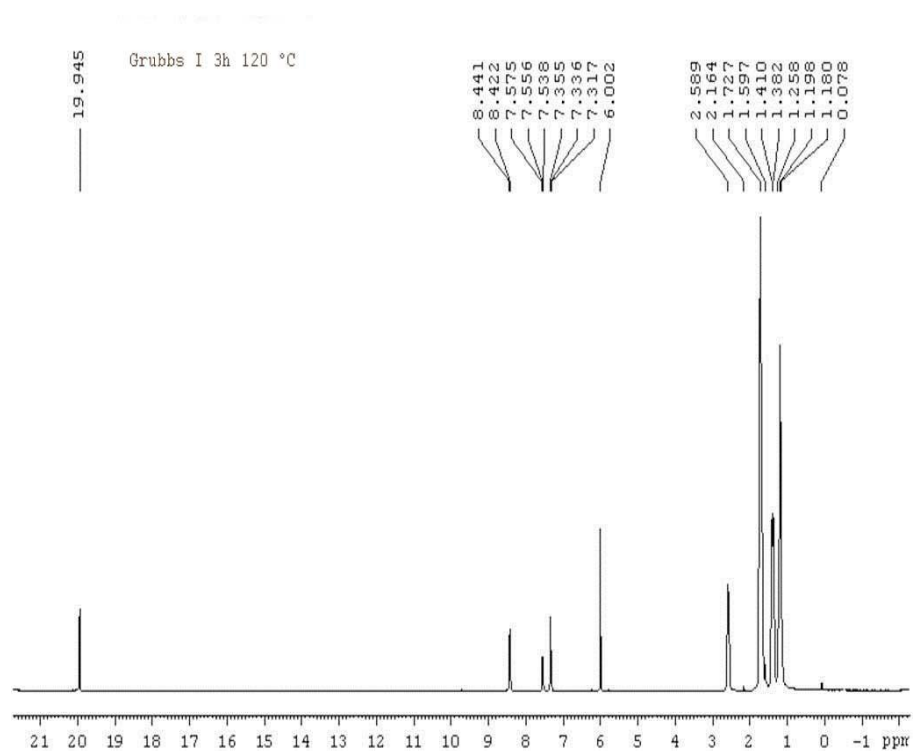


Figure 72: ^1H NMR spectrum for Grubbs' catalyst after a thermal treatment of 3 h at 120 °C in air

Test 7 - air

The Grubbs catalyst was placed in a vial left to the air. The vial was then placed in an oil bath at a temperature of 25 °C for 6 h. After this time, the catalyst was characterized by ^1H NMR analysis, using as a solvent TCDE. Solution color: purple. The spectrum (Figure 73) shows all signals of first generation Grubbs' complex.

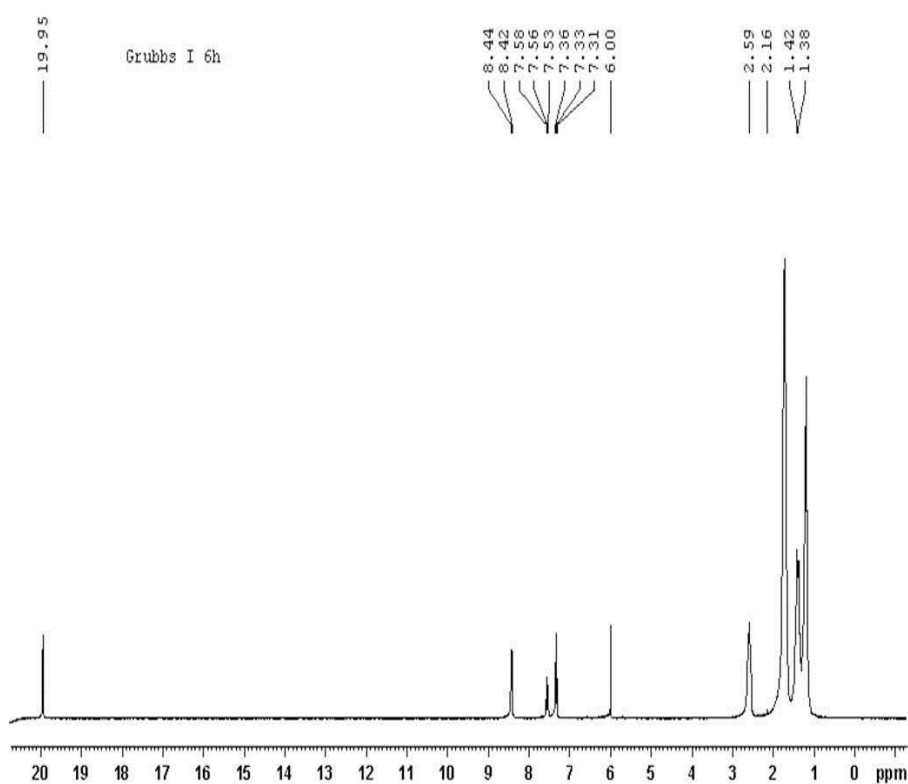


Figure 73: ^1H NMR spectrum for Grubbs' catalyst after a thermal treatment of 6 h at 25 °C in air

Test 8 - air

The Grubbs catalyst was placed in a vial left to the air. The vial was then placed in an oil bath at a temperature of 25 °C for 24 h. After this time, the catalyst was characterized by ^1H NMR analysis, using as a solvent TCDE. Solution color: purple. The spectrum (Figure 74) shows all signals of first generation Grubbs' complex.

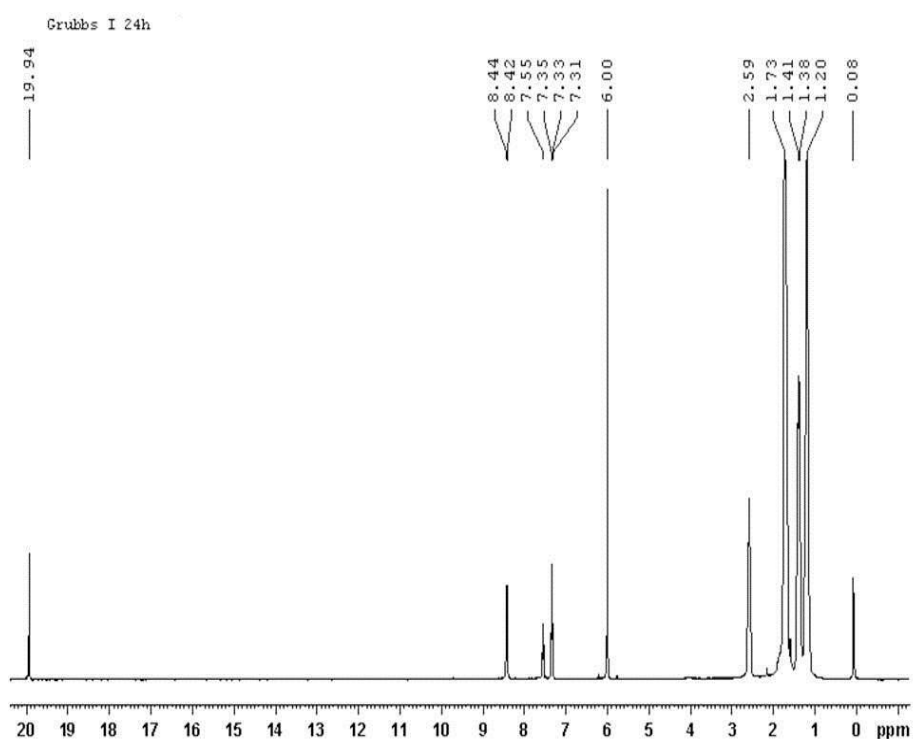


Figure 74: ^1H NMR spectrum for Grubbs' catalyst after a thermal treatment of 24 h at 25 °C in air

The summary of result of the thermolytic decomposition of Grubbs' catalyst is reported in Table 4.4.

Test	Temperature (°C)	Time (h)	Initial state of catalyst	Environment	Final state of catalyst
1	120	1	solid	nitrogen	Not decomposed
2	120	15	solid	nitrogen	Not decomposed
3	150	1	solid	nitrogen	Not decomposed
4	150	3.58	solid	nitrogen	Not decomposed
5	150	2,25	solid	air	Decomposed
6	120	3	solid	air	Not decomposed
7	25	6	solid	air	Not decomposed
8	25	24	solid	air	Not decomposed

Table 4.4: Summary of results on thermolytic decomposition of Grubbs' catalyst in different environment at different temperatures

As can be seen from Table. 4.4 for a residence time of 2.25 h at 150 °C in air, the first generation Grubbs' catalyst decomposes, so have not been tested at higher temperatures.

The results of tests 7 and 8 have been very useful because it allowed us to understand that, at room temperature, the treatments on Grubbs' catalyst can be made easily in the air.

4.4 Self-healing Systems

The chemical formulation of the self-healing systems on which experimentation was carried out is outlined below:

Matrix system EHA:

- *Epon 828 (63% by wt)*
- *Heloxy 71 (37% by wt)*
- *Ancamine K54 (10% by wt to mixture Epon 828 + Heloxy)*

Self-healing system EHA + Catalyst + Microcapsules:

- *Matrix EHA*
- *1st generation Grubbs' catalyst (5% by wt to EHA)*
- *DCPD filled microcapsules (20% by wt to EHA)*

The order of mixing the components is the following:

the monomers precursors of epoxy, the Heloxy 71 flexibilizer and Ancamine K54 curing agent, are mixed at room temperature in the liquid phase resulting in a mixture with the composition as previously indicated.

Catalyst powders are added and mixed before the inclusion of the microcapsules.

The whole mixture is then poured into molds for the cure at chosen curing conditions.

We decided to test the following samples:

Sample B was obtained by dispersing finely pulverized Grubbs' first catalyst (5 wt %) in EHA matrix and polymerizing this last mixture by a two-stage curing cycle: a first isothermal stage at 80 °C for 9 h and a second isothermal stage with the higher temperature of 120 °C for 2 h.

Sample C was obtained by dispersing finely pulverized Grubbs' catalyst (5 wt %) and DCPD-filled microcapsules at the concentration of 20 wt % into the mixture EHA before the "curing" treatment which was the same as Sample B.

4.4.1 Thermogravimetric analysis

Thermal degradation in air of self-healing sample Sample C (red curve) is shown in Figure 75, where the thermogravimetric curve of the microcapsules (blu curve) is also reported for comparison.

The oxidation of Sample C substantially occurs in the temperature range of 200 – 560 °C.

The self-healing specimen is stable up to 220 °C where it begins to degrade.

The sudden decrease in weight around 220 °C of the microcapsules is due to the explosion of microcapsules and rapid evaporation of DCPD.

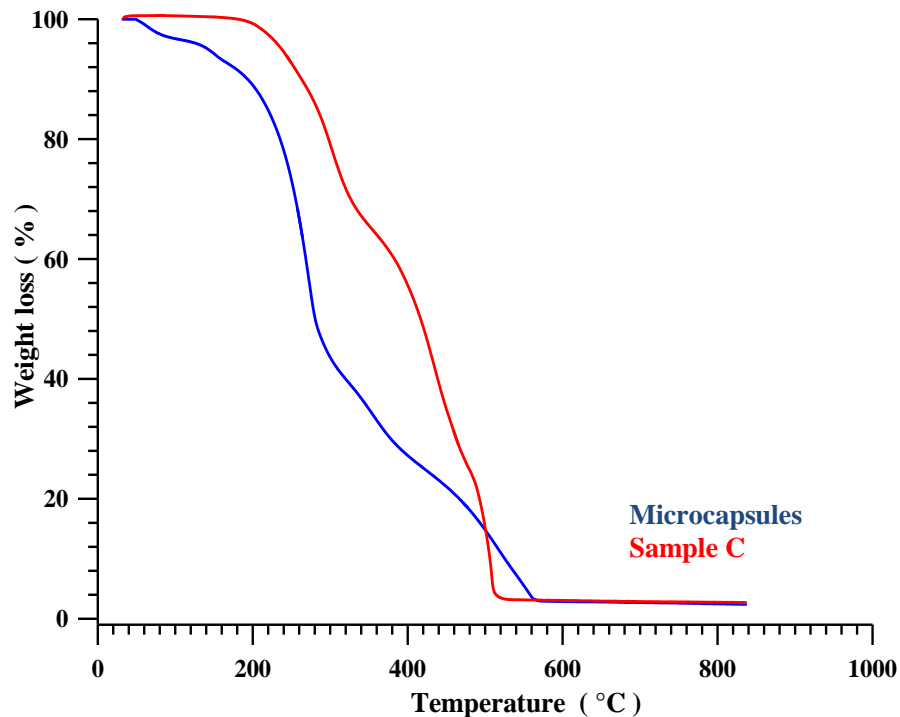


Figure 75: TGA curves of Microcapsules (blu) and Sample C (red)

4.4.2 Grubbs' Catalyst Stability inside Self-healing System: FT/IR and ^1H NMR Analysis

4.4.2.1 Infrared Analysis of Catalyst inside Self-healing sample

To analyze the catalytic activity directly inside self-healing specimen, Sample C was cut by a serrated blade; the powder which was produced from the sample was collected in a mortar and a drop of healing agent (DCPD) was added before dispersing the sample powder into the KBr disk for FTIR investigation.

In Figure 76 is shown FTIR spectrum of Sample C treated with DCPD. We can notice the presence of the peak at 968 cm^{-1} characteristic of ring-opened poly(DCPD).

This proves that the embedded catalyst, showing ability to polymerize the healing agent, is active also for a self healing sample cured up to $120\text{ }^\circ\text{C}$.

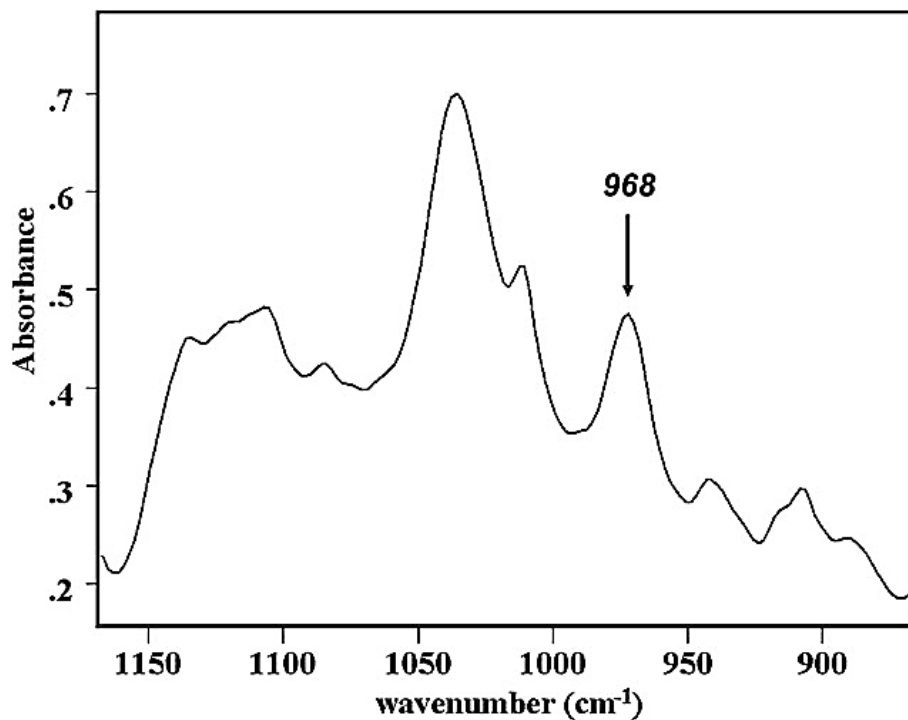


Figure 76: FT/IR spectrum of Sample C powder treated with DCPD

4.4.2.2 Spectroscopy Analysis of Catalyst inside Self-healing sample

The stability of the catalyst was also analyzed for the powder embedded inside epoxy system.

A fragment of cured Sample C was reduced to coarse powder and placed in a 10 ml tube containing 2 ml of anhydrous CH_2Cl_2 .

The solution was shaken for about 20 minutes (to allow the passage of the Grubbs catalyst in solution). Afterwards the solution was filtered and the solvent was removed under vacuum.

The residue was subjected to ^1H NMR analysis using TCDE as a solvent. The spectrum (Figure 77) shows all signals of first generation Grubbs' complex.

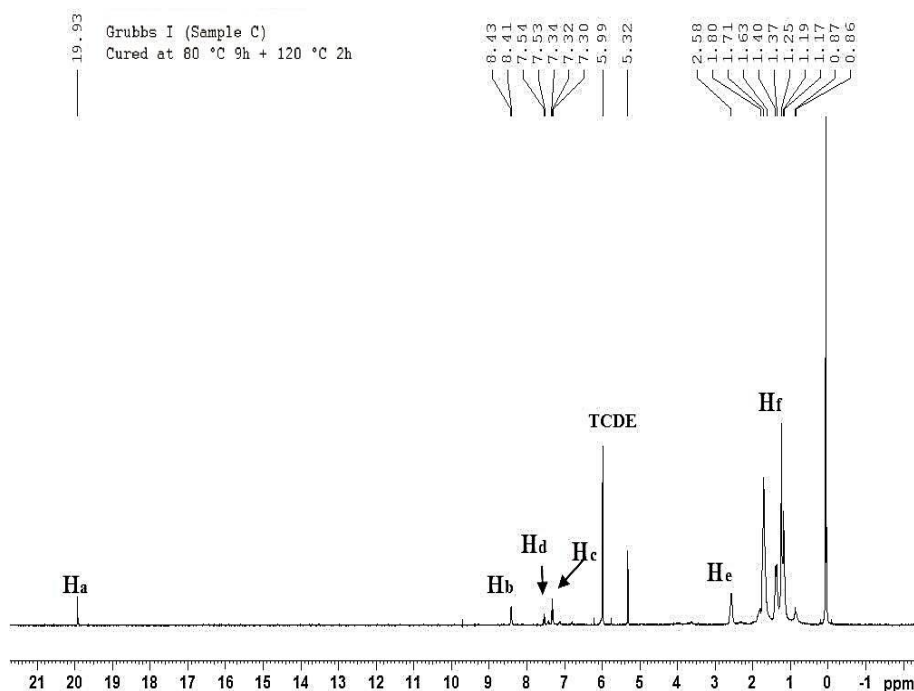


Figure 77: ^1H NMR spectrum first generation Grubbs' catalyst extracted from Sample C cured at 80 °C 9h + 120 °C 2h

To analyze the thermolytic decomposition of first generation Grubbs' catalyst inside epoxy matrix other two samples were manufactured (Sample D and Sample E). These samples had the same composition of Sample B (without microcapsules), but were cured at different temperatures:

Sample D: was obtained by dispersing finely pulverized Grubbs' first catalyst (5 wt %) in sample EHA, utilizing for the polymerization of the mixture two-different stage of the curing cycle: a first isothermal stage at 80 °C for 4 h and a second isothermal stage with the higher temperature of 150 °C for 2 h.

Sample E: was obtained as Sample D, but with a different curing cycle, consisting in a first isothermal stage at stage at 80 °C for 4 h and a second isothermal stage with the higher temperature of 180 °C for 2 h.

The extraction procedure and ¹H NMR analysis of Grubbs' catalyst embedded in these sample are the same as Sample C.

The results of the thermolytic decomposition of G1 catalyst embedded in the epoxy matrix are summerixed in Table 4.5.

Sample	Curing Cycle Temperature (time)	Catalyst state after treatment
B	80 °C (9h) + 120 °C (2h)	Not decomposed
C	80 °C (9h) + 120 °C (2h)	Not decomposed
D	80 °C (9h) + 150 °C (2h)	Partially decomposed
E	80 °C (9h) + 180 °C (2h)	Decomposed

Table 4.5: Thermolytic decomposition of first generation Grubbs' catalyst embedded in epoxy matrix

Grubbs' catalyst has shown to be extraordinarily tolerant toward the different kinds of functional groups of the epoxy formulations up to 120 °C.

From Table 4.5 we can see that at high curing temperatures (150 – 180 °C), first generation Grubb's catalyst embedded in exopy matrix it's decomposed.

4.4.3 Dynamic Mechanical Analysis on Self-Healing Samples

We have tested a self-healing specimen to determine the mechanical parameters (elastic modulus and stiffness) and then compared this system with an epoxy matrix in two different forms: one with and another without catalyst powder.

Figure 78 shows the loss factor, $\tan \delta$, of the self-healing system (Sample C) compared with EHA-[80 °C, 9 h + 120 °C, 2 h] and B samples as a function of temperature. The dynamic mechanical spectra of the three samples show $(T_g)_{DMA}$ in the same range of temperature.

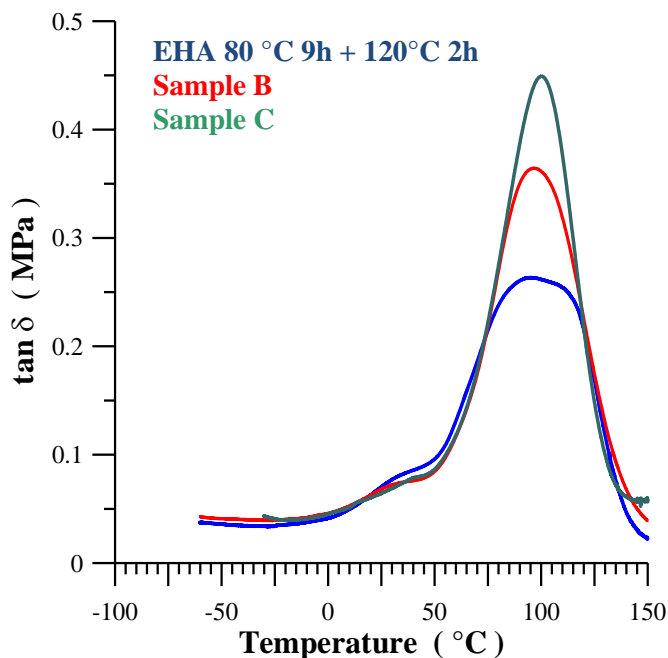


Figure 78: Loss factor $\tan \delta$ for EHA [80 °C, 9h + 120 °C, 2h], Sample B and Sample C

In Table 4.6 elastic modulus of sample EHA-[80 °C, 9h + 120 °C, 2h] is compared with B and C samples in the temperature range between -50 and 50 °C. The storage modulus values are high for all the samples, but in particular the self-healing sample (Sample C) has the highest elastic moduli in all the temperature range,. It is interesting to note that, for the same curing cycle, the presence of catalyst powder (Sample B) causes a slight decrease in the elastic modulus value with respect to the epoxy matrix. It seems likely that in a way the catalyst

powder interrupts the cross-linking reactions locally determining a slight decrease in the elastic modulus. This decrease could be also due to embrittlement effects caused by the catalyst powder.

Temperature (°C)	EHA [80 °C 9h + 120 °C 2h] (MPa)	Sample B (MPa)	Sample C (MPa)
-50	1240	1120	1604
-25	1160	1062	1606
0	1042	980	1647
25	820	780	1574
50	490	410	1290

Table 4.6: Elastic modulus (MPa) of EHA [80 °C, 9h + 120 °C, 2h], Sample B and Sample C in the temperature range between -50 and 50 °C

A large recovery in elastic modulus is gained for the whole self-healing formulation (Sample C) at all the explored temperatures, proving that well-distributed microcapsules, synthesized with a described procedure, contribute to improve the mechanical characteristics of the sample.

Sample C treated up to 200 °C in dynamic mechanical analysis as described, was subjected to morphological investigation.

Sample C was broken, covered with a layer of gold/palladium 250 Å thick and observed by scanning electron microscopy.

A cross-sectional view of our self-healing specimen is reported in the SEM images of Figure 79 which shows that the microcapsules in the epoxy matrix are homogeneously dispersed as evident from the absence of agglomerations.

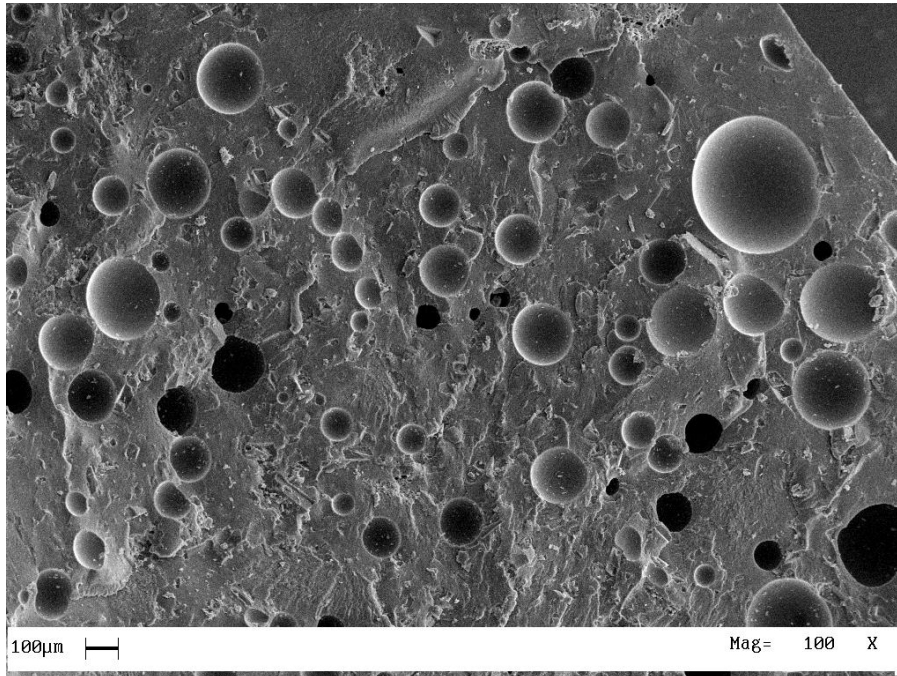


Figure 79: SEM image of self-healing specimen section (Sample C) after DMA up to 200 °C (Magnification 100X)

A magnification made on many areas of the specimen showed a good adhesion of the microcapsules to epoxy matrix (see Figure 80) even after heat treatment at 200 °C made by applying mechanical stress to the material.

We investigated 24 areas of this sample and we found only two areas where the microcapsules appear partially debonded from the matrix (see Figure 81). In Figure 81 we can see the debonding zone and the distribution of catalysts' particles within the matrix (geometric voids left by the catalyst).

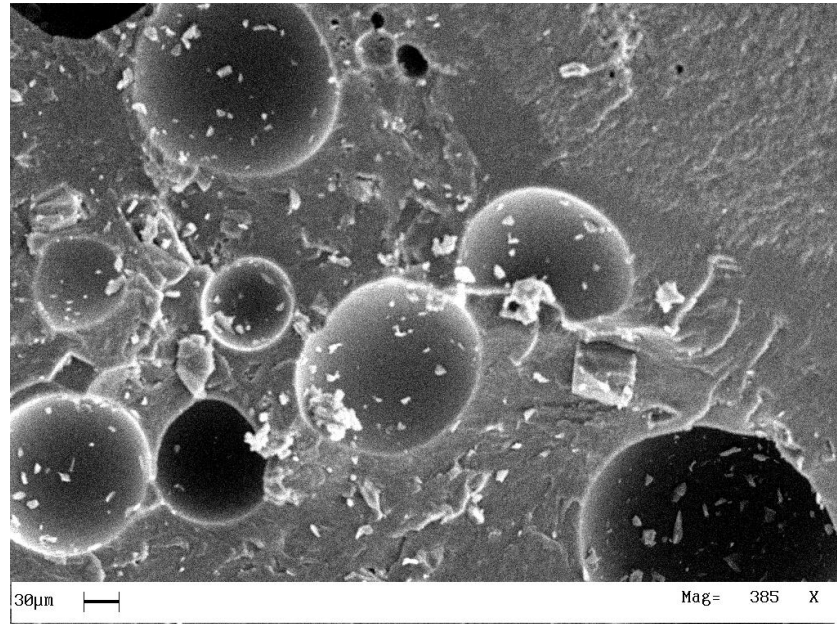


Figure 80: SEM image of an area of self-healing specimen (Sample C) after DMA up to 200 °C (Magnification 385X)

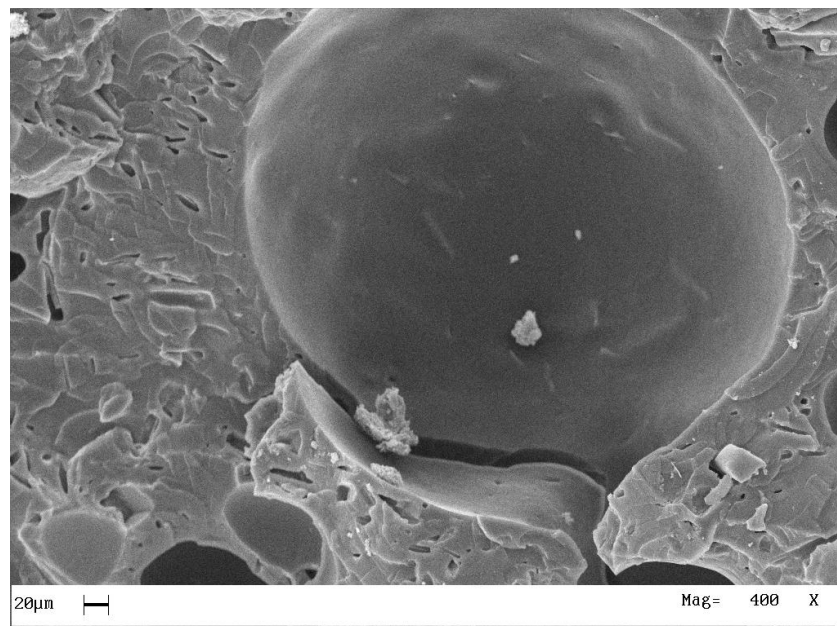


Figure 81: SEM image of a different area of self-healing specimen (Sample C) after DMA up to 200 °C (Magnification 400X)

4.5 Romp Reaction of DCPD with 1st Generation Grubbs' Catalyst.

Tests to assess the reaction rate and yield of ROMP reaction activated by the first generation Grubbs' catalysts on the substrate (DCPD) at different temperatures were conducted. For each test, in a vial equipped with a sealing stopper, 5 mg of G1 catalyst were weighed in dry box. With a graduated syringe, the volume of dicyclopentadiene, to obtain a ratio catalyst/monomer equal to 1:1000, 1:2000 or 1:5000 was added. The reaction was conducted at the set temperature for a predetermined time. The product was recovered from the vial to be weighed in order to evaluate the yield of the reaction.

The conversion percentage for each sample is the ratio between the polymer obtained at the end of reaction and the initial weight of the monomer. The first three tests were performed with a 1:1000 catalyst/monomer ratio (moles) at three different temperatures: 25, 0 and 10°C. To get the right catalyst/monomer ratio, 5 mg of catalyst and a volume of 0.817 ml of dicyclopentadiene have been used (the calculations are given below)

G1(Aldrich) MW = 822.91 g/mol;

DCPD MW = 132.20 g/mol; DCPD density = 0.982 g/ml;

mol G1 = $(5 \times 10^{-3}) / (822.91) = 6.07 \times 10^{-6}$ mol;

$[\text{mol G1}] / [\text{mol DCPD}] = 1/1000 = \text{mol } 6.07 \times 10^{-6} / \text{DCPD mol}$

mol DCPD = 6.07×10^{-3} mol;

g DCPD = 0.802 g

ml DCPD = 0.817 ml.

Test 1

The reaction was carried out for 15 minutes at 25 °C. After this time few drops of ethyl vinyl ether were added and the contents of the vial was poured into a beaker containing methanol to coagulate the polymer. The latter was filtered, washed with CH₂Cl₂, coagulated in methanol and finally dried under vacuum. (coagulation of the polymer with methanol is carried out only when, for the appointed time, the reaction doesn't reaches completion. The yield of the reaction was 34%.

Test 2

The vial containing the G1 catalyst and DCPD was placed in a bath of ice and water at a temperature of 0 °C. The procedure followed is the same as the previous one. The reaction was allowed to go for 5 minutes. At this temperature the DCPD is solid and then the catalyst is unable to carry out the metathesis reaction: this is the reason why is not recovered any product. The yield of the reaction was 0%. This test showed that the self-healing functionality for a such system is not active at 0 °C.

Test 3

The reaction was carried out for 30 minutes at 10 °C and has been not observed metathesis products, even if the DCPD was liquid at that temperature. The self-healing functionality of the formulated composite, based on the metathesis reaction of DCPD activated by the first-generation Grubbs' catalyst, is not active if the damaged material does not exceed the temperature of 10 °C.

Test 4

In this test a catalyst/monomer ratio of 1:2000 was used (5 mg of G1 + 1.63 ml of DCPD). The procedure followed is the same as the previous ones. The reaction was carried out for 20 minutes at 25 °C. In this case, we obtained a yield of 3.7%. This demonstrated that a higher amount of DCPD compared to the amount of catalyst, lowers the yield of the reaction dramatically. Then we can not reduce the amount of the catalyst in the polymer matrix without drastically reducing the efficiency of self-healing functionality.

Test 5

In this test a catalyst/monomer ratio of 1:5000 was used. The procedure followed is the same as the previous ones. The reaction was carried out for 2 h at 25 °C. In this case, we obtained a yield of 3.8%. These results are summarized in Table 4.7 which allows an immediate comparison of data.

Test	Catalyst/monomer ratio	Temperature (°C)	Time (min)	Yields%
1	1:1000 G1/DCPD	25	15	34
2	1:1000 G1/DCPD	0	5	0
3	1:1000 G1/DCPD	10	30	0
4	1:2000 G1/DCPD	25	20	3.7
5	1:5000 G1/DCPD	25	120	3.8

Table 4.7: Reaction rate and yield of ROMP reaction of DCPD with 1st generation Grubbs' catalyst.

4.6 Early Systems: Conclusions

The formulated self-healing composite showed drawbacks related to our technical targets, these mainly regard the thermal stability of the Grubbs' catalyst inside the epoxy resin during the curing cycle and the activation of the metathesis reaction in the working conditions of aircrafts which can reach values of temperatures as low as -50°C .

Remarkable results emerged from this early studied systems are listed below:

- Thermal stability of 1st generation Grubbs' catalyst is reduced in oxidizing atmosphere, infact, a heat treatment of 2.25 h at 150°C causes the decomposition of the catalyst. For this reason it is not possible curing the matrix at high temperatures (technical target: $170/180^{\circ}\text{C}$) necessary for high mechanical properties' systems.
- The self-healing functionality of the formulated composite, based on the metathesis reaction of DCPD activated by the first-generation Grubbs' catalyst, is not active if the damaged material does not exceed the temperature of 10°C . This make the formulated composite to be impractical for structural advanced applications such as aircrafts. In the following parts of this work we will show how to overcome this drawbacks with the choice of an appropriate new healing agent and choice of new ROMP catalysts stable at higher temperatures and active at very low temperatures.

Results and Discussions:

New Systems

5 New Systems: Introduction

Early self-healing systems we have formulated, with the use of dicyclopentadiene (DCPD) as healing agent, have shown their limits particularly at low temperatures. This monomer, in fact, is active in the metathesis reaction only at temperatures greater than 10 °C. This problem has been addressed successfully using a new bifunctional healing agent, 5-ethylidene-2-norbornene (ENB), sterically more tensioned respect DCPD and with a lower melting point. In this section we describe the results on:

- the characterization of microcapsules filled with new healing agent ENB;
- the analysis of the catalytic activity (kinetic and thermodynamic) of first generation (G1) and second generation (G2) Grubbs' catalysts in Ring Opening Metathesis Reaction (ROMP) with 5-ethylidene-2-norbornene (ENB) as substrate.

As for Early Systems, the epoxy matrix used was a blend of diglycidyl ether of bisphenol A (EPON 828) and a high molecular-weight epoxy flexibilizer, HELOXY 71.

The curing agent is Phenol, 2,4,6-tris[(dimethylamino) methyl] (Ancamine K54).

The scheme of the formulation of New Systems is shown in Figure 82 (a) and (b) (for chemical structures and details of compounds see Materials section).

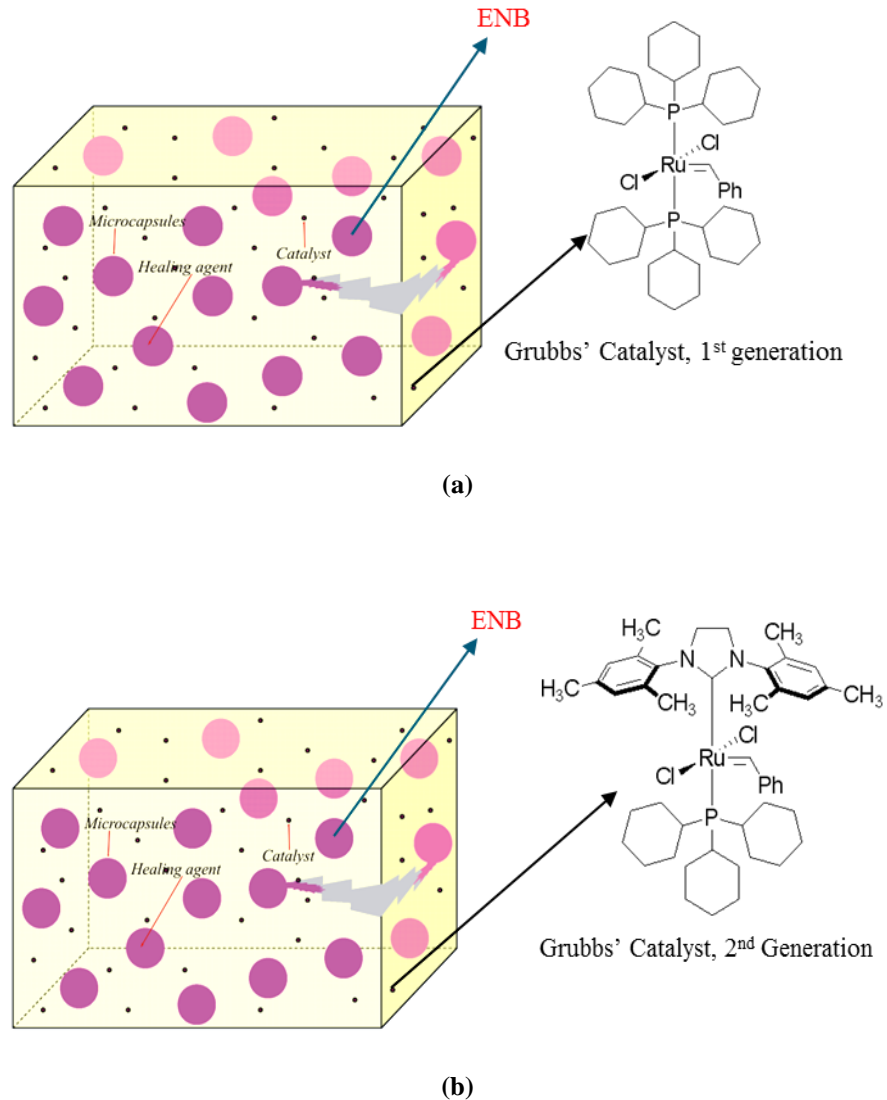


Figure 82: Self-healing systems: (a) EHA + G1 + ENB filled microcapsules; (b) EHA + G2 + ENB filled microcapsules

As for Early Samples, EHA matrix was obtained by mixing Epon 828 with Heloxy 71 flexibilizer at the concentration of 63%: 37% (by wt) epoxide to flexibilizer. Ancamine K54 was added at the concentration of 10:100 (by wt) hardener to mixture (Epon 828 and Heloxy 71).

5.1 Microcapsules Characterization

The microcapsules, with the outer shell composed of poly(urea-formaldehyde) and the inner shell of ethylene maleic anhydride copolymer (EMA) were prepared by *in situ* polymerization in an oil-in-water emulsion in accord with a procedure already described in previous chapter.

The only change, with respect to the aforementioned synthesis procedure, consisted of using ENB instead of DCPD. According to such a procedure, a desired dimension range can be selected by a suitable variation of the process parameters during the synthesis stage, and/or with the use of molecular sieves

Figure 83 and 84 show a sample of microcapsules at two different magnifications: most relevant fraction of capsules has 1-2 μm diameter.

The microcapsules have a spherical and rough shape. Roughness, in contrast to the debris is a desirable morphological characteristic to achieve greater adhesion of capsules with the epoxy matrix in the formulation of the self-healing composite.

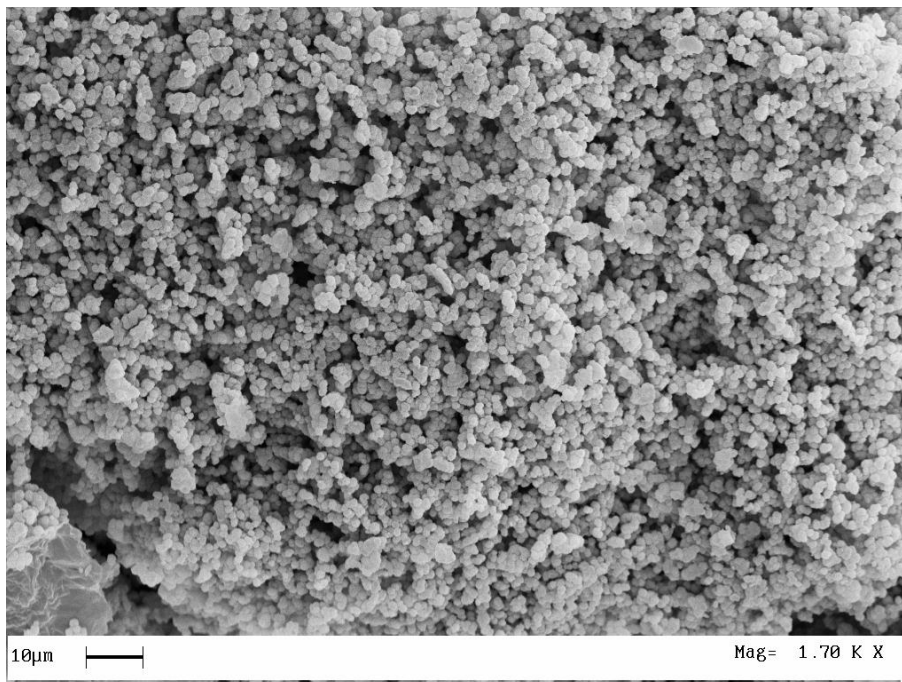


Figure 83: Microcapsules filled of ENB, 1700X magnifications

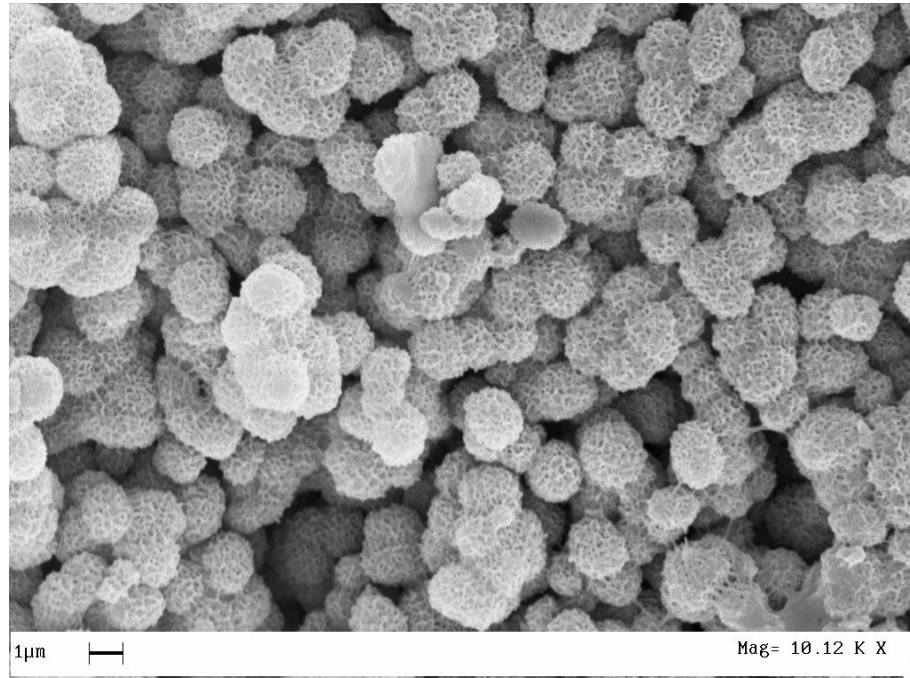


Figure 84: Microcapsules filled of ENB, 10120X magnifications

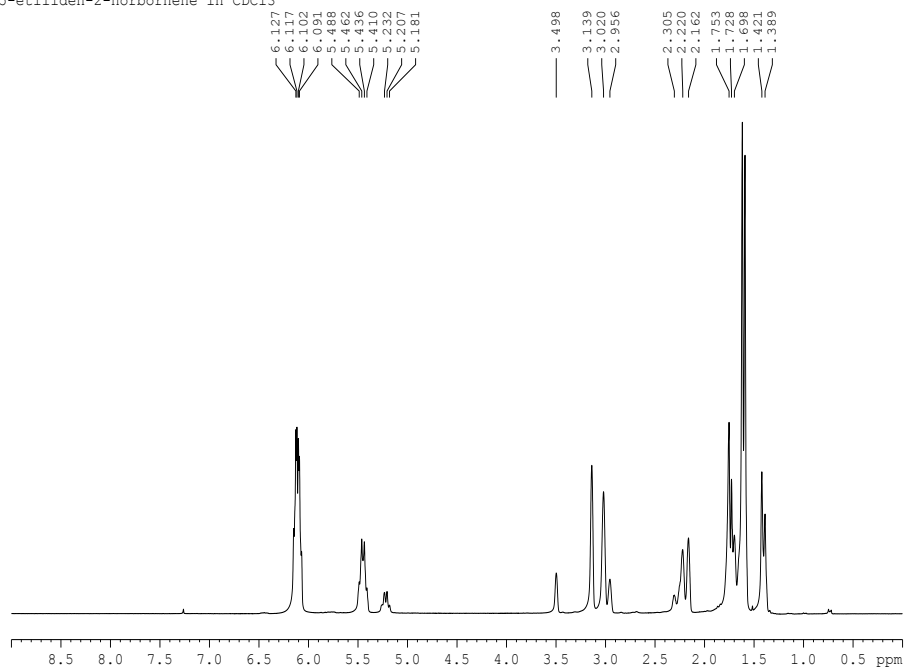
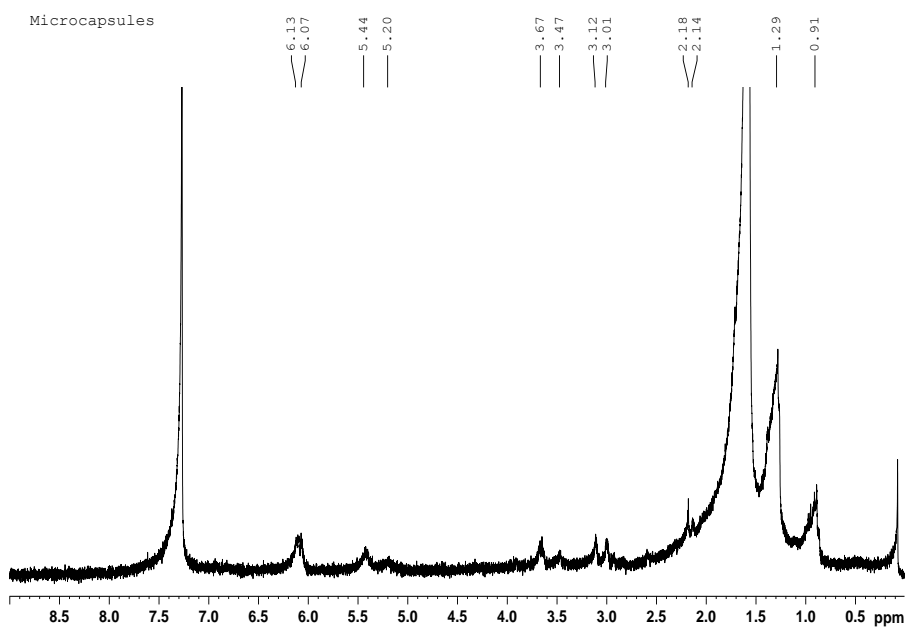
5.1.1 Check of ENB healing agent content: ^1H NMR Analysis

As previously done for DCPD filled microcapsules, we have checked the healing agent (ENB) content in the new synthesized microcapsules with ^1H NMR spectroscopy.

The microcapsules were pulverized in a mortar and transferred to a vials containing deuterated chloroform as solvent (CDCl_3). Everything was left under stirring for about half an hour. After this time, the microcapsules were filtered and the soluble was subjected to ^1H NMR analysis.

Figure 85 shows the ^1H NMR spectrum of 5-ethylidene-2-norbornene in CDCl_3 solvent.

Figure 86 refers to the the ^1H NMR spectrum of soluble part of microcapsules.

5-ethyliden-2-norbornene in CDCl₃**Figure 85:** ¹H NMR spectrum of 5-ethylidene-2-norbornene in CDCl₃ solvent**Figure 86:** ¹H NMR spectrum of soluble part of microcapsules

The spectrum, in Figure 86 of the soluble part of microcapsules, shows all the signals related to the presence of 5-ethylidene-2-norbornene confirming that the encapsulation of the healing agent was successfully achieved.

From Figure 87, the overlapping of spectra of Figure 85 and Figure 86, the presence of monomer in the microcapsules is evident: the signals of the pure monomer overlap with the extract from the microcapsules. Additional signals in the spectrum of Figure 86 could be due to molecules forming the shell of the microcapsules "dragged" by the solvent.

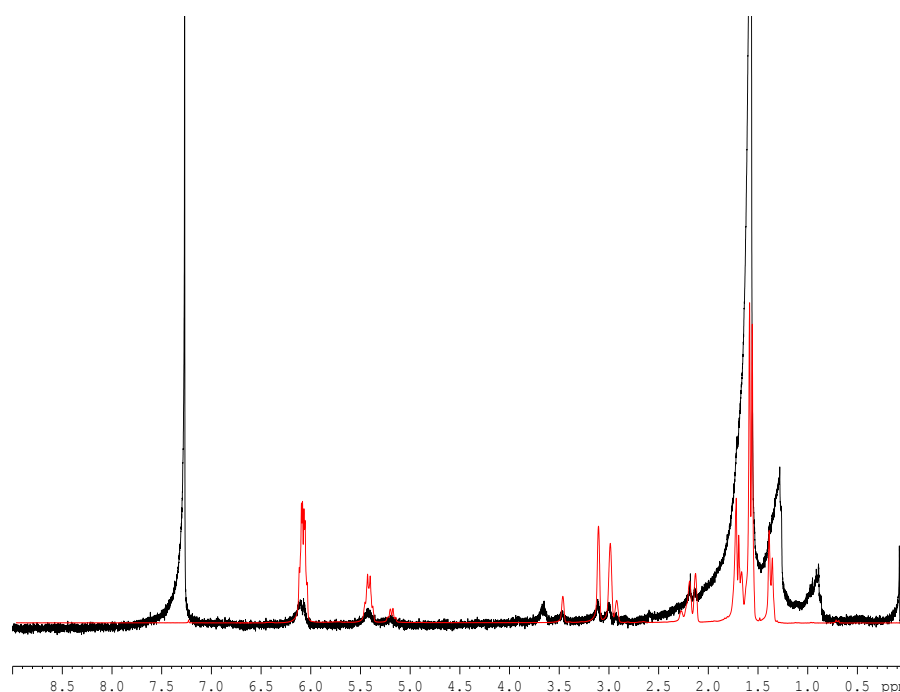


Figure 87: ^1H NMR spectrum of soluble part of microcapsules and 5-ethylidene-2-norbornene

5.1.2 Microcapsules filled with ENB: Thermal Analysis (TGA-DSC)

Thermogravimetric curves of the microcapsules in air (red line) and nitrogen (black line) are shown in Figure 88. Thermal stability in air and nitrogen of the microcapsules is similar up to 280 °C, dropping suddenly in weight around 200 °C. This sudden weight loss is due to the explosion of microcapsules and rapid evaporation of the

polymerizer agent. Above 280 °C, the degradation in air is faster with respect to nitrogen because of the oxygens' oxidized effects. The degradation in air in the temperature range of 250 – 560 °C occurs by fragmentation of the polymer structure shell (urea/formaldehyde) and elimination of ammonia, amines, CO₂ etc. The last two steps of degradation involve cyclisation reactions which form structures more thermally stable than the original ones as already found for thermal degradation of urea/formaldehyde polycondensate. In air the more thermally stable structures which still remain degrade at about 500 °C.

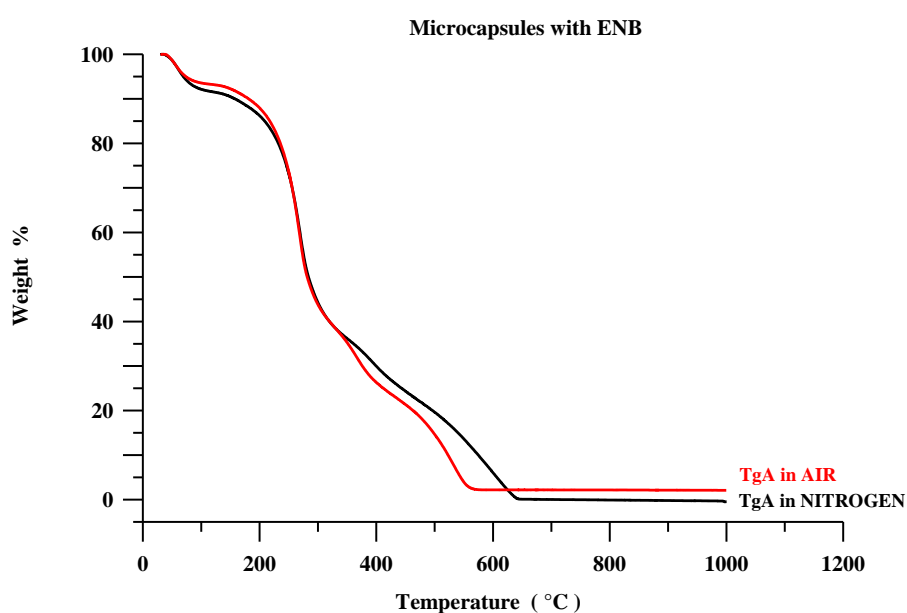


Figure 88 TGA curves in air (red) and nitrogen (black) of Microcapsules filled with ENB

The DSC thermogram of the microcapsules, (Figure 89) shows two endothermic peaks; a small one between 50-120 °C and a large one centered at 260 °C. The first endothermic peak is due to impurities of water and free formaldehyde progressively eliminated during the dynamic thermal treatment between 50-120 °C. In fact, the formaldehyde is one of the components used for the synthesis of the microcapsule walls based on the reaction of urea with formaldehyde. The peak at a higher temperature, between 200 and 270 °C, corresponding to the first step of weight loss in the thermogravimetric curve, is due to the explosion of microcapsules and the evaporation of the polymerizer agent ENB. Degradation of the urea/formaldehyde

shell started at 200 °C with the increase of the inside pressure of microcapsules.

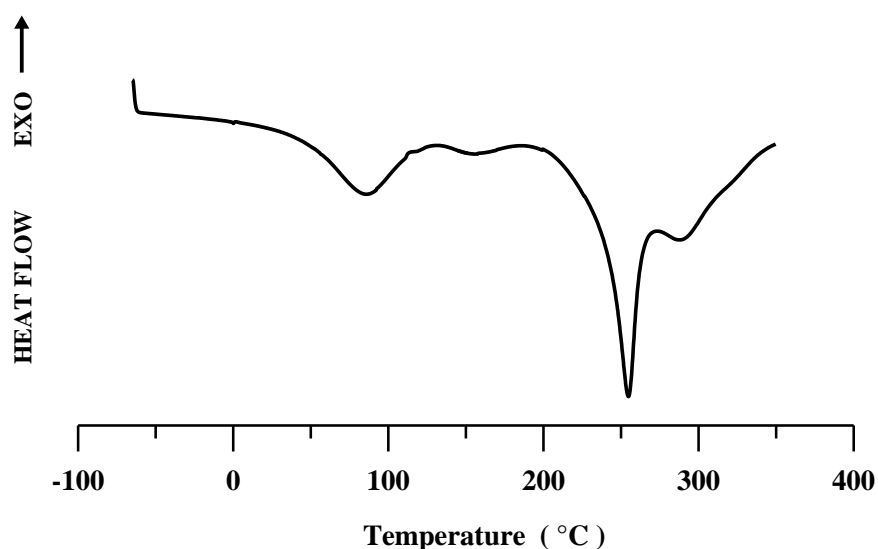


Figure 89 DSC curve of Microcapsules filled with ENB

5.2 Romp Reaction of ENB with 1st Generation Grubbs' Catalyst.

Test 1

In a vial equipped with a sealing stopper, 5 mg of G1 catalyst were weighed in dry box; with a graduated syringe the volume of 5-ethylidene-2-norbornene, to obtain a ratio catalyst/monomer equal to 1:1000 was added. The reaction was carried out at 25 °C for 30 sec. The product was recovered from the vial to be weighed in order to evaluate the yield of the reaction: 725 mg of product are recovered. The Yield of reaction is calculated as the ratio between the polymer obtained at the end of reaction and the initial weight of the monomer. The calculations are given below:

G1(Aldrich) MW = 822.91 g/mol;

5-ethylidene-2-norbornene MW 120.12 g/mol;

5-ethylidene-2-norbornene density = 0.893 g/ml;

mol cat. G1 = $(5 \cdot 10^{-3} \text{g}) / (822.91 \text{g mol}^{-1}) = 6.07 \cdot 10^{-6} \text{mol}$

$[\text{mol G1}]/[\text{mol 5-ethylidene-2-norbornene}] = 1/1000 =$
 $6.07 \cdot 10^{-6} [\text{mol G1}]/6.07 \cdot 10^{-3} [\text{mol 5-ethylidene-2-norbornene}]$
 $\text{mol 5-ethylidene-2-norbornene} = 6.07 \cdot 10^{-3} \text{ mol}$
 $\text{g 5-ethylidene-2-norbornene} = 0.729 \text{ g}$
 $\text{ml 5-ethylidene-2-norbornene} = 0.816 \text{ ml.}$

Test 2,3,4,5 and 6

The experimental procedure followed for these tests is the same as the previous one, but the reaction was carried out at 0, -10, -20, -30, -40 °C respectively.

Test 7 and 8

Tests 7 and 8 were performed by varying the catalyst / monomer ratio in order to evaluate the influence of this ratio on the rate and the yield of metathesis reaction. The catalyst / monomer ratio for two tests are 1:2000 and 1:5000 respectively. The reaction was carried out at 25 °C. The results of all tests are summarized in Table 5.1.

Test	Catalyst/monomer ratio	Temperature (°C)	Time (min)	Yields%
1	1:1000 G1/ENB	25	0.5	100
2	1:1000 G1/ENB	0	13	100
3	1:1000 G1/ENB	-10	60	17
4	1:1000 G1/ENB	-20	1440	79
5	1:1000 G1/ENB	-30	1440	74
6	1:1000 G1/ENB	-40	1440	0
7	1:2000 G1/ENB	25	0.5	100
8	1:5000 G1/ENB	25	0.5	100

Table 5.1: Reaction rate and yield of ROMP reaction of ENB with 1st generation Grubbs' catalyst

The Table 5.1 shows that the metathesis reaction of G1 catalyst with ENB as substrate is active even at -30 °C, whereas at -40 °C there is no longer activity.

This excellent result allows us to formulate systems with self-healing functionality active even at a temperature of 30 °C sub-zero.

Another useful information that emerges from analysis of data is that at room temperature (for ratios catalyst/monomer investigated) did not record any change in the speed and yield of the metathesis reaction with changes in the molar ratio of catalyst and monomer (see tests 1, 7 and 8).

A comparison with the DCPD (see Table.4.7) used for the formulation of the first self-healing systems, highlights the many advantages of new healing agent ENB:

- with respect to DCPD, the ENB allows the self-healing functionality to work in a temperature range wider of 40 °C. In fact, with the G1 catalyst, the metathesis reaction of DCPD is not active if the temperature does not exceeds 10 °C.

- ROMP of ENB is realized with extremely fast reaction rate with respect to DCPD: at 25 °C, the yield reaction reaches the value of 100% after a reaction time of 30 seconds (in the case of DCPD, the yield is about 34% after a reaction time of 15 minutes).

- In the case of DCPD there is a strong variation in the speed and yield of the metathesis reaction at varying molar ratio of catalyst and monomer (compare tests 4 and 5 of Table 4.7 with the tests 7 and 8 of Table 5.1). In the case of DCPD decreasing the amount of catalyst compared to the monomer there is a significant loss in performance and speed of the metathesis reaction. This is not the case for ENB.

This result allows to formulate a self-healing system using a smaller amount of catalyst G1.

5.3 Romp Reaction of ENB with 2nd Generation Grubbs' Catalyst.

We carried out tests to assess the reaction rate and yield of ROMP reaction activated by second generation Grubbs' catalyst with the substrate ENB at different temperatures:

second generation Grubbs' catalyst (G2) Aldrich MW 848.98 g/mol;
5-ethylidene-2-norbornene MW 120.12 g/mol;

5-ethylidene-2-norbornene density = 0.893 g/ml;
 mol cat. G2 = $(5 \cdot 10^{-3} \text{ g}) / (848.98 \text{ g mol}^{-1}) = 5.88 \cdot 10^{-6} \text{ mol}$
 $[\text{mol G2}] / [\text{mol 5-ethylidene-2-norbornene}] = 1/1000 =$
 $= \text{mol } 5.88 \cdot 10^{-6} / 5\text{-ethylidene-2-norbornene mol};$
 mol 5-ethylidene-2-norbornene = $5.88 \cdot 10^{-3} \text{ mol};$
 g 5-ethylidene-2-norbornene = 0.707 g;
 ml 5-ethylidene-2-norbornene = 0.792 ml.

The results of all tests performed with ENB and second generation Grubbs' catalyst are summarized in Table 5.2

Test	Catalyst/monomer ratio	Temperature (°C)	Time (min)	Yields%
1	1:1000 G2/ENB	25	1	99
2	1:1000 G2/ENB	0	50	100
3	1:1000 G2/ENB	-20	60	79
4	1:1000 G2/ENB	-30	1440	74

Table 5.2: Reaction rate and yield of ROMP reaction of ENB with 2nd generation Grubbs' catalyst

As well as for G1, also for second generation Grubbs' catalyst (G2) the ROMP reaction with ENB is active up to -30 °C.

A comparison between the yield and rate reaction of the two catalysts G1 and G2 with ENB as substrate was performed with a 1:1000 catalyst/monomer ratio. Table 5.3 shows these results.

We can notice that, at room temperature G1 and G2 have both high catalytic activity and the yields are 100% in short times.

At 0 °C G1 have a faster reaction rate respect with G2, whereas there is no difference between the two catalysts at lower temperatures (-20 and -30 °C).

Catalyst	Catalyst/monomer ratio	Temperature (°C)	Time (min)	Yields%
Grubbs I	1:1000 (ENB)	25°	0,5	100
Grubbs I	1:1000 (ENB)	0°	13	100
Grubbs I	1:1000 (ENB)	-20°	1440	79
Grubbs I	1:1000 (ENB)	-30°	1440	74
Grubbs II	1:1000 (ENB)	25°	1	99
Grubbs II	1:1000 (ENB)	0°	50	100
Grubbs II	1:1000 (ENB)	-20 °C	1440	79
Grubbs II	1:1000 (ENB)	-30 °C	1440	74

Table 5.3: Reaction rate and yield of ROMP reaction of ENB with G1 and G2 catalysts

5.4 Thermolytic Decomposition of 2nd Generation Grubbs' Catalyst: ¹H NMR Analysis

We report most significant data of thermolytic decomposition of 2nd generation Grubbs' catalyst (G2) [*1,3-Bis-(2,4,6-trimethylphenyl)-2(imidazolidinylidene)(dichlorophenylmethylene)(tricyclohexylphosphine)ruthenium*].

This catalyst was characterized by ¹H NMR analysis after thermal treatments in inert atmosphere or in air. The solvent used to obtain ¹H NMR spectra was TCDE. Results are listed in Table 5.4.

Temperature (°C)	Time (h)	Initial state of catalyst	Environment	Catalyst state (after treatment)
120	24	solid	nitrogen	Not decomposed
150	3.66	solid	nitrogen	Not decomposed
130	5	solid	air	Not Decomposed
150	1	solid	air	Not decomposed
180	1	solid	air	Decomposed

Table 5.4: Summary results on thermolytic decomposition in air and nitrogen atmosphere of 2nd generation Grubbs' catalyst

Table 5.5 shows the thermolytic decomposition of G2 catalyst inside the epoxy matrix EHA, after three different curing cycle:

Sample F: EHA + 5% G2 + 10% Cap (ENB) cured up to 120 °C

Sample G: EHA + 5% G2 + 10% Cap (ENB) cured up to 150 °C

Sample J: EHA + 5% G2 + 10% Cap (ENB) cured up to 180 °C

Sample	Curing Cycle Temperature (time)	Catalyst state after treatment
F	80 °C (9h) + 120 °C (2h)	Not decomposed
G	80 °C (9h) + 150 °C (2h)	Not decomposed
J	80 °C (9h) + 180 °C (2h)	Decomposed

Table 5.5: Summary results on thermolytic decomposition of 2nd generation Grubbs' catalyst embedded in epoxy matrix for different curing cycles

We can notice that unlike G1, G2 catalyst has great stability in air even after a thermal treatment at 150 °C. However, when G2 catalyst is in the presence of functional groups of the epoxy matrix of self-healing composite, shows a stability very similar to the G1 and undergoes thermal degradation, which disables it, just as for the G1.

5.5 New Systems: Conclusions

Microcapsules were prepared with the “core” of 5-ethylidene-2-norbornene (ENB). Proton magnetic resonance confirmed that the encapsulation of this healing agent has been successfully achieved.

The ENB healing agent allows to formulate self-healing systems with a healing functionality active even at a temperature of $-30\text{ }^{\circ}\text{C}$ with two different catalysts G1 and G2. With respect to DCPD, the ENB allows the self-healing functionality to work in a temperature range wider of $40\text{ }^{\circ}\text{C}$. In fact, with the G1 catalyst, the metathesis reaction of DCPD is not active at temperatures equal or below $10\text{ }^{\circ}\text{C}$.

With ENB as substrate for Romp reaction, at room temperature and at $0\text{ }^{\circ}\text{C}$, G1 and G2 catalysts have high catalytic activity (conversions of 100% in a very small time); at these temperatures G1 have a reaction rate faster than G2. At lower temperatures (-20 , $-30\text{ }^{\circ}\text{C}$) there is no difference between reaction rates of G1 and G2.

Catalysts G1 and G2 are stable during curing process of epoxy matrix at temperatures up to $150\text{ }^{\circ}\text{C}$.

However, despite this interesting results, the limitations related our technical targets remain:

- self-healing functionality must be active at at low working temperatures of aircrafts which can reach values as low as $-50\text{ }^{\circ}\text{C}$.
- Curing temperature required for high mechanical properties' systems must be in the range of $170\text{ }^{\circ}\text{C}$ - $180\text{ }^{\circ}\text{C}$.

In the next chapter we shall see that these limitations have been overcome with the use of new first and second generation Hoveyda-Grubbs' catalysts, resistant to higher temperatures and developed to withstand critical environments.

Results and Discussions:

Latter Systems

6 Latter Systems: Introduction

In this section we will show the results on the last self-healing system analyzed.

During my research different formulations were tested which have been gradually improved to suit performance requirements for a structural advanced material to be applied to aeronautical vehicles.

All previous systems, with first and second generation Grubbs' catalysts and DCPD or ENB as substrate (in Romp reaction) showed great limitations regards thermal stability of the catalysts under optimal curing conditions of the epoxy resins and efficiency of self-healing functionality at operating temperatures of the aircrafts.

Early self-healing systems, we have formulated with the use of the dicyclopentadiene, have shown their limitations particularly at low temperatures: the monomer is not active in metathesis reaction at temperatures equal or below 10 °C.

This problem has been successfully tackled with the proposal of the new agent healing, 5-ethylidene-2-norbornene. For the system which involves the use of ENB filled microcapsules, first-and second-generation Grubbs' catalysts were active even at low temperatures. In particular, it was possible to have a self-healing functionality active even at -30 °C. However, this noticeable result does not resolve the critical issues relating to the stability of the catalysts at high curing temperatures. For this reason we decided to test new Romp catalysts, more thermally stable and developed for more critical environments: first and second generation Hoveyda-Grubbs' catalysts: HG1 [Dichloro(*o*-isopropoxyphenylmethylene) (tricyclohexylphosphine)ruthenium(II)] and HG2 [(1,3-Bis-(2,4,6-

trimethylphenyl)-2-imidazolidinylidene)dichloro(o-isopropoxyphenylmethylene) ruthenium].

The design of latter studied systems consists of an epoxy matrix, microcapsules filled with, 5-ethylidene-2-norbornene (ENB) as healing agent and 1st or 2nd generation Hoveyda Grubbs' catalysts (Figure 90).

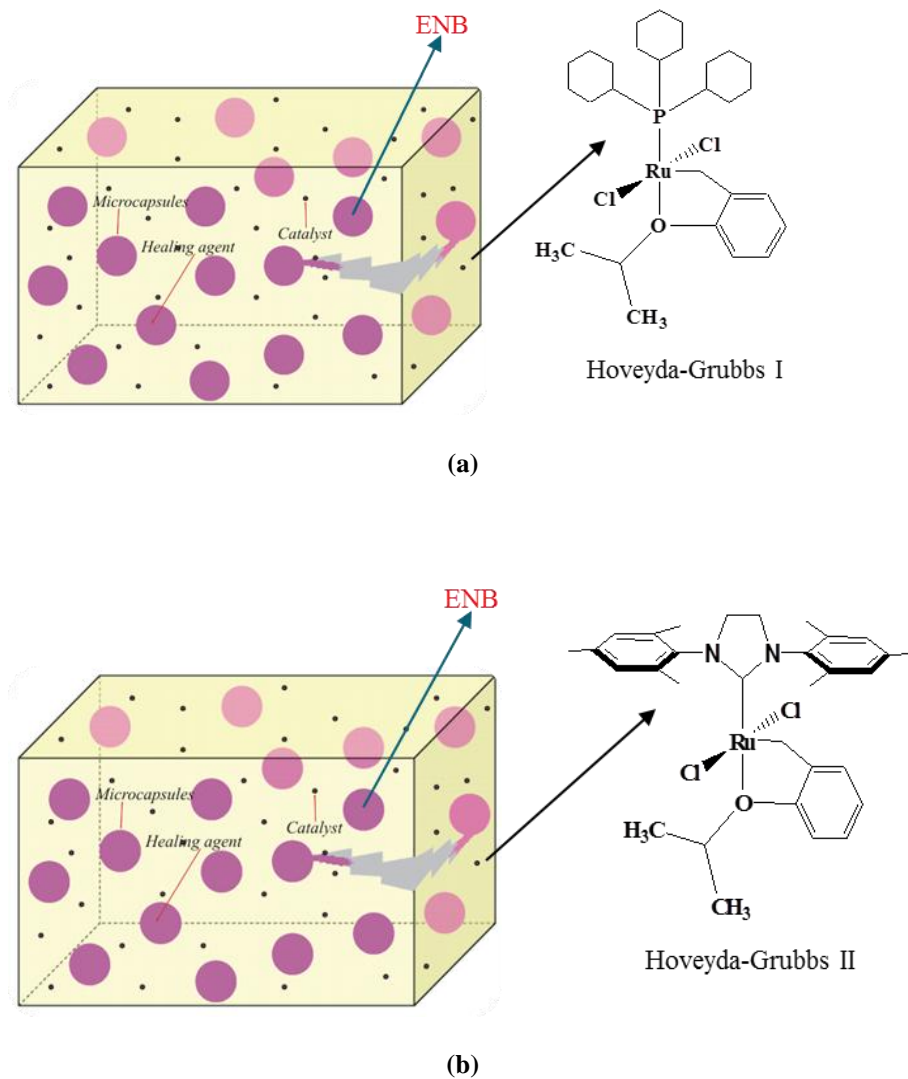


Figure 90: Self- healing systems: (a) Epoxy matrix + HG1 + ENB filled microcapsules; (b) Epoxy matrix+ HG2 + ENB filled microcapsules

At first, the epoxy matrix used was a blend of diglycidyl ether of bisphenol A (EPON 828) and flexibilizer HELOXY 71.

Only for most promising systems, Heloxy 71 was replaced with a different flexibilizer 1-4 Butandioldiglycidylether (BDE), which reduces viscosity of uncured matrix and also improve mechanical properties of final composite (see Material section for details).

Phenol, 2,4,6-tris[(dimethylamino) methyl] (Ancamine K54) was the curing agent for all matrix formulations.

6.1 Morphology of Hoveyda Grubbs' Catalys HG1 and HG2

At the same catalyst percentage in the formulation, the higher efficiency of self healing is reached with a high surface area/mass of the particles ratio. For this purpose, for old Grubbs' catalysts, morphological investigation was carried out through scanning electron microscopy to evaluate the size of catalysts' particles and thus the suitability of the powders in the self-healing systems.

The catalyst particles were found to have a significantly large size for their direct use in the final formulation of the resin; to overcome this drawback, the catalyst powders were pulverized into particles of smaller size (directly from solid state), by mechanical agitation through the use of a small magnet.

The particles of the first generation Hoveyda-Grubbs' catalyst are smaller than those corresponding to the Grubbs' catalyst and their size seem fairly homogeneous, so no treatment was done.

To get a qualitative idea of dispersion of particles' size, Figure 91 and 92 show the investigations performed at comparable magnifications of two different samples of HG1.

Figure 93 shows SEM image of the HG1 catalyst at lower magnifications: we can see that the size of the particles are quite homogeneous, and only few catalysts' particles have larger size.

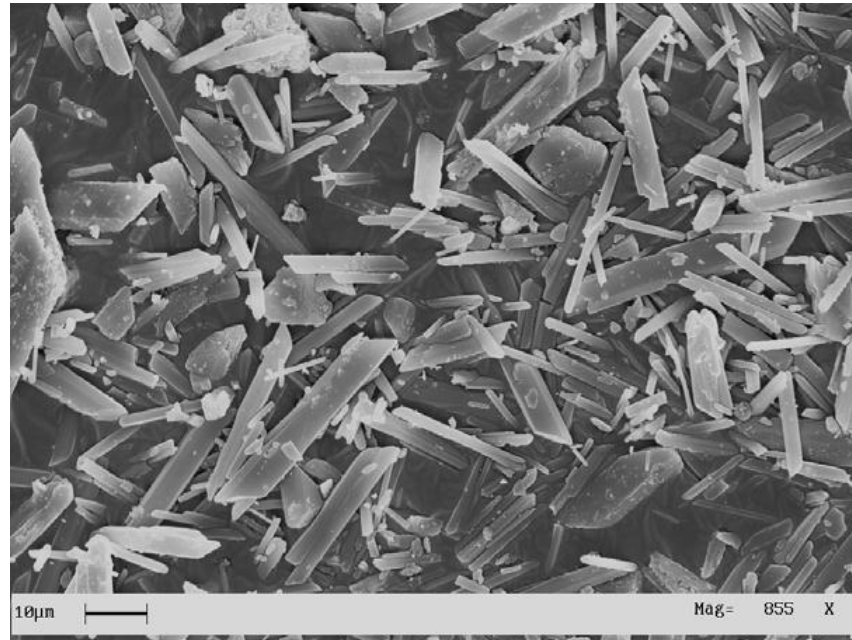


Figure 91: SEM image of a sample of HG1 powders (Magnification 855X)

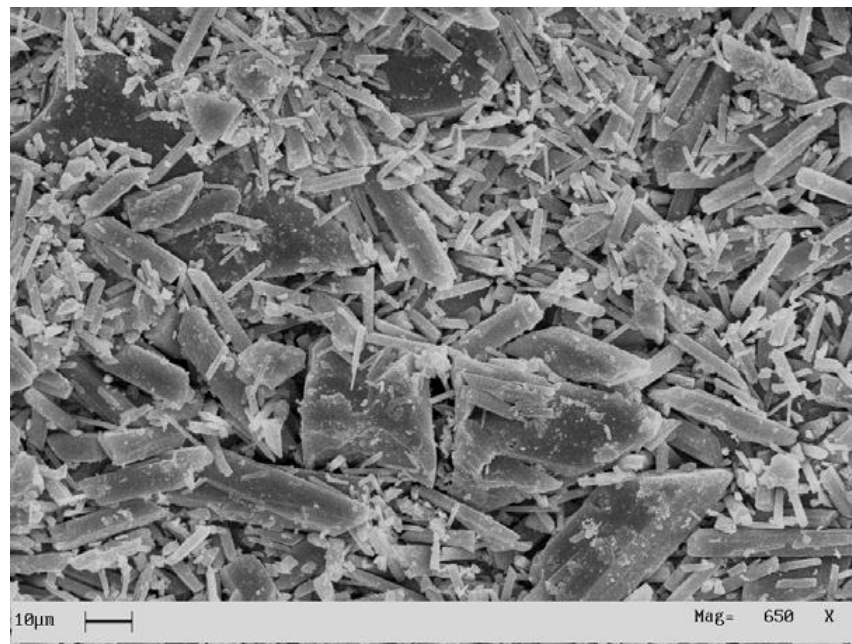


Figure 92: SEM image of a different sample of HG1 powders (Magnification 650X)

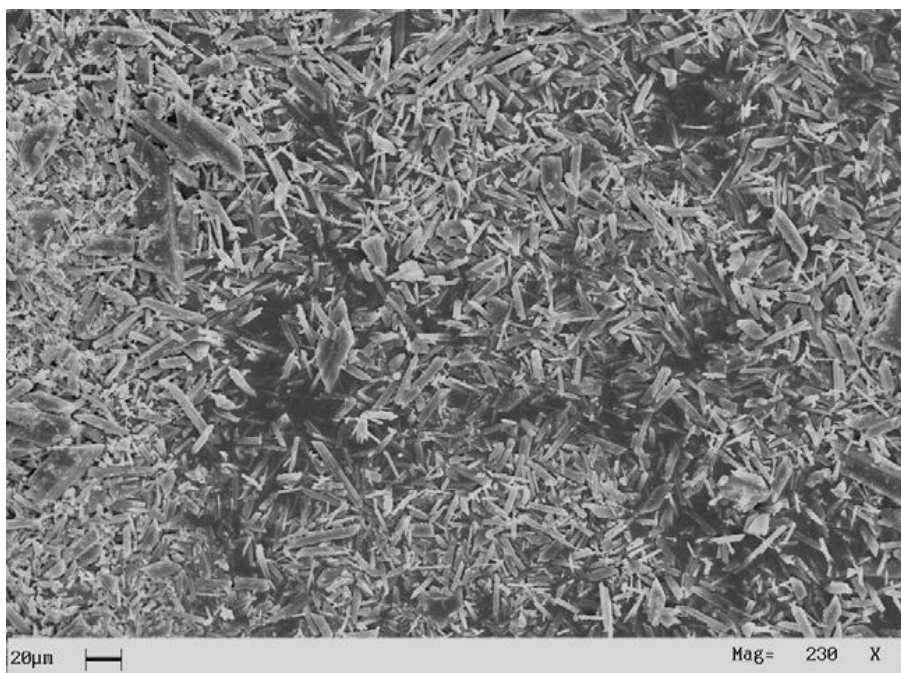


Figure 93: SEM image of HG1 powders (Magnification 230X)

In Figure 94 and 95 SEM images of second generation Hoveyda-Grubbs' catalyst (HG2) powders are reported.

HG2 powders consist of particles with larger size respect HG1 powders.

The size distribution of HG2 particles is not homogeneous as the particles of HG1. However no treatment of size reduction was done for HG2 particles.

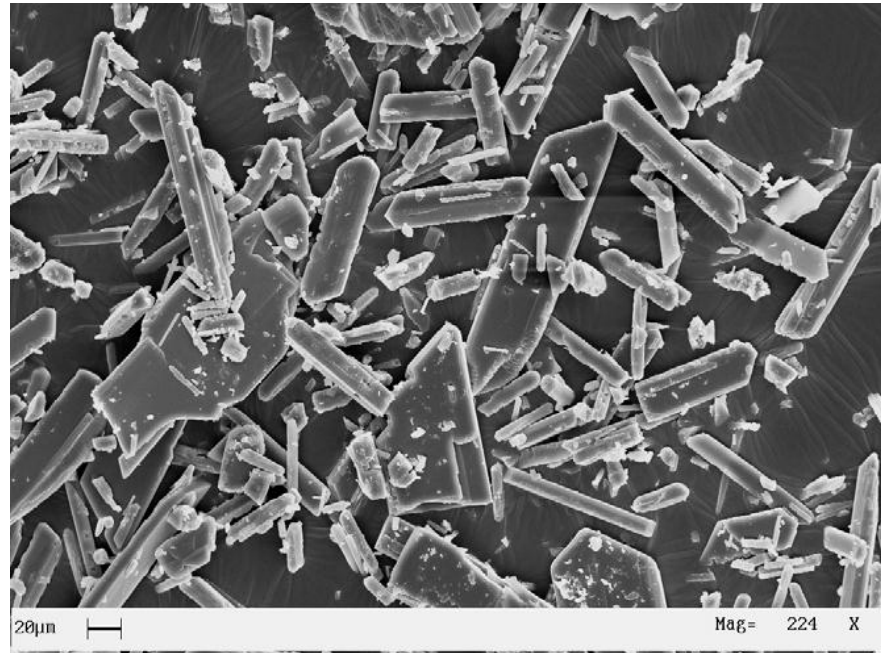


Figure 94: SEM image of HG2 powders (Magnification 224X)

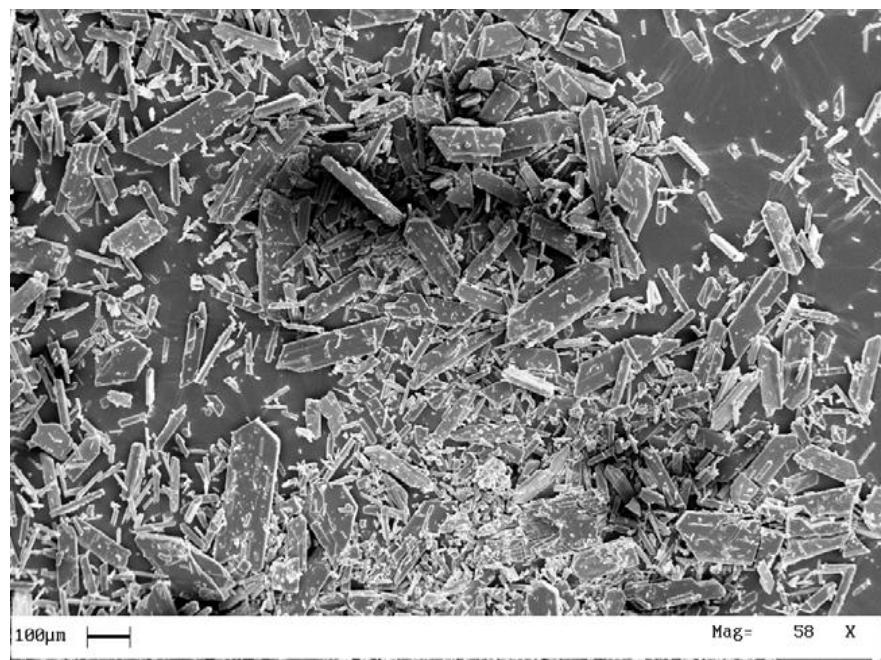


Figure 95: SEM image of HG2 powders (Magnification 58X)

6.2 Evaluation of Thermal Stability of Hoveyda Grubb's Catalysts, HG1 and HG2

6.2.1 Thermogravimetric Analysis (TGA)

Thermal stability of HG1 and HG2 catalysts was first evaluated by thermogravimetric analysis for the two catalysts in the form of thin powder. Thermogravimetric curves obtained in a dry air atmosphere in the temperature range between 0-1000 °C are reported in Figure 96; the graph shows also the thermogravimetric curves of G1 and G2 catalysts for comparison. The insert is an enlarged image of the thermogravimetric curves in the range 160-300 °C.

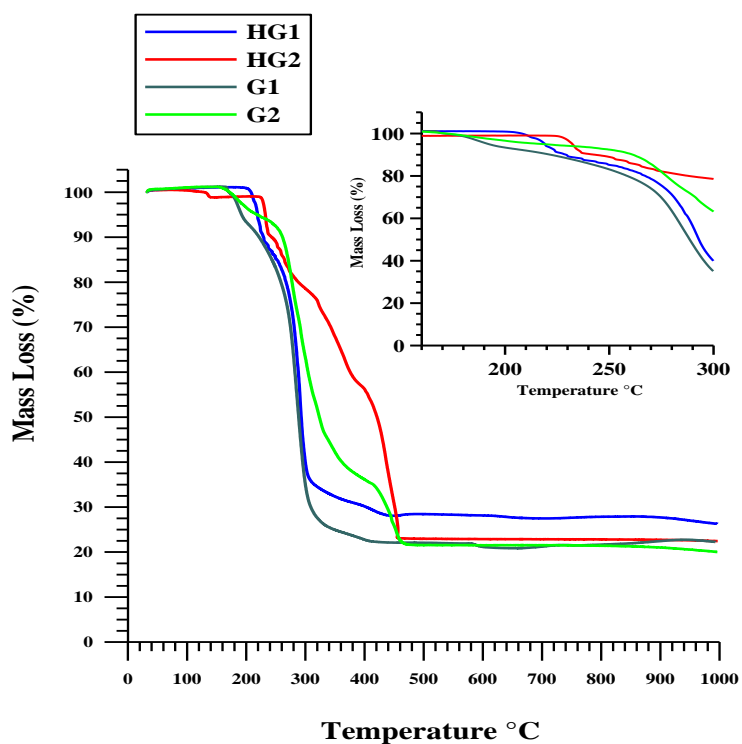


Figure 96 TGA curves obtained in a dry air atmosphere in the temperature range of 0°C–1000 °C. Insert: TGA curves in the temperature range of 150 °C–300 °C

From TGA curves we can see that for Hoveyda-Grubbs' catalysts HG1 and HG2, mass loss at the beginning is observed at 205 °C and 225 °C respectively, whereas for both the Grubbs' catalysts G1 and G2, mass loss at the beginning falls in the temperature range between 165-170 °C. Hoveyda-Grubbs' catalysts exhibit improved thermal stability with respect to Grubbs' catalysts and, the higher temperature of beginning degradation is found for HG2 (~20 °C greater than HG1). From these data it could be deduced that the HG2 catalyst imposes less critical limitations in the processing and curing of self-healing epoxy matrix and, for this reason, it was chosen among the Hoveyda-Grubbs' catalysts to be studied as a potential candidate for a self-healing system.

6.2.2 Thermolytic decomposition of HG1 and HG2 - ¹H NMR Analysis

The thermolytic stability of first and second generation Hoveyda-Grubbs' catalysts was evaluated in air and nitrogen atmosphere with the catalysts in powder form, kept at different temperatures directly from the solid state, which was the form they were dispersed in the epoxy mixture to manufacture self-healing systems. The catalyst powder, after the thermal treatment, was dissolved in the deuterated solvent (deuterated chloroform – CDCl₃) immediately before the ¹H NMR spectra recording. In the Table 6.1 are shown the results obtained from analysis of NMR spectra of the two catalysts.

Catalyst	Time (h)	Temperature (°C)	Environment	State after treatment
HG1	3	150	air	Not Decomposed
HG2	3	150	air	Not Decomposed
HG1	2	180	nitrogen	Not Decomposed
HG2	2	180	nitrogen	Not Decomposed
HG1	2	180	air	Not Decomposed
HG2	2	180	air	Not Decomposed

Table 6.1 Results of NMR spectra in air and Nitrogen for HG1 and HG2

In Table 6.2 the results of thermolytic decomposition of first and second generation Grubbs' catalyst are compared with the data reported for HG1 and HG2.

Catalyst	Time (h)	Temperature (°C)	Environment	State after treatment
G1	4	150	nitrogen	Not Decomposed
G2	4	150	nitrogen	Not Decomposed
G1	3	150	air	Decomposed
G2	1	150	air	Not Decomposed
G2	1	180	air	Decomposed
HG1	2	180	air	Not Decomposed
HG2	2	180	air	Not Decomposed

Table 6.2 Comparison of thermolytic decomposition results for HG1 and HG2, with G1 and G2

We can notice that Hoveyda-Grubbs' catalysts show exceptional stability after a thermal treatment at 180 °C in air atmosphere, but Grubbs' catalysts are completely decomposed. The thermal stability of the catalysts was also analyzed for the powder embedded inside the epoxy matrix (after the curing process at high temperatures). The catalysts were extracted by chloroform from the epoxy matrix and analyzed by ¹H NMR spectroscopy. In particular, the epoxy matrices containing the different catalysts were cured at high temperatures between 150 and 180 °C.

The matrix EHA was obtained by mixing Epon 828 with Heloxy 71 flexibilizer at a concentration of 63%: 37% (by wt) epoxide to flexibilizer. Ancamine K54 was added at a concentration of 10:100 (by wt) hardener to mixture (Epon 828 and Heloxy 71). Catalysts' powders were homogeneously dispersed in the matrix. All the samples were polymerized by a two-stage curing cycle: a first isothermal stage at 125 °C for 1 hour and a second isothermal stage with higher temperatures (up to 180 °C) for 2 hours. These results are summarized in Table 6.3. As we already know from previous experiments, Grubbs' catalysts are extraordinarily tolerant toward the

different kinds of functional groups of the epoxy formulations at high temperatures up to 150 °C. It is interesting to observe that Grubbs' 1st generation catalyst (decomposed in air at 150 °C) is stable if the thermal treatment at 150 °C is imposed on the catalyst powder embedded in the epoxy matrix. Despite the unexpected and exceptional stability of the Grubbs' catalysts, it is not possible to formulate self-healing systems related to ring-opening metathesis polymerization of the healing agent when a curing temperature of 180 °C is scheduled.

Sample	Curing cycle Temperature (Time)	Catalyst state after treatment
EHA-G1 (150)	125 °C (1h) + 150 °C (2h)	Not decomposed
EHA-G1 (180)	125 °C (1h) + 180 °C (2h)	Decomposed
EHA-G2 (150)	125 °C (1h) + 150 °C (2h)	Not decomposed
EHA-G2 (180)	125 °C (1h) + 180 °C (2h)	Decomposed
EHA-HG1 (150)	125 °C (1h) + 150 °C (2h)	Not decomposed
EHA-HG1 (180)	125 °C (1h) + 180 °C (2h)	Not Decomposed
EHA-HG2 (150)	125 °C (1h) + 150 °C (2h)	Failure in extraction
EHA-HG2 (180)	125 °C (1h) + 180 °C (2h)	Failure in extraction

Table 6.3 Results of thermolytic decomposition of Grubbs and Hoveyda-Grubbs' catalysts extracted from epoxy matrices

This experimentation has revealed that is possible to reach a curing temperature of 180 °C with first generation Hoveyda-Grubbs' catalyst (HG1). This catalyst, unlike what was expected, has demonstrated exceptional stability in the presence of functional groups of the resin, even at a temperature of 180 °C. For second generation Hoveyda-Grubbs' catalyst (HG2), the performed tests were unable to determine its potential use in epoxy self-healing systems manufactured by a

process curing at 180 °C (NMR spectra revealed no presence of HG2 signals in deuterated solvent). To verify if it is possible to extend the curing temperature up to 180 °C, different tests and methods were performed for systems with powders of HG2 catalyst embedded in the epoxy matrix.

6.2.3 Thermolytic decomposition of HG1 and HG2 - Infrared Analysis

Infrared analysis is a very useful way to identify metathesis products and therefore catalyst activity. The manufactured EHA-HG1(180) and EHA-HG2 (170) samples were cut by a serrated blade; the powder which was produced from each sample was collected in two separate mortars and a drop of healing agent (5-ethylidene-2-norbornene - ENB) was added to each before dispersing the powder samples into the KBr disks for FTIR investigation. In Figure 97 FTIR spectra of the EHA-HG1(180) and EHA-HG2 (170) powder treated with ENB are reported. The highlighted peak at 966 cm^{-1} is characteristic of ring-opened poly(ENB).

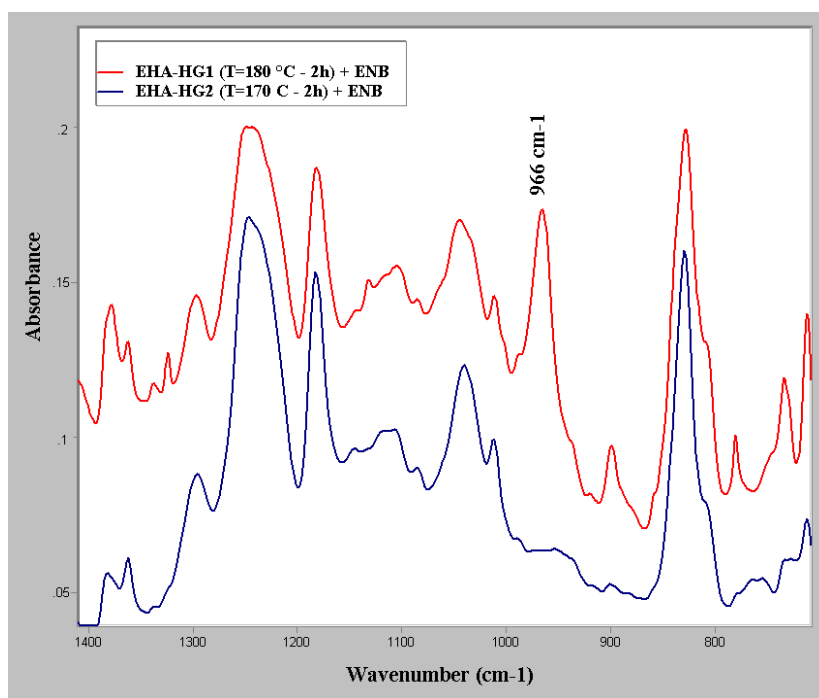


Figure 97: FTIR spectra of the EHA-HG1(180) and EHA-HG2 (170) powders treated with ENB. The highlighted peak at 966 cm^{-1} is characteristic of ring-opened poly(ENB)

Infrared spectroscopy of the EHA-HG1(180) sample (red spectrum) indicates an absorption at 966 cm^{-1} attributable to trans-substituted alkenes, characteristic of the ring-opened cross-linked product, poly(ENB), whereas, the HG2 catalyst shows an inability to polymerize the ENB monomer (see blue spectrum), providing evidence that the embedded catalyst is inactive also for a curing temperature of the epoxy formulation lower than $180\text{ }^{\circ}\text{C}$.

In light of the TGA results which show for HG2 a higher temperature of beginning degradation than HG1 ($\sim 20\text{ }^{\circ}\text{C}$), the unexpected results obtained from FT/IR investigation have spurred us to undertake an investigation aimed at understanding the reactivity of the two different catalysts HG1 and HG2 inside the epoxy resins.

First we analyzed the behavior of the HG2 catalyst in the only epoxy precursor (Epon 828) at different temperatures. Figure 98 shows FTIR spectra of a mixture obtained by dispersing the HG2 catalyst (5% wt) in the Epon 828 epoxy precursor (EHG2-sample) and submitting this mixture to an increase of temperature between $100\text{ }^{\circ}\text{C}$ and $180\text{ }^{\circ}\text{C}$ for different treatment times.

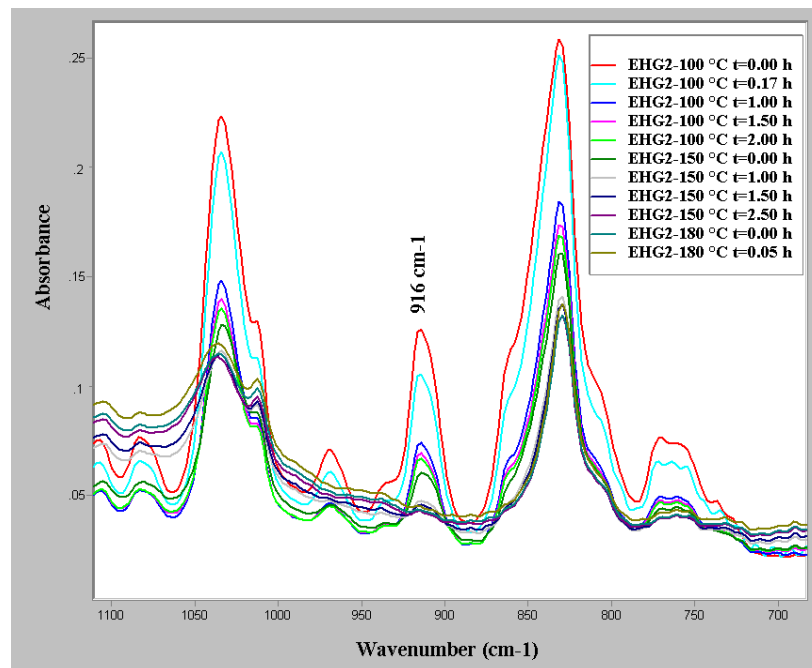


Figure 98: FTIR spectra of EHG2 sample between $100\text{ }^{\circ}\text{C}$ and $180\text{ }^{\circ}\text{C}$ for increasing times. The highlighted peak at 916 cm^{-1} is characteristic of the oxirane ring

This sample is only obtained by mixing the epoxy precursor and the HG2 catalyst powders: no other components were added to the mixture, and in particular, no curing agent was mixed in the formulation.

In Figure 98 is highlighted the most intense band of the epoxy ring at 916 cm^{-1} which is attributed to asymmetrical ring stretching in which the C-C bond is stretching during contraction of the C-O bond. In the initial spectrum, (EHG2-100 °C t=0.00 h – red curve), the band at 916 cm^{-1} is very evident. The intensity of this peak decreases by increasing the treatment temperature. The peak completely disappears for a treatment time of 60 minutes at 150 °C. The resin treated at 150 °C for 1 or 2 hours shows the same spectrum of the resin after a treatment at 180 °C (with a complete absence of the peak at 916 cm^{-1}).

It can be deduced that, the presence of the HG2 catalyst in the epoxy precursors involves a progressive and rapid disappearance of the signal to 916 cm^{-1} , even if no curing agent was blended into the mixture. Infrared spectroscopy can be used to follow the curing process by determining the decrease of the band at 916 cm^{-1} due to the epoxy group,²³ but in this case, where no curing agent is present, the decrease of the peak at 916 cm^{-1} can be attributed only to the reactions of the epoxy precursor oligomer with the catalyst powder.

To confirm the interpretation validity of this last result the epoxy precursor **E** (without catalyst) was submitted to an increase of temperature between 100 and 180 °C under the same experimental conditions as the previous mixture (E-HG2).

This last experiment was carried out to clarify if the decrease of the intensity peak at 916 cm^{-1} could be attributed to other independent factors from the presence of the catalyst, such as the possible polymerization reactions activated by free radicals due to the thermal degradation of the epoxy precursor.

FTIR spectra of this sample are reported in Figure 99: the peak at 916 cm^{-1} is also very evident in the spectrum of the sample treated up to 180 °C.

These last results explain our difficulty in extracting the HG2 catalyst from the epoxy formulations and its ineffectiveness in the activation of the ring-opening metathesis polymerization. It is probable that the catalyst extraction is impossible because it is chemically bonded to the epoxy matrix which also irreversibly changes its reactivity.

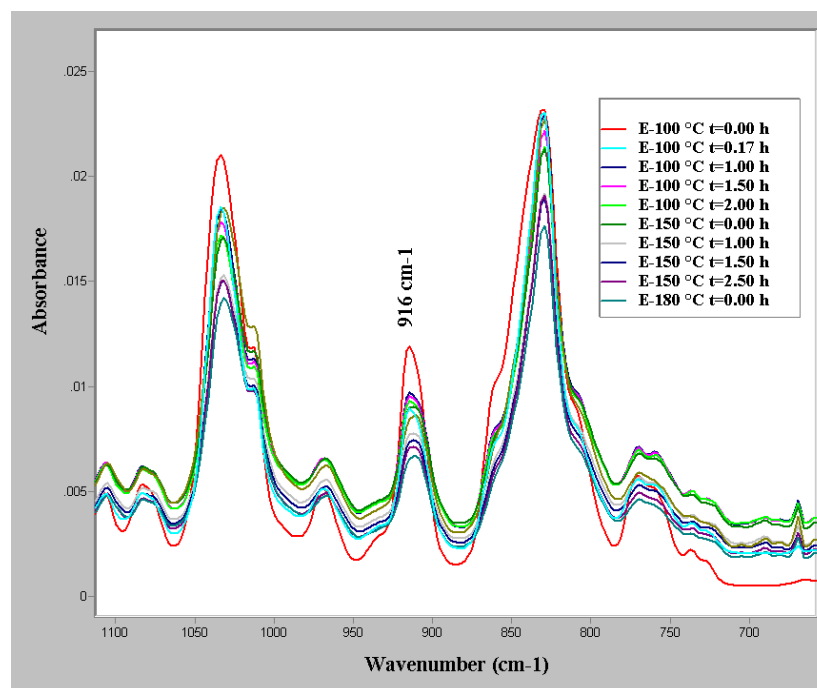


Figure 99: FTIR spectra of E sample between 100 °C and 180 °C for increasing times

Our objective was the choice of a catalyst that could also activate the metathesis reaction (ROMP) within a self-healing system cured up to 180 °C. The only catalyst able to meet our requirement was the Hoveyda-Grubbs' 1st generation catalyst.

For this reason our self-healing systems are formulated using the HG1 catalyst and a curing process up to 180 °C.

The possibility of carrying out the setting process at higher temperatures gives the material improved chemical, physical and mechanical characteristics.

6.3 Romp Reaction of ENB with first and second generation Hoveyda-Grubbs' Catalysts

Ring-Opening Metathesis Polymerization (ROMP) was carried out using ENB with HG1 and HG2 catalysts at different temperatures.

For the each tests, a molar ratio between catalyst and reactive monomer of 1:1000 was used. Two separate vials containing the catalyst and the monomer (ENB) were placed, before the start of the tests for about half an hour at the polymerization temperature.

The Yield (%) of reaction is calculated as the ratio between the polymer obtained at the end of reaction and the initial weight of the monomer. In Table 6.4 the results of the metathesis activity of the first generation Hoveyda-Grubbs catalyst (HG1) with ENB as substrate are reported.

HG1/ENB ratio	Initial monomer (g)	Polymer produced (g)	Temperature (°C)	Time (min)	Yield (%)
1/1000	0.99	0.95	25	0.5	96
1/1000	0.99	0.92	-20	1440	93
1/1000	0.99	0.98	-40	1440	99
1/1000	0.99	0.97	-40	240	98
1/1000	0.99	0.98	-50	450	99

Table 6.4: Conversion percentage (Yields %) in the ROMP reaction of ENB with HG1 catalyst

Table 6.5 shows the results of Romp rriaction of HG2 with ENB:

HG2/ENB ratio	Initial monomer (g)	Polymer produced (g)	Temperature (°C)	Time (min)	Yield (%)
1/1000	0.99	0.93	25	8	94
1/1000	0.99	0.93	-20	1440	94
1/1000	0.99	0.91	-40	1440	92
1/1000	0.99	0.90	-50	450	91

Table 6.5: Conversion percentage (Yields %) in the ROMP reaction of ENB with HG2 catalyst

The data show that with ENB as polymerizer agent and Hoveyda-Grubbs 1 and Hoveyda-Grubbs 2 as catalysts, the metathesis reaction is also active at -50 °C. The reaction rate is very fast for both the catalysts, but for HG1 is faster (respect HG2) as we can see from the data at 25 °C.

6.3.1 Evaluation of Cross-linked Fraction of Metathesis Products

Another aspect that is considered in relation to the ROMP of ENB with Hoveyda-Grubbs' catalysts, concerns the degree of crosslinking of the metathesis products. The degree of crosslinking of the product of metathesis of ENB was evaluated, with both catalysts HG1 and HG2, making extraction of the insoluble fraction products of the metathesis in cis-trans decahydronaphthalene (decaline). The experimental procedure is as follows:

Cross-linked fraction of polymers was determined, according to the ASTM method D2765-84, as the percent of the original weight of the sample after extracting for 6 h in boiling decahydronaphthalene (decaline, a mixture of cis and trans isomers). The extraction was followed by drying at 150 °C in a vacuum oven. As suggested by this standard method, to avoid polymer degradation during the extraction procedure, an antioxidant agent has to be used. In particular, 2,2'-methylene-bis-(4-methyl-6-tert-butyl phenol) was dissolved in decaline (1 wt%), before the extraction tests.

Three samples were prepared and were subjected to exhaustive extraction in cis-trans decahydronaphthalene:

Sample 1: Metathesis product of ENB + HG1 obtained at room temperature (25 °C), with a catalyst/monomer ratio of 1/1000

Sample 2: Metathesis product of ENB + HG2 obtained at room temperature (25 °C), with a catalyst/monomer ratio of 1/1000

Sample 3: Metathesis product of ENB + HG1 obtained at -50 °C, with a catalyst/monomer ratio of 1/1000.

Table 6.6 shows these results. The insoluble fraction, corresponding to cross-linked polymer in metathesis product, is high for both the catalysts at room temperature. HG1 catalyst give a more cross-linked polymer at 25 °C respect HG2. The insoluble fraction of the polymer reduces significantly lowering the temperature at which the metathesis reaction occurs, as we can see from data at -50 °C, obtained for the sample with ENB and HG1.

Sample	Temperature (°C)	Reaction time (min)	Yield %	Insoluble fraction %	Soluble fraction %
Sample 1	25	0.5	96	60	40
Sample 2	25	8	94	42	58
Sample 3	-50	450	99	10	90

Table 6.6: Cross-linked fraction of metathesis products of ENB with HG1 and HG2 catalyts

6.3.2 Phase Separation Tests for DCPD + ENB blends in different proportions (2.5%, 5% of DCPD) at -50 °C

To increase the cross-linked fraction of metathesis products, blends of ENB/DCPD was also used as healing agent.

At low temperatures, it was necessary to carry out phase separation tests on this blends because the two monomers have very different melting points (see Materials section for details).

Here we describe the experimental procedure followed.

A thermostatic bath was prepared dipping a cooling coil of a gas cryostat in a beaker containing ethanol (Temperature set point = -50°C). The temperature control was performed by immersion in the beaker of a thermocouple directly connected to the cryostat. Once the set point temperature was reached, two vials containing the ENB/DCPD blends (2.5% and 5% wt. of DCPD) were immersed in the thermostatic bath. Periodically the vials were removed from the thermostatic bath for visual inspection.

Figure 100 and Figure 101 shows the blends (at -50 °C) after 1 h and after 5 h respectively: even after 5 h at -50 °C the blends look clear and perfectly homogeneous: there is no phase separation.

This test was also performed increasing the weight percent of DCPD in the blends.

The same test performed on ENB+DCPD blends with 10% and 15 % wt. content of DCPD shown phase separation after 1 h at -50 °C.



Figure 100: ENB/ 2.5% DCPD and ENB/ 5%DCPD blends after 1h at -50 °C



Figure 101: ENB/ 2.5% DCPD and ENB/ 5%DCPD blends after 5h at -50 °C

Table 6.7 shows, at different temperature, the cross-linked fraction of metathesis products of ENB/DCPD blends with HG1 catalyst compared with cross linked fraction of products of only ENB and HG1.

Blend	Temp. (°C)	Reac. time (min)	DCPD %	Yield %	Insoluble fract.%	Soluble fract.%
1 (OnlyENB)	25	0.5	0	96	60	40
1	25	0.66	2.5	99	81	19
2	25	0.66	5	99	87	13
4 (onlyENB)	-50	450	0	99	10	90
5	-50	450	2.5	80	76	24
6	-50	450	5	77	75	25

Table 6.7: Cross-linked fraction of metathesis product of ENB/DCPD blends in different proportions and at different temperature

As we can see from Table 6.7, for the metathesis product obtained by ring-opening metathesis polymerization at room temperature the cross-linked fraction for the blend with %5 of DCPD is 87% where for only ENB it is 60% and at -50 °C the cross-linked fraction for blend with the same proportion of DCPD is 75%, where for only ENB is 10%.

6.4 Self-healing Systems

Hoveyda-Grubbs' 1st generation catalyst (HG1), showed a higher thermal stability (over all catalysts tested in this work) and optimal reactivity for ROMP metathesis reaction at low temperatures. For these reasons our self-healing systems are formulated using the HG1 catalyst and a curing process up to 180 °C.

Finally we developed systems with a self-healing functionality based on ROMP metathesis reaction of ENB triggered by first generation Hoveyda-Grubbs' catalyst. The formulation scheme of the best self-healing system on which experimentation was focused is reported in Figure 102:

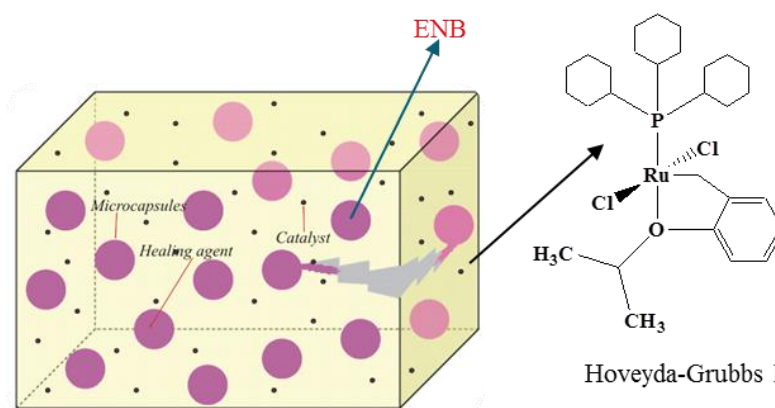


Figure 102: Last Self-healing system, based on Romp reaction of ENB triggered by HG1

We evaluated chemical and physical properties of self-healing systems with three different polymer matrix compositions EHA, EBA1, EBA2 (see Figure 103).

Epon 828 (E) and the Ancamine K 54 (A) are the same components as the previous formulations.

The EBA formulations differ from EHA formulation for the chemical nature of the flexibilizer: for the EBA formulations, Heloxy 71 (H) has been replaced with the reactive diluent BDE, 1-4 Butandiol diglycidylether (B), which allows a more fluid mixture in the initial phase of preparation of the uncured matrix.

The formulations EBA1 and EBA2 differ only in the concentration of reactive diluent BDE.

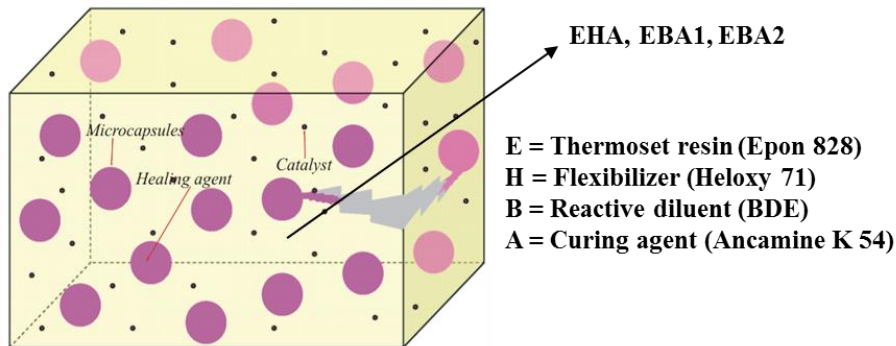


Figure 103: Scheme of different matrix compositions, EHA, EBA1, EBA2

The compositions of the three different matrix systems are reported below:

- **EHA:** Epon 828 (63%)
Heloxy 71 (37%)
Ancamine K 54 (10% wt. respect E+H)
- **EBA1:** Epon 828 (90%)
BDE (10%)
.....Ancamine K 54 (10% wt. respect E+B)
- **EBA2:** Epon 828 (80%)
BDE (20%)
.....Ancamine K 54 (10% wt. respect E+B)

6.4.1 Dynamic Mechanical Properties of Self-healing Systems

We evaluated dynamic mechanical properties in a wide range of temperatures of self-healing systems with EHA, EBA1 and EBA2 matrix compositions.

The EHA system showed a behavior quite different from systems containing reactive diluent. In particular, for the EHA system was found the need of a curing process with a first stage at fairly low temperatures (between 70 and 80 °C) to get the best mechanical performance. This was not shown for the formulations containing reactive diluent, as they can be cured with a first stage at higher temperatures of 120 or even 125 °C (this is the curing cycle suggested by the project managers of our Industrial Partner, Alenia Aeronautica).

For formulations with BDE was analyzed the mechanical behavior with two different curing cycles: a curing cycle with a first step at 80 °C for 4 hours and a second step at 170 or 180 °C for 2 h, and a curing cycle with a first step at 125 °C for 1 h and a second step at 170 or 180 °C for 2 h. At low temperatures (up to 50 °C), the elastic dynamic moduli of the specimens cured with these two curing cycles are the same.

All EBA formulations show greater fluidity, higher glass transition temperatures and elastic moduli than EHA formulations.

Figure 104 shows the dynamic elastic modulus for EBA1 and EBA2 formulations cured with a first step at 80 °C (4 h) and a second step at 170 or 180 °C (2 h).

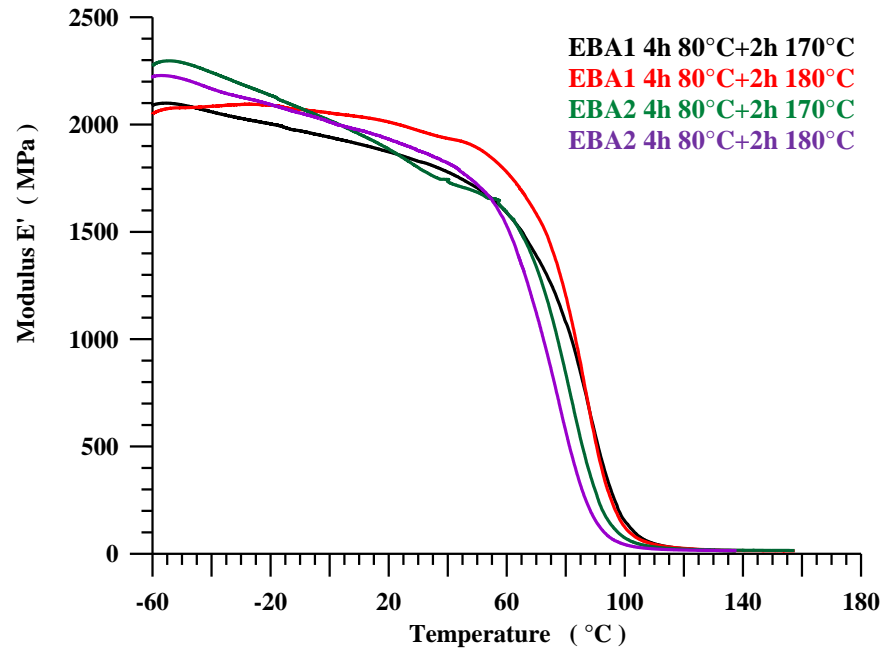


Figure 104: Dynamic Elastic Modulus for EBA1 and EBA2 formulations cured at 80 °C (4h) + 170 or 180 °C (2h)

The modulus is always higher than that recorded for the EHA system.

Figure 105 shows the loss factor, $\text{Tan } \delta$, for the same formulations and the same curing cycles.

For all formulations, $\text{Tan } \delta$ opens at higher temperatures than the EHA system. The highest glass transition temperature is for formulation with 10% of reactive diluent (EBA1). The difference of 10 °C in the

second step of the curing cycle (170 or 180 °C) does not have a great effect on $\text{Tan } \delta$.

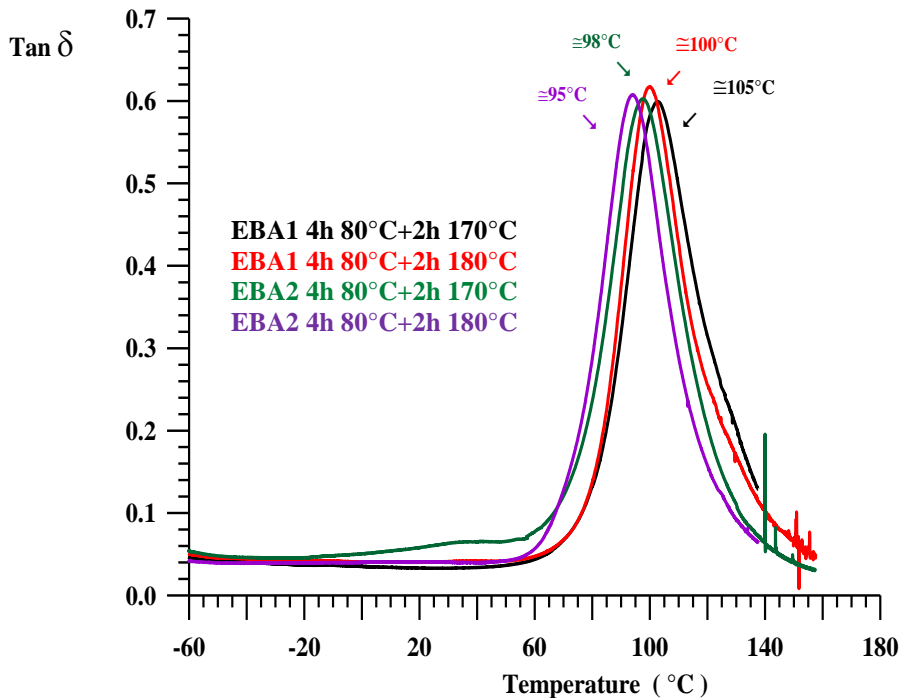


Figure 105: Loss factor ($\text{Tan } \delta$) for EBA1 and EBA2 formulations cured at 80 °C (4h) + 170 or 180 °C (2h)

The $\text{Tan } \delta$ curves for EBA matrices cured with a first step at 125 °C for 1 h and a second step at 170 or 180 °C for 2 h are quite similar.

For global formulations (self-healing formulations), there was a difference even more pronounced (than the one reported for the matrix systems alone) between the EHA specimens loaded with HG1 catalyst and microcapsules and EBA specimens loaded with the same components at similar concentrations.

In Figure 106 Loss factor curves ($\text{Tan } \delta$) for EBA and EHA formulations are reported. All formulations have a 5% wt. content of HG1 catalyst and 10%wt. of microcapsules filled with ENB healing agent; only for EBA1 formulation is reported also a sample with 15 % of microcapsuled. This allows to understand the influence of the concentration of microcapsules and curing conditions on glass transition of the systems.

EBA samples was cured by two stage curing cycle: a first isothermal stage at 125 °C (1h) and a second isothermal stage at 170 °C (2h) or a second isothermal stage at 180 °C (2h).

Only for EHA formulation we tried to optimize the mechanical properties by choosing as first step of the curing cycle a temperature of 80 °C for 4 h; the second step for this sample is the same as EBA formulations.

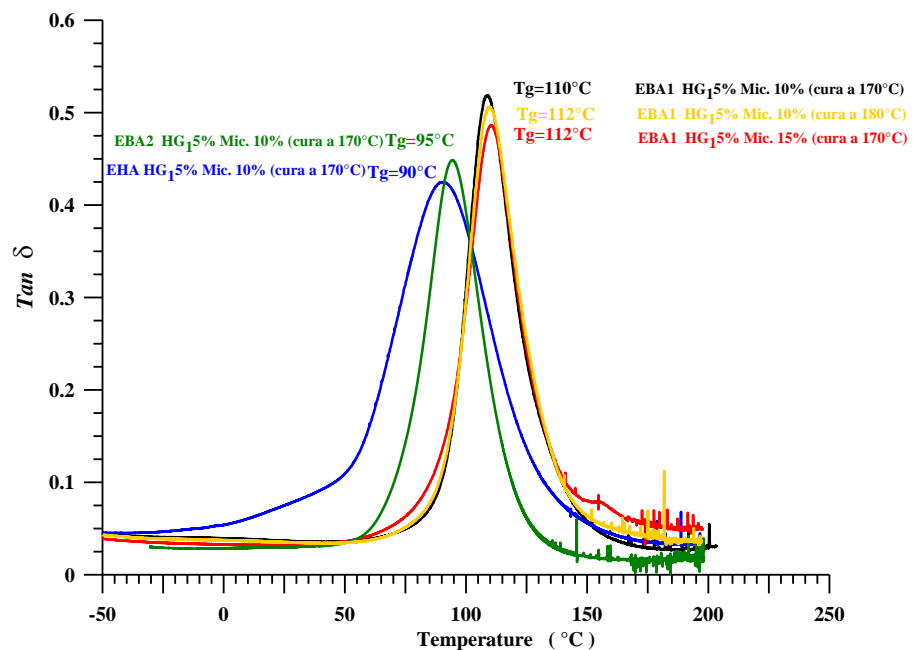


Figure 106: Glass transition temperatures (T_g) for self-healing formulations cured up 170 or 180 °C

The highest glass transition temperatures (T_g) are for EBA1 formulations with a concentration of microcapsules of 10-15%.

Tan δ for EBA1 formulations is narrower and opens to a value of 30 °C higher than the formulation EHA.

The lowest glass transition temperature is recorded for the EHA formulation.

EBA2 formulation has a glass transition higher than EHA, but lower than EBA1 formulations, (as already seen for matrix system).

The concentration of the microcapsules and 2nd step temperature (170 or 180 °C) do not have much influence on the T_g of the specimens. These parameters have a rather small effect on the elastic modulus which is higher for formulations cured at the higher temperature of 180 °C (see Figure 107).

Figure 107 shows that, for the same matrix formulation and at same curing conditions, an increase of microcapsules 10 to 15% causes a slight decrease in dynamic modulus.

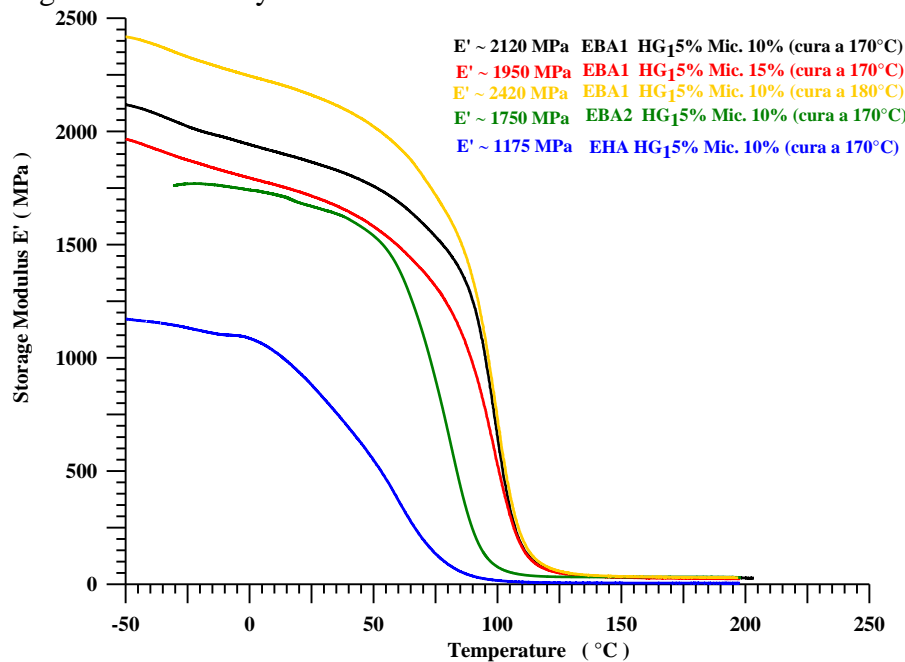


Figure 107: Dynamic Elastic Modulus for self-healing formulations cured up 170 or 180 °C

Table 6.8 shows storage moduli for the analyzed self-healing formulations in a range of temperature between -50 and 50 °C:

The table shows that the dynamic elastic modulus for all EBA formulations is elevated (also up to 70 °C): at 70 °C, the lower modulus (1103MPa) is recorded for the formulation EBA2 with HG1 5% and 10% of microcapsules (with a curing cycle up to 170 °C).

At 70 °C EHA formulation shows a very low value of elastic modulus (198 MPa).

This value imposes limits on the applicability of this system in a temperature range greater than or equal to 50 °C.

System	E' -50 (MPa)	E' -30 (MPa)	E' -10 (MPa)	E' 0 (MPa)	E' +10 (MPa)	E' +30 (MPa)	E' +50 (MPa)	E' +70 (MPa)
EHA HG1 5% Mic10% 170	1175	1145	1100	1085	1029	819	548	198
EBA1 HG1 5% Mic10% 170	2120	2048	1975	1940	1910	1847	1758	1592
EBA1 HG1 5% Mic10% 180	2418	2350	2277	2245	2214	2139	2020	1802
EBA1 HG1 5% Mic15% 170	1966	1892	1824	1795	1765	1694	1580	1383
EBA2 HG1 5% Mic10% 170	-	1760	1757	1740	1720	1652	1539	1103

Table 6.8 Dynamic elastic moduli for self-healing formulation in the range of temperature between -50 and 50 °C

6.4.2 Thermal Analysis of Self-healing Systems

6.4.2.1 Differential Scanning Calorimetry of self-healing samples

In Figure 108 are shown DSC curves for self-healing samples with EBA1 matrix system. All curves are compared with the DSC curve of the initial formulation EBA1 with 10% of catalyst HG1. This formulation was analyzed immediately after preparation (without undergoing any curing process) to assess the range of temperature at which crosslinking processes occurs. This interval, under dynamic condition is between 80 and 230 °C. For all chosen curing conditions (which include curing cycles with a second step at 170 or 180 °C), the specimens show a flat curve in the temperature range between 80 and 230 °C, indicating that the selected conditions have allowed efficient curing of all formulations. Similar results are obtained for self-healing samples which have EBA2 as matrix formulation (see Figure 109).

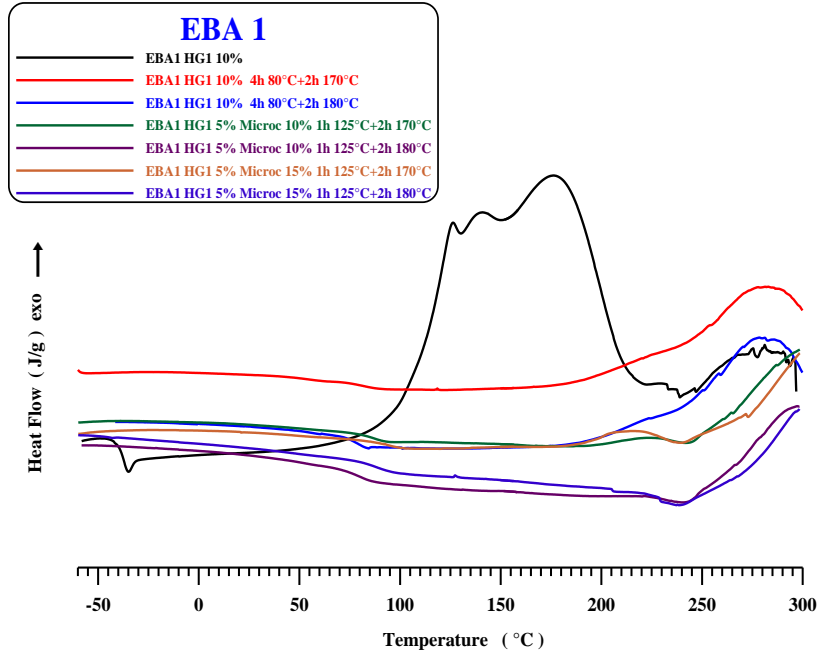


Figure 108: DSC curves of self-healing specimens with EBA1 matrix formulation cured up 170 and 180 °C

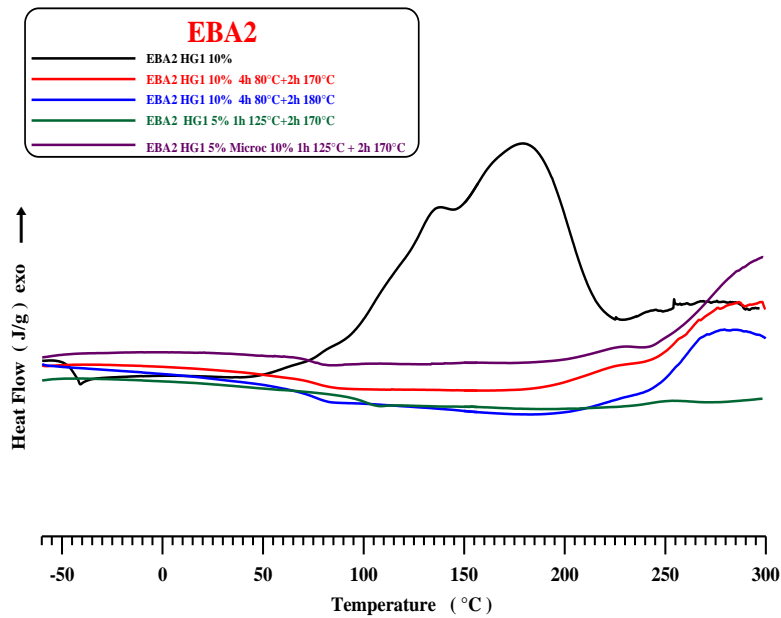


Figure 109: DSC curves of self-healing specimens with EBA1 matrix formulation cured up 170 and 180 °C

6.4.2.2 Thermogravimetric Analysis of self-healing samples

Figure 110 shows the thermogravimetric curves in air and nitrogen of EBA system loaded with the 5% HG1 catalyst and 10% of microcapsules. The formulation was cured with a cycle at 125 °C (1h) + 170 °C (2h). Analysis was in air and Nitrogen.

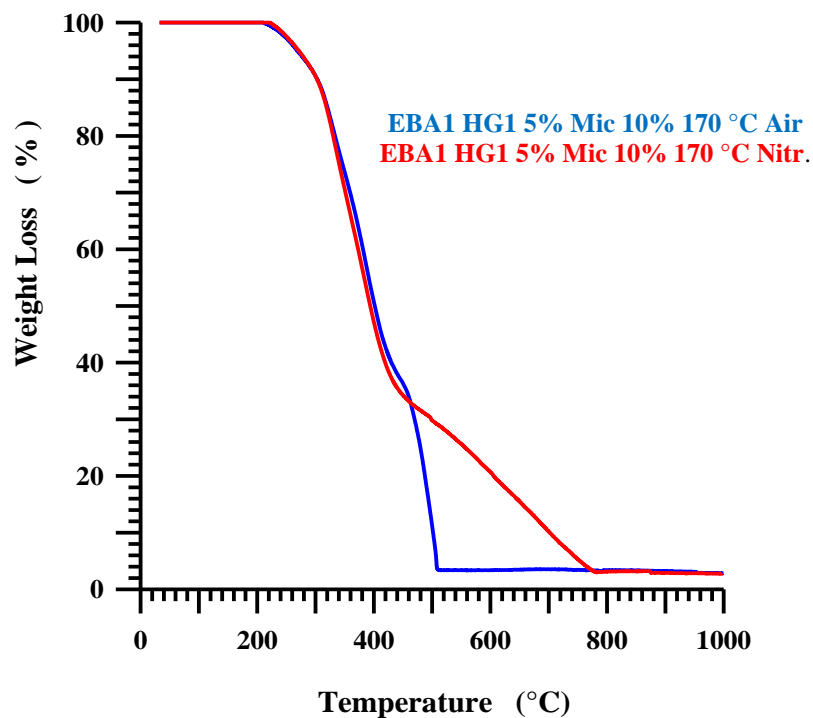


Figure 110: TGA curves in air and nitrogen for self-healing system EBA1 + HG1 5% + Mic 10 % cured up 170 °C

From the curves it emerges that the first stage of degradation is the same in air and in an inert environment. The temperature of beginning degradation is at 240 °C. A curing cycle conducted up to 180 °C does not change the temperature of beginning degradation of the samples (see Figure 111).

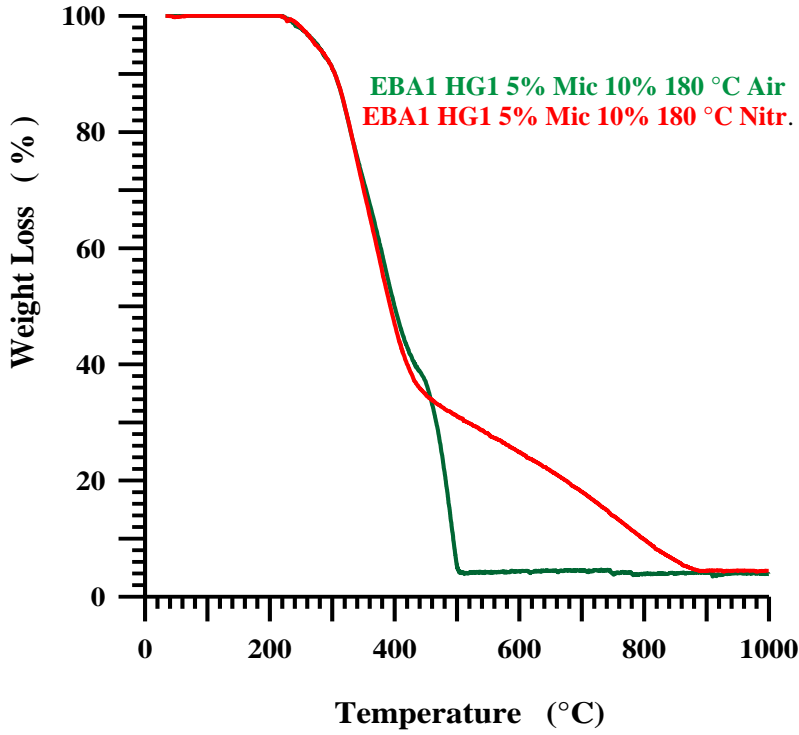


Figure 111: TGA curves in air and nitrogen for self-healing system EBA1 + HG1 5% + Mic 10 % cured up 180 °C

Similar results are obtained for self-healing samples which have EBA2 as matrix formulation.

From the point of view of thermal degradation, the EBA formulations (loaded or not) show a behavior similar to that shown by the EHA formulation.

6.5 Evaluation of Self-healing Efficiency

The experimental procedure for self-healing efficiency evaluation was conducted following the protocol established by White et al. [40, 65,67] (see Methods section). As we already know, crack healing efficiency “ η ” is defined as the ability to recover fracture toughness (K_{IC}) and, for the Tapered Double Cantilever Beam (TDCB) geometry, the healing efficiency is simply calculated as the ratio of critical fracture loads (P_C) for the healed and virgin samples:

$$\eta = \frac{K_{IChealed}}{K_{ICvirgin}} = \frac{P_{Chealed}}{P_{Cvirgin}} \quad (\text{eq.6.1}).$$

6.5.1 Design and Realization of the Molds for the Manufacturing of Self-healing Specimens

The first phase of experimentation concerned the realization of the molds for manufacturing of self-healing specimens as required by protocol.

First we decided to realize silicone rubber molds for the manufacturing of TDCB specimens, in order to avoid adhesion phenomena that normally are established between the resin and mold and to facilitate the extraction of the sample from the mold after the curing process. Figure 112 shows a photograph of the molds with the metallic core utilized for their realization:

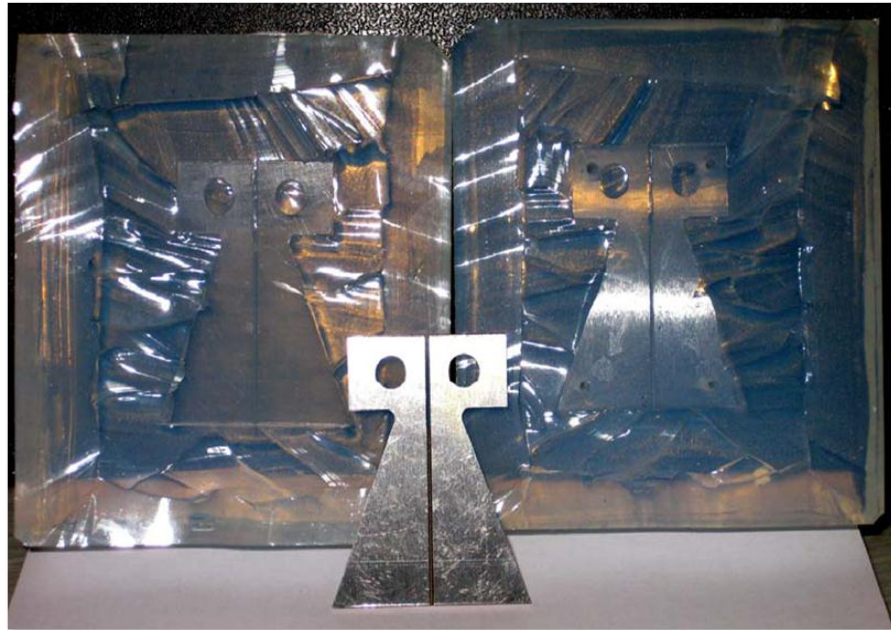


Figure 112: Silicone Rubber Molds for self-healing specimens with TDCB geometry

Unfortunately the results of tests performed with this type of mold have shown that they are impractical for the intended purpose: in fact, during the pouring of resin (before the curing process), the sensitive parts of the mold (e.g.: the very thin central wing), which define the final geometry of the sample, don't maintain their structure and also after the curing process, during the extraction of the specimen, they are destroyed (as they are intimately attached to the sample) making the mold unusable for subsequent preparations.

It was therefore considered more appropriate to use metallic molds. Figure 113 shows the project designs of these molds:

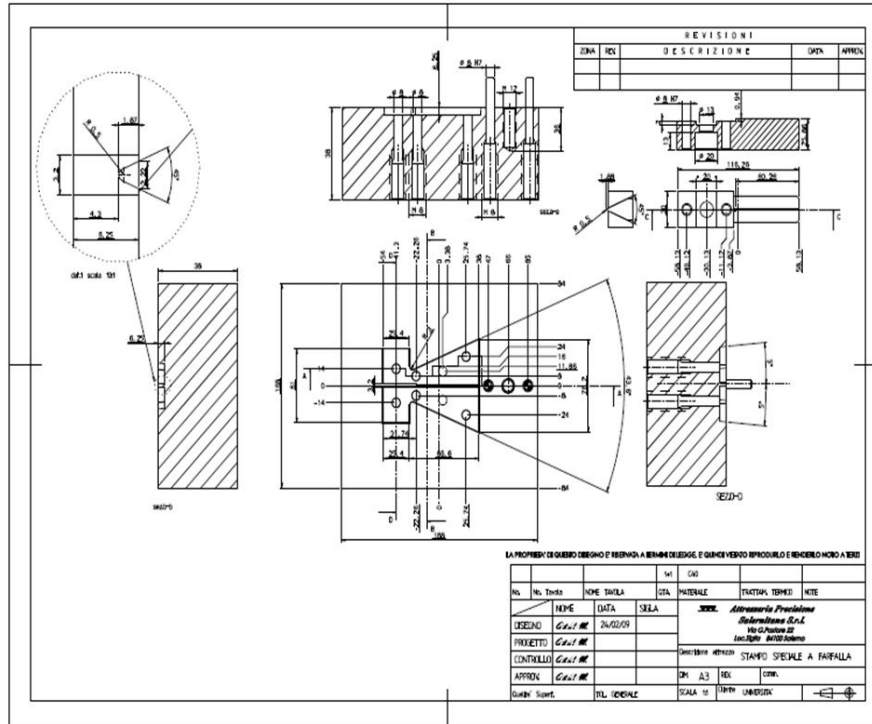


Figure 113: Project designs of metallic molds for self-healing specimens with TDCB geometry

In Figure 114 is reported a picture of the two metallic molds. The figure shows the picture of the molds before pouring the fluid mixture. Before pouring the fluid resin, teflon is sprayed on the molds, in order to facilitate the extraction of the specimens after the curing process.

Figure 115 shows a picture of two cured samples before extraction and Figure 116 shows the same cured samples just before self-healing efficiency test.



Figure 114 Metallic Molds (with teflon sprayed) for self-healing specimens with TDCB geometry



Figure 115: Cured Self-healing Samples before extraction from the molds



Figure 116: Cured Self-healing samples after extraction from metallic molds

6.5.2 Self-healing Efficiency Tests

The self-healing specimens were obtained by mechanically mixing in the liquid phase, at room temperature, the following components that are added in the followed order:

1. precursors of epoxy monomers (Epon 828)
2. flexibilizer (Heloxy 71 or reactive diluent BDE)
3. curing agent (Ancamine K 54)
4. catalyst powder (HG1)
5. synthesized microcapsules (filled with ENB healing agent)

Here we reported the data obtained from self-healing efficiency tests of all analyzed formulations with the provided curing cycles.

For all samples are reported:

Formulations;

Curing conditions;

Compositions;

Load-Displacement curves;

Critical loads (P_C) of Healed and Virgin sample;

Efficiency values.

Sample Formulation: EBA1 HG1 5% Mic 10%**Curing conditions: 125 °C for 1 h + 170 °C for 2 h****Composition:**

Epon828 = 22.5g;

BDE =2.5g (10% wt Epon+BDE);

Ancamine K 54 = 2.5g (10% wt Epon +BDE);

HG1 = 1.25g (5% wt Epon +BDE);

Microcapsule with ENB = 2.5g (10% wt Epon +BDE);

Figure 117 shows Load-Displacement curves for the Virgin sample and after the healing process (Healed).

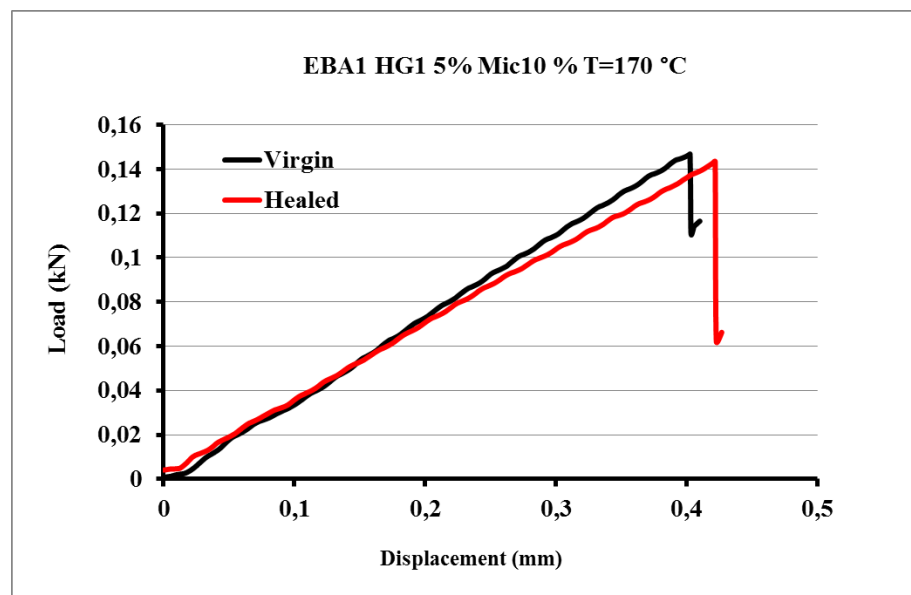


Figure 117: Load-Displacement Curves for Virgin and Healed sample EBA1 HG1 5% Mic 10% cured up 170 °C

Pc(Virgin)=0.1468 kN**Pc(Healed)=0.1435 kN****Efficiency=97.75%**

Sample Formulation: EBA1 HG1 5% Mic 10%**Curing conditions: 125 °C for 1 h + 180 °C for 2 h****Composition:**

Epon828 = 22.5g;

BDE =2.5g (10% wt Epon+BDE);

Ancamine K 54 = 2.5g (10% wt Epon +BDE);

HG1 = 1.25g (5% wt Epon +BDE);

Microcapsule with ENB = 2.5g (10% wt Epon +BDE);

Figure 118 shows Load-Displacement curves for the Virgin sample and after the healing process (Healed).

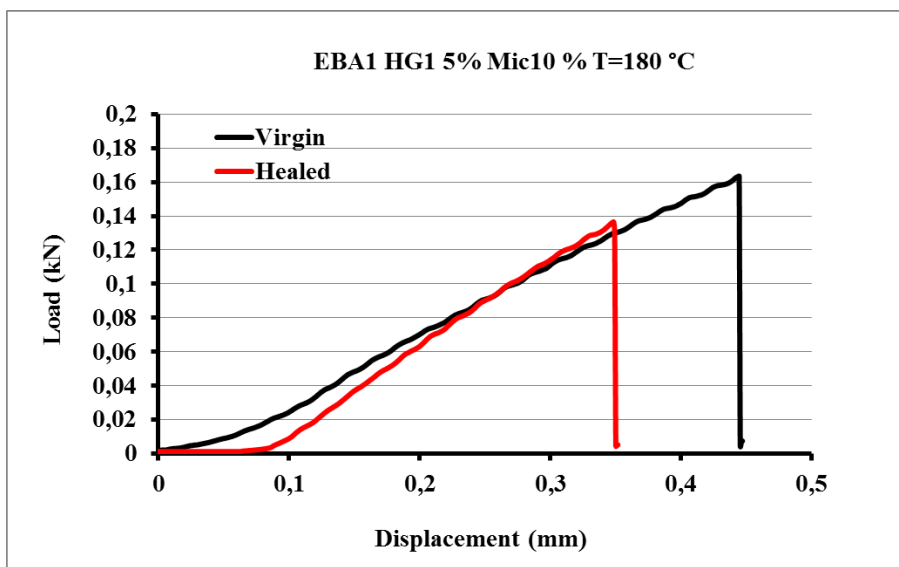


Figure 118: Load-Displacement Curves for Virgin and Healed sample EBA1 HG1 5% Mic 10% cured up 180 °C

Pc(Virgin)= 0.1635kN**Pc(Healed)= 0.1366kN****Efficiency=83,54%**

Sample Formulation: EBA2 HG1 5% Mic 10%**Curing conditions: 125 °C for 1 h + 170 °C for 2 h****Composition:**

Epon828 = 20g;

BDE =5g (20% wt Epon+BDE);

Ancamine K 54 = 2.5g (10% wt Epon +BDE);

HG1 = 1.25g (5% wt Epon +BDE);

Microcapsule with ENB = 2.5g (10% wt Epon +BDE);

Figure 119 shows Load-Displacement curves for the Virgin sample and after the healing process (Healed).

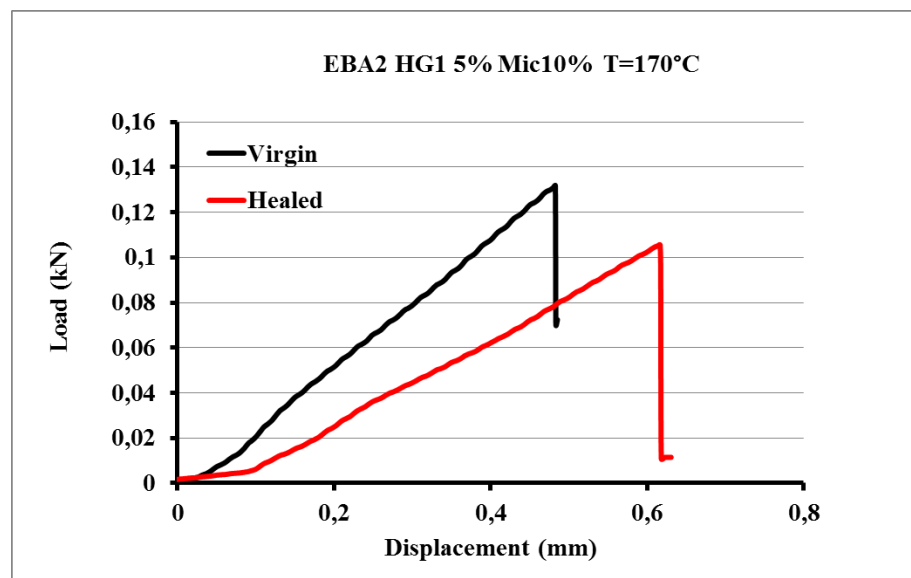


Figure 119: Load-Displacement Curves for Virgin and Healed sample EBA2 HG1 5% Mic 10% cured up 170 °C

Pc(Virgin)=0.1318 kN**Pc(Healed)=0.1056 kN****Efficiency=80.12%**

Sample Formulation: EBA2 HG1 5% Mic 10%**Curing conditions: 125 °C for 1 h + 180 °C for 2 h****Composition:**

Epon828 = 20g;

BDE =5g (20% wt Epon+BDE);

Ancamine K 54 = 2.5g (10% wt Epon +BDE);

HG1 = 1.25g (5% wt Epon +BDE);

Microcapsule with ENB = 2.5g (10% wt Epon +BDE);

Figure 120 shows Load-Displacement curves for the Virgin sample and after the healing process (Healed).

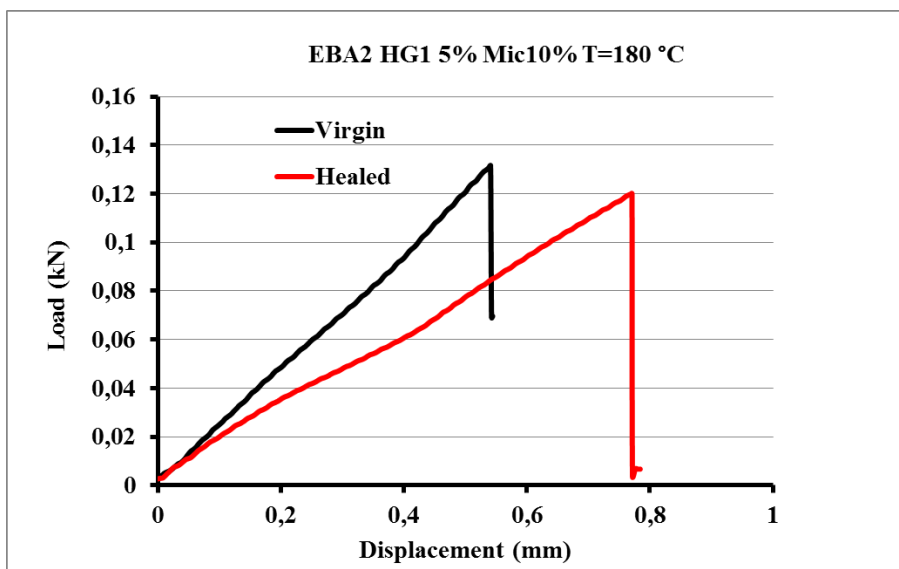


Figure 120: Load-Displacement Curves for Virgin and Healed sample EBA2 HG1 5% Mic 10% cured up 180 °C

Pc(Virgin)=0.1318 kN**Pc(Healed)=0.1201 kN****Efficiency=91.12%**

Sample Formulation: EHA HG1 5% Mic 10%**Curing conditions: 125 °C for 1 h + 170 °C for 2 h****Composition:**

Epon828 = 15.75g;

Heloxy 71 =9.25g (37% wt Epon+Heloxy 71);

Ancamine K 54 = 2.5g (10% wt Epon +Heloxy 71);

HG1 = 1.25g (5% wt Epon +Heloxy 71);

Microcapsule with ENB = 2.5g (10% wt Epon +Heloxy 71);

Figure 121 shows Load-Displacement curves for the Virgin sample and after the healing process (Healed).

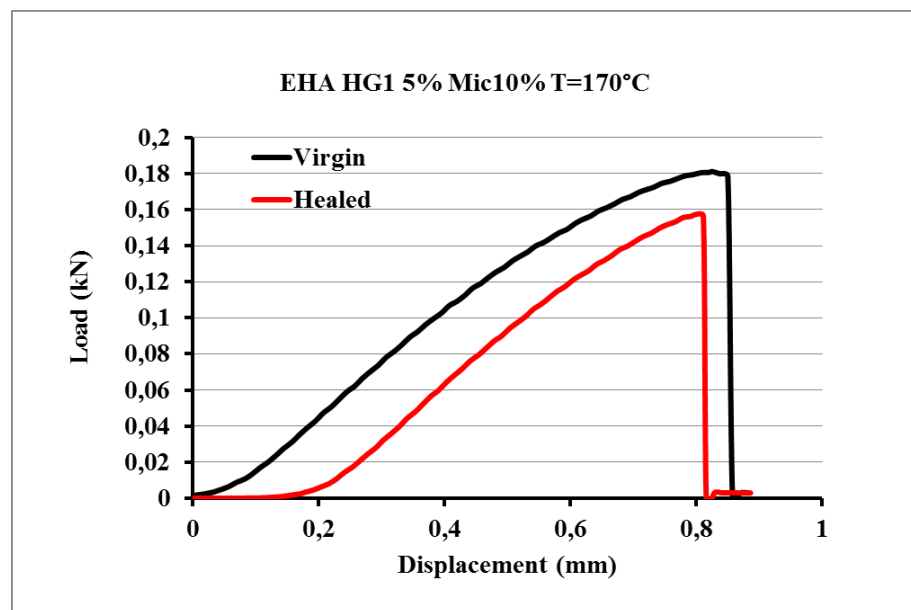


Figure 121: Load-Displacement Curves for Virgin and Healed sample EHA HG1 5% Mic 10% cured up 170 °C

Pc(Virgin)=0.1807 kN**Pc(Healed)=0.1572 kN****Efficiency=87.00%**

Sample Formulation: EHA HG1 5% Mic 10%**Curing conditions: 125 °C for 1 h + 180 °C for 2 h****Composition:**

Epon828 = 15.75g;

Heloxy 71 =9.25g (37% wt Epon+Heloxy 71);

Ancamine K 54 = 2.5g (10% wt Epon +Heloxy 71);

HG1 = 1.25g (5% wt Epon +Heloxy 71);

Microcapsule with ENB = 2.5g (10% wt Epon +Heloxy 71);

Figure 122 shows Load-Displacement curves for the Virgin sample and after the healing process (Healed).

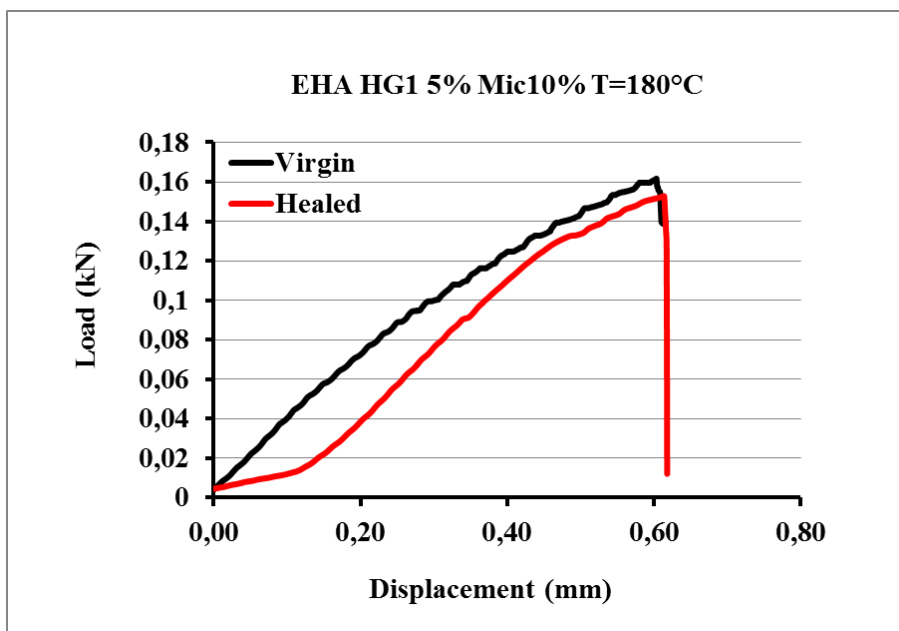


Figure 122: Load-Displacement Curves for Virgin and Healed sample EHA HG1 5% Mic 10% cured up 180 °C

Pc(Virgin)=0.1616 kN**Pc(Healed)=0.1527 kN****Efficiency=94.50%**

Sample Formulation: EBA1 HG1 5% Mic 17.2%**Curing conditions: 125 °C for 1 h + 170 °C for 2 h****Composition:**

Epon828 = 22.5g;

BDE =2.5g (10% wt Epon+BDE);

Ancamine K 54 = 2.5g (10% wt Epon +BDE);

HG1 = 1.25g (5% wt Epon +BDE);

Microcapsule with ENB = 4.3g (17.2% wt Epon +BDE);

Figure 123 shows Load-Displacement curves for the Virgin sample and after the healing process (Healed).

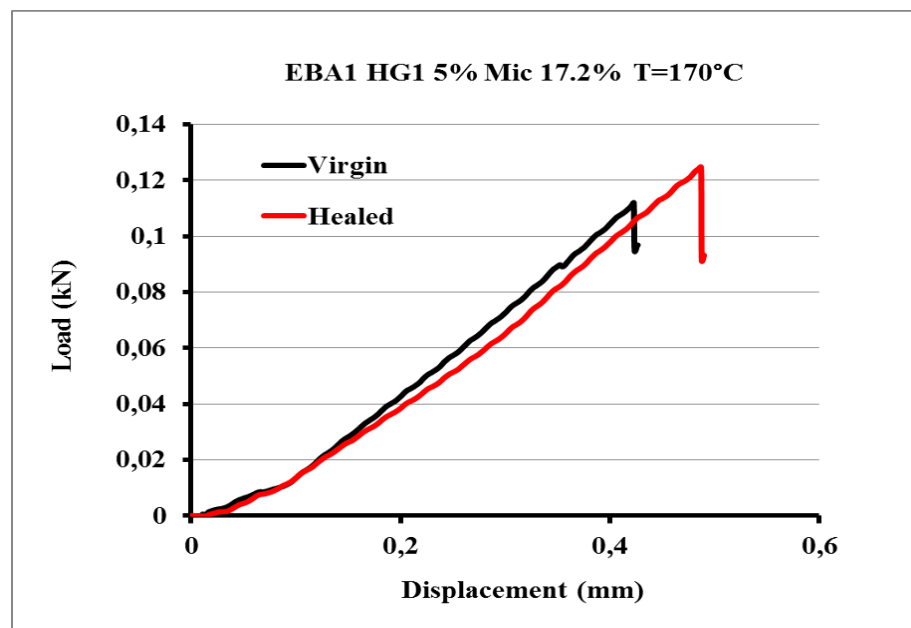


Figure 123: Load-Displacement Curves for Virgin and Healed sample EBA1 HG1 5% Mic 17.2% cured up 170 °C

Pc(Virgin)=0.1119 kN**Pc(Healed)=0.1247 kN****Efficiency=111.44%**

Sample Formulation: EBA1 HG1 10% Mic 20%**Curing conditions: 125 °C for 1 h + 170 °C for 2 h****Composition:**

Epon828 = 22.5g;

BDE =2.5g (10% wt Epon+BDE);

Ancamine K 54 = 2.5g (10% wt Epon +BDE);

HG1 = 2.5g (5% wt Epon +BDE);

Microcapsule with ENB = 5g (20% wt Epon +BDE);

Figure 124 shows Load-Displacement curves for the Virgin sample and after the healing process (Healed).

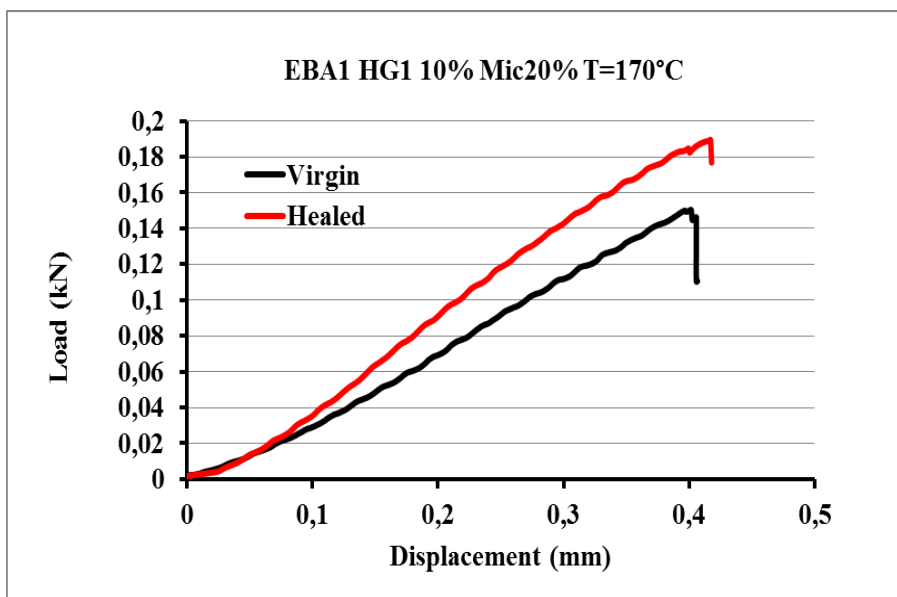


Figure 124: Load-Displacement Curves for Virgin and Healed sample EBA1 HG1 10% Mic 20% cured up 170 °C

Pc(Virgin)=0.1503 kN**Pc(Healed)=0.1896 kN****Efficiency=123.45%**

The self-healing efficiency tests, conducted at room temperature, gave good results for almost all formulations analyzed. Almost all samples showed an efficiency higher than 90%.

Samples EBA1 cured up 170 °C showed the higher values of efficiency.

For samples EBA1 cured up 170 °C with a microcapsules concentration higher than 10 % wt. the efficiency is over 100%.

For another specimen EBA1 HG1 5% Mic 20%, cured up to 170 °C (this data are not reported here) the self-healing efficiency was 129.73%. This test were performed several times giving always very high efficiency values, out all expectations.

Slightly lower efficiency is recorded for EBA formulation cured up 180 °C. At curing temperature up to 180 °C high values of efficiency (94.50%) were recorded for EHA samples.

Figure 125 compares self-healing efficiency values for all analyzed formulations and for the two different curing cycles. We can notice that the temperature of second step of curing cycle does not have so much influence on self-healing efficiency, even if the EBA1 formulations show highest efficiency values at a curing cycle up to 170 °C.

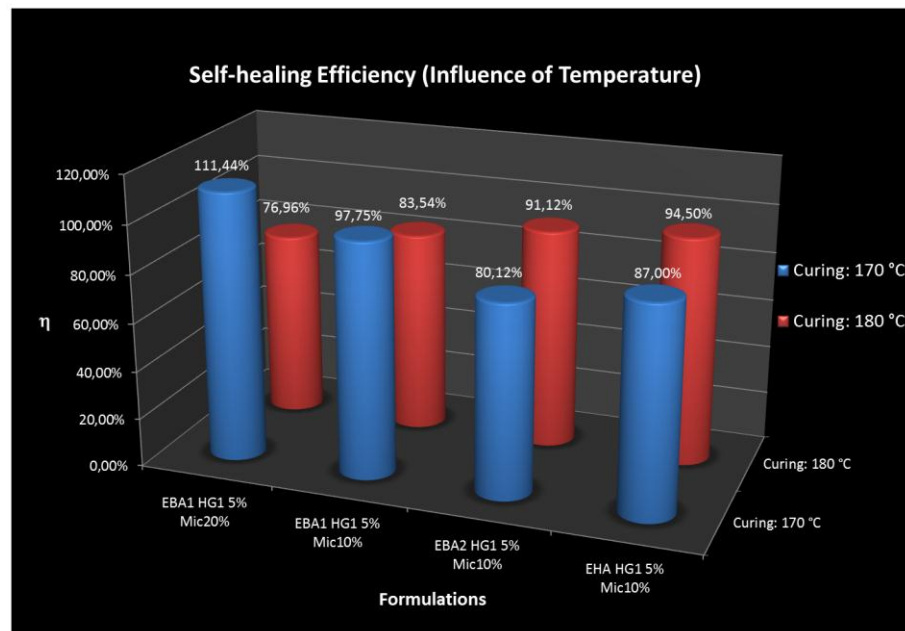


Figure 125: Self-healing efficiency with different formulations and curing cycles

Instead, the efficiency values are affected by the concentration of microcapsules in the formulation of the self-healing composite as we can see in Figure 126, where are compared self-healing samples with different amounts of microcapsules:

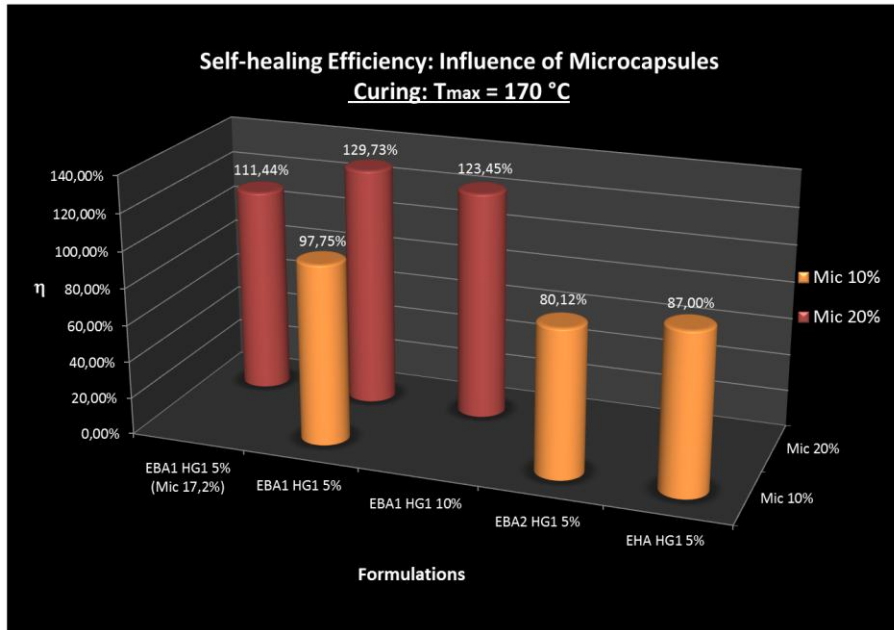


Figure 126: Self-healing efficiency of samples with different amounts of microcapsules

A cross-sectional view of our self-healing specimens (A, B, C,) is reported in the SEM images of Figure 127 which shows: healed crack faces (A); an ampler view of the self-healing specimen sections where the metathesis product, inside microcapsules after damage, can also be observed (C) with a magnification on the metathesis product (B).

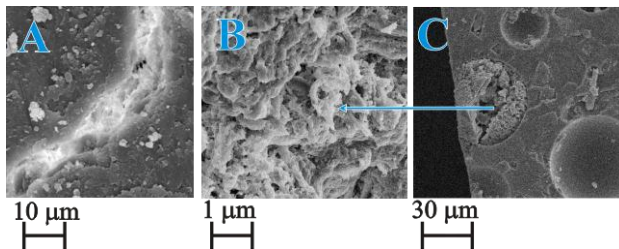


Figure 127. (C) Self-healing specimen sections with metathesis product inside of the microcapsules after damage; (B) magnification on the metathesis product inside the microcapsule; (A) healed crack faces closed by means of the metathesis product inside a crack.

6.6 System Scale - up: Development of Carbon Fiber Composite

After the valuation of the self-healing efficiency, we decided to realized a carbon fiber composite.

This experimentation was conducted at C.I.R.A. (Italian Aerospace Research Center) of Capua (CE), Italy, with liquid infusion process.

The Liquid Infusion Process (LIP) is a technique that uses vacuum pressure to drive resin into a laminate (fiberglass, carbon fiber, and Kevlar) [88]. Materials such as fiberglass, carbon fiber, and Kevlar are laid dry into the mold and the vacuum is applied before resin is introduced. Once a complete vacuum is achieved, resin is literally sucked into the laminate via carefully placed tubing.

Figure 128 shows a scheme of vacuum bag and tools used in a LIP.

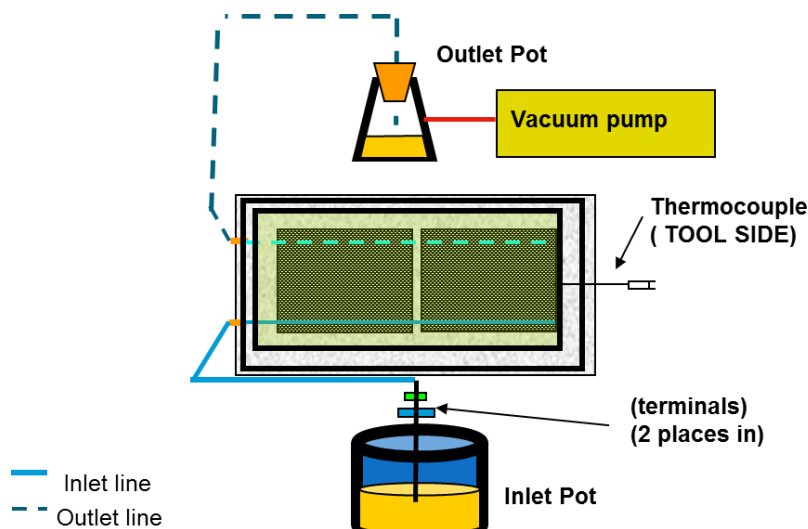


Figure 128 Schematic configuration of tools in a Liquid Infusion Process

The work plan included:

- Trials of viscosity (evaluation of the parameters of LPI)
- Trials of Gel Time
- Liquid Infusion Process
- Optical analysis of panels

First it was decided to realize a carbon fiber panel using a formulation of the resin without self- healing components. The composition of the resin was:

Thermoset resin (Epon 828) = 80 %

Reactive diluent (BDE) = 20%

Curing agent (Ancamine K 54) = 10% (wt. respect Epon+BDE)

Reinforcing fibers: 15 plies Injectex G1157 carbon fibers (Hexcel)

The composition with 20% of BDE was chosen to minimize the viscosity of the system.

The curing cycle chosen consisted of two isothermal steps:

1 h at 125 °C + 2 h at 170 °C.

Pressure in autoclave was 6 bar.

Figure 129 and 130 show the vacuum bag realized and the moment of fibers impregnation respectively.

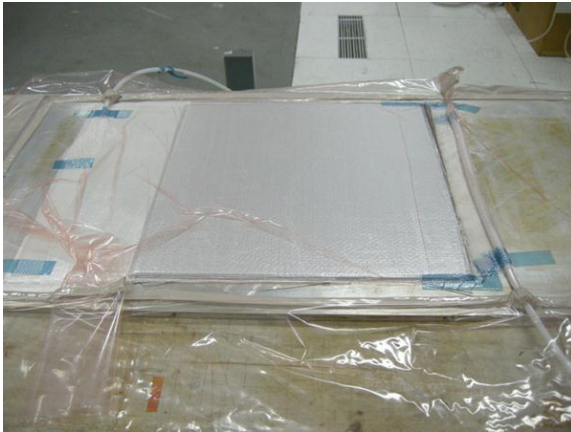


Figure 129: Vacuum bag realized

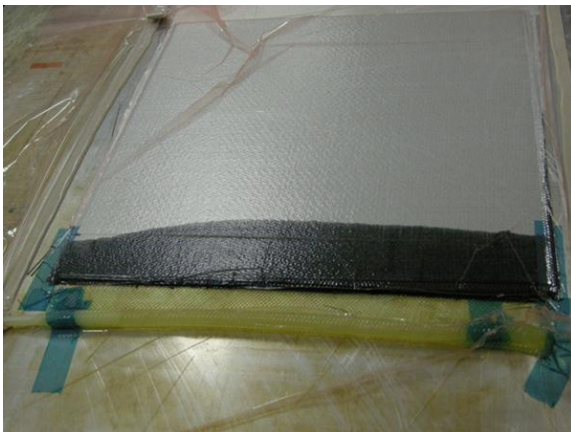


Figure 130: Moment of Fiber Impregnation

Figure 131 and 132 show the autoclave utilized for curing process and the realized panel.

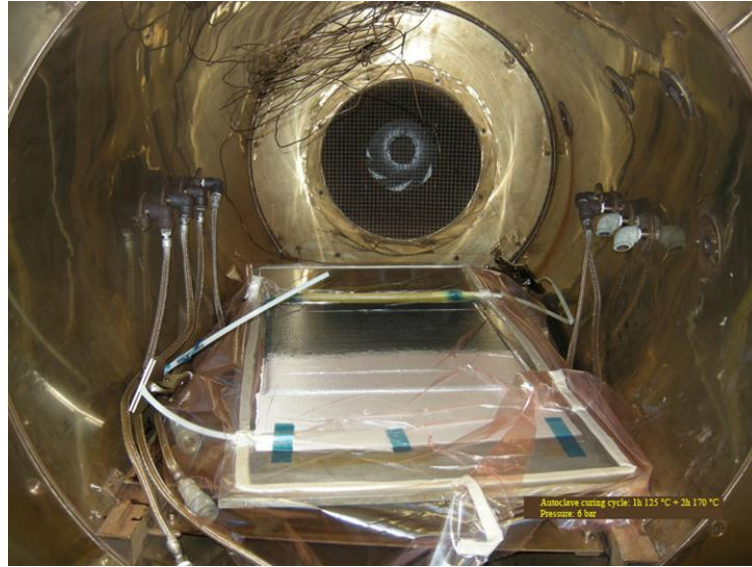


Figure 131 Autoclave used for curing process of the panel

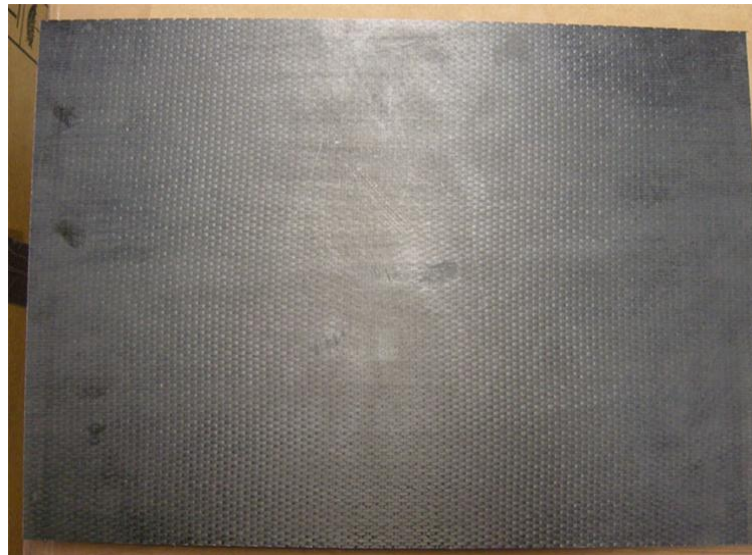


Figure 132 Realized panel

The cured panel (40 x 25 x 0.4 cm) was of excellent craftsmanship. The fibers appeared completely and uniformly impregnated. The overall appearance of the panel was satisfactory.

We decided to realize a second panel with self-healing components (10 % in wt. respect E+B of ENB filled microcapsules) and the same matrix and fiber compositions.

The panel was not realized because problems of fibers impregnation occurred with the process of liquid infusion: microcapsules caused a sharp increase in the viscosity of the system and prevented the resin to flow and impregnate the fibers.

We therefore found that the realization of a panel with a self-healing functionality as the self-healing system we realized, was not feasible with a Liquid Infusion Process.

Conclusions

7. Conclusions

During my Ph.D. work a self-healing composite which works actively and quickly at temperatures reaching as low as $-50\text{ }^{\circ}\text{C}$, has been formulated, prepared and characterized. To ensure high mechanical performances, this composite can be cured at high temperatures up to $180\text{ }^{\circ}\text{C}$, without deactivating the sel-healing functionality.

Inspired in terms of design by the system of White et al. which has been shown to be a pioneer in the development of self-healing polymeric materials, for our self-healing system attention has been focused on a composite material consisting of a thermosetting matrix (resin epoxy) in which are dispersed powders of catalyst active in metathesis reactions of olefins, and microcapsules containing a reactive monomer capable of polymerize and crosslink after metathesis reaction.

In order to obtain a high performances material and to achieve our technical targets related to aircrafts operational conditions, several systems were investigated that differ for the nature and the composition of the epoxy matrix, catalyst and active monomer used.

In Early Systems we have prepared and tested a self-healing specimen containing a finely pulverized Grubbs' first generation catalyst and microcapsules filled with liquid DCPD.

The epoxy matrix was a blend of epoxy resins and flexibilizer (Epon 828 and Heloxy 71) and an anionic initiator (Ancamine K 54 curing agent) which showed very little chemical interaction with the Grubbs' catalyst.

The Early Systems showed drawbacks which regarded the thermal stability of the Grubbs' catalyst inside the epoxy resin during the curing cycle and the activation of the metathesis reaction.

We found that 1st generation Grubbs' catalyst was decomposed at 150 °C in oxidant atmosphere. For this reason it was not possible curing the matrix at high temperatures (technical target: 170/180 °C) necessary to obtain a composite with high mechanical properties.

About the metathesis reaction of DCPD activated by the first-generation Grubbs' catalyst, we found that it was not active if the damaged material did not exceed the temperature of 10 °C, so a such formulated self-healing composite was not suitable for applications in structural advanced materials such as aircrafts.

This last drawback was overcome with the choice of a new healing agent in New Systems.

In New Systems microcapsules were prepared with the "core" of 5-ethylidene-2-norbornene (ENB).

The ENB healing agent allowed to formulate self-healing systems with a healing functionality active even at a temperature of -30 °C and with a faster kinetics (respect DCPD) with both 1st and 2nd generation Grubbs' catalysts.

However, self-healing functionality was not active at working temperatures of aircrafts as low as -50°C and also, was not possible to cure the composite at a temperatures range between 170 °C - 180 °C because at that temperatures the G1 and G2 catalysts were deactivated.

All above limitations have been successfully overcome with the introduction of new Hoveyda-Grubbs' catalysts, which were found to be stable at higher temperatures and active at very low temperatures.

In Latter Systems we found that best self-healing systems are those that rely self-healing functionality on metathesis reaction of ENB triggered by 1st generation Hoveyda-Grubbs' catalyst (HG1).

The romp reaction is active at working temperature conditions of aircrafts, even at temperatures below -50 °C.

The HG1 catalyst (active in the romp reaction of ENB with a very fast kinetics) doesn't deactivate at curing temperature of the matrix up to 180 °C. This make possible to obtain high performance materials, suitable for advanced applications such as aeronautics applications.

The matrix can be formulated with a new reactive diluent (BDE) that provides a greater fluidity of the initial mixture and the best mechanical performance of self-healing composite with highest values of glass transition temperature and elastic modulus.

For Latter Systems Almost all formulations show self-healing efficiency over 90%.

For samples EBA1 (10 % wt of reactive diluent) cured up 170 °C with a microcapsules concentration higher than 10 % wt. the self-repair effect allows the healed material to have a critical load ($P_{C\text{Healed}}$) higher than the critical load ($P_{C\text{Virgin}}$) of the virgin material and efficiency is over 100%.

A glimpse on the future....

There is no doubt that the development of self-healing materials of this type is based on the imitation of repair methods of biological systems. One of the biggest differences, however, is that, while biological systems implement self-repair in stages (multi-step) involving various biological and chemical agents, in synthetic self-healing systems repair is done in one step by a single healing agent. Extensive research in this direction could lead to the development of innovative materials provided with a “circulatory system” that continually transports substances in damaged areas for repairing. This new generation of structural materials will have self-healing mechanisms of living beings.

Bibliography

- [1] Riefsnider KL, Schulte K, Duke JC. Long term failure behaviour of composite materials. *ASTM STP* 1983;813: 136–59.
- [2] C. Dry and W. McMillan, *Smart Material. Structures*, 1997, 6, 35–39.
- [3] Dong Yang Wu, Sam Meure, David Solomon Self-healing polymeric materials: A review of recent developments, *Prog. Polym. Sci.* 33 (2008) 479–522.
- [4] Vincenzo Amendola, Moreno Meneghetti, Self-healing at the nanoscale, *The Royal Society of Chemistry* 2009 1, 74–88.
- [5] Kessler MR. 2007. Self-healing: a new paradigm in materials design. *Proc. Inst. Mech. Eng. G* 221(4):479–95.
- [6] Dry CM, Sottos NR. Passive smart self-repair in polymer matrix composite materials. In: *Conference on recent advances in adaptive and sensory materials and their applications*. Virginia, USA: Technomic; 1992. p. 438–44.
- [7] B.J. Blaiszik, S.L.B. Kramer, S.C. Olugebefola, J.S. Moore, N.R. Sottos, and S.R. White, *Self-Healing Polymers and Composites*, *Annu. Rev. Mater. Res.* 2010. 40:179–211.
- [8] Baker AA, Jones R, Callinan RJ. Damage tolerance of graphite epoxy composites. *Compos Struct* 1985;4:15–44.

- [9] Kinloch AJ. Mechanics and mechanisms of fracture of thermosetting epoxy polymers. *Adv Polym Sci* 1985;72: 45–67.
- [10] Ritchie RO. Mechanisms of fatigue-crack propagation in ductile and brittle solids. *Int J Fract* 1999;100:55–83.
- [11] Sauer JA, Richardson GC. Fatigue of polymers. *Int J Fract* 1980;16:499–532.
- [12] Ritchie RO. Mechanisms of fatigue crack-propagation in metals, ceramics and composites—role of crack tip shielding. *Mater Sci Eng Part A—Struct Mater Prop Microstruct Process* 1988;103:15–28.
- [13] Yousefpour A, Hojjati M, Immarigeon JP. Fusion bonding/welding of thermoplastic composites. *J Thermoplast Compos Mater* 2004;17:303–41.
- [14] Wool RP, O'Connor KM. A theory of crack healing in polymers. *J Appl Phys* 1981;52:5953-63.
- [15] Ageorges C, Ye L, Hou M. Advances in fusion bonding techniques for joining thermoplastic matrix composites: a review. *Compos Part A—Appl Sci Manuf* 2001;32: 839–57.
- [16] Wool RP, O'Connor KM. Time-dependence of crack healing. *J Polym Sci Part C—Polym Lett* 1982;20:7–16.
- [17] Kim HJ, Lee KJ, Lee HH. Healing of fractured polymers by interdiffusion. *Polymer* 1996;37:4593–7.
- [18] Paul J, Jones R. Repair of impact damaged composites. *Eng Fract Mech* 1992;41:127–4
- [19] Y. C. Yuan, T. Yin, M. Z. Rong, M. Q. Zhang Self healing in polymers and polymer composites. Concepts, realization and outlook: A review *eXPRESS Polymer Letters Vol.2, No.4 (2008) 238–250*.
- [20] Diels O, Alder K. Syntheses in the hydroaromatic series. I. Addition of “diene” hydrocarbons. *Liebigs Ann Chem* 1928;460:98-122.
-

[21] Chen X, Dam MA, Ono K, Mal A, Shen H, Nutt SR, Sheran K, Wudl F. A thermally re-mendable cross-linked polymeric material. *Science* 2002;295:1698-1702.

[22] Plaisted TA, Nemat-Nasser S. Quantitative evaluation of fracture, healing and rehealing of a reversibly cross-linked polymer. *Acta Materialia* 2007;55:5684-5696.

[23] Tian Q, Yuan YC, Rong MZ, Zhang MQ. A thermally remendable epoxy resin. *J Mater Chem* 2009;19:1289-1296.

[24] Murphy EB, Bolanos E, Shaffner-Hamann C, Wudl F, Nutt SR, Auad ML. Synthesis and characterization of a single-component thermally remendable polymer network: Staudinger and Stille revisited. *Macromolecules* 2008;41:5203-5209.

[25] Hayes SA, Jones FR, Marshiya K, Zhang W. A self-healing thermosetting composite material. *Composites Part A* 2007;38:1116-1120.

[26] Kalista SJ, Ward TC, Oyetunji Z. Self-healing of poly(ethylene-co-methacrylic acid) copolymers following projectile puncture. *Mech Adv Mater Struct* 2007;14:391-397.

[27] Varley RJ, van der Zwaag S. Development of a quasi-static test method to investigate the origin of self-healing in ionomers under ballistic conditions. *Polym Testing* 2008;27:11-19.

[28] S.-Y. Cho, J.-G. Kim and C.-M. Chung: 'A fluorescent crack sensor based on cyclobutane-containing crosslinked polymers of tricinnamates', *Sens. Actuators B*, 2008, 134B, 822–825.

[29] Cordier P, Tournilhac F, Soulie-Ziakovic C, Leibler L. 2008. Self-healing and thermoreversible rubber from supramolecular assembly. *Nature* 451(7181):977–80.

[30] Montarnal D, Tournilhac F, Hidalgo M, Couturier J, Leibler L. 2009. Versatile one-pot synthesis of supramolecular plastics and self-healing rubbers. *J. Am. Chem. Soc.* 131(23):7966–67.

[31] Kersey FR, Loveless DM, Craig SL. A hybrid polymer gel with controlled rates of cross-link rupture and self-repair. *J Roy Soc Interface* 2007;4:373-380.

[32] J. M. J. Paulusse and R. P. Sijbesma: ‘Reversible mechanochemistry of a PdII coordination polymer’, *Angew. Chem. Int. Ed.*, 2004, 43, 4460–4462.

[33] O’Connor K, Wool R. 1980. Optical studies of void formation and healing in styrene-isoprene-styrene block copolymers. *J. Appl. Phys.* 51(10):5075–79.

[34] Wool R, O’Connor K. 1981. Theory of crack healing in polymers. *J. Appl. Phys.* 52(10):5953–63.

[35] McGarel JO, Wool RP. 1987. Craze growth and healing in polystyrene. *J. Polym. Sci. B* 25(12):2541–60.

[36] Lin CB, Lee SB, Liu KS. Methanol-induced crack healing in poly(methyl methacrylate). *Polym Eng Sci* 1990;30: 1399–406.

[37] Rahmathullah MAM, Palmese GR. 2009. Crack-healing behavior of epoxy-amine thermosets. *J. Appl. Polym. Sci.* 113(4):2191–201.

[38] Morton J, Godwin EW. Impact response of tough carbon fibre composites. *Composite Struct* 1989;13:1-19.

[39] Trask RS, Williams GJ, Bond IP. Bioinspired self-healing of advanced composite structures using hollow glass fibres. *J Roy Soc Interface* 2007;4:363-371.

[40] White S. R., Sottos N. R., Geubelle P. H., Moore J. S., Kessler M. R., Sriram S. R., Brown E. N., Viswanathan S.: Autonomic healing of polymer composites. *Nature*, **409**, 794–797 (2001).

[41] Dry C. Procedures developed for self-repair of polymer matrix composite materials. *Composite Struct* 1996;35:263-269.

[42] Dry C, McMillan W. Three-part methylmethacrylate adhesive system as an internal delivery system for smart responsive concrete. *Smart Mater Struct* 1996;5:297-300.

- [43] M. Motuku, U. K. Vaidya and G. M. Janowski: 'Parametric studies on self-repairing approaches for resin infused composites subjected to low velocity impact', *Smart Mater. Struct.*, 1999, 8, 623–638.
- [44] Bleay SM, Loader CB, Hawyes VJ, Humberstone L, Curtis PT. A smart repair system for polymer matrix composites. *Composites Part A* 2001;32:1767-1776.
- [45]. Hucker M., Bond I., Foreman A., Hudd J., Optimisation of hollow glass fibers and their composites. *Adv. Comp. Lett.* 199; 8:181-189.
- [46] Trask RS, Williams GJ, Bond IP. Bioinspired self-healing of advanced composite structures using hollow glass fibres. *J Roy Soc Interface* 2007;4:363-371.
- [47] Pang JWC, Bond IP. A hollow fibre reinforced polymer composite encompassing self-healing and enhanced damage visibility. *Composite Sci Technol* 2005;65:1791-1799.
- [48] Pang JWC, Bond IP. 'Bleeding composites' - damage detection and self-repair using a biomimetic approach. *Composites Part A* 2005;36:183-188.
- [49] Hucker M., Bond I., Bleay S., Haq S., Experimental evaluation of unidirectional hollow glass fiber/epoxy composites under compressive loading. *Composites Part A*, 2003; 34-927-932.
- [50] Jang BZ, Chen LC, Hwang LR, Hawkes JE, Zee RH. The response of fibrous composites to impact loading. *Polym Composites* 1990;11:144-157.
- [51] Williams G., Trask R., Bond I., A self-healing carbon fiber reinforced polymer for aerospace applications, *Composites Part A* 2007; 38:1525-1532.
- [52] Trask R.S., Bond I.P., Biomimetic self-healing on advanced composite structures using hollow glass fibers, *Smart Mater. Struct.* 2006; 15:704-710.
-

- [53] H. A. Liu, B. E. Gnade and K. J. Balkus, Jr: 'A delivery system for self-healing inorganic films', *Adv. Funct. Mater.*, 2008, 18, 3620–3629.
- [54] N. Fikru: 'Self-healing of fiber reinforced polymer composites', MSc thesis, Louisiana State University, Baton Rouge, LA, USA, 2009.
- [55] Toohey KS, Sottos NR, Lewis JA, Moore JS, White SR. 2007. Self-healing materials with microvascular networks. *Nat. Mater.* 6(8):581–85.
- [56] Williams HR, Trask RS, Bond IP. 2007. Self-healing composite sandwich structures. *SmartMater. Struct.* 16(4):1198–207.
- [57] Asua JM. Miniemulsion polymerization. *Prog Polym Sci* 2002;27:1283-1346.
- [58] Brown EN, Kessler MR, Sottos NR, White SR. In situ poly(urea-formaldehyde) microencapsulation of dicyclopentadiene. *J Microencapsulation* 2003;20:719-730.
- [59] Keller MW, Sottos NR. Mechanical properties of microcapsules used in a selfhealing polymer. *Exper Mech* 2006;46:725-733.
- [60] Brown E.N., White S.R., Sottos N.R., Microcapsule induced toughening in a self-healing composite. *J.Mater. Sci.* 2004; 36: 1703-1710.
- [61] Rule JD, Sottos NR, White SR. Effect of microcapsule size on the performance of self-healing polymers. *Polymer* 2007;48:3520-3529.
- [62] Blaiszik BJ, Sottos NR, White SR. Nanocapsules for self-healing materials. *Composite Sci Technol* 2008;68:978-986.
- [63] Jones AS, Rule JD, Moore JS, Sottos NR, White SR. Life extension of self-healing polymers with rapidly growing fatigue cracks. *J Roy Soc Interface* 2007;4:395-403.
-

- [64] White S. R., Sottos N. R., Geubelle P. H., Moore J. S., Siriram S. R., Kessler M. R., Brown E. N.: Multifunctional autonomically healing composite material. US Patent 6 858 659, USA, (2005).
- [65] Brown E. N, Sottos N. R., White S. R.: Fracture testing of a self-healing polymer composite. *Experimental Mechanics*, **42**, 372–379 (2002).
- [66] Rule J. D., Sottos N. R., White S. R., Moore J. S.: The chemistry of self-healing polymers. *Education in Chemistry*, **42**, 130–132 (2005).
- [67] E. N. Brown, S. R. White and N. R. Sottos: ‘Retardation and repair of fatigue cracks in a microcapsule toughened epoxy composite – Part II: In situ self-healing’, *Compos. Sci. Technol.*, 2005, 65, 2474–2480.
- [68] Kessler MR, Sottos NR, White SR. Self-healing structural composite materials. *Composites Part A* 2003;34:743-753.
- [69] J. D. Rule and J. S. Moore: ‘ROMP reactivity endo- and exodicyclopentadiene’, *Macromolecules*, 2002, 35, 7878–7882.
- [70] T. C. Mauldin, J. D. Rule, N. R. Sottos, S. R. White and J. S. Moore: ‘Self-healing kinetics and stereoisomers of dicyclopentadiene’, *J. R. Soc. Interface*, 2007, 4, 389–393.
- [71] Liu X, Lee JK, Yoon SH, Kessler MR. 2006. Characterization of diene monomers as healing agents for autonomic damage repair. *J. Appl. Polym. Sci.* 101(3):1266–72.
- [72] Rule JD, Brown EN, Sottos NR, White SR, Moore JS. Wax-protected catalyst microspheres for efficient selfhealing materials. *Adv Mater* 2005;17:205–8.
- [73] Kamphaus JM, Rule JD, Moore JS, Sottos NR, White SR. A new self-healing epoxy with tungsten (VI) chloride catalyst. *J Roy Soc Interface* 2008;5:95-103.
- [74] Cho S. H., Andersson H. M., White S. R., Sottos N. R., Braun P. V.: Polydimethylsiloxane-based selfhealing materials. *Advanced Materials*, **18**, 997–1000 (2006).
-

[75] Keller M. K., White S. R., Sottos N. R.: A self-healing poly(dimethyl siloxane) elastomer. *Advanced Functional Materials*, **17**, 2399–2404 (2007).

[76] M. Z. Rong, M. Q. Zhang and W. Zhang: ‘A novel self-healing epoxy system with microencapsulated epoxy and imidazole curing agent’, *Adv. Compos. Lett.*, 2007, 16, 167–172.

[77] Yin T, Rong MZ, Zhang MQ, Yang GC. Self-healing epoxy composites - preparation and effect of the healant consisting of microencapsulated epoxy and latent curing agent. *Composite Sci Technol* 2007;67:201-212.

[78] Caruso M. M., Delafuente D. A., Ho V., Moore J. S., Sottos N. R., White S. R.: Solvent-promoted self-healing materials. *Macromolecules*, **40**, 8830–8832 (2007).

[79] G. Lewis, B. Wellborn, L. Jones II and P. Biggs: ‘A room temperature autonomically-healing PMMA bone cement: influence of composition on fatigue crack propagation rate’, *J. Appl. Biomater. Biomech.*, 2009, 7, 90–96.

[80] P. Biggs, L. Jones II, B. Wellborn and G. Lewis: ‘A self-healing PMMA bone cement: Influence of crystal size of Grubbs’ catalyst’, *IFMBE Proc.*, 2009, 14, 147–150.

[81] K. Vehlow, S. Maechling, and S. Blechert: ‘Ruthenium Metathesis Catalysts with Saturated Unsymmetrical N-Heterocyclic Carbene Ligands’, *Organometallics* 2006, 25-28.

[82] I. M. Ward, D. W. Hadley: ‘An Introduction to Mechanical Properties of Solid Polymers’, Wiley 2002.

[83] W.H. Brown: ‘Introduzione alla Chimica Organica’, Edises 1999.

[84] J. Coates: ‘ Interpretation of Infrared Spectra, a Pratical Approach’, *Encyclopedia of Analytical Chemistry*, John Wiley & Sons Ltd, 2000.

[85] Mostovoy, S., Crosley P.B., and Ripling, E.J., ‘Use of Crack-Line Loaded Specimens for measuring Plain-Strain Fracture Toughness,’ *J. Mater.*, **2**, 661–681 (1967).

-
- [86] Irwin, G.R., and Kies, J.A., 'Critical Energy Rate Analysis of Fracture Strength', Am. Welding Soc. J., **33**, 193-s–198-s (1954).
- [87] Guadagno, L.; Vertuccio, L.; Sorrentino, A, Raimondo, M., Naddeo, C., Vittoria, V., Iannuzzo, G., Calvi, E.; Russo, S.: 'Mechanical and barrier properties of epoxy resin filled with multi-walled carbon nanotubes'. Carbon 47(10), 2419-2430 (2009).
- [88] Crivelli Visconti, I.; Caprino, G., Langella, A.: 'Materiali Compositi, Tecnologie-Progettazione-Applicazioni', Hoepli, 2010.
- [89] Nebiyu Fikru "Self-healing of fiber reinforced polymer composites". B.Sc., Addis Ababa University, 2003, August 2009.
- [90] <http://en.wikipedia.org>.
-

I would like to say thank you to my Supervisor, Professor Liberata Guadagno for her presence, patience and strong support: this would not have been possible without her.

Thanks also to Professor P. Longo for his advice and support. Thanks to the Engineers A. Albolino (Alenia Aeronautica), S. Russo (Alenia Aeronautica) and F. Lenzi (Cyttec Engineered Materials) for their support and friendship.

Thanks to Professor V. Vittoria for her presence and advices. Thanks to Doctors M. Raimondo (Rex), C. Naddeo, A. Mariconda and to Engineer L. Vertuccio (Gigi): they revealed to me the secrets of a good researcher.

Thanks to Engineers C. Vitiello and L. Scatteia for their precious work at CIRA.

Thanks to Professor L. Incarnato for her kindness in making available her laboratory and equipments.

Thanks also to Doctors M. Stanzione, L. Tammaro, V. Bugatti and G. Gorrasi for their precious advice and friendship.

Special thanks to my best (UNISA) friend Pina (Engineer G. Russo is too serious): she doesn't have much patience, but a great heart.

Thanks also to Gennaro, Ilaria and Pask (Marciello Pascalino for best friends only): they are so special to me.

Thanks to my lifelong friends Marco, Antonella, Fabio and Fausto for their presence in almost every critical moments of my life.

Thanks to my sister Rosanna and Mimmo: I think of you everyday.

A special thank you to my dear Valentina for her love, support, patience and understanding: we both know that life isn't a rose without thorns.

Finally, I would to say thanks to my parents Italo and Angelina for their strong support and love: I know I don't say it often, but I love you.